



THE UNIVERSITY *of* EDINBURGH

This thesis has been submitted in fulfilment of the requirements for a postgraduate degree (e. g. PhD, MPhil, DClinPsychol) at the University of Edinburgh. Please note the following terms and conditions of use:

- This work is protected by copyright and other intellectual property rights, which are retained by the thesis author, unless otherwise stated.
- A copy can be downloaded for personal non-commercial research or study, without prior permission or charge.
- This thesis cannot be reproduced or quoted extensively from without first obtaining permission in writing from the author.
- The content must not be changed in any way or sold commercially in any format or medium without the formal permission of the author.
- When referring to this work, full bibliographic details including the author, title, awarding institution and date of the thesis must be given.

A Pathway towards the Inverse Design of All-Composite Honeycomb Core Sandwich Panels

Jasotharan Sriharan



Institute for Infrastructure and Environment
University of Edinburgh

A Thesis Submitted in Partial Fulfilment of the
Requirements for the
Degree of Doctor of Philosophy

May 2024

Abstract

All-composite honeycomb cellular core sandwich panels are gaining wide popularity in lightweight structure applications due to their high specific stiffness and strength and multi-functional benefits. The honeycomb cellular core sandwich panels consist of a honeycomb core sandwiched between two face sheets. The performance of such sandwich panel is related to multiple geometric and material parameters of the core and face sheets. Due to a large number of parameters and their complex interactions affecting the performance of the honeycomb cellular core sandwich panels, the optimal design of sandwich panels is difficult and demands a systematic approach by the designer.

This thesis focuses on developing the necessary design tools required for the accurate and efficient inverse design of all-composite honeycomb core sandwich panels considering the key geometric and material parameters of the core and face sheets. First, a strain energy-based homogenisation model is developed to calculate the in-plane and out-of-plane effective stiffnesses of the laminated composite honeycomb core. Unlike the other existing models, the proposed model is applicable for all types of honeycomb cellular core geometries and both single lamella or laminated walls of different materials. Therefore, the proposed model contributes towards significantly enhancing the state of knowledge on the design of honeycomb cellular core sandwich panels. The proposed homogenisation model was validated using the finite element (FE) analysis results of different honeycomb core geometry and material combinations. The results from the proposed model and FE analysis showed a good agreement for all the different honeycomb core configurations considered in the study.

Next, the sandwich panels with honeycomb cores were analysed for the global responses using the equivalent models based on the first-order shear deformation theory (FSDT). The honeycomb cores in the sandwich panels were represented as a homogeneous continuum with the effective stiffness matrix obtained from the proposed homogenisation model. The sandwich panels were analysed for the deflections and in-plane normal stresses of the face sheets under static bending

and the global critical buckling load under uniaxial compression using the equivalent models. The predictions were compared against results from the FE models of the sandwich panels with the actual core structure. A good agreement was found between the predictions from the proposed models and the FE results.

Since the proposed equivalent model for the sandwich panels cannot capture the possible local failures which are essential part of the sandwich panel design, new simplified semi-analytical models were developed to explicitly consider the local failures. A semi-analytical approach was developed for predicting the critical shear buckling load of the laminated composite honeycomb cores of different shapes. In the proposed model, two different boundary conditions were considered for the edges of the core walls. While using simply-supported boundaries for all the edges of the core wall gave conservative predictions of the critical shear buckling load, boundary conditions of rotationally restrained longer edges of the wall gave very close predictions of the critical shear buckling strain to the results from the FE analysis. The effect of different fibre lay-ups and shear loading conditions on the shear buckling strength were investigated for honeycomb cores with different shapes. A semi-analytical model was also proposed to predict the intracellular buckling of laminated composite face sheets with non-rectangular cells. The proposed approach was formulated to be as general as possible to take into account different geometric shapes of the cell, rotational restraints at the boundaries of the cell, and different loading conditions which had not been considered in the existing analytical solutions. Using the proposed approach, first, intracellular buckling of laminated composite face sheets with hexagonal cell was studied under various compressive loadings. While the proposed approach with simply-supported boundaries for the cell gave conservative results, predictions with rotationally restrained boundaries for cell gave very close predictions to the FE results considering various conditions such as different cell sizes, core density, face sheet's fibre lay-up and loadings. The effect of all these different parameters on the intracellular cellular buckling load of the laminated composite face sheets were also studied.

Keywords: Lightweight, All-composite, Laminated composite, Cellular core, Honeycomb core, Sandwich panel, Homogenisation model, Effective stiffness, Equivalent model, Shear buckling, Intracellular buckling, Semi-analytical, Inverse design.

Lay summary

Sandwich panels are widely used in lightweight construction in many industries, including aerospace, automotive, and civil engineering. A Sandwich panel consist of three main components: two thin and strong face sheets separated by a thick and light core. With the advancement of material and manufacturing technologies, a large number of material and geometric choices are available to select from when designing sandwich panels. Many geometric and material parameters and their complex interactions affecting the performance of sandwich panels have made determining the best design of sandwich panels a difficult task. Often, systematic approaches based on inverse design approach are used for the design of sandwich panels.

In recent years, all-composite honeycomb cellular core sandwich panels have gained wide recognition in lightweight sandwich structure applications due to their high specific stiffness and strength and multi-functional characteristics. Due to the complexity of material and geometric parameters and their interactions related to all-composite honeycomb core sandwich panels, most of the existing models for inverse design cannot be used for all-composite sandwich panels. Those can be used are only applicable for a very limited range of material and geometric options. Therefore, there is a need to develop more generally applicable models to carry out the inverse design of all-composite honeycomb core sandwich panels, which will enable better design of the all-composite sandwich panels.

Therefore, this thesis focuses on developing the design tools required for the accurate and efficient inverse design of all-composite honeycomb core sandwich panels, considering important parameters related to the geometry and materials of the core and face sheets. Since carrying out calculations for the exact geometry of the honeycomb cores is difficult and computationally demanding, the complex geometry of the honeycomb core is approximated by an equivalent homogenised core. Theoretical models were developed to determine the equivalent stiffness of the homogenised core for various types of honeycomb cellular core geometries and materials. The proposed homogenisation model was validated using the finite element (FE) analysis of the honeycomb cores, and the results from the proposed model and

FE analysis showed a very good agreement. Theoretical models were also developed to predict the global stiffness response of all-composite honeycomb core sandwich panels, where core stiffness was determined from the above-described theoretical models. This model saves significant computational time compared to detailed FE models. The effectiveness of the theoretical models in predicting the responses of sandwich panels was evaluated against the 3D FE models for various thickness ranges of symmetric and asymmetric face sheets and for the honeycomb cores with different fibre lay-up.

In the design of the honeycomb core sandwich panels, it's also important to consider failures such as local buckling of the face sheets and cell walls. Because the theoretical models represent the honeycomb cores as a homogeneous continuum, those models cannot capture local buckling failures. Therefore, a semi-analytical approach was developed to predict the critical shear buckling load of the laminated composite honeycomb cores with different shapes. The effect of different fibre lay-ups and the direction of shear loadings on the shear buckling strength were investigated for honeycomb cores with different shapes. The comparisons between the FE results and the proposed semi-analytical model for the core wall buckling showed a very good agreement. A semi-analytical model was also proposed to predict the intracellular buckling of laminated composite face sheets with non-rectangular cells. The proposed approach was formulated as a general approach to consider different geometric shapes of the cell and suitable boundary and different loading conditions, which had not been considered in the existing analytical solutions. Using the proposed approach, first, intracellular buckling of laminated composite face sheets with hexagonal cell was studied under various compressive loadings. The effect of different cell size, core density, face sheet fibre layup, and loadings were investigated using the proposed semi-analytical model and FE analysis. The results from the proposed semi-analytical model and FE showed a very good agreement for all the different cases considered in the study.

Acknowledgement

Firstly, I sincerely thank my supervisor, Professor Dilum Fernando, for giving me this opportunity to do my PhD. I greatly appreciate his outstanding support and guidance towards my PhD. In addition to his support for this work, Professor Fernando has always been an inspiration to me, whose humility and sincerity I will always strive for. I am grateful for his mentorship and leadership, which gave me the room to make mistakes and learn and improve my skills as a researcher. I would also like to thank my co-supervisor, Dr Marcelo Dias, for his advice and encouragement throughout my PhD. The number of hours of in-depth discussion helped me a lot to improve my work and the outputs of my research. Having your support and guidance readily accessible has been invaluable. My humble thanks go to Professor Sondipon Adhikari for his valuable advice and support. Your willingness to share your expertise and take the time to offer thoughtful insights has been immensely beneficial to my PhD. It was an absolute pleasure working under their guidance and support.

I would like to thank all my colleagues in the Mechanics of Architected Systems and Structures (MASS) research group, especially Darshana, Adriano, Leo, and Sithija, for making my PhD journey enjoyable at the University of Edinburgh. They have been always a great companion to me over the years. I thank them for all the great talks related to my research and outside of the research and all the great moments during this PhD journey.

I am sincerely thankful to the Institute for Infrastructure and Environment, University of Edinburgh, for providing the necessary resources, facilities, and a conducive environment for my research.

I would like to thank Professor Chinthaka Mallikarachchi and Professor Ruwan Weerasekera at the University of Moratuwa, Sri Lanka, for their support and guidance in finding the best position for my PhD.

I would also like to thank all my friends and relatives who are not in Edinburgh but have found time to communicate with me and motivate me constantly. It had been

a tremendous moral support and energy buster to me whenever I felt bit down during this journey.

I cannot find the words to express my gratitude for the love and support from my mother Sivapackijam, father Sriharan, wife Inthuja and brother Parathan. Thank you for believing in me and bearing with me in all the difficult times. Without their love and support, I would never have achieved this place.

Declaration by Author

I hereby declare that the thesis titled “An Inverse Approach to the Design of Honeycomb Core Sandwich Panels” presented for the Degree of Philosophy has been composed by myself and that the work contained herein is my own except where explicitly stated otherwise in the text. I also confirm that this work has not been submitted for any other degree or professional qualification.

Jasotharan Sriharan

03/05/2024

List of Publications

Conference Papers:

- **Sriharan, J.**, Dias, M., Fernando, D., & Adhikari, S. Pathway towards inverse design of sandwich panels: Equivalent shell model for cellular core sandwich panels. In *SAMPE EUROPE Conference and Exhibition 2022*, Hamburg, Germany, 15-17 November 2022.
- **Sriharan, J.**, Dias, M., Fernando, D., & Adhikari, S. Prediction of local buckling of composite cellular core in sandwich panels. In *UK Association for Computational Mechanics (UKACM) Conference 2023*, Warwick, UK, 19-21 April 2023.
- **Sriharan, J.**, Dias, M., Fernando, D., & Adhikari, S. Inverse design of light weight sandwich panels. In *9th Annual World Congress of Advanced Materials-2023 (WCAM-2023)*, Tokyo, Japan, 10-12 May 2023.

Refereed Journal Papers:

- **Sriharan, J.**, Dias, M., Fernando, D., & Adhikari, S. A unified approach for the prediction of the effective properties of laminated composite cellular core. *Engineering Structures* (2024), 299, 117106.

Table of Contents

Abstract	i
Lay summary	iii
Acknowledgement	v
Declaration by Author	vii
List of Publications	viii
Table of Contents	ix
List of Figures	xiii
List of Tables	xix
List of Abbreviations and Symbols	xxii
Chapter 1:	1
Introduction	1
1.1 Background.....	1
1.2 Motivation and aim	6
1.3 Significant contributions of the thesis	8
1.4 Outline of the thesis	8
1.5 References.....	10
Chapter 2:	13
Literature Review	13
2.1 General	13
2.2 Materials and manufacturing techniques for sandwich structures.....	15
2.3 Theory and analysis approach for the sandwich panels	21
2.3.1 Theories for analysing the sandwich panels	21
2.3.2 Effective elastic properties of honeycomb core.....	23
2.4 Failure predictions in sandwich panels	28

2.4.1	Global buckling and shear crimping	28
2.4.2	Cell wall buckling	29
2.4.3	Wrinkling of the face sheets	30
2.5	Intracellular buckling	33
2.6	Design methodology for sandwich panels	35
2.7	Summary and research gaps	36
Chapter 3:		47
Effective stiffness matrix of laminated composite wall honeycomb core.....		47
3.1	General	47
3.2	Strain-energy based homogenisation.	47
3.2.1	Strain energy density of the honeycomb core RVE	50
3.2.2	Solving equations to get the effective stiffness components	60
3.3	Force-equilibrium based approach.....	62
3.4	Prediction of effective stiffness properties.....	66
3.4.1	Effective properties of laminated composite wall honeycomb core	66
3.4.2	Comparison of effective properties of honeycomb cores with different shapes	79
3.4.3	Design charts for the predictions of effective properties	87
3.5	Conclusions	93
	References	94
Chapter 4:		97
Equivalent model of the laminated composite honeycomb core sandwich panels		97
.....		97
4.1	General	97
4.2	Equivalent model for the sandwich panels	98
4.2.1	Displacement fields.....	99
4.2.2	Stress and strain relationships.....	100
4.2.3	Stress resultants	101

4.2.4	Equivalent transverse shear stiffness	103
4.3	Analysis of the sandwich panels	107
4.3.1	Analysis for linear static bending of sandwich panels	108
4.3.2	Influence of important parameters of sandwich panels on the accuracy of equivalent models	119
4.3.3	Analysis for global buckling of sandwich panels	121
4.3.4	Sandwich panels with different honeycomb core shapes	122
4.3.5	Comparison of the predictions with existing experimental studies	123
4.4	Conclusions	125
4.5	References.....	126
Chapter 5:	129
Local buckling of laminated composite honeycomb core in sandwich panels	129
5.1	General.....	129
5.2	Shear buckling of the core walls	130
5.2.1	Relationship between the shear strain of each plate and the global transverse shear strain of the core.....	131
5.2.2	Critical shear buckling load of the composite plate	136
5.2.3	Determination of rotational stiffness.....	140
5.3	Theoretical analysis	142
5.3.1	Hexagonal core with identical plates.....	142
5.3.2	Hexagonal core with non-identical plates.....	144
5.4	Shear buckling of honeycomb core with different shapes	146
5.5	Validation of the proposed approach	150
5.5.1	Predictions of the shear buckling for the hexagonal core.....	152
5.5.2	Influence of important parameters	159
5.5.3	Comparisons between different honeycomb core shapes	166
5.6	Conclusions	168

5.7	References.....	168
Chapter 6:	170
Local buckling of face sheets in sandwich panels.....		170
6.1	General.....	170
6.2	Intracellular buckling of sandwich panels.....	171
6.2.1	Admissible displacement function.....	171
6.2.2	Minimisation of the total potential energy of the plate.....	175
6.2.3	Rotational restraint stiffness at the boundaries of the cell.....	180
6.3	Validation of the proposed approach.....	183
6.3.1	The effect of cell size on the intracellular buckling.....	184
6.3.2	The effect of core density on the intracellular buckling.....	190
6.3.3	The effect of the face sheet fibre lay-up on the intracellular buckling.....	193
6.3.4	Comparison of predictions with existing experimental studies.....	196
6.4	Intracellular buckling of face sheets with different cell shapes.....	198
6.4.1	Comparison of intracellular buckling of different cell shapes.....	199
6.5	Conclusions.....	205
6.6	References.....	205
Chapter 7:	207
Conclusions.....		207
7.1	Summary of key findings and impacts.....	207
7.2	Recommendations for future research.....	209
Appendix.....		xxvi

List of Figures

Fig. 1.1: Illustration of the use of sandwich panels for various applications from the different sectors	2
Fig. 1.2: (a) A sandwich panel consisting of (b) upper and lower face sheets and core.	2
Fig. 1.3: Honeycomb cores of different geometries and FRP materials configurations.	3
Fig. 1.4: Illustration of the parameters related to the design of honeycomb core sandwich panels.....	3
Fig. 1.5: Illustration of (a) backward and (b) forward method of inverse design techniques	6
Fig. 1.6: Schematic of the typical inverse design procedure for the honeycomb core sandwich panels.....	6
Fig. 2.1: Different types of sandwich panels used in sandwich structures	14
Fig. 2.2: Periodic cellular cores: 3D lattices of (a) truss type and (b) textile type and 2D prismatic cores of (c) corrugated type and (d) honeycomb type.	16
Fig. 2.3: Different manufacturing techniques for honeycomb cores.....	19
Fig. 2.4: Process of hierarchical wall square core fabrication using CFRP and foam (Feng et al. 2018). Reproduced with permission from the publisher.	20
Fig. 2.5: Illustration of concept of homogenisation of periodic honeycomb core	24
Fig. 2.6: Force-equilibrium approach to calculate the effective in-plane elastic modulus (a) RVE under in-plane force (b) total deflection of the inclined member due to (c) axial (d) shear and (e) bending deformations.	25
Fig. 2.7: Node region of hexagonal core considered by Malek & Gibson (2015).. ...	26
Fig. 2.8: Typical failure modes of sandwich panels (CMH-17 2013).....	28
Fig. 2.9: Different wrinkling modes of sandwich panel: a) antisymmetric b) symmetric and c) one-sided.	30
Fig. 2.10: Boundary conditions and geometry considered in (a) Fokker (b) Thomsen & Banks (2003) intracellular buckling models.	34
Fig. 3.1: A periodic honeycomb structure: (a) actual configuration (b) homogenous effective continuum body and RVE of (c) actual configuration and (d) effective continuum body.....	48

Fig. 3.2: (a) RVE of periodic honeycomb core fabricated out of (b) laminated composite walls consisting of (c) fibre layers at different orientations.	51
Fig. 3.3: The decomposition of the RVE into cell wall elements.	53
Fig. 3.4: Nodal displacements of the cell wall in (a) global (b) local coordinates.	54
Fig. 3.5: Schematic of deformation pattern of the unit cell under the application of uniform stress field σ_{11}	64
Fig. 3.6: (a) Boundaries of typical RVE for application of boundary conditions (b) RVE of hexagonal core for the FE models.....	68
Fig. 3.7: RVEs of (a) square (b) mixed rhombus-triangular and (c) triangular honeycomb core used in the analysis of proposed models.....	80
Fig. 3.8: RVEs of (a) square (b) mixed rhombus-triangular and (c) triangular honeycomb core used in FE models.	80
Fig. 3.9: Comparison of (a) effective stiffness Q_{11}^H of the laminated composite wall honeycomb cores and (b) percentage error of predictions relative to FE analysis. ...	81
Fig. 3.10: Comparison of (a) effective stiffness Q_{22}^H of the laminated composite wall honeycomb cores and (b) percentage error of predictions relative to FE analysis. ...	82
Fig. 3.11: Comparison of (a) effective stiffness Q_{12}^H of the laminated composite wall honeycomb cores and (b) percentage error of predictions relative to FE analysis. ...	83
Fig. 3.12: Comparison of (a) effective stiffness Q_{66}^H of the laminated composite wall honeycomb cores and (b) percentage error of predictions relative to FE analysis. ...	84
Fig. 3.13: Comparison of (a) effective stiffness Q_{44}^H of the laminated composite wall honeycomb cores and (b) percentage error of predictions relative to FE analysis. ...	85
Fig. 3.14: Comparison of (a) effective stiffness Q_{55}^H of the laminated composite wall honeycomb cores and (b) percentage error of predictions relative to FE analysis. ...	86
Fig. 3.15: Influence of wall stiffness parameters on (a) Q_{11}^H or Q_{22}^H (b) Q_{12}^H and (c) Q_{66}^H of the hexagonal core.....	89
Fig. 3.16: Influence of wall stiffness parameters on (a) Q_{11}^H or Q_{22}^H (b) Q_{12}^H and (c) Q_{66}^H of the triangular core.	90
Fig. 3.17: Influence of wall stiffness parameters on (a) Q_{11}^H or Q_{22}^H (b) Q_{12}^H and (c) Q_{66}^H of the square core.	91
Fig. 3.18: Influence of wall stiffness parameters on (a) Q_{11}^H or Q_{22}^H (b) Q_{12}^H and (c) Q_{66}^H of the mixed rhombus-triangular core.....	92

Fig.4.1: (a) A sandwich panel and (b) typical section across the 1-3 plane of the sandwich panel under consideration.	99
Fig.4.2: Illustration of deformation of the sandwich panel in 1-3 plane according to FSDT.....	99
Fig.4.3: Forces and moments acting on the sandwich panel.	101
Fig.4.4: Typical transverse shear strain variation in (a) homogenous isotropic plate and (b) sandwich panels.	104
Fig.4.5: (a) Simply-supported and (b) cantilever sandwich panels considered for the analysis.	108
Fig.4.6: Contour maps of the displacement of (a) 3D model and (b) equivalent model of the simply-supported sandwich panel having hexagonal core of fibre lay-up [45/-45/0/-45/45].	110
Fig.4.7: Contour maps of the displacement of (a) 3D model and (b) equivalent model of the cantilever sandwich panel having hexagonal core of fibre lay-up [45/-45/0/-45/45].	110
Fig.4.8: Comparison of displacement of 3D models and equivalent models of the simply-supported sandwich panels having hexagonal core of different fibre lay-up.	111
Fig.4.9: Comparison of displacement of 3D models and equivalent models of the cantilever sandwich panels having hexagonal core of different fibre lay-up.....	111
Fig.4.10: Contour maps of the in-plane normal stress σ_{11} of the simply supported sandwich panel consisting of hexagonal core with fibre lay-up [45/-45/0/-45/45]. ...	114
Fig.4.11: Comparisons of in-plane normal stress σ_{11} of the simply-supported sandwich panels along axis-1 for different fibre lay-up of the hexagonal core.	115
Fig.4.12: Contour maps of the in-plane normal stress σ_{11} of the cantilever sandwich panel consisting of hexagonal core with fibre lay-up [45/-45/0/-45/45].	116
Fig.4.13: Comparisons of in-plane normal stress σ_{11} of the cantilever sandwich panels along axis-1 for different fibre lay-up of the hexagonal core.....	117
Fig.4.14: Sandwich panel under uniaxial loading for the global buckling analysis.	121
Fig.4.15: Comparison of maximum displacements of the sandwich panels with different honeycomb core shapes.	123
Fig.4.16: (a) All-CFRP sandwich panel under three-point loading and (b) failure due to face fracture.	124

Fig.4.17: Comparisons of load-displacement behaviour from the 3-point bending experiments of Wei et al. (2020) and the equivalent models.....	125
Fig. 5.1: (a) Contour map of the shear strain of the hexagonal core with fibre lay-up [45/-45/0/-45/45] and b) variation of the shear strain at lower (L), middle (M) and upper (U) points of the core walls.....	131
Fig. 5.2: (a) RVE of hexagonal core with the nodal numbers and characteristic dimensions, (b) deformed shape of the plate under positive shear strain..	132
Fig. 5.3: Illustration of the global transverse shear strains of typical honeycomb RVE.	134
Fig. 5.4: Repetition of the RVEs to form the periodic honeycomb core.....	134
Fig. 5.5: (a) Composite plate subjected to in-plane shear (b) rotationally restrained plate along longer edges.	138
Fig. 5.6: Flowchart for the calculation of critical shear buckling strain of a honeycomb core	142
Fig. 5.7: Deformed configuration of RVE with identical composite plates under the shear load (a) γ_{13} (b) γ_{23} and (c) $\gamma_{13} / \gamma_{23} = 1$	143
Fig. 5.8: Failure phase map of the hexagonal core with identical orthotropic plates.	144
Fig. 5.9: Deformed configuration of RVE with non-identical composite plates under the shear load (a) γ_{13} (b) γ_{23} and (c) $\gamma_{13} / \gamma_{23} = 1$	145
Fig. 5.10: Failure phase map of the hexagonal core with non-identical orthotropic plates. Plate-I has double thickness of plate-II and plate-III.	146
Fig. 5.11: RVEs of (a) triangular core (b) rectangular core.	147
Fig. 5.12: Deformed configuration of triangular RVE with identical composite plates under the shear load (a) γ_{13} (b) γ_{23} and (c) $\gamma_{13} / \gamma_{23} = 1$	148
Fig. 5.13: Failure phase map of the triangular core with identical orthotropic plates.	149
Fig. 5.14: Deformed configuration of square RVE with identical composite plates under the shear load (a) γ_{13} (b) γ_{23} and (c) $\gamma_{13} / \gamma_{23} = 1$	150
Fig. 5.15: FE models analysed for the shear load (a) γ_{13} (b) γ_{23} and (c) $\gamma_{13} / \gamma_{23} = 1$	151
Fig. 5.16: Top view and side view of critical buckling mode shapes.	157

Fig. 5.17: Variation of the critical shear buckling strain with different length ratio between plate-I and plate-II for the shear load	160
Fig. 5.18: Variation of the critical shear buckling strain with the angle θ between the plates.....	162
Fig. 5.19: Variation of the critical shear buckling strain and shear buckling strength with the relative core density of the honeycomb.....	164
Fig. 5.20: Comparison of the (a) critical shear strains and (b) percentage of difference in predictions between with and without the consideration of bend-twist coupling for different shear loads.....	165
Fig. 5.21: Comparison of critical shear strain between honeycomb cores with different shapes	167
Fig.6.1: (a) A sandwich panel with intracellular buckling and (b) typical hexagonal cell of factsheet subjected to uniform biaxial compressive force.	171
Fig.6.2: Rectangular plate of all edges rotationally restrained subjected to biaxial compression.....	172
Fig.6.3: A hexagonal cell (a) with approximate boundaries defined using polynomial functions and (b) with the boundary moments at the rotationally restrained edges.	175
Fig.6.4: Typical section of the deformed shape of sandwich panel under axial compression and bending.	181
Fig.6.5: Illustration of rotational restrain provided by the core walls against buckling of face sheets under (a) axial compression and (b) bending of sandwich panel.	181
Fig.6.6: The sandwich panel considered for the intracellular buckling analysis.	184
Fig. 6.7: Variation of intracellular buckling loads with cell sizes under different axial compressive loadings.....	185
Fig. 6.8: Comparison of intracellular buckling loads of different cell sizes from various methods for the uniaxial compression in direction-1.	187
Fig. 6.9: Comparison of intracellular buckling loads of different cell sizes from various methods for the uniaxial compression in direction-2.	187
Fig. 6.10: Variation of intracellular buckling loads with relative core density under different axial compressive loadings.....	191
Fig. 6.11: Comparison of intracellular buckling loads for different relative core density from various analytical methods for the uniaxial compression in direction-1.....	193
Fig.6.12: Comparisons of intracellular buckling loads for different relative core density from various analytical methods for the uniaxial compression in direction-2.....	193

Fig.6.13: Comparisons of intracellular buckling loads for different fibre lay-up of the face sheet under uniaxial compression in direction-1.....	195
Fig.6.14: Comparisons of intracellular buckling loads for different fibre lay-up of the face sheet under uniaxial compression in direction-2.....	195
Fig.6.15: Comparisons of intracellular buckling loads for different fibre lay-up of the face sheet under biaxial compression.	196
Fig.6.16: (a) All-CFRP sandwich panel tested under axial compression and (b) intracellular buckling mode of failure (Wei et al. 2022).....	197
Fig.6.17: Comparison of intracellular buckling predictions with the experimental results of Wei et al. (2022).	198
Fig. 6.18: Illustration of definition of the displacement functions for the (a) rhombus and (b) triangular cells.....	199
Fig. 6.19: Different cell shapes considered for the analysis of intracellular buckling.	200
Fig. 6.20: Comparison of intracellular buckling loads of different cell shapes consisting of equal inscribed circle under uniaxial compression (a) direction-1 and (b) direction-2.....	203
Fig. 6.21: Comparison of intracellular buckling loads of different cell shapes of equal area under uniaxial compression in (a) direction-1 and (b) direction-2.....	204

List of Tables

Table 2.1: Comparison of structural efficiency of sandwich panels in terms of weight (HexWeb™ 1999).....	14
Table 3.1: Mechanical properties of composite wall material.....	67
Table 3.2: Material configurations of the laminated composite walls.	67
Table 3.3: Boundary conditions, deformed shapes, and the total strain energy of the hexagonal core RVE with material configuration 1.	68
Table 3.4: Boundary conditions applied to RVEs to get the effective shell stiffness.	71
Table 3.5: Effective stiffness Q_{11}^H for the regular laminated composite wall hexagonal core.	72
Table 3.6: Effective stiffness Q_{22}^H for the regular laminated composite wall hexagonal core.	73
Table 3.7: Effective stiffness Q_{12}^H for the regular laminated composite wall hexagonal core.	74
Table 3.8: Effective stiffness Q_{66}^H for the regular laminated composite wall hexagonal core.	75
Table 3.9: Effective stiffness Q_{44}^H for the regular laminated composite wall hexagonal core.	76
Table 3.10: Effective stiffness Q_{55}^H for the regular laminated composite wall hexagonal core.	77
Table 4.1: Comparison of normalised maximum displacements of simply-supported sandwich panels.....	112
Table 4.2: Comparison of normalised maximum displacements of cantilever sandwich panels.....	113
Table 4.3: Comparison of normalised maximum displacements for different face sheet to sandwich panel thickness ratios with core fibre lay-up of [45/-45/0/-45/45].....	119
Table 4.4: Comparison of normalised maximum displacements for different face sheet to sandwich panel thickness ratios with core fibre lay-up of [0/0/90/0/0].	120
Table 4.5: Comparison of normalised maximum displacements for different upper face sheet to lower face sheet thickness ratios with core fibre lay-up of [45/-45/0/-45/45].	120

Table 4.6: Comparison of normalised maximum displacements for different upper face sheet to lower face sheet thickness ratios with core fibre lay-up of [0/0/90/0/0].	120
Table 4.7: Comparison of global buckling loads under uniaxial compression.....	122
Table 5.1: Material configurations of the core walls.	151
Table 5.2: Critical shear strain of the hexagonal core ($\rho^* = 0.072$) under $\gamma_{13} = \gamma$ (positive) and $\gamma_{23} = 0$	152
Table 5.3: Critical shear strain of the hexagonal core ($\rho^* = 0.072$) under $\gamma_{13} = \gamma$ (negative) and $\gamma_{23} = 0$	152
Table 5.4: Critical shear strain of the hexagonal core ($\rho^* = 0.072$) under $\gamma_{13} = 0$ and $\gamma_{23} = \gamma$ (positive).	153
Table 5.5: Critical shear strain of the hexagonal core ($\rho^* = 0.072$) under $\gamma_{13} = 0$ and $\gamma_{23} = \gamma$ (negative).	153
Table 5.6: Critical shear strain of the hexagonal core ($\rho^* = 0.072$) under $\gamma_{13} = \gamma$ and $\gamma_{23} = \gamma$ (positive).	153
Table 5.7: Critical shear strain of the hexagonal core ($\rho^* = 0.072$) under $\gamma_{13} = \gamma$ (negative) and $\gamma_{23} = \gamma$ (negative).	154
Table 5.8: Critical shear strain of the hexagonal core ($\rho^* = 0.036$) under $\gamma_{13} = \gamma$ (positive) and $\gamma_{23} = 0$	154
Table 5.9: Critical shear strain of the hexagonal core ($\rho^* = 0.036$) under $\gamma_{13} = \gamma$ (negative) and $\gamma_{23} = 0$	155
Table 5.10: Critical shear strain of the hexagonal core ($\rho^* = 0.036$) under $\gamma_{13} = 0$ and $\gamma_{23} = \gamma$ (positive).	155
Table 5.11: Critical shear strain of the hexagonal core ($\rho^* = 0.036$) under $\gamma_{13} = 0$ and $\gamma_{23} = \gamma$ (negative).	155
Table 5.12: Critical shear strain of the hexagonal core ($\rho^* = 0.036$) under $\gamma_{13} = \gamma$ (positive) and $\gamma_{23} = \gamma$ (positive).	156
Table 5.13: Critical shear strain of the hexagonal core ($\rho^* = 0.036$) under $\gamma_{13} = \gamma$ (negative) and $\gamma_{23} = \gamma$ (negative).	156
Table 5.14: Comparison of maximum of critical shear buckling strain of different honeycomb core shapes.	167
Table 6.1: Comparison of intracellular buckling load of sandwich panels with different cell sizes under axial uniaxial compression in direction-1.	184

Table 6.2: Comparison of intracellular buckling load of sandwich panels with different cell sizes under uniaxial compression in direction-2.....	185
Table 6.3: Comparison of intracellular buckling load of sandwich panels with different cell sizes under biaxial compression.	185
Table 6.4: Comparison of intracellular buckling load of sandwich panels with different cell sizes under bending about axis-2.	189
Table 6.5: Comparison of intracellular buckling load of sandwich panels with different cell sizes under bending about axis-1.	189
Table 6.6: Comparison of intracellular buckling load of sandwich panels with different cell sizes under biaxial bending.....	189
Table 6.7: Comparison of intracellular buckling load of sandwich panels with different relative core density under uniaxial compression in direction-1.	190
Table 6.8: Comparison of intracellular buckling load of sandwich panels with different relative core density under uniaxial compression in direction-2.	190
Table 6.9: Comparison of intracellular buckling load of sandwich panels with different relative core density under biaxial compression.....	191
Table 6.10: The fibre lay-ups considered for the face sheets.	194

List of Abbreviations and Symbols

Abbreviations

2D	Two dimensional
3D	Three dimensional
CFRP	Carbon fibre reinforced polymer
CLT	Classical laminate theory
EHSAPT	Extended higher order sandwich panel theory
ESLT	Equivalent single layer theory
FE	Finite element
FRP	Fibre reinforced polymer
FSDT	First-order shear deformation theory
GFRP	Glass fibre reinforced polymer
HSAPT	higher order sandwich panel theory
HSDT	Higher-order shear deformation theory
LWT	Layer-wise theory
RR	Rotationally restrained
RVE	Representative volume element
SS	Simply supported
ZZT	Zigzag theory

Symbols

$\bar{A}_{ij}, \bar{D}_{ij}, \bar{B}_{ij}$	Membrane, bending, and membrane-bending coupling stiffness components of the laminate with respect to mid-plane in $\bar{1}, \bar{2}, \bar{3}$ coordinate system
A_{ij}, D_{ij}, B_{ij}	Membrane, bending, and membrane-bending coupling stiffness components of laminate or sandwich panel with respect to mid-plane in 1,2,3 coordinate system

$\bar{a}_{ij}, \bar{d}_{ij}, \bar{b}_{ij}$	Membrane, bending, and membrane-bending coupling compliance components of laminate with respect to mid-plane in $\bar{1}, \bar{2}, \bar{3}$ coordinate system
a_{ij}, d_{ij}, b_{ij}	Membrane, bending, and membrane-bending coupling compliance components of laminate or sandwich panel with respect to mid-plane in 1,2,3 coordinate system
\mathbf{C}^H	Effective elasticity tensor of the core in 1,2,3 coordinate system
C_{ijkl}^H	Component of the effective elasticity tensor
D	Diameter of the inscribed circle within a cell
d	Distance between the neutral plane and mid plane of core wall
E_i^H	Effective elastic modulus of the core in global i -direction
$\bar{\mathbf{F}}$	Generalised nodal force vector of the wall element in $\bar{1}, \bar{2}, \bar{3}$ coordinate system
\mathbf{F}_p	In-plane force vector of the sandwich panel in 1,2,3 coordinate system
\mathbf{F}_s	Transverse shear force vector of the sandwich panel in 1,2,3 coordinate system
$\bar{F}_{(i)j}$	In-plane force acting at node i in the j -direction of the core wall element in $\bar{1}, \bar{2}, \bar{3}$ coordinate system
F_{ij}	Force per unit length in i^{th} direction acting on a plane perpendicular to j -direction in 1,2,3 coordinate system
\bar{F}_{ij}	Force per unit length in i^{th} -direction acting on a plane perpendicular to j -direction in $\bar{1}, \bar{2}, \bar{3}$ coordinate system
\bar{F}_{cr}	Critical buckling load of the laminate
G_{ij}^H	Effective shear modulus of the core
$\bar{\mathbf{G}}$	Matrix relating the normal strain to the vector of nodal forces of the core wall element in $\bar{1}, \bar{2}, \bar{3}$ coordinate
H	Total thickness of sandwich panel
h	Thickness/Depth of the core
$\bar{\mathbf{K}}$	Stiffness matrix of the wall element of core/laminate in $\bar{1}, \bar{2}, \bar{3}$ coordinate
\bar{K}_{ij}	Component of stiffness matrix $\bar{\mathbf{K}}$ at $(i, j)^{th}$ position

k_1, k_2	Stiffnesses of rotational restraints along the boundaries of composite plate perpendicular to direction- $\bar{1}$ and direction- $\bar{2}$
k_{ij}	Curvature of the composite laminate or sandwich panel in 1,2,3 coordinate system
\bar{k}_{ij}	Curvature of the composite laminate in $\bar{1}, \bar{2}, \bar{3}$ coordinate system
l_i	Length of i^{th} plate of the honeycomb core
\mathbf{M}_p	Vector of moments acting on the sandwich panel in 1,2,3 coordinate system
$\bar{M}_{(i)}$	Moment at node i of the wall element about $\bar{3}$ direction
\bar{M}_{ij}	Moment per unit length acting in $\bar{1}, \bar{2}, \bar{3}$ coordinate system
M_{ij}	Moment per unit length acting in 1,2,3 coordinate system
\mathbf{Q}_p^H	Effective in-plane stiffness matrix of the core in 1,2,3 coordinate system
\mathbf{Q}_s^H	Effective transverse shear stiffness matrix of the core in 1,2,3 coordinate system
Q_{ij}^H	Component of the effective stiffness matrix of the core
\mathbf{Q}_p	In-plane stiffness matrix of a lamina of sandwich panel in 1,2,3 coordinate system
\mathbf{Q}_s	Equivalent transverse shear stiffness matrix of the sandwich panel in 1,2,3 coordinate system
Q_{ij}^k	Component of the in-plane stress stiffness of k^{th} lamina in 1,2,3 coordinate system
\bar{Q}_{ij}	Component of the in-plane stress stiffness of a lamina in $\bar{1}, \bar{2}, \bar{3}$ coordinate system
p, q, r	Characteristics dimensions of the RVE
R	Degree of rotational restraint along boundaries of the composite plate
\mathbf{T}	Transformation matrix relating local and global displacement of the core wall
t	Thickness of the core wall
t_f	Thickness of the face sheet of the sandwich panel

$\underline{u}, \bar{\underline{u}}$	Vector of nodal displacements in 1,2,3 and $\bar{1}, \bar{2}, \bar{3}$ coordinate systems
U_b	Strain energy of the composite laminate due to bending
U_r	Strain energy of the composite laminate due to rotational restraint along the boundaries
$u_{(i)j}, \bar{u}_{(i)j}$	Displacement of node i in the global and local j -direction
$\bar{u}_i^a, \bar{u}_i^b, \bar{u}_i^s$	Normal displacement components of the core wall due to axial, bending and shear in local i -direction
V	Work done by the applied load on composite laminate
v_i^o	Displacement at point (x_1, x_2) of the reference plane in global i^{th} direction
v_i	Displacement at point (x_1, x_2, x_3) in global i -direction
v_{ij}^H	Effective Poisson's ratio of the homogenised core
w	Strain energy density of the RVE of the core
α	Skew angle of the buckling wave measured counterclockwise with respect to positive direction- $\bar{1}$
β_s	Non dimensional parameter defining effect transverse shear stiffness of the laminate
θ	Angle between the honeycomb core walls
ϕ	Angle of fibre orientation of the lamina measured counterclockwise with respect to the positive direction- $\bar{1}$
$\varphi(i)$	Rotation at i^{th} node about direction-3
ψ_i	Rotation of the plane perpendicular to global i -direction
ρ^*	Relative core density
$\varepsilon_{0,ij}$	Normal strain at the reference plane of sandwich panel in $\bar{1}, \bar{2}, \bar{3}$ coordinate system
$\bar{\varepsilon}_{0,ij}$	Normal strain at the reference plane of composite wall in $\bar{1}, \bar{2}, \bar{3}$ coordinate system
$\bar{\varepsilon}_{ij}$	Normal strain component in $\bar{1}, \bar{2}, \bar{3}$ coordinate system
ε_{ij}	Normal strain component in 1,2,3 coordinate system
$\gamma_{0,ij}$	Shear strain at the reference plane of composite wall in 1,2,3 coordinate system

$\bar{\gamma}_{0,ij}$	Shear strain at the reference plane of composite wall in $\bar{1}, \bar{2}, \bar{3}$ coordinate system
γ_{ij}	Shear strain of sandwich panel in 1,2,3 coordinate system
$\bar{\gamma}_{ij}$	Shear strain of composite wall in $\bar{1}, \bar{2}, \bar{3}$ coordinate system
$\bar{\sigma}_{ij}$	Normal stress of a lamina in $\bar{1}, \bar{2}, \bar{3}$ coordinate system
σ_{ij}^k	Normal stress of k^{th} lamina in 1,2,3 coordinate system
τ_{ij}	shear stress of a lamina in $\bar{1}, \bar{2}, \bar{3}$ coordinate system
τ_{ij}^k	Normal stress of k^{th} lamina in 1,2,3 coordinate system

Remark: Other symbols not mentioned here may be locally defined in the thesis. If appropriate, some of the symbols mentioned above may have duplicate definitions and may also locally redefined in parts of the thesis.

Chapter 1:

Introduction

1.1 Background

The quest for structural panels with high specific strength and stiffness was the main driver behind the concept of sandwich panel systems within the aerospace industry, which started in the 1930s (Zenkert 1997). Later, engineers started using sandwich panels for many applications in several other industries (Fig. 1.1), such as automotive, marine, construction, energy, etc. (Zenkert 1997). A sandwich panel consists of three main components: two thin, stiff and strong face sheets separated by a thick and light core (Fig. 1.2). Widespread material combinations are available to choose from for the face sheets and core of sandwich panels (Feng et al. 2020). Among the several types of core systems, the honeycomb cellular core is one of the commonly used core systems in sandwich panels, mainly due to its high specific strength and stiffness (Ashby & Gibson, 1997). The honeycomb cores can be fabricated using different materials ranging from metallic to non-metallic and can be of different core shapes (Fig. 1.3). With the advancement of materials and manufacturing technologies, the use of fibre-reinforced polymer (FRP) materials (e.g. Carbon fibre reinforced polymer (CFRP), Glass fibre reinforced polymer (GFRP)) for both face sheets and core (referred to as all-composite honeycomb core sandwich panels) has been made a feasible option. Such all-composite honeycomb core sandwich panels not only satisfy the structural requirements of high specific stiffness and strength but also can satisfy other multi-functional requirements such as energy absorption, acoustic absorption, thermal insulation and fire shielding, thermal transfer, and ballistic resistance (Russell et al. 2008, 2011; Feng et al. 2018; Pehlivan & Baykasoğlu 2019; Chen et al. 2021; Wei et al. 2019, 2020, 2022). Selection of the correct combination of materials and geometry of honeycomb cellular core and face sheets is important as the performance of the panel, especially the stiffness and strength of the sandwich panel are governed by the material and geometric parameters of the core and the face sheets (Fig 1.4). Transverse shear deformations of the core are likely to occur due to significantly different mechanical properties of the core and face sheets; thus, simple

structural theories such as Kirchhoff-Love plate theory cannot be used to analyse the behaviour of cellular core sandwich panels (Zenkert 1997). The complex behaviour of the sandwich panels presents a significant challenge to the design engineers in choosing the right material and geometric combinations to meet the required performance criteria. In most cases, designers have sought to use existing pre-assembled systems for solutions rather than designing new systems. The choice of materials and geometry in such pre-assembled systems are made based on engineering intuition and, thus, may not provide the best solution. Better design of sandwich panels requires an approach which considers the influence of many numbers of possible geometric and material combinations in a systematic way and provides solutions considering the trade-off between the different aspects of target performance criteria.



Fig. 1.1: Illustration of the use of sandwich panels for various applications from the different sectors (<https://thermhx.com/de/anwendungen-fuer-wabenkerne-und-wabenplatten/>). Reproduced with permission from publisher.

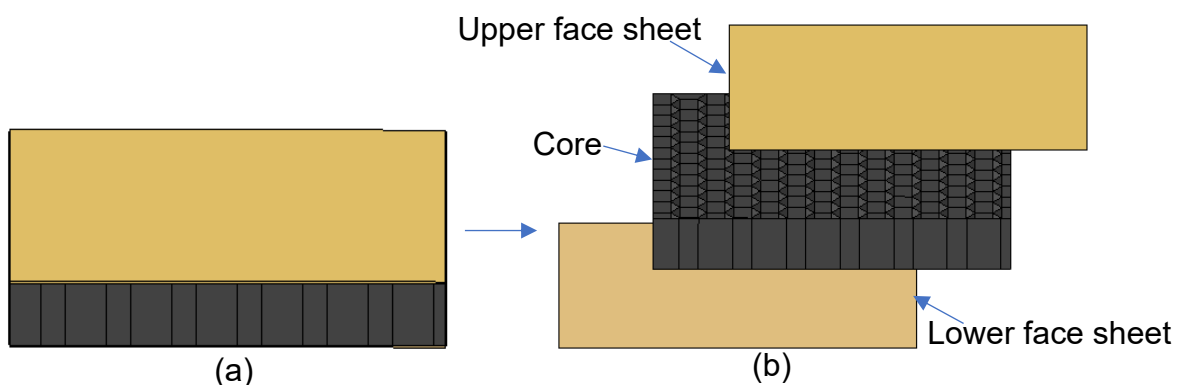


Fig. 1.2: (a) A sandwich panel consisting of (b) upper and lower face sheets and core.

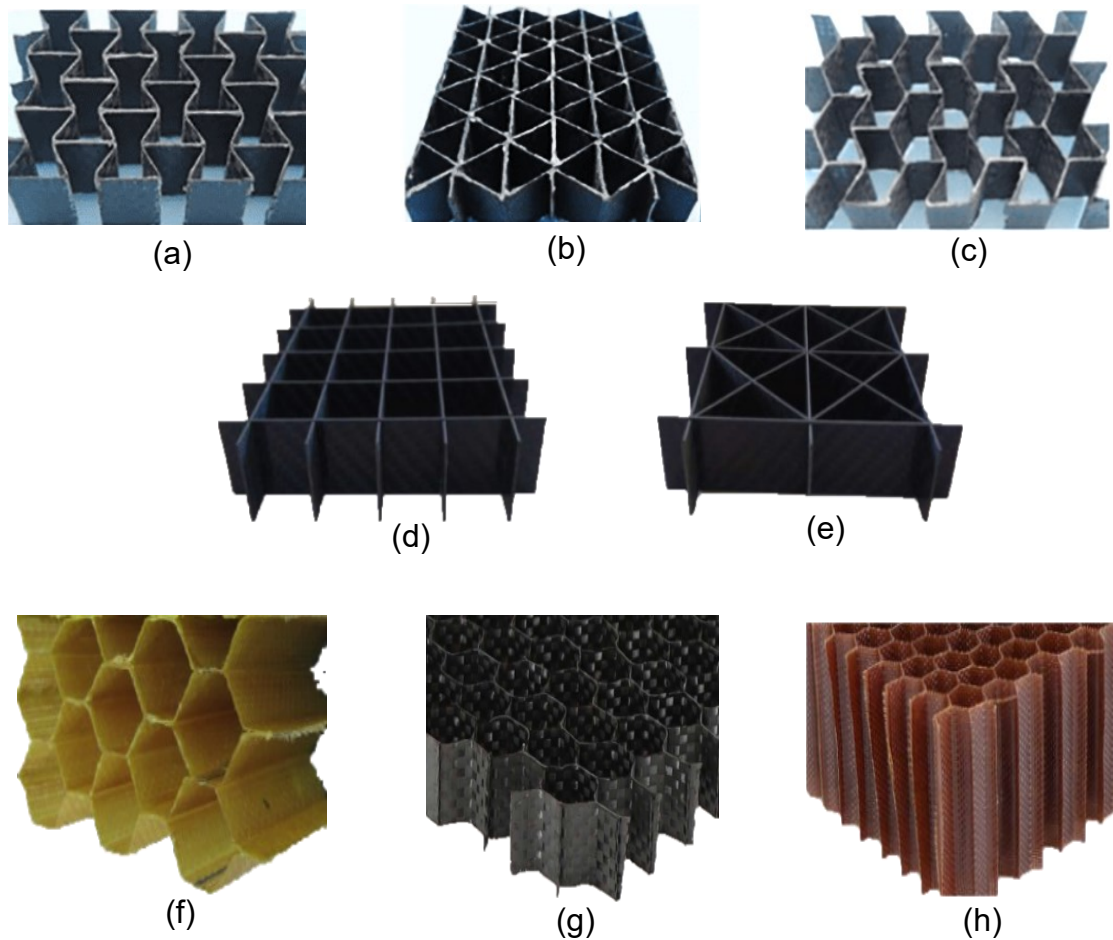


Fig. 1.3: Honeycomb cores of different geometries and FRP materials configurations [(a-c): Wei et al. 2020a; (d-e): Kiyak & Kaman 2019; (f): Hou et al. (2014) and (g-h): <https://www.euro-composites.com/en/honeycomb-core-portfolio-3/>.
Reproduced with permission from publisher.

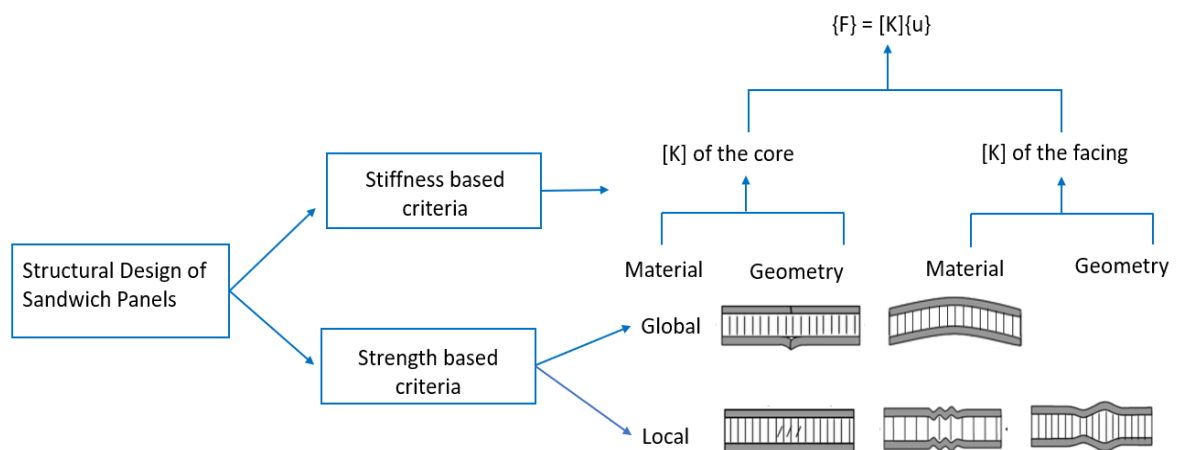


Fig. 1.4: Illustration of the parameters related to the design of honeycomb core sandwich panels.

Inverse design approach (Fig 1.5) is often used to select the best choices for design parameters in engineering designs (Loonen et al. 2022). Concepts of inverse

design can also be applied to the design of sandwich panels. Based on the number of variables considered in the design related to the geometry and materials of the core and face sheets, loading and boundary conditions of the sandwich panel and other design constraints, the inverse design approach for the problem can be a backward or forward approach (Loonen et al. 2022). In the backward approach, a direct inverse of the objective function is achieved analytically for the problem, whereas the forward approach is the systematic and intelligent use of direct functions to search for the domain of possible alternatives under defined constraints to determine the best options satisfying the target performance requirements. Although the backward approach is possible for a simple sandwich panel design with the minimal number of variables (Vinson 1986; Triantafillou & Gibson 1987; Murthy et al. 2006; Meidell 2009), forward approach (Fig 1.6) is often preferred when many variables are involved (Gantovnik et al. 2002; Tan & Soh 2007; Catapano & Montemurro 2014; Abouhamzeh & Sadighi 2016; Coburn & Weaver 2016; Xu et al. 2017; Fan et al. 2018; Irisarri et al. 2021; Santos et al. 2022; Seyyedrahmani et al. 2022; Wei et al. 2020b, 2022). The forward design approach can be carried out using different techniques, such as failure maps (Russel et al. 2011; Wei et al. 2020, 2022) or search algorithms. Latter is often preferred for the optimal design of the sandwich panel with a large number of variables (Gantovnik et al. 2002; Tan & Soh 2007; Hudson et al. 2010; Catapano & Montemurro 2014; Abouhamzeh & Sadighi 2016; Coburn & Weaver 2016; Xu et al. 2017; Fan et al. 2018). Regardless of the algorithms used, inverse design involves several iterative calculations. Thus, the sandwich panels are often modelled as equivalent models where the cellular core is represented as a homogenous continuum with effective stiffness properties for computational efficiency. Several beam and shell theories (Caliri Jr et al. 2016; Irfan & Siddiqui 2019) exist to model sandwich panels as equivalent models, but their complexity and accuracy vary depending on underlying assumptions and the number of variables used in the formulation of the theory. However, regardless of the theory used for the equivalent model of sandwich panels, the honeycomb cores are always represented as a homogenous continuum with effective stiffness properties. Different approaches exist to get the effective stiffness of the honeycomb cellular cores (Somnic & Jo 2022). However, most of the existing analytical models are for the hexagonal honeycomb core (i.e. honeycomb cellular core consisting of hexagonal cells) and consider only the isotropic materials for the core. Studies on the effective properties of laminated composite honeycomb cores are very

limited (Wang & Wang 2018), and there is no generalised simplified model for composite honeycomb cores of different shapes. The numerical homogenisation approaches typically rely on finite element (FE) analysis of representative volume elements (RVEs) of the cellular cores and allows the users to study more complex geometries (Penado 2013; Montemurro et al. 2016) and different materials. However, due to the significant efforts required in detailed numerical modelling, this approach is not practical when a large number of choices are available for different variables.

In addition to the stiffness, the strength of the sandwich panel is also an important performance to consider in the design of the sandwich panel. Although equivalent models are capable of predicting global responses such as rupture of face sheets and global buckling, the equivalent models cannot be directly used to predict most of the local failures, such as local buckling of core walls and face sheets commonly observed in honeycomb core sandwich panels. In analytical approaches towards the optimal designs of sandwich panels, these failures are often taken into account using simplified analytical or semi-analytical equations. In the past, many studies have been carried out on the local failure due to wrinkling of face sheets and analytical and semi-analytical solutions were proposed for wrinkling of isotropic (Hoff & Maunters 1945; Plantema 1966; Allen 1969; Niu & Talreja 1999; Birman 2004) and orthotropic (Vonach & Rammerstorfer 2000; Pozorski et al. 2021) cores. However, the studies on the other failure modes, such as buckling of the core walls and intracellular buckling, are very limited and existing solutions were found to be significantly under or overpredicting the failure loads due to underlying assumptions regarding the material, geometry, and loading and boundary conditions (Thomsen & Banks 2004). As these predictions based on the existing solutions for the local failures affect the accuracy of the inverse design, even with the most advanced search algorithms, accurate solutions may not be achieved. The accuracy and efficiency of the inverse design process for the sandwich panel depend significantly on the accuracy of the simplified approaches used to predict the stiffness and strength. Therefore, to determine the best material and geometry combinations of all-composite honeycomb core sandwich panels for the target structural performance, it is necessary to develop a methodology to accurately predict the stiffness and strength of sandwich panels with

the ability to consider a wide range of parameters affecting the performance while keeping the computational demand low.

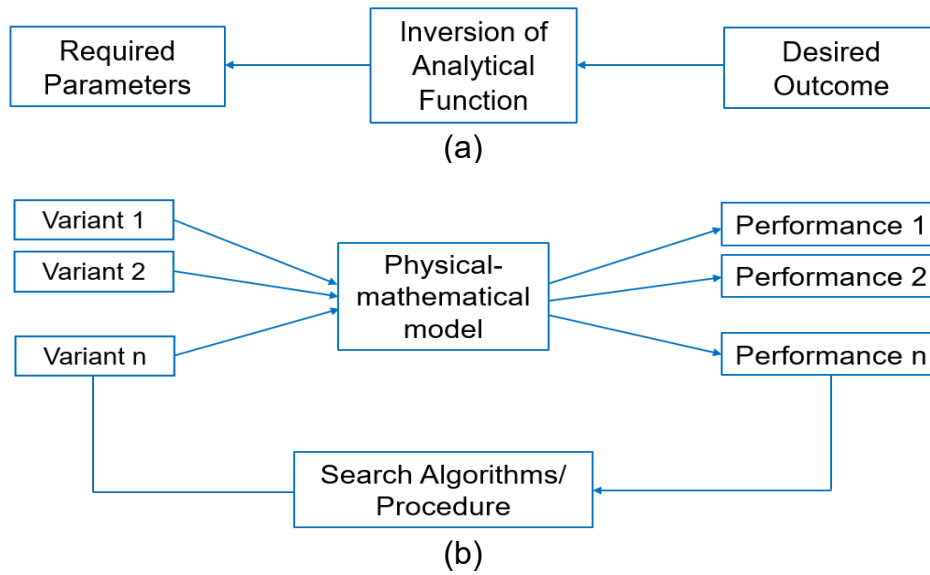


Fig. 1.5: Illustration of (a) backward and (b) forward method of inverse design techniques (Loonen et al. 2022).

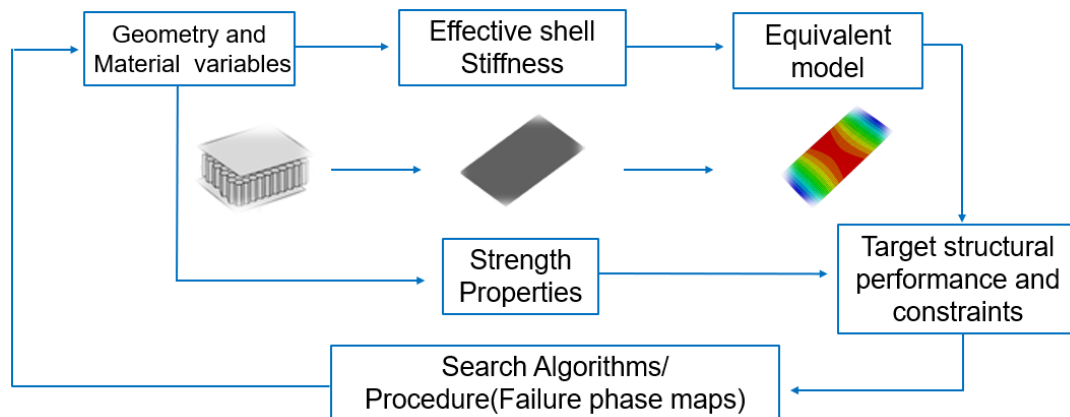


Fig. 1.6: Schematic of the typical inverse design procedure for the honeycomb core sandwich panels.

1.2 Motivation and aim

Motivated by the need for a systematic methodology to design the all-composite honeycomb core sandwich panels, this PhD thesis is aimed at developing necessary analytical and semi-analytical models to accurately determine the stiffness and strength of all-composite honeycomb cellular core sandwich panels, which could facilitate the accurate inverse design of the all-composite honeycomb core sandwich panels considering the wide range of geometric and material parameters of the face sheets and the core. The key objectives of the thesis are:

- To propose an analytical or semi-analytical approach to predict the effective stiffnesses of the laminated composite honeycomb cores with different shapes and material configurations,
- To propose an analytical or semi-analytical approach to predict the local buckling of the laminated composite honeycomb cores with different shapes and material configurations under different shear loadings conditions,
- To propose an analytical or semi-analytical approach to predict the local buckling of the laminated composite face sheets with different cell shapes and material configurations under axial compression and bending,
- To investigate the effectiveness of the equivalent models of the sandwich panels in predicting the responses compare to 3D models with the actual discrete honeycomb cores, and
- To validate the proposed analytical or semi-analytical models using the FE analysis.

This study only considers periodic composite honeycomb cellular cores as shown in Fig. 1.3. Hereafter, the honeycomb cores of different cell shapes will be referred to simply by their cell shape (e.g. hexagonal core, triangular core, rectangular core etc). In all the analytical and semi-analytical derivations in the following chapters, the material is assumed to be linear elastic and the reach of yield or maximum material strength is considered as a failure. As this present study, mainly focuses on developing the generalised theoretical models to facilitate the inverse design, the proposed models are mainly validated against corresponding FE predictions and other existing theoretical models. Since the analytical and semi-analytical models are developed under idealised conditions taking into account of various critical parameters related to geometry, materials and loadings, FE analysis is used for direct comparisons and validations of several different cases considered. Investigating the corresponding nonlinear effects such influence of imperfections, material nonlinearities, post buckling behaviour etc. falls beyond the scope of present study; therefore, detailed numerical models or/and experiments incorporating those effects are not used for the validations.

1.3 Significant contributions of the thesis

This thesis presents innovative methodologies aimed at facilitating the accurate and efficient inverse design of all-composite honeycomb core sandwich panels with different material and geometry configurations for both the core and face sheets. Initially, a strain energy-based homogenisation model is developed, incorporating laminate theory to derive an explicit strain energy density function for honeycomb RVEs with varying shapes. Moreover, effective stiffness matrices are derived for laminated honeycomb cores considering different shapes and material configurations. Additionally, generalised semi-analytical models are developed to address local buckling phenomena in the laminated composite honeycomb cores and intracellular buckling in the composite face sheets comprising different materials and geometric configurations under various loading conditions. This research bridges existing knowledge gaps in the inverse design of all-composite honeycomb core sandwich panels by offering versatile, efficient, and robust analytical and semi-analytical models for predicting effective stiffness and local buckling failures across various material, geometric, and loading configurations of the sandwich panels. The thesis provides readers with a fundamental understanding of how different core and face sheet geometries and materials influence the stiffness and strength behaviour of sandwich panels. It also enables efficient predictions, broadening the applicability of the inverse design process to tailor the all-composite sandwich panel designs to meet specific performance requirements. Consequently, this work advances the state-of-the-art in lightweight advanced sandwich panel design.

1.4 Outline of the thesis

The content of the thesis is presented in 7 chapters. Chapter 1 presents an introduction and the motivation and aim of the thesis.

Chapter 2 presents a detailed review of the existing literature related to the topic of this PhD thesis. It consists of past studies regarding different types of face sheet and core material, shell theories and shell elements proposed for sandwich panel analysis, different types of homogenisation approaches for the honeycomb cellular cores, analytical models for the local failures, and the inverse design methodologies for sandwich panels.

Chapter 3 presents the formulation of a strain energy-based homogenisation approach for the laminated composite honeycomb cores with different shapes and material configurations. The predictions of the in-plane and out-of-plane effective stiffnesses for the honeycomb cores with different materials and geometric configurations from the proposed approach are validated using the results from FE models. The predictions from other existing analytical models for the laminated composite cellular core were also evaluated against the proposed approach.

In Chapter 4, the global responses of sandwich panels using the equivalent single-layer FE models of the sandwich panels are compared with the detailed 3D FE models with the actual discrete honeycomb cores. The honeycomb cores of equivalent models were represented as a homogenous continuum with effective stiffnesses calculated using the proposed approach in Chapter 3. The global responses under static bending and uniaxial compression were evaluated for the sandwich panels with different honeycomb core configurations.

Chapter 5 presents a simplified semi-analytical approach to predict the shear buckling of loads of the laminated composite honeycomb cores. The predictions for shear buckling load for honeycomb cores from the proposed approach were validated from the results from FE for the honeycomb core with different shapes and material configurations. The effect of the different material and geometric configurations of the honeycomb cores on the shear buckling loads were investigated.

In Chapter 6, a semi-analytical approach is presented for the intracellular buckling of laminated composite face sheets sandwich panels. The proposed semi-analytical approach was formulated such that it can be used for predictions of the intracellular buckling load of the face sheets with different cell shapes, considering important parameters related to boundary and loading conditions of the cell. The predictions for intracellular buckling load of sandwich panels with honeycomb cores using the proposed approach are validated from the results from FE. The comparisons were also made with the results from existing analytical models for the intracellular buckling loads. The effect of different materials and geometric parameters on the intracellular buckling load are also investigated.

Chapter 7 presents key findings and impacts from this research and also recommends ideas for future works which could be extended from the current research.

1.5 References

- Abouhamzeh, M., & Sadighi, M. (2016). Buckling optimisation of sandwich cylindrical panels. *Curved and Layered Structures*, 3(1).
- Allen, H. G. (1969). *Analysis and Design of Structural Sandwich Panels*: Pergamon.
- Ashby, M. F., & Gibson, L. J. (1997). Cellular solids: structure and properties. *Press Syndicate of the University of Cambridge, Cambridge, UK*, 175-231.
- Birman, V., & Bert, C. W. (2004). Wrinkling of composite-facing sandwich panels under biaxial loading. *Journal of Sandwich Structures & Materials*, 6(3), 217-237.
- Birman, V., & Kardomateas, G. A. (2018). Review of current trends in research and applications of sandwich structures. *Composites Part B: Engineering*, 142, 221-240. doi:10.1016/j.compositesb.2018.01.027
- Burton, W., & Noor, A. (1997). Assessment of continuum models for sandwich panel honeycomb cores. *Computer Methods in Applied Mechanics and Engineering*, 145(3-4), 341-360.
- Caliri Jr, M. F., Ferreira, A. J., & Tita, V. (2016). A review on plate and shell theories for laminated and sandwich structures highlighting the Finite Element Method. *Composite Structures*, 156, 63-77.
- Catapano, A., & Montemurro, M. (2014). A multi-scale approach for the optimum design of sandwich plates with honeycomb core. Part II: the optimisation strategy. *Composite Structures*, 118, 677-690. doi:https://doi.org/10.1016/j.compstruct.2014.07.058
- Chen, X., Yu, G., Wang, Z., Feng, L., & Wu, L. (2021). Enhancing out-of-plane compressive performance of carbon fiber composite honeycombs. *Composite Structures*, 255, 112984.
- Fan, H.-T., Wang, H., & Chen, X.-H. (2018). Optimization of multi-sandwich-panel composite structures for minimum weight with strength and buckling considerations. *Science and Engineering of Composite Materials*, 25(2), 229-241. doi:10.1515/secm-2015-0171
- Feng, L.-J., Yang, Z.-T., Yu, G.-C., Chen, X.-J., & Wu, L.-Z. (2018). Compressive and shear properties of carbon fiber composite square honeycombs with optimized high-modulus hierarchical phases. *Composite Structures*, 201, 845-856.
- Feng, Y., Qiu, H., Gao, Y., Zheng, H., & Tan, J. (2020). Creative design for sandwich structures: A review. *International Journal of Advanced Robotic Systems*, 17(3), 1729881420921327.
- Gantovnik, V. B., Gürdal, Z., & Watson, L. T. (2002). A genetic algorithm with memory for optimal design of laminated sandwich composite panels. *Composite Structures*, 58(4), 513-520.
- Hoff, N. J., & Mautner, S. (1945). The buckling of sandwich-type panels. *Journal of the Aeronautical Sciences*, 12(3), 285-297.

- Hou, Y., Neville, R., Scarpa, F., Remillat, C., Gu, B., & Ruzzene, M. (2014). Graded conventional-auxetic Kirigami sandwich structures: Flatwise compression and edgewise loading. *Composites Part B: Engineering*, 59, 33-42.
- Hudson, C. W., Carruthers, J. J., & Robinson, A. M. (2010). Multiple objective optimisation of composite sandwich structures for rail vehicle floor panels. *Composite Structures*, 92(9), 2077-2082. doi:<https://doi.org/10.1016/j.compstruct.2009.10.018>
- Irisarri, F.-X., Julien, C., Bettebghor, D., Lavelle, F., Guerin, Y., & Mathis, K. (2021). A general optimization strategy for composite sandwich structures. *Structural and Multidisciplinary Optimization*, 63(6), 3027-3044. doi:10.1007/s00158-021-02849-8
- Irfan, S., & Siddiqui, F. (2019). A review of recent advancements in finite element formulation for sandwich plates. *Chinese Journal of Aeronautics*, 32(4), 785-798.
- Kiyak, B., & Kaman, M. O. (2019). Mechanical properties of new-manufactured sandwich composite having carbon fiber core. *Journal of Composite Materials*, 53(22), 3093-3109.
- Loonen, R. C. G. M., de Vries, S., & Goia, F. (2022). Inverse design for advanced building envelope materials, systems and operation. In *Rethinking Building Skins* (pp. 377-402).
- Meidell, A. (2009). Minimum weight design of sandwich beams with honeycomb core of arbitrary density. *Composites Part B: Engineering*, 40(4), 284-291. doi:10.1016/j.compositesb.2009.01.003
- Montemurro, M., Catapano, A., & Doroszewski, D. (2016). A multi-scale approach for the simultaneous shape and material optimisation of sandwich panels with cellular core. *Composites Part B: Engineering*, 91, 458-472. doi:<https://doi.org/10.1016/j.compositesb.2016.01.030>
- Murthy, O., Munirudrappa, N., Srikanth, L., & Rao, R. (2006). Strength and stiffness optimization studies on honeycomb core sandwich panels. *Journal of Reinforced Plastics and Composites*, 25(6), 663-671.
- Niu, K., & Talreja, R. (1999). Modeling of Wrinkling in Sandwich Panels under Compression. *Journal of Engineering Mechanics*, 125(8), 875-883.
- Pehlivan, L., & Baykasoğlu, C. (2019). An experimental study on the compressive response of CFRP honeycombs with various cell configurations. *Composites Part B: Engineering*, 162, 653-661.
- Penado, F. E. (2013). Effective elastic properties of honeycomb core with fiber-reinforced composite cells. *Open Journal of Composite Materials*, 3(04), 89.
- Plantema, F. J. (1966). *Sandwich construction: the bending and buckling of sandwich beams, plates, and shells*: Wiley.
- Pozorski, Z., Pozorska, J., Kreja, I., & Smakosz, Ł. (2021). On Wrinkling in Sandwich Panels with an Orthotropic Core. *Materials*, 14(17), 5043.
- Pütz, M., Lafont, U., Wittlich, M., Markestain, E., Herrmann, C., & Fischer, H. (2023). 3D honeycomb for advanced manufacturing for space application. *CEAS Space Journal*, 15(1), 203-211. doi:10.1007/s12567-022-00444-1
- Russell, B., Deshpande, V., & Wadley, H. (2008). Quasistatic deformation and failure modes of composite square honeycombs. *Journal of mechanics of materials and structures*, 3(7), 1315-1340.
- Russell, B., Liu, T., Fleck, N., & Deshpande, V. (2011). Quasi-static three-point bending of carbon fiber sandwich beams with square honeycomb cores. *Journal of Applied Mechanics*, 78(3).

- Santos, L., Izzuddin, B. A., & Macorini, L. (2022). Gradient-based optimisation of rectangular honeycomb core sandwich panels. *Structural and Multidisciplinary Optimization*, 65(9), 242. doi:10.1007/s00158-022-03341-7
- Seyyedrahmani, F., Khandar Shahabad, P., Serhat, G., Bediz, B., & Basdogan, I. (2022). Multi-objective optimization of composite sandwich panels using lamination parameters and spectral Chebyshev method. *Composite Structures*, 289. doi:10.1016/j.compstruct.2022.115417
- Somnic, J., & Jo, B. W. (2022). Status and challenges in homogenization methods for lattice materials. *Materials*, 15(2), 605.
- Tan, X., & Soh, A. (2007). Multi-objective optimization of the sandwich panels with prismatic cores using genetic algorithms. *International Journal of Solids and Structures*, 44(17), 5466-5480.
- Thomsen, O. T., & Banks, W. M. (2004). An improved model for the prediction of intra-cell buckling in CFRP sandwich panels under in-plane compressive loading. *Composite Structures*, 65(3-4), 259-268.
- Triantafillou, T. C., & Gibson, L. J. (1987). Minimum weight design of foam core sandwich panels for a given strength. *Materials Science and Engineering*, 95, 55-62.
- Vinson, J. R. (1986). Optimum design of composite honeycomb sandwich panels subjected to uniaxial compression. *AIAA Journal*, 24(10), 1690-1696.
- Vonach, W. K., & Rammerstorfer, F. G. (2000). Wrinkling of thick orthotropic sandwich plates under general loading conditions. *Archive of Applied Mechanics*, 70, 338-348.
- Wang, R., & Wang, J. (2018). Modeling of honeycombs with laminated composite cell walls. *Composite Structures*, 184, 191-197. doi:10.1016/j.compstruct.2017.09.054
- Wei, X., Xiong, J., Wang, J., & Xu, W. (2020). New advances in fiber-reinforced composite honeycomb materials. *Science China Technological Sciences*, 63(8), 1348-1370. doi:10.1007/s11431-020-1650-9
- Wei, X., Wu, Q., Gao, Y., & Xiong, J. (2020a). Bending characteristics of all-composite hexagon honeycomb sandwich beams: experimental tests and a three-dimensional failure mechanism map. *Mechanics of Materials*, 148, 103401.
- Wei, X., Wu, Q., Gao, Y., Yang, Q., & Xiong, J. (2022b). Composite honeycomb sandwich columns under in-plane compression: Optimal geometrical design and three-dimensional failure mechanism maps. *European Journal of Mechanics-A/Solids*, 91, 104415.
- Zenkert, D. (1997). *The handbook of sandwich construction: Engineering Materials Advisory Services*.

Chapter 2:

Literature Review

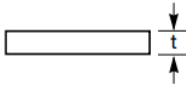
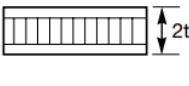
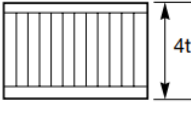
2.1 General

Sandwich panels consist of two thin and strong face sheets connected to either side of a core. The concept of the sandwich panel was first discussed by Duleau and Fairbarain in the 1820s. However, sandwich panels were successfully deployed much later for the construction of 'Mosquito' aircraft during World War II (Zenkert 1997). Since then, extensive research on the analysis and design of the sandwich panels, materials development for cores and face sheets, and manufacturing technologies had been carried out. Studies on sandwich panels have been continued due to advancements in material and manufacturing technologies. Especially the recent advancements in composite materials and manufacturing technologies have provided widespread possibilities for material and geometry selections for sandwich panels, often making the existing research inadequate to deal with the new materials and geometric options. Therefore, the demand for research on different aspects of sandwich panels is still extensive.

Sandwich structures are currently popular not only in aerospace applications but also in several other applications such as wind and tidal turbines (Thomsen 2009), automobiles (Ning et al. 2007; Hara & Özgen 2016; Hou et al. 2022), infrastructure (Manalo et al. 2017), marine applications (Palomba et al. 2022) etc. The construction of sandwich structures typically involves the utilization of various types of sandwich panels, each offering unique benefits and tailored to specific requirements. These panels can be broadly categorized into: a) truss core sandwich panels b) honeycomb core sandwich panels c) foam core sandwich panels and d) corrugated core sandwich panels (Fig. 2.1). The adoption of sandwich structures in the applications is primarily motivated by their multitude of advantages over traditional structural elements. Especially, sandwich panels exhibit a superior flexural stiffness-to-weight ratio and strength-to-weight ratio compared to monocoque and other architectural configurations as shown by the comparison in Table 2.1(HexWeb™ 1999). This heightened efficiency in material utilization translates into enhanced performance and

reduced overall weight, aligning with the contemporary emphasis on lightweight and sustainable design practices across industries. In addition, sandwich panels also provide several other functional benefits based on the material selection for the face sheets and core, such as energy absorption, acoustic absorption, thermal insulation and fire shielding, thermal transfer, and ballistic resistance (Ashby 2005; Feng et al. 2020).

Table 2.1: Comparison of structural efficiency of sandwich panels in terms of weight (HexWeb™ 1999).

	Solid Metal Sheet	Sandwich Construction	Thicker Sandwich
			
Relative Stiffness	100	700 7 times more rigid	3700 37 times more rigid!
Relative Strength	100	350 3.5 times as strong	925 9.25 times as strong!
Relative Weight	100	103 3% increase in weight	106 6% increase in weight

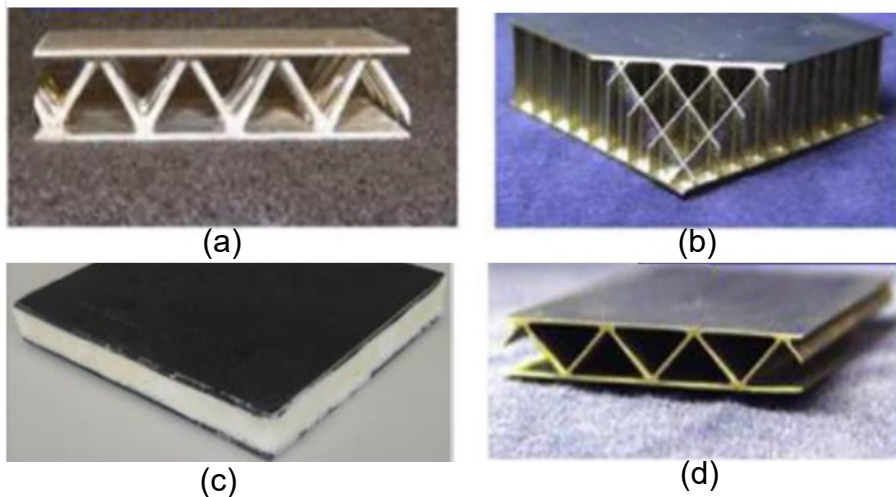


Fig. 2.1: Different types of sandwich panels used in sandwich structures: (a) truss core sandwich panel (b) honeycomb core sandwich panel (c) foam core sandwich panel and (d) corrugated core sandwich panel (Feng et al. 2020). Reproduced with permission from the publisher.

2.2 Materials and manufacturing techniques for sandwich structures

In general, any structural material which can be obtained in the form of thin sheets, can be used as face sheets of sandwich panels (Allen 1969). When selecting the material for the face sheet, properties such as high flexural stiffness, high compressive and tensile strength, impact resistance, surface finish, and environmental and wear resistance are generally considered to be primary interests by designers. Commonly used face materials can be classified into two main categories as metallic and non-metallic face materials. Materials like steel, stainless steel and aluminium are some examples of metallic face sheets, and plywood, cement composites, wood veneer, and fibre composites are some examples of non-metallic face sheets. Since the core of the sandwich panel is primarily subjected to transverse shear, material selection for the core is mainly driven by the transverse shear strength and stiffness properties. In addition, low density and other functional properties such as thermal insulation and acoustic insulation are also properties of concern (Zenkert 1997). The cores in the sandwich panels can be broadly categorised as solid cores, foam cores and periodic cellular cores (Laszczyk 2011). Balsa wood is an example of the solid core, which is a low-density wood with a density range from 100kg/m^3 - 300kg/m^3 . Balsa wood is one of the first materials used for the core in load-carrying sandwich structures (Zenkert 1997). Balsa wood has also been used as the core in many different sandwich structure applications, such as bridge decks, wind turbine blades and boats (Borrega & Gibson 2015; Shir Mohammadi & Nairn 2017). Foam cores can be of metallic (E.g., Aluminium foam) or polymeric (E.g., expanded polystyrene (EPS), Polyetherimide (PMI) foam, polyvinyl chloride (PVC) and Polyurethane (PU)) (Zenkert 1997). Foam cores could be manufactured to get different density (10kg/m^3 - 800kg/m^3) based on the design requirements by changing the volume fractions, size and morphology of the pores (close-cells), connectivity of the struts (open-cells), etc (Laszczyk, 2011; Khan et al. 2020). Foam cores are generally less expensive in comparison to periodic cellular cores. Because the surface preparation and shaping of the foam cores are relatively simple, they can be easily connected to face sheets by adhesive bonding. Also foam cores have very good thermal insulation and acoustic absorption characteristics (Zenkert 1997). Periodic cellular cores are systematically organised cellular materials which can have different configurations in terms of

geometry and materials (Laszczyk, 2011). Periodic cellular cores can be classified mainly into 3D lattices and 2D prismatic cellular cores (Fig. 2.2) (Wadley 2006). 3D lattice cores can be of truss type or textile type, and 2D prismatic cores can be of corrugated type or honeycomb type (Wadley 2006). Periodic cellular cores offer a high stiffness-to-weight ratio and strength-to-weight ratio in comparison to solid and foam cores (Zenkert 1997). With the advancement of material and manufacturing technologies, the periodic cellular cores could be architected to give several functional properties by combining different materials and geometric configurations (Feng et al. 2018). Among the different types of cellular cores, the honeycomb core is one of the most used cellular cores in sandwich panels (Feng et al. 2018). This literature review mainly focuses on the studies of the honeycomb cellular core (Fig.2.2(d)) sandwich panels, while research on other types of core systems is discussed where necessary. The honeycomb cores with different cell shapes are specifically referred by its shape (e.g., hexagonal core, rectangular core, triangular core etc) and commonly referred as 'honeycomb' in this thesis.

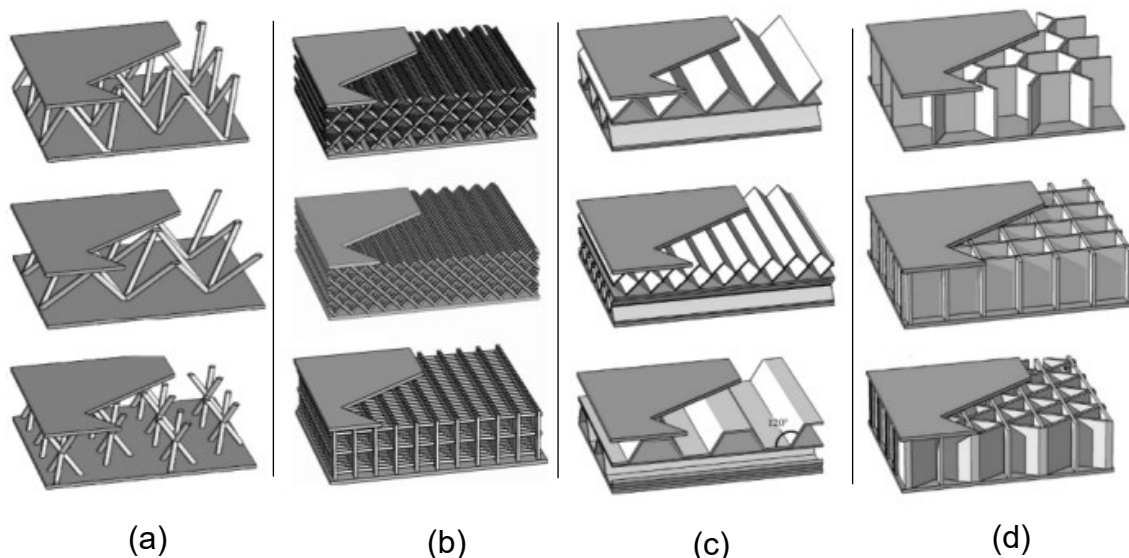
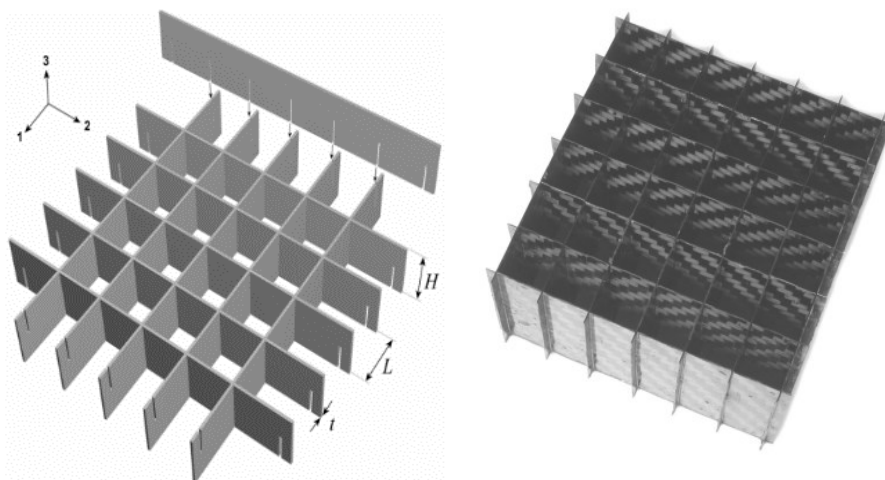


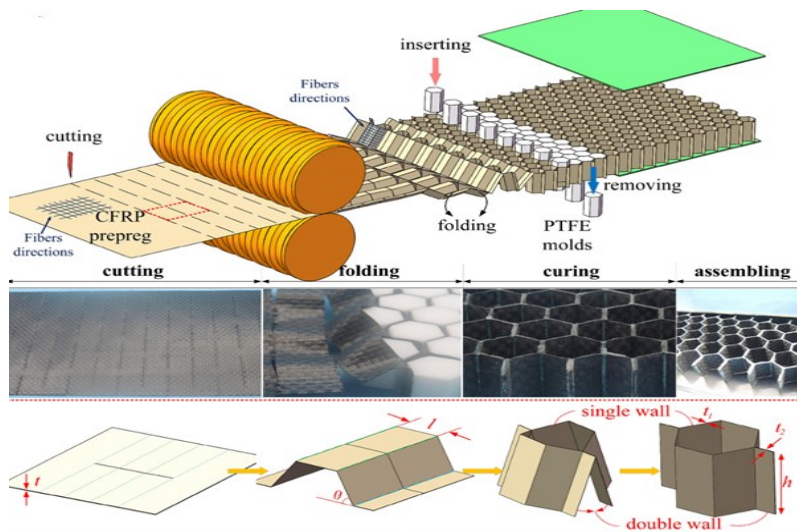
Fig. 2.2: Periodic cellular cores: 3D lattices of (a) truss type and (b) textile type and 2D prismatic cores of (c) corrugated type and (d) honeycomb type (Wadley 2006).

Early research studies related to honeycomb cores mainly focused on studying the behaviour of metal sandwich panels having metal (E.g., Steel/Aluminium) honeycomb cores (Kee et al. 1999; Cote et al. 2004, 2006; Crupi et al. 2012). With the advancement of composite material technologies, materials such as carbon fibre reinforced polymer (CFRP) and glass fibre reinforced polymer (GFRP) were

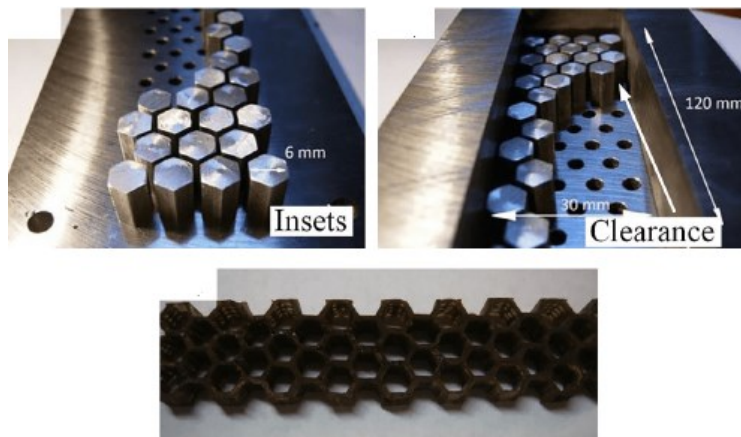
introduced for face sheets to reduce the overall weight of the sandwich panels (Shi et al. 2014). With the advancement in manufacturing technologies, researchers have recently investigated the options of using fibre reinforced polymer (FRP) composites or hybrid materials for both the honeycomb cores and face sheets. The all-composite honeycomb core sandwich panels have opened up the possibility to further improve the design of sandwich panels for lightweight and other multi-functional applications. Number of researchers have investigated applications of GFRP (Cote et al. 2009), Kevlar based FRP (Hou et al. 2014; Kumar et al. 2019), CFRP (Russell et al. 2008,2011; Feng et al. 2018; Pehlivan & Baykasoğlu 2019; Chen et al. 2021; Wei et al. 2019, 2020, 2022), natural fibres (Stocchi et al. 2014; Vitale et al. 2017), and hybrids such as wood-GFRP laminates (Ou et al. 2019) for the fabrication of cellular cores. Depending on the composite materials used and honeycomb core shapes, different techniques (Fig. 2.3) such as interlocking (Russell et al. 2008, 2011) (Fig 2.3(a)), tailor folding (Wei et al. 2019, 2020, 2022) (Fig. 2.3(b)), compression moulding (Stocchi et al. 2014) (Fig 2.3(c)), vacuum-assisted resin transfer moulding (Vitale et al. 2017) (Fig 2.2(d)), 3D printing(Sugiyama et al. 2018)(Fig 2.3(e)) and kirigami (Saito et al. 2011; Hou et al. 2014)(Fig 2.3(f)) have been used to manufacture the composite honeycomb cores.



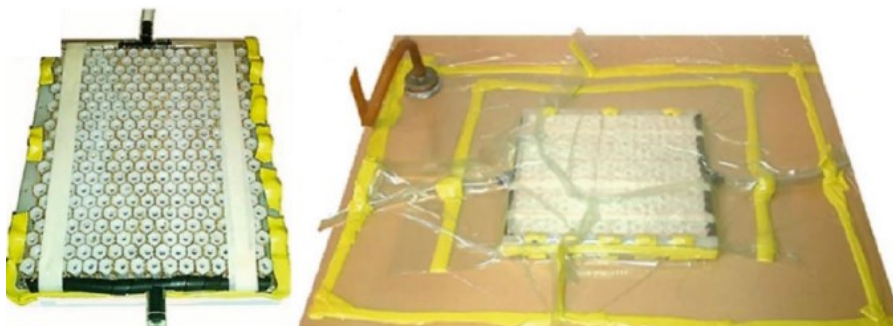
(a) Fabrication of CFRP square core using interlock technique (Russell et al. 2008).
 Reproduced with permission from the publisher.



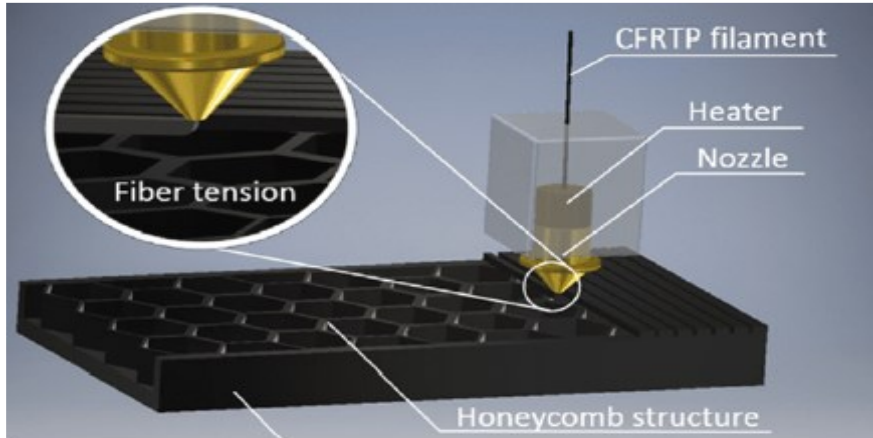
(b) Fabrication of CFRP hexagonal core using tailor folding technique (Wei et al. 2020). Reproduced with permission from the publisher.



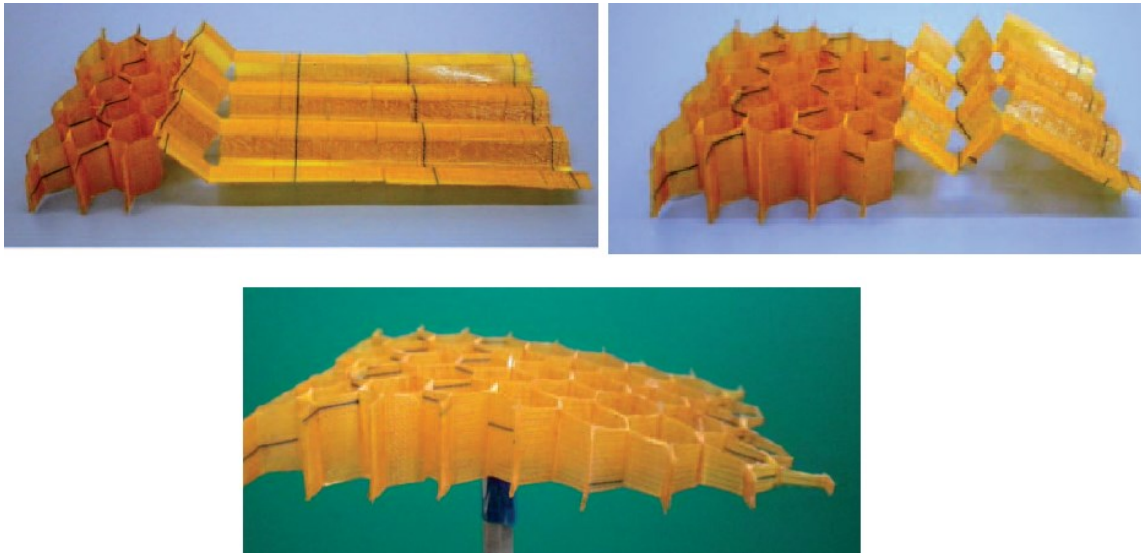
(c) Fabrication of natural fibre hexagonal core using compression moulding technique (Stocchi et al. 2014). Reproduced with permission from the publisher.



(d) Fabrication of natural fibre hexagonal core using Vacuum-assisted resin transfer moulding technique (Vitale et al. 2017). Reproduced with permission from the publisher.



(e) Fabrication of CFRP hexagonal core using 3D printing technique (Sugiyama et al. 2018). Reproduced with permission from the publisher.



(f) Fabrication of Kevlar hexagonal core using kirigami folding technique (Saito et al. 2011). Reproduced with permission from the publisher.

Fig. 2.3: Different manufacturing techniques for honeycomb cores.

Existing studies on the mechanical performance of the honeycomb cores are largely limited to the square shape cores (Russell et al. 2008 & 2011; Ou et al. 2019) and the honeycomb cores (Stocchi et al. 2014; Vitale et al. 2017; Wei et al. 2019, 2020, 2022). Existing experimental studies have revealed that the fibre orientation of the composite core walls significantly affects the mechanical performance of the cores, but length to width ratio of core walls has little effect on the mechanical performance of the honeycomb cores (Russel et al. 2008). Experimental investigations available on the honeycomb cores are often limited to specific fibre directions; Russel et al. (2011)

used (0/90⁰) plies for the face sheets and (+/-45⁰) woven CFRP for the square core and studied 3-point bending characteristics of sandwich panels; Wei et al. (2020, 2022) experimentally investigated bending and uniaxial compression characteristic of all-composite honeycomb core sandwich panels consisting of CFRP core with (0/90) and (45/-45) laminated composite walls. Only few researchers have investigated the mechanical performance of hybrid core systems (Feng et al. 2018; Ou et al. 2019). Ou et al. (2019) used timber-GFRP hybrid wall cores and found that such hybrid cores provide good performance in concrete-timber sandwich panels. Feng et al. (2018) found that using foam-CFRP sandwiches as core walls in sandwich panels (Fig. 2.4) significantly improved the out-of-plane compressive and shear response in comparison with the regular CFRP walls square core sandwich panels.

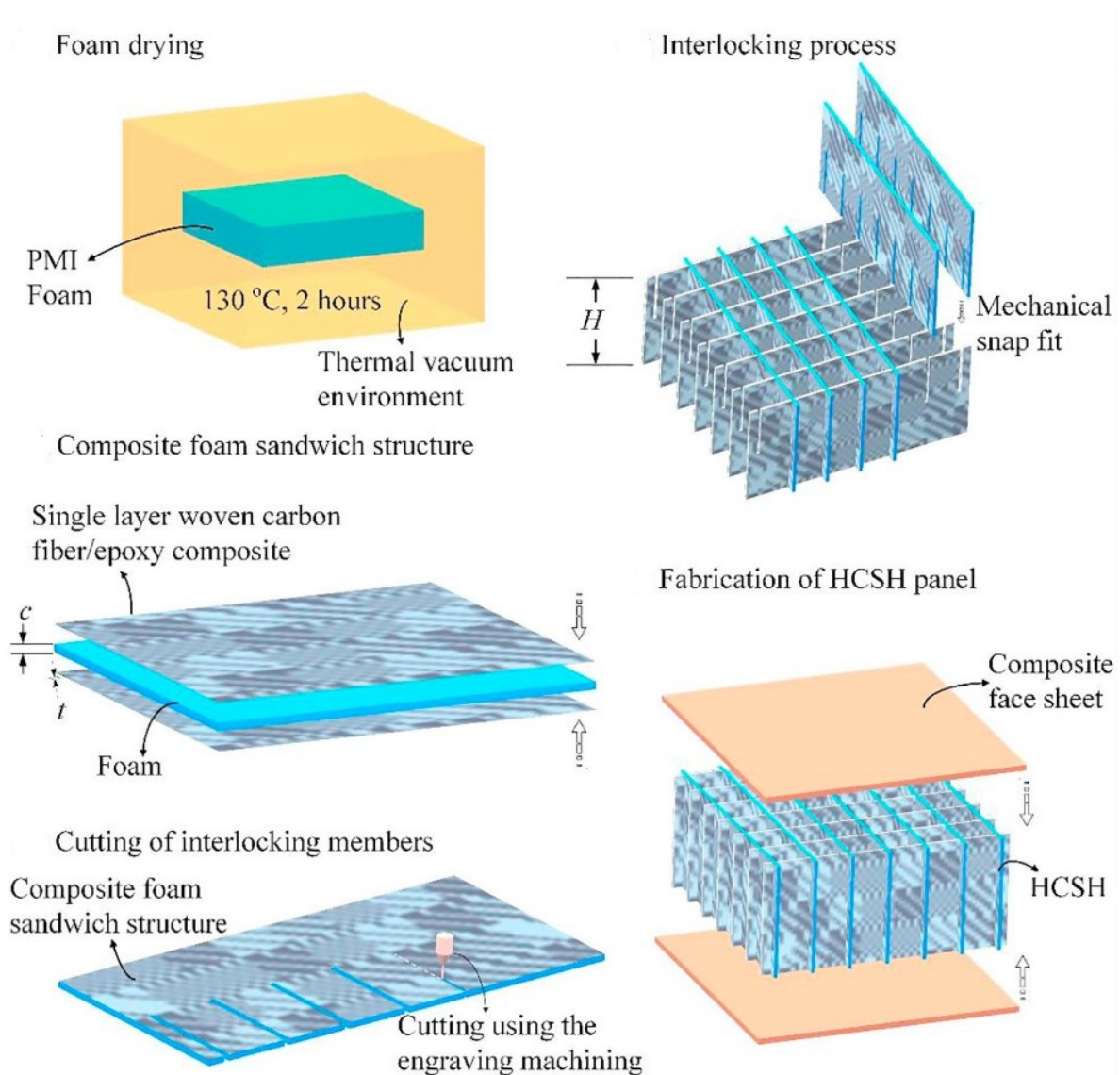


Fig. 2.4: Process of hierarchical wall square core fabrication using CFRP and foam (Feng et al. 2018). Reproduced with permission from the publisher.

2.3 Theory and analysis approach for the sandwich panels

2.3.1 Theories for analysing the sandwich panels

In the past, many shell and plate theories have been proposed for the analysis of composite and sandwich structures. Based on the assumption of the displacement field used, these theories can be mainly classified into mainly three categories: equivalent single-layer (ESL) theories, discrete layer-wise (LW) theories, and Zigzag theories (ZZ).

In the ESL approach, the laminated composite and sandwich panels are represented by a statically equivalent single layer. The displacement field of an equivalent single layer is assumed to be continuous through the thickness and generally approximated using a polynomial series. One of the oldest and most well-known theories of this approach is the classical laminate theory (CLT) (Kollár 2003) which is based on the kinematics assumptions of Kirchhoff thin plate theory (Kirchhoff 1850). This theory assumes that:

1. Cross sections remain plane before and after the deformation and
2. Cross sections remain perpendicular to the reference surface before and after the deformation.

As the second assumption of the CLT assumes there are no transverse shear deformations, the application of the CLT is limited to thin laminates.

Another well-known ESL theory is the first-order shear deformation (FSDT) theory, which is based on Reissner-Mindlin's hypotheses (Reissner 1945; Mindlin 1951). FSDT relaxes the second assumption of the CLT and predicts a constant shear variation across the thickness. Because of the constant shear variation, FSDT requires a shear correction factor. A number of different methods have been proposed to estimate the shear correction factor for the sandwich and laminated structures (Vlachoutsis 1992; Birman & Bert 2002; Huang & Kardomateas 2002; Vrabie, Chiriac & Băetu 2017).

In order to improve the kinematic assumptions of FSDT, higher-order shear deformation theories (HSDT) have been developed (Ferreira et al. 2005; Aydogdu 2009; Tounsi et al. 2013; Hamidi et al. 2015; Mahi and Tounsi 2015). Different versions

of HSDT have been proposed using polynomial, trigonometric and hyperbolic functions for the displacement assumptions (Mantari & Soares, 2012). HSDT satisfies shear stress-free boundary conditions at the top and bottom surface of sandwich panels and does not require the shear correction factor. However, HSDT does not satisfy the requirement of interface shear stress continuity at the interfaces between the cores and face sheets.

LW theories divide the plate into a number of different layers in the thickness direction (not needed to be equal to the number of plies in the laminate). Among several existing LW theories, some of them were formulated considering the behaviour of core and face sheets separately (Frostig et al. 1992; Siddiqui 2015). These theories assume that face sheets satisfy Euler-Bernoulli's assumptions and differ in their approximation of the displacement field for the core. Such theories proposed by Frostig et al. (1992) and Siddiqui (2015) are also referred to as higher order sandwich panel theory (HSAPT) and extended higher order sandwich panel theory (EHSAPT), respectively, in the literature. Several other LW theories were also proposed based on different functions for the approximation of displacement field in each layer (Plagianakos & Saravanos 2009; Mantari et al. 2012; Goswami & Becker 2016). Those theories accurately satisfy interface shear stress continuity between the layers. However, due to the number of additional variables used, the computational cost is much higher than ESL theories.

To take advantage of computational efficiency of ESL theories and to improve the interface shear stress continuity like in LW theories, a special type of theory known as 'Zigzag' theories have been proposed (Cho & Averill 2000; Icardi 2001; Pandit et al. 2008; Tessler et al. 2010; Bhar & Satsangi 2011). In such theories, the in-plane displacements have piece-wise variation across the plate thickness and the number of unknowns is made independent of the number of layers by equating the transverse shear stresses at the layer interfaces of the laminate. Analytical solutions (Frostig & Baruch 1993; Phan et al. 2012) based on the above-mentioned theories were used to analyse sandwich panels with simple geometry, loading and boundary conditions. However, solving the governing equations for more complex cases is not always possible (Irfan & Siddiqui 2019). Therefore, the analytical approach limits the design of sandwich panels for different applications.

In recent years, many studies have been carried out to formulate beam elements and shell elements for the analysis of sandwich panels based on HSDT theories (Bhar & Satsangi 2011; Thai & Choi 2013; Marjanović et al. 2016), ZZ theories (Xiaohui et al. 2012; Barut et al. 2013; Eijo et al. 2013; Versino et al. 2013), and LW theories (Hu et al. 2009; Mantari et al. 2012; Pandey & Pradyumna 2015; Yuan et al. 2015; Irfan & Siddiqui, 2021). Most of these elements have been formulated focusing on the linear static analysis of the sandwich panels. Only a few researchers (Yu et al. 2015; Yuan et al. 2016; Yuan & Kardomateas 2018) have focused on the finite element (FE) formulation for the geometric nonlinear analysis of sandwich panels based on HSAPT and EHASPT. Some of them studied the nonlinear linear buckling behaviour of sandwich panels under uniaxial compressive loads (Yu et al. 2015; Yuan & Kardomateas 2018), while others studied nonlinear responses of sandwich panels under 3-point bending (Yuan et al. 2016). Although FE elements based on modern theories perform better in terms of accuracy in comparison with the elements based on FSDT (Panda & Natarajan, 1981), they are computationally expensive due to an additional number of freedoms, and implementation of those elements is a challenging task. On the other hand, models based on FSDT are very often used due to their simplicity in analysis and programming. It requires, however, an accurate estimation of the shear correction factor.

2.3.2 Effective elastic properties of honeycomb core

For the purpose of computational efficiency, the analysis of sandwich panels is generally performed using effective properties instead of analysing the actual 3D geometry of the core structure (Catapano & Montemurro 2014b; Namvar & Vosoughi 2020; Santos et al. 2022). The actual heterogeneous body of the honeycomb structure is represented by an equivalent homogeneous medium. Once effective mechanical properties are known, the relevant sandwich shell/plate theories can be used to analyse the sandwich structure. This provides reasonably accurate results when the overall dimension of the sandwich panel is considerably larger than the characteristic dimensions of the representative volume element (RVE) of the core. The concept of the homogenisation approach to get effective properties is illustrated in Fig.2.5.

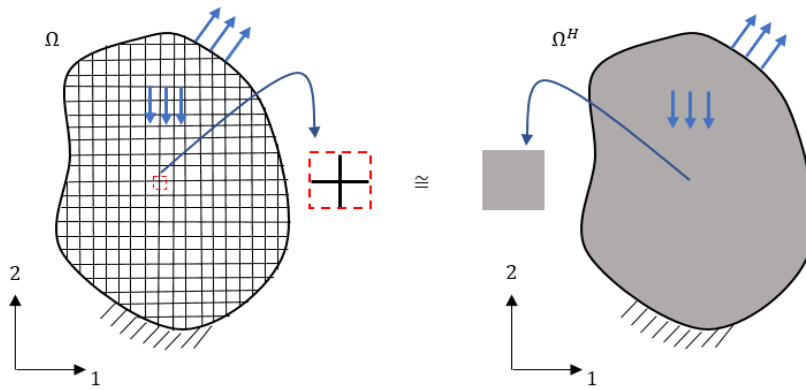


Fig. 2.5: Illustration of concept of homogenisation of periodic honeycomb core (Somnic & Jo 2022).

Consider a periodic honeycomb structure (Ω) subjected to some external loads and boundary conditions, and an effective homogeneous medium (Ω^H) having the same boundaries and external loads (Fig. 2.5). The mechanical behaviour of RVE of the actual structure (Ω) has to be equivalent to the mechanical behaviour of RVE of the homogenised element of the effective medium. The constitutive equations for the effective properties of the homogenised medium have to be determined in such a way that the mechanical behaviour of Ω and Ω^H is equivalent on the macroscopic level (Somnic & Jo 2022).

Researchers have followed different methodologies to get the effective properties of honeycomb cores. These methodologies can be broadly categorised into different approaches such as the force-equilibrium approach (Master & Evans 1996; Gibson & Asby 1997; Balawi & Abot 2008; Malek & Gibson 2015; Mukherjee & Adhikari 2021), strain energy approach (Becker 1998; Hohe & Backer 2001; Xu and Qiao 2002; Li et al. 2016), asymptotic expansion approach (Shi & Tong 1995; Xu et al. 2001), and FE-based approach (Catapano & Montemurro 2014a; Sorohan et al. 2018). In the force-equilibrium-based approach, each cell wall of the RVE is assumed to be an equivalent beam and the deformation of the RVE under applied external force is calculated considering the deformation of each wall and effective properties are calculated based on the average stress of the RVE (Fig. 2.6). The strain energy-based approach assumes that the effective properties of the RVE of the actual honeycomb core and homogenised core are equivalent if the strain energy between both RVEs is equal under the condition of equal average strain. The asymptotic expansion approach considers the length scale of RVE and periodic structure in the system and uses power

series expansion to represent the displacement fields and stress fields in the system. Then the effective properties are obtained by considering the volume average of stress.

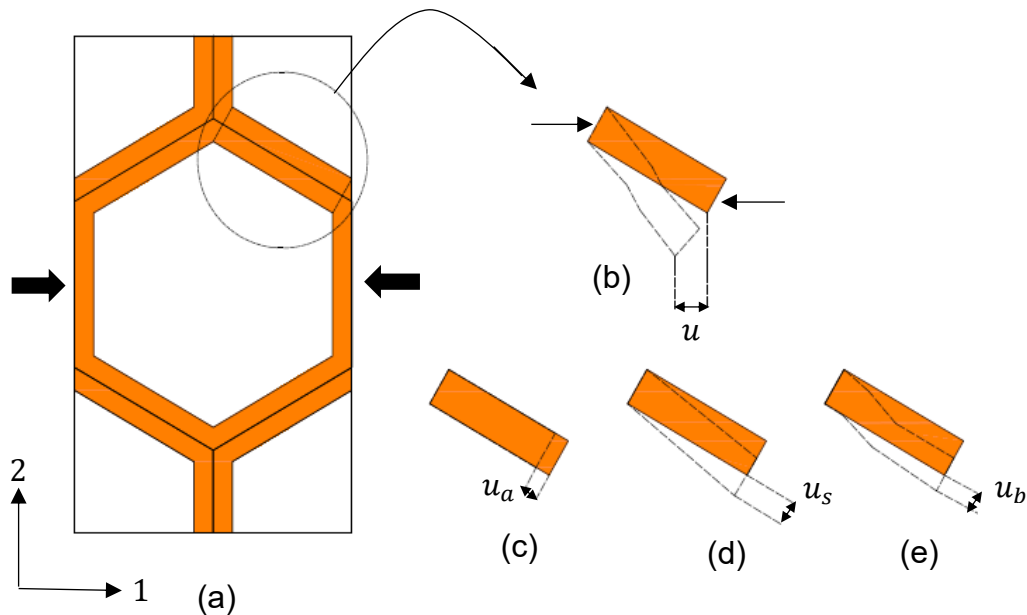


Fig. 2.6: Force-equilibrium approach to calculate the effective in-plane elastic modulus (a) RVE under in-plane force (b) total deflection of the inclined member due to (c) axial (d) shear and (e) bending deformations (Malek & Gibson 2015).

Early studies on homogenisation mainly focused only on the out-of-plane properties of the hexagonal honeycomb core (Kelsey et al. 1958). Such approaches presented lower-bound solutions based on the statically admissible stress field and upper-bound solutions based on kinematically admissible displacement and strain fields. Gibson et al. (1982) used the force equilibrium approach and presented closed-form solutions for in-plane effective properties of the hexagonal core considering only the bending deformation of the wall. Since then, further improved models were proposed, also considering additional deformation modes of honeycomb walls, e.g. bending, stretching, and hinging mechanism of the walls (Master & Evans 1996) and bending, stretching, and shear deformation of the cell walls (Gibson & Asby 1997). Models proposed also varied in terms of the details of the cell wall geometry considered in the analysis, especially the effect from the wall joints (Balawi & Abot 2008, Malek & Gibson 2015). In proposed models for in-plane and out-of-plane properties of hexagonal core developed by Malek & Gibson (2015), the effective length of the walls was reduced to consider the wall joint node effects (Fig. 2.7). However, this effect could be neglected for thin walls or low relative density honeycomb, where equations for in-plane properties reduce to Gibson & Asby (1997) model. Mukherjee

& Adhikari (2021) considered walls as Euler-Bernoulli beam elements to derive equations for in-plane effective properties of the hexagonal honeycomb core. While above presented models vary in terms of different assumptions made and the type of properties they considered, all those models only considered the effective properties of the hexagonal cores. In addition to the hexagonal cores, it is also common to have honeycomb cores with other geometric shapes such as triangular, rectangular etc. (Fig.2.1(d)) in the sandwich panels (Shah & Kapania 2020).

Some efforts have also been made in developing theoretical models for predicting the effective properties of the honeycomb cores of different shapes (Hohe & Backer 2001a; Wang & McDowell 2004). Such models were derived either based on strain energy-based (Hohe & Backer 2001a), force-equilibrium based (Wang & McDowell 2004), or two-scale asymptotic expansion technique based (Xu et al. 2001) approaches. Often solutions were also limited to either in-plane (Wang & McDowell 2004) or out-of-plane (Xu et al. 2001) properties. In addition, most of the studies also ignored the possible skin effects on the core in predicting the effective properties. Several advanced models (Becker 1998; Hohe & Becker 2001b; Xu & Qiao 2002; Li et al. 2016) considered the skin effect where displacement of the core adjacent to the face sheets was considered to be influenced by displacements of face sheets but the core displacements away from the face sheets were unconstrained. It was found that skin effects are significant for honeycomb cores with lower depth but can be ignored for cores with higher wall length to core depth ratio.

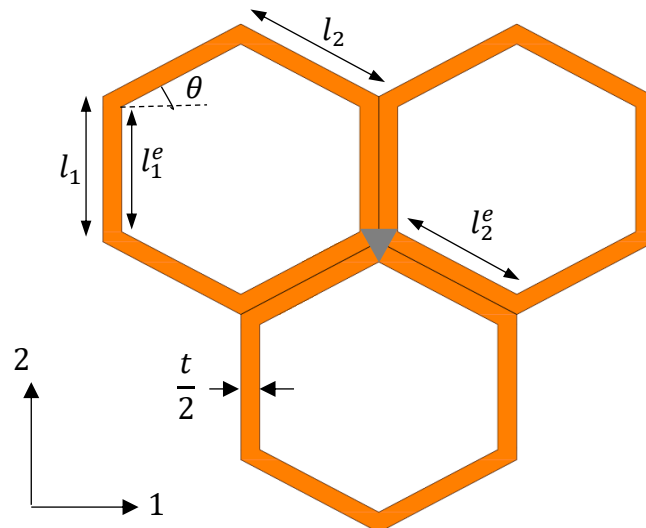


Fig. 2.7: Node region of hexagonal core considered by Malek & Gibson (2015). l_1^e and l_2^e are effective bending lengths of walls of the core with uniform thickness (t).

Apart from analytical approaches, several researchers used FE-based homogenisation to validate their analytical models or to get effective properties of the honeycomb cores. Grediac (1993) used FE to study the out-of-plane shear properties of the hexagonal core and proposed an empirical solution to take into account the skin effect in calculating the out-of-plane shear properties. Shell and solid elements were mainly used to model the RVE of the honeycomb cores. In some instances where through-thickness normal stress is significant, solid elements were used instead of shell elements (Catapano & Montemurro 2014; Malek & Gibson 2015). Nonetheless, most studies used shell elements (Grediac 1993; Burton & Noor 1997; Hohe & Becker 2001; Penado 2013; Li et al. 2015) due to computational efficiency. The FE studies presented above focused mainly on honeycomb cores with isotropic materials cell walls.

Only limited studies are available on the effective properties of multi-layered or laminated composite wall honeycomb cores. Wang & Wang (2019) have presented an analytical model for a hexagonal honeycomb core combining the CLT and Gibson et al. (1982) modelling approach. They have only considered the effect of walls with two plies having orthotropic material properties in the principal direction of the walls. However, they have not studied the effect of different fibre orientations and fibre layer sequences in their analysis. Krishnamurthy & Saether (2019) studied the effective properties of multifunctional hexagonal cores having multi-layer isotropic materials for the wall. They calculated the effective membrane modulus of the multi-layered walls using CLT and then modified Gibson et al. (1982) using effective membrane modulus of the wall to calculate the effective stiffness properties of the honeycomb cores. However, calculating the bending deformation of the multi-layered wall using membrane modulus may not give accurate results due to potential transverse shear deformations (Min et al. 2019). Because Wang & Wang (2019) and Krishnamurthy & Saether (2019) do not account for the stretching effect of the wall, the resulting formula for in-plane Poisson's ratios gave the value of 1 for the regular honeycomb core making the equivalent in-plane stiffness calculation for the plate or shell analysis impossible.

2.4 Failure predictions in sandwich panels

Failures in sandwich panels can be global or local (Fig 2.8) (CMH-17 2013). Global failures are fracture (composite) or yielding (metal) of face sheets and global buckling. Local failure can occur due to either material failure or instability. Common local failures in the sandwich panel are shear buckling and compression buckling of the core, shear fracture and crushing of core walls, local indentation, faces sheets-core debonding, wrinkling, and intra-cellular buckling (CMH-17 2013, Wei et al. 2020, 2022). Sandwich panels are generally analysed using the equivalent shell or plate theory, which is not capable of predicting most of the local failures. Some research on the local stability failure of sandwich structures are discussed in this section.

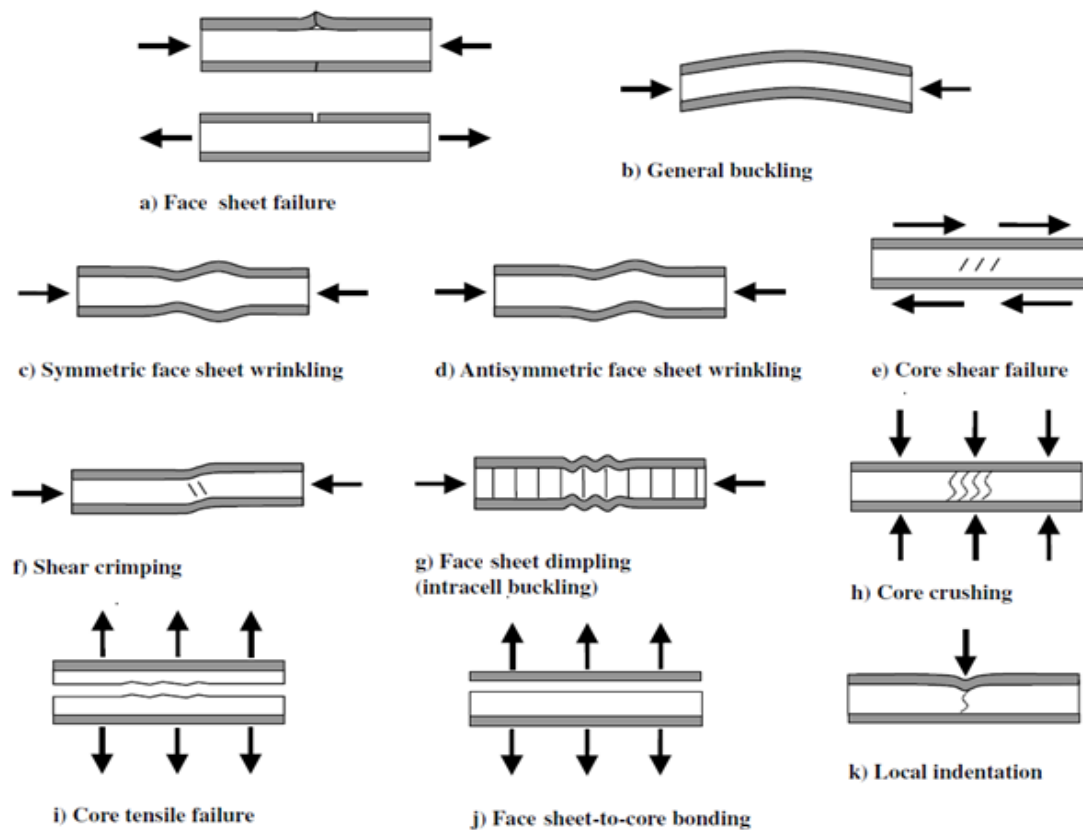


Fig. 2.8: Typical failure modes of sandwich panels (CMH-17 2013). Reproduced with permission from publisher.

2.4.1 Global buckling and shear crimping

Global buckling of the sandwich beam can be written as in Eq. (2.1) taking into account transverse shear in the core (Allen 1969):

$$\frac{1}{F_{crg}} = \frac{1}{F_{crE}} + \frac{1}{F_s} \quad (2.1)$$

where F_{crG} , F_{crE} and F_s are the global buckling load, Euler's buckling load and the shear crimping load of the sandwich beam. The equation (2.2) holds only when the face sheets of the sandwich panel are thin, and the in-plane stiffness of the core is negligible. Shear crimping typically occurs in the sandwich panels where out-of-plane shear stiffness is very low, which leads to wavelength approaching zero. The shear crimping load for the unit width of a sandwich panel consisting of symmetric face sheets can be expressed as in Eq. (2.2) (Léotoing et al. 2002a):

$$F_s = G^c \frac{(h+t_f)^2}{h}. \quad (2.2)$$

where t_f and h are the thickness of the face sheet and depth of the core respectively and G^c is the transverse shear modulus of core respectively.

2.4.2 Cell wall buckling

Cell wall buckling occurs mainly due to shear or compression in the core walls. Shear buckling of the core wall could occur when the sandwich panel is subjected to bending (Wei et al. 2020). Compression buckling of the cell wall could occur due to flat-wise compression or excessive bending of the face sheets of the sandwich panels (Wei et al. 2020, 2022). Several analytical models have been developed to predict the out-of-plane compression and shear buckling strength of hexagonal honeycomb cores (Zhang & Ashby 1992, Shi & Tong 1994, Pan et al. 2008, Banerjee et al. 2010). In calculating the elastic compression buckling strength of the hexagonal honeycomb cores, it is assumed that all walls of a cell will undergo the same deformation, thus strength is taken as the sum of the buckling load carried by the individual walls (Zhang & Ashby 1992). However, for shear buckling, strength is taken as the strength of the first wall failing due to buckling (Zhang & Ashby 1992). This is reasonable as the first wall buckling results in loss of rotational stiffness provided to the adjacent faces, thus those walls are also likely to buckle without any further increase in load. In terms of considering the effects of adjacent faces on buckling of the cell walls, many existing studies assumed common edges are either clamped (Zhang & Ashby 1992) or pinned (Pan et al. 2008; Banerjee et al. 2010). Only a few models considered the rotational restraint provided by adjacent walls at the onset of buckling (Shi & Tong 1994). In terms of the loading conditions, some studies considered shear loads in two major directions as uncoupled (Zhang & Ashby 1992), while some considered coupled action of the

shear loads in two major directions (Shi & Tong 1994). Latter obviously is a more accurate assumption as shear buckling depends on the effective loading direction. All the existing studies discussed above in this section were limited to hexagonal honeycomb shapes with identical thickness walls or double-thickness vertical wall.

López Jiménez & Triantafyllidis (2013) and Qiu et al. (2020) proposed analytical models to predict the out-of-plane compression and shear buckling of the honeycomb cores of different shapes. The method combines Bloch wave (Martín-Palma et al. 2006) representation theorem for the eigenmode with the analytical solution of the linearised von Kármán plate equations to analyse the representative volume element (RVE). Different honeycomb core shapes, including the hexagonal and square cores, were analysed. However, neither model considered composite wall honeycomb cores. Recently, Pathirana (2020) presented an analytical approach to calculate the out-of-plane compression buckling of composite honeycomb cores considering boundary conditions as rotationally restrained along the unloaded edges. Pathirana (2020) used the Ritz method and carried out linear buckling analysis considering the energy due to rotational springs at the edges.

2.4.3 Wrinkling of the face sheets

Compressive forces on the face sheets may generate short-wave buckling that occurs across multiple honeycomb core cells (Ley et al. 1999). This failure mode is called wrinkling of face sheets. Three types of wrinkling failure modes could be observed in sandwich panels: antisymmetric wrinkling, symmetric wrinkling, and one-sided wrinkling (Fig. 2.9) (Ginot. et.al. 2021). Symmetric (Fig. 2.9(a)) and one-sided wrinkling (Fig. 2.9(b)) are predominant wrinkling modes in honeycomb sandwich structures because of the high out-of-plane to in-plane elastic modulus ratio of the core. However, the wrinkling load approach to the same value regardless of mode when the depth of the core is sufficiently high (Vonarch & Rammerstorfer 2000a; Ginot et al. 2021).

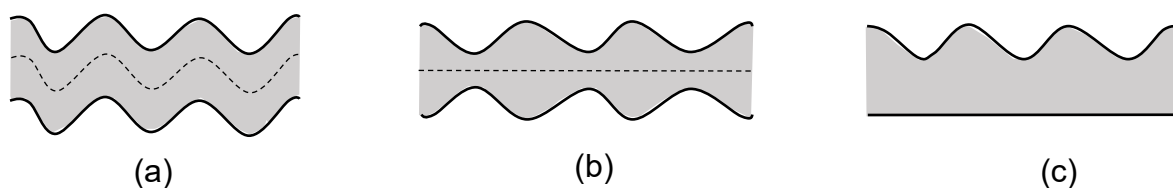


Fig. 2.9: Different wrinkling modes of sandwich panel: (a) antisymmetric (b) symmetric and (c) one-sided.

The simplest analytical model to predict the wrinkling load is Winkler's elastic foundation model (Hemp 1948) where the core is considered as an array of continuously distributed linear springs. Only the out-of-plane elastic modulus is considered and out-of-plane shear stiffness for the core is assumed as zero. The Winkler foundation model (Hemp 1948) can be written as in Eq. 2.3:

$$F_{crw}^{Winkler} = \sqrt{\frac{2t_f^3}{3h}} \sqrt{E^f E^c}, \quad (2.3)$$

where t_f and h are the thickness of the face sheet and depth of the core respectively and E^f and E^c are the elastic modulus of the face sheet and core respectively.

Noticing the wrinkling wave decay out over the length of the face core, Hoff & Maunters (1945) used a linear decay function to describe the damping out of the wave in the core together with the sinusoidal function to describe the displacement of the face sheet. They derived equations for wrinkling of the foundation of a thick core considering the strain energy due to out-of-plane normal and shear deformation of the core and the bending energy of the face sheets. This was further modified later by using an exponential decay function to describe the damping out of the wave in the core (Plantema 1966). Using Airy's stress function (Sadd 2009) to characterise the stresses in the core, Allen (1969) and Niu & Talreja (1999) solved the governing differential equations of face sheets supported on thick core and thin core. The formulas (Hoff & Maunters 1945; Plantema 1966; Allen 1969) for the critical wrinkling load of a thick isotropic core can be generally expressed as in Eq. (2.4):

$$F_{crw}^{Iso} = C_w t_f \sqrt[3]{E^f E^c G^c}, \quad (2.4)$$

where C_w is constant and E^f, E^c and G^c are the elastic modulus of the face sheet, elastic modulus and shear modulus of the core respectively. The value of constant C_w varies from 0.78 to 0.91 depending on the method of analytical derivation of the equations. The equations (2.3) and (2.4) were derived assuming an isotropic continuum core and uniaxial loading condition. Comparing different analytical solutions based on isotropic core assumption to the numerical solutions, Ginot et al. (2021) revealed that predictions for the critical wrinkling stress for honeycomb core by the analytical models developed based on isotropic continuum core are unreliable, having larger deviations compared to numerical results. However, Ginot et al. (2021)

did not study and evaluate the analytical models which are based on transversely isotropic or orthotropic core assumptions.

Some researchers (Birman 2004) also considered the wrinkling of a sandwich having a composite face sheet and isotropic core. Vonach & Rammerstorfer (2000a, 2000b) studied the wrinkling of sandwich panels of the general configuration under biaxial loading. In their study, they used the Airy stress function to characterise the stress of the transversely isotropic core. They found that it is important to consider the in-plane elastic modulus of the core in addition to the out-of-plane elastic and shear modulus in the transversely isotropic or orthotropic core. Vonach & Rammerstorfer (2000b) have demonstrated that the in-plane to out-of-plane elastic modulus ratio influences the wrinkling load of orthotropic core sandwich panels. The analytical solutions were expressed in implicit form because of the complexity of the problem they have considered. Recently, Pozorski et al. (2021) used a similar approach to Vonach & Rammerstorfer (2000a) and derived an analytical formula for the wrinkling stress of sandwich beams having a transversely isotropic core that can be expressed in a similar form to the Eq. (2.5):

$$F_{crw}^{Ortho} = 0.826t_f \sqrt[3]{E_1^f a_c^2}, \quad (2.5)$$

where E_1^f effective elastic modulus of the face sheet in direction-1 and a_c is constant depends on the effective mechanical properties of the transversely isotropic core. In addition to analytical and semi-analytical models specific for the wrinkling, some researchers also proposed unified approaches for the global buckling and wrinkling of the sandwich panels in order to understand the possible interactions between the buckling modes. The unified approaches for the global buckling and wrinkling were developed based on HSAPT (Frostig & Baruch 1993) and EHSAPT (Hu et al. 2009; Yu et al. 2015; Yuan & Kardomateas 2018) and focused on the linear (Frostig & Baruch 1993; Léotoing et al. 2002a) and nonlinear buckling (Léotoing et al. 2002b; Hu et al. 2009; Yu et al. 2015; Yuan & Kardomateas 2018) analysis of sandwich panels under uniaxial compression. While most of the studies for the unified approaches used FE formulations to solve the buckling problems considering isotropic core and orthotropic core (Hu et al. 2009; Yu et al. 2015; Yuan & Kardomateas 2018), some used analytical and semi-analytical (Frostig & Baruch 1993; Léotoing et al. 2002a) approach

considering the isotropic core. It has been identified in the past that the wrinkling load of sandwich panels with the orthotropic core is influenced by the in-plane to out-of-plane elastic modulus ratio of the core; therefore, the fibre orientations and layer sequence of core walls of the composite cellular core could affect wrinkling load of sandwich panels which may need to be investigated further to understand the influence on the wrinkling load.

2.5 Intracellular buckling

Intracellular buckling is also short-wave buckling, but unlike wrinkling, it occurs within an individual cell of the honeycomb core. Only very limited studies are available on the intracellular buckling of sandwich panels. The classical formula (Norris 1964) for intracellular buckling was first proposed based on an empirical approach and can be written as in Eq. (2.6):

$$F_{crd}^{Classical} = C_d \frac{E^f t_f}{(1-(\nu^f)^2)} \left(\frac{t_f}{D}\right)^2, \quad (2.6)$$

where E^f and ν^f are elastic modulus and Poisson's ratio of the face sheet material respectively. t_f is the thickness of the face sheet and C_d is the empirical coefficient derived based on experimental data. C_d has been estimated to be equal to 2 for the regular hexagonal cell. D is equal to the diameter of the largest circle that can be inscribed within the honeycomb cell (Fig.2.10(a)). Equation (2.6) is commonly used in sandwich panel design for conservative prediction of the intracellular buckling load because of its simple form. Eq. (2.6) was defined for the isotropic face sheet, and it was found that Eq. (2.6) is not sufficient for reasonable prediction for a strongly orthotropic face sheet (Blass 1984). Later, an improved analytical formula was proposed by Fokker Aircraft (Blass 1984) considering the orthotropic face sheet (Fig.2.9(a)) and it is given by Eq. (2.7):

$$F_{crd}^{Fokker} = \left(\frac{\pi}{D}\right)^2 [\bar{D}_{11}^f + 2(\bar{D}_{12}^f + 2\bar{D}_{66}^f) + \bar{D}_{22}^f], \quad (2.7)$$

where \bar{D}_{ij}^f is the component of the bending stiffness matrix of the composite face sheet and D is equal to the diameter of the largest circle that can be inscribed within the honeycomb cell (Fig.2.9(a)). The Eq. (2.7) is simply an equation for predicting the critical buckling load of a simply supported (SS) orthotropic square plate with side length of D . Thomsen & Banks (2004) investigated intracellular buckling of the regular

hexagonal cell using experimental and analytical approaches. In their analytical model, they assumed the boundary conditions as clamped for horizontal (or vertical) sides and simply supported (SS) for inclined sides (Fig.2.10(b)). The analytical equation can be expressed as:

$$F_{crd}^{Th} = \left(\frac{\pi}{q^2}\right)^2 [\bar{D}_{11}^f \left(\frac{q}{p}\right)^2 + \frac{8}{3}(\bar{D}_{12}^f + 2\bar{D}_{66}^f) + \frac{16}{3}\bar{D}_{22}^f \left(\frac{p}{q}\right)^2]. \quad (2.8)$$

where \bar{D}_{ij}^f is component of bending stiffness matrix of the composite faces sheet and p and q are the dimensions of the approximate rectangle geometry (Fig.2.8(b)) considered by Thomsen & Banks (2004). Comparison between the experimental and analytical results from Thomsen & Banks (2004) showed a good agreement; however, only limited experimental data were compared.

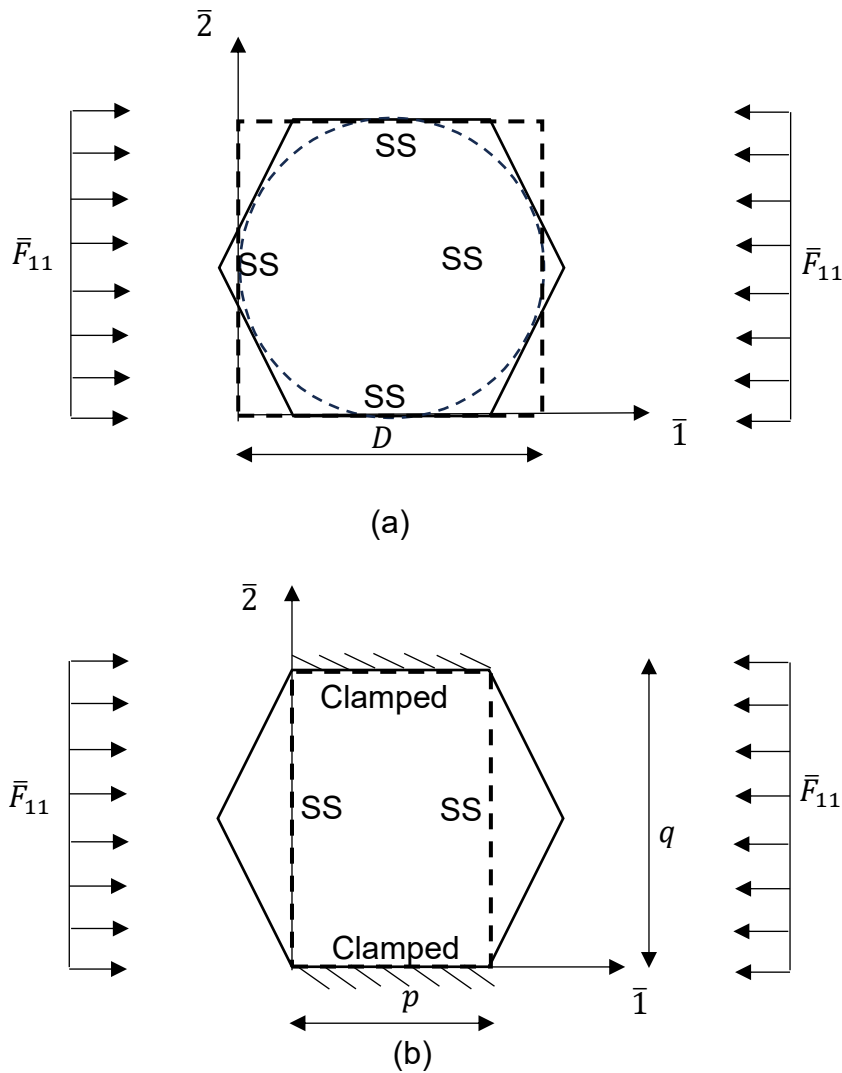


Fig. 2.10: Boundary conditions and geometry considered in (a) Fokker (b) Thomsen & Banks (2003) intracellular buckling models.

Analytical models for intracellular buckling were developed based on the assumed boundary conditions and approximated geometry to provide a simplified solution. There are multiple factors, which could influence intracellular buckling such as loading condition and direction, the geometry of the core, core material parameters etc.

2.6 Design methodology for sandwich panels

The design of sandwich panels involves consideration of various geometric and material parameters of face sheets and core. While trial and error methods can be used to select the material and geometry and to provide the target performance of the sandwich panel, such methodologies cannot consider a wide range of geometric and material options available to the designers. Most often the inverse design approach (Loonen et al. 2022) is used for systematic and intelligent selections of the design parameters.

Amongst the simplest techniques used for the inverse design of sandwich structures are the direct inverse of analytical solutions (Gibson 1984; Murthy et al. 2006) referred to as the backward method (Loonen et al. 2022) of inverse design. However, the applicability of this method is limited to simple problems with a minimal number of variables and often with a single objective function.

Sandwich panels with multiple design variables are designed using failure maps or systematic search algorithms such as evolutionary algorithms. This is referred to as the forward method (Loonen et al. 2022) of inverse design in the literature. Failure maps (Petras & Sutcliffe 2000; Russel et al. 2011; Wei et al. 2020, 2022) are used for identifying the failure modes of the design and optimising the design parameters for optimal load-weight ratio considering the simultaneous failures of components. The optimal load weight ratio is obtained in the vicinity of the simultaneous failure regions of the map. Using the failure map for the inverse design provides a certain level of flexibility in terms of the number of variables, which can be rationally optimised for the design. However, a more general way to consider a larger number of variables with multiple objectives is to use efficient search algorithms. A number of different algorithms have been used for the inverse design including genetic algorithm (Gantovnik et al. 2002; Tan & Soh 2007; Catapano & Montemurro 2014b; Abouhamzeh & Sadighi 2016; Coburn & Weaver 2016; Xu et al. 2017), particle swarm

algorithm (Hudson et al. 2009), ant colony algorithm (Aymerich & Serra 2008; Hudson et al. 2010), simulated annealing algorithm (Di Sciuva et al. 2002; Hudson et al. 2010) etc. These algorithms are typically used together with FE (Catapano & Montemurro 2014b; Abouhamzeh & Sadighi 2016) or analytical equations (Gantovnik et al. 2002; Tan & Soh 2007; Hudson et al. 2010; Coburn & Weaver 2016) for structural analysis using the equivalent model. Genetic algorithms have been used extensively for the optimisation of sandwich structures among several other algorithms (Wang & Sobey 2020). However, the reasons for the selection of the particular algorithm are not very clear in the existing literature. Only a few studies have investigated and compared the performance of different algorithms for the optimisation of sandwich structures and are typically limited to simple problems with a limited number of variables and one or two objective functions (Di Sciuva et al. 2002; Aymerich & Serra 2008; Hudson et al. 2011). According to their studies, the genetic algorithm is identified as less efficient compared to other algorithms such as particle swarm, simulated annealing and ant colony algorithms. Nonetheless, the genetic algorithm remains one of the most commonly used optimisation algorithms for sandwich structures to date.

It is clear that regardless of search algorithms, for efficient and systematic inverse design, it is important to have a simplified equivalent model, which takes into account the geometric and material configuration of the core and face sheets on the overall stiffness of the sandwich panels and accurate analytical equations for local failure predictions.

2.7 Summary and research gaps

With the advancement in manufacturing and material technologies, many options are available for materials and geometry of the cores and face sheets of sandwich panels. Since a large number of variables are involved in the design of honeycomb core sandwich panels, the selection of the optimal or near-optimal parameters for the geometry and material for the face sheets and core to provide the target performance needs a robust, systematic and efficient inverse design approach. The inverse design approach for the sandwich panels uses techniques such as failure mode maps and search algorithms together with analytical and semi-analytical models for the stiffness and strength predictions for the analysis. Regardless of the selection techniques used for the inverse design, the basis for the inverse design approach

relies on the homogenisation models used to predict the effective stiffness matrix of the honeycomb core and the models used to predict the failures in the sandwich panels. Considering the trade-off between the computational efficiency and accuracy of inverse design solutions, the honeycomb core sandwich panels are analysed as equivalent continuum shell/beam models based on the homogenised core properties. However, the equivalent shell/beam models based homogenised core for the sandwich panels cannot capture the local buckling failures in the honeycomb core and face sheets; therefore, analytical and semi-analytical models are used to predict the local buckling failures in the inverse design of sandwich panels.

In past studies, the primary focus has been on proposing suitable algorithms for the inverse design. Efficiency and the applicability of the inverse design approach depend not only on the search algorithms used for material and geometry selections but also on the analytical or semi-analytical methods used for predicting stiffness and failure modes. While having an efficient algorithm is crucial for handling the numerous geometric and material variables associated with sandwich panel design efficiently, achieving wider applicability of the inverse design approach for all-composite honeycomb core sandwich panels necessitates efficient and robust analytical or semi-analytical models to estimate stiffness considering parameters such as stacking sequences and fibre orientations, as well as failure models to predict local buckling failures considering various geometric, materials, and loading conditions.

While predictions of the effective stiffness matrix of the honeycomb core using existing approaches provide reasonably good results, those are either limited to the certain shapes of the core or limited to isotropic cell walls. A general solution for equivalent stiffness prediction applicable for many different core shapes considering the different fibre orientations and stacking sequence is necessary to facilitate the inverse designs for the all-composite honeycomb core sandwich panels. Similarly, models for predicting local buckling failures in honeycomb cores and face sheets are limited by certain honeycomb core shapes, specific loading conditions, material configurations etc. Therefore, for broader and more efficient applicability of inverse design for all-composite sandwich panels under various conditions, it is essential to develop robust analytical or semi-analytical models that can accommodate considerations of different materials, geometries, and loadings when calculating stiffness and local buckling failures.

References

- Abouhamzeh, M., & Sadighi, M. (2016). Buckling optimisation of sandwich cylindrical panels. *Curved and Layered Structures*, 3(1).
- Allen, H. G. (1969). *Analysis and Design of Structural Sandwich Panels*: Pergamon.
- Ashby, M. F. (2005). Materials selection in mechanical design [1 online resource (xiv, 603 pages) : illustrations](3rd edition ed.).
- Ashby, M. F., & Gibson, L. J. (1997). Cellular solids: structure and properties. *Press Syndicate of the University of Cambridge, Cambridge, UK*, 175-231.
- Aydogdu, M. (2009). A new shear deformation theory for laminated composite plates. *Composite Structures*, 89(1), 94-101.
- Aydogdu, M. (2009). A new shear deformation theory for laminated composite plates. *Composite Structures*, 89(1), 94-101.
- Aymerich, F., & Serra, M. (2008). Optimization of laminate stacking sequence for maximum buckling load using the ant colony optimization (ACO) metaheuristic. *Composites Part A: Applied Science and Manufacturing*, 39(2), 262-272. doi:<https://doi.org/10.1016/j.compositesa.2007.10.011>
- Balawi, S., & Abot, J. (2008). A refined model for the effective in-plane elastic moduli of hexagonal honeycombs. *Composite Structures*, 84(2), 147-158.
- Banerjee, S., Battley, M., & Bhattacharyya, D. (2010). Shear strength optimization of reinforced honeycomb core materials. *Mechanics of Advanced Materials and Structures*, 17(7), 542-552.
- Barut, A., Madenci, E., & Tessler, A. (2013). C0-continuous triangular plate element for laminated composite and sandwich plates using the {2, 2}-Refined Zigzag Theory. *Composite Structures*, 106, 835-853.
- Becker, W. (1998). The in-plane stiffnesses of a honeycomb core including the thickness effect. *Archive of Applied Mechanics*, 68(5), 334-341.
- Bhar, A., & Satsangi, S. (2011). Accurate transverse stress evaluation in composite/sandwich thick laminates using a C0 HSDT and a novel post-processing technique. *European Journal of Mechanics-A/Solids*, 30(1), 46-53.
- Birman, V., & Bert, C. W. (2002). On the choice of shear correction factor in sandwich structures. *Journal of Sandwich Structures & Materials*, 4(1), 83-95.
- Birman, V., & Bert, C. W. (2004). Wrinkling of composite-facing sandwich panels under biaxial loading. *Journal of Sandwich Structures & Materials*, 6(3), 217-237.
- Borrega, M., & Gibson, L. J. (2015). Mechanics of balsa (*Ochroma pyramidale*) wood. *Mechanics of Materials*, 84, 75-90. doi:10.1016/j.mechmat.2015.01.014
- Burton, W., & Noor, A. (1997). Assessment of continuum models for sandwich panel honeycomb cores. *Computer Methods in Applied Mechanics and Engineering*, 145(3-4), 341-360.
- Catapano, A., & Montemurro, M. (2014a). A multi-scale approach for the optimum design of sandwich plates with honeycomb core. Part I: homogenisation of core properties. *Composite Structures*, 118, 664-676.
- Catapano, A., & Montemurro, M. (2014b). A multi-scale approach for the optimum design of sandwich plates with honeycomb core. Part II: the optimisation strategy. *Composite Structures*, 118, 677-690.
- Chen, X., Yu, G., Wang, Z., Feng, L., & Wu, L. (2021). Enhancing out-of-plane compressive performance of carbon fiber composite honeycombs. *Composite Structures*, 255, 112984.

- CMH-17: Wichita State. (2013). *Composite Materials Handbook Volume 6. Structural Sandwich Composites*. SAE International.
- Cho, Y., & Averill, R. (2000). First-order zig-zag sublaminar plate theory and finite element model for laminated composite and sandwich panels. *Composite Structures*, 50(1), 1-15.
- Coburn, B. H., & Weaver, P. M. (2016). Buckling analysis, design and optimisation of variable-stiffness sandwich panels. *International Journal of Solids and Structures*, 96, 217-228.
- Cote, F., Deshpande, V., & Fleck, N. (2006). The shear response of metallic square honeycombs. *Journal of mechanics of materials and structures*, 1(7), 1281-1299.
- Cote, F., Deshpande, V., Fleck, N., & Evans, A. (2004). The out-of-plane compressive behavior of metallic honeycombs. *Materials Science and Engineering: A*, 380(1-2), 272-280.
- Cote, F., Russell, B., Deshpande, V., & Fleck, N. (2009). The through-thickness compressive strength of a composite sandwich panel with a hierarchical square honeycomb sandwich core.
- Crupi, V., Epasto, G., & Guglielmino, E. (2012). Collapse modes in aluminium honeycomb sandwich panels under bending and impact loading. *International Journal of Impact Engineering*, 43, 6-15.
- Di Sciuva, M., Gherlone, M., & Lomario, D. (2003). Multiconstrained optimization of laminated and sandwich plates using evolutionary algorithms and higher-order plate theories. *Composite Structures*, 59(1), 149-154.
- Eijo, A., Oñate, E., & Oller, S. (2013). A four-noded quadrilateral element for composite laminated plates/shells using the refined zigzag theory. *International Journal for Numerical Methods in Engineering*, 95(8), 631-660.
- Feng, L.-J., Yang, Z.-T., Yu, G.-C., Chen, X.-J., & Wu, L.-Z. (2018). Compressive and shear properties of carbon fiber composite square honeycombs with optimized high-modulus hierarchical phases. *Composite Structures*, 201, 845-856.
- Feng, Y., Qiu, H., Gao, Y., Zheng, H., & Tan, J. (2020). Creative design for sandwich structures: A review. *International Journal of Advanced Robotic Systems*, 17(3), 1729881420921327.
- Ferreira, A., Roque, C., & Jorge, R. (2005). Analysis of composite plates by trigonometric shear deformation theory and multiquadrics. *Computers & Structures*, 83(27), 2225-2237.
- Frostig, Y., Baruch, M., Vilnay, O., & Sheinman, I. (1992). High-order theory for sandwich-beam behavior with transversely flexible core. *Journal of Engineering Mechanics*, 118(5), 1026-1043.
- Frostig, Y., & Baruch, M. (1993). High-order buckling analysis of sandwich beams with transversely flexible core. *Journal of Engineering Mechanics*, 119(3), 476-495.
- Gantovnik, V. B., Gürdal, Z., & Watson, L. T. (2002). A genetic algorithm with memory for optimal design of laminated sandwich composite panels. *Composite Structures*, 58(4), 513-520.
- Gibson, I., & Ashby, M. F. (1982). The mechanics of three-dimensional cellular materials. *Proceedings of the Royal Society of London. A. Mathematical and Physical Sciences*, 382(1782), 43-59.
- Gibson, L. (1984). Optimization of stiffness in sandwich beams with rigid foam cores. *Materials Science and Engineering*, 67(2), 125-135.

- Ginot, M., d'Ottavio, M., Polit, O., Bouvet, C., & Castanié, B. (2021). Benchmark of wrinkling formulae and methods for pre-sizing of aircraft lightweight sandwich structures. *Composite Structures*, 273, 114387.
- Goswami, S., & Becker, W. (2016). Analysis of sandwich plates with compressible core using layerwise refined plate theory and interface stress continuity. *Journal of Composite Materials*, 50(2), 201-217.
- Grediac, M. (1993). A finite element study of the transverse shear in honeycomb cores. *International Journal of Solids and Structures*, 30(13), 1777-1788.
- Hamidi, A., Houari, M. S. A., Mahmoud, S., & Tounsi, A. (2015). A sinusoidal plate theory with 5-unknowns and stretching effect for thermomechanical bending of functionally graded sandwich plates. *Steel Compos. Struct*, 18(1), 235-253.
- Hara, D., & Özgen, G. O. (2016). Investigation of Weight Reduction of Automotive Body Structures with the Use of Sandwich Materials. *Transportation Research Procedia*, 14, 1013-1020.
- Hara, D., & Özgen, G. O. (2016). Investigation of Weight Reduction of Automotive Body Structures with the Use of Sandwich Materials. *Transportation Research Procedia*, 14, 1013-1020.
- Hemp, W. (1948). On a theory of sandwich construction.
- HexWeb™ Honeycomb Attributes and Properties: A comprehensive guide to standard Hexcel honeycomb materials, configurations, and mechanical properties, Hexcel Composites, Pleasanton, CA, Nov. 1999
- Hoff, N. J., & Mautner, S. (1945). The buckling of sandwich-type panels. *Journal of the Aeronautical Sciences*, 12(3), 285-297.
- Hohe, J., & Becker, W. (2001). An energetic homogenisation procedure for the elastic properties of general cellular sandwich cores. *Composites Part B: Engineering*, 32(3), 185-197.
- Hohe, J., & Becker, W. (2001). A refined analysis of the effective elasticity tensor for general cellular sandwich cores. *International Journal of Solids and Structures*, 38(21), 3689-3717.
- Hou, W., Shen, Y., Jiang, K., & Wang, C. (2022). Study on mechanical properties of carbon fiber honeycomb curved sandwich structure and its application in engine hood. *Composite Structures*, 286, 115302.
- Hou, Y., Neville, R., Scarpa, F., Remillat, C., Gu, B., & Ruzzene, M. (2014). Graded conventional-auxetic Kirigami sandwich structures: Flatwise compression and edgewise loading. *Composites Part B: Engineering*, 59, 33-42.
- Hu, H., Belouettar, S., Potier-Ferry, M., & Makradi, A. (2009). A novel finite element for global and local buckling analysis of sandwich beams. *Composite Structures*, 90(3), 270-278.
- Huang, H., & Kardomateas, G. A. (2002). Buckling and initial postbuckling behavior of sandwich beams including transverse shear. *AIAA Journal*, 40(11), 2331-2335.
- Hudson, C. W., Carruthers, J. J., & Robinson, A. M. (2009). Application of particle swarm optimisation to sandwich material design. *Plastics, rubber and composites*, 38(2-4), 106-110.
- Hudson, C. W., Carruthers, J. J., & Robinson, A. M. (2010). A comparison of three population-based optimization techniques for the design of composite sandwich materials. *Journal of Sandwich Structures & Materials*, 13(2), 213-235.

- Hudson, C. W., Carruthers, J. J., & Robinson, A. M. (2010). Multiple objective optimisation of composite sandwich structures for rail vehicle floor panels. *Composite Structures*, 92(9), 2077-2082.
- Icardi, U. (2001). Higher-order zig-zag model for analysis of thick composite beams with inclusion of transverse normal stress and sublaminates approximations. *Composites Part B: Engineering*, 32(4), 343-354.
- Irfan, S., & Siddiqui, F. (2019). A review of recent advancements in finite element formulation for sandwich plates. *Chinese Journal of Aeronautics*, 32(4), 785-798. doi:10.1016/j.cja.2018.11.011
- Irfan, S., & Siddiqui, F. (2021). A novel finite element formulation based on extended higher-order theory for sandwich plates of arbitrary aspect ratio. *Journal of Sandwich Structures & Materials*, 23(2), 711-735. doi:10.1177/1099636220975290
- Jiménez, F. L., & Triantafyllidis, N. (2013). Buckling of rectangular and hexagonal honeycomb under combined axial compression and transverse shear. *International Journal of Solids and Structures*, 50(24), 3934-3946.
- Jiménez, F. L., & Triantafyllidis, N. (2013). Buckling of rectangular and hexagonal honeycomb under combined axial compression and transverse shear. *International Journal of Solids and Structures*, 50(24), 3934-3946.
- Kee Paik, J., Thayamballi, A. K., & Sung Kim, G. (1999). The strength characteristics of aluminum honeycomb sandwich panels. *Thin-Walled Structures*, 35(3), 205-231.
- Kelsey, S., Gellatly, R., & Clark, B. (1958). The shear modulus of foil honeycomb cores: A theoretical and experimental investigation on cores used in sandwich construction. *Aircraft Engineering and Aerospace Technology*.
- Khan, T., Acar, V., Aydin, M. R., Hülágü, B., Akbulut, H., & Seydibeyoğlu, M. Ö. (2020). A review on recent advances in sandwich structures based on polyurethane foam cores. *Polymer Composites*, 41(6), 2355-2400.
- Kirchhoff, G. (1850). Über das Gleichgewicht und die Bewegung einer elastischen Scheibe. *Journal für die reine und angewandte Mathematik (Crelles Journal)*, 1850(40), 51-88.
- Krishnamurthy, T., & Saether, E. (2019). *Estimation of Effective Elastic Properties of General Multifunctional Honeycomb Structures Using a Unit Cell Method*. Paper presented at the AIAA Scitech 2019 Forum.
- Kumar, A., Angra, S., & Chanda, A. K. (2023). Fabrication and mechanical characterisation of composite sandwich structure having kevlar honeycomb core. *Advances in Materials and Processing Technologies*, 1-18. doi:10.1080/2374068X.2023.2193441
- Laszczyk, L. (2011). *Homogenization and topological optimization of architected panels* (Doctoral dissertation, PhD thesis, Grenoble University).
- Léotoing, L., Drapier, S., & Vautrin, A. (2002a). First applications of a novel unified model for global and local buckling of sandwich columns. *European Journal of Mechanics-A/Solids*, 21(4), 683-701.
- Léotoing, L., Sylvain Drapier, and Alain Vautrin. "Nonlinear interaction of geometrical and material properties in sandwich beam instabilities." *International Journal of Solids and Structures* 39, no. 13-14 (2002b): 3717-3739.
- Ley, R. P., Lin, W., & Mbanefo, U. (1999). *Facesheet wrinkling in sandwich structures* (No. NAS 1.26: 208994).
- Li, R., & Kardomateas, G. A. (2008). Nonlinear high-order core theory for sandwich plates with orthotropic phases. *AIAA Journal*, 46(11), 2926-2934.

- Li, Y., Abbès, F., Hoang, M., Abbès, B., & Guo, Y. (2016). Analytical homogenization for in-plane shear, torsion and transverse shear of honeycomb core with skin and thickness effects. *Composite Structures*, 140, 453-462.
- Loonen, R. C., de Vries, S., & Goia, F. (2022). Inverse design for advanced building envelope materials, systems and operation. In *Rethinking Building Skins* (pp. 377-402): Elsevier.
- Mahi, A., & Tounsi, A. (2015). A new hyperbolic shear deformation theory for bending and free vibration analysis of isotropic, functionally graded, sandwich and laminated composite plates. *Applied Mathematical Modelling*, 39(9), 2489-2508.
- Malek, S., & Gibson, L. (2015). Effective elastic properties of periodic hexagonal honeycombs. *Mechanics of Materials*, 91, 226-240.
- Manalo, A., Aravinthan, T., Fam, A., & Benmokrane, B. (2017). State-of-the-Art Review on FRP Sandwich Systems for Lightweight Civil Infrastructure. *Journal of Composites for Construction*, 21(1), 04016068.
- Mantari, J., Oktem, A., & Soares, C. G. (2012). A new trigonometric layerwise shear deformation theory for the finite element analysis of laminated composite and sandwich plates. *Computers & Structures*, 94, 45-53.
- Mantari, J. L., & Soares, C. G. (2012). Analysis of isotropic and multilayered plates and shells by using a generalized higher-order shear deformation theory. *Composite Structures*, 94(8), 2640-2656.
- Martín-Palma, R. J., Martínez-Duart, J., & Agulló-Rueda, F. (2006). *Nanotechnology for microelectronics and optoelectronics*. Elsevier.
- Masters, I., & Evans, K. (1996). Models for the elastic deformation of honeycombs. *Composite Structures*, 35(4), 403-422.
- Min, L., Fernando, D., Gilbert, B., & You, Z. (2020). Hybrid FRP-timber thin-walled Cee section columns under axial compression: Numerical modelling. *Thin-Walled Structures*, 157, 107029.
- Mukherjee, S., & Adhikari, S. (2021). A general analytical framework for the mechanics of heterogeneous hexagonal lattices. *Thin-Walled Structures*, 167, 108188.
- Murthy, O., Munirudrappa, N., Srikanth, L., & Rao, R. (2006). Strength and stiffness optimization studies on honeycomb core sandwich panels. *Journal of Reinforced Plastics and Composites*, 25(6), 663-671.
- Nallim, L. G., Oller, S., Oñate, E., & Flores, F. G. (2017). A hierarchical finite element for composite laminated beams using a refined zigzag theory. *Composite Structures*, 163, 168-184.
- Namvar, A. R., & Vosoughi, A. R. (2020). Design optimization of moderately thick hexagonal honeycomb sandwich plate with modified multi-objective particle swarm optimization by genetic algorithm (MOPSOGA). *Composite Structures*, 252, 112626.
- Ning, H., Janowski, G. M., Vaidya, U. K., & Husman, G. (2007). Thermoplastic sandwich structure design and manufacturing for the body panel of mass transit vehicle. *Composite Structures*, 80(1), 82-91.
- Niu, K., & Talreja, R. (1999). Modeling of Wrinkling in Sandwich Panels under Compression. *Journal of Engineering Mechanics*, 125(8), 875-883.
- Norris, C. B. (1964). *Short-column compressive strength of sandwich constructions as affected by size of cells of honeycomb core materials* (Vol. 26): US Department of Agriculture, Forest Service, Forest Products Laboratory.

- Ou, Y., Fernando, D., & Gattas, J. M. (2019). Experimental investigation of a novel concrete-timber floor panel system with digitally fabricated FRP-timber hollow core component. *Construction and Building Materials*, 227, 116667.
- Palomba, G., Epasto, G., & Crupi, V. (2022). Lightweight sandwich structures for marine applications: a review. *Mechanics of Advanced Materials and Structures*, 29(26), 4839-4864.
- Palomba, G., Epasto, G., & Crupi, V. (2022). Lightweight sandwich structures for marine applications: a review. *Mechanics of Advanced Materials and Structures*, 29(26), 4839-4864.
- Pan, S.D., Wu, L.Z., & Sun, Y.G. (2008). Transverse shear modulus and strength of honeycomb cores. *Composite Structures*, 84(4), 369-374.
- Panda, S., & Natarajan, R. (1981). Analysis of laminated composite shell structures by finite element method. *Computers & Structures*, 14(3-4), 225-230.
- Pandey, S., & Pradyumna, S. (2015). A new C0 higher-order layerwise finite element formulation for the analysis of laminated and sandwich plates. *Composite Structures*, 131, 1-16.
- Pandit, M. K., Sheikh, A. H., & Singh, B. N. (2008). An improved higher order zigzag theory for the static analysis of laminated sandwich plate with soft core. *Finite elements in analysis and design*, 44(9-10), 602-610.
- Pathirana, S. T. (2020). *Local Buckling Analysis of Composite Corrugated and Honeycomb Structures*: Washington State University.
- Pehlivan, L., & Baykasoğlu, C. (2019). An experimental study on the compressive response of CFRP honeycombs with various cell configurations. *Composites Part B: Engineering*, 162, 653-661.
- Penado, F. E. (2013). Effective elastic properties of honeycomb core with fiber-reinforced composite cells. *Open Journal of Composite Materials*, 3(04), 89.
- Petras, A., & Sutcliffe, M. (1999). Failure mode maps for honeycomb sandwich panels. *Composite Structures*, 44(4), 237-252.
- Plagianakos, T. S., & Saravanos, D. A. (2009). Higher-order layerwise laminate theory for the prediction of interlaminar shear stresses in thick composite and sandwich composite plates. *Composite Structures*, 87(1), 23-35.
- Plantema, F. J. (1966). *Sandwich construction: the bending and buckling of sandwich beams, plates, and shells*: Wiley.
- Pozorski, Z., Pozorska, J., Kreja, I., & Smakosz, Ł. (2021). On Wrinkling in Sandwich Panels with an Orthotropic Core. *Materials*, 14(17), 5043.
- Qiu, C., Guan, Z., Guo, X., & Li, Z. (2020). Buckling of honeycomb structures under out-of-plane loads. *Journal of Sandwich Structures & Materials*, 22(3), 797-821.
- Russell, B., Deshpande, V., & Wadley, H. (2008). Quasistatic deformation and failure modes of composite square honeycombs. *Journal of mechanics of materials and structures*, 3(7), 1315-1340.
- Russell, B., Liu, T., Fleck, N., & Deshpande, V. (2011). Quasi-static three-point bending of carbon fiber sandwich beams with square honeycomb cores. *Journal of Applied Mechanics*, 78(3).
- Sadd, M. H. (2009). *Elasticity: theory, applications, and numerics*. Academic Press.
- Saito, K., Agnese, F., & Scarpa, F. (2011). A Cellular Kirigami Morphing Wingbox Concept. *Journal of Intelligent Material Systems and Structures*, 22(9), 935-944. doi:10.1177/1045389x11416030

- Santos, L., Izzuddin, B. A., & Macorini, L. (2022). Gradient-based optimisation of rectangular honeycomb core sandwich panels. *Structural and Multidisciplinary Optimization*, 65(9), 242.
- Shah, U. B., & Kapania, R. K. (2020). Failure of hexagonal and triangular honeycomb core sandwich panels. *AIAA Journal*, 58(11), 4923-4940.
- Shi, G., & Tong, P. (1994). Local buckling of honeycomb sandwich plates under action of transverse shear forces. *AIAA Journal*, 32(7), 1520-1524.
- Shi, G., & Tong, P. (1995). The derivation of equivalent constitutive equations of honeycomb structures by a two scale method. *Computational mechanics*, 15(5), 395-407.
- Shi, S.S., Sun, Z., Hu, X.Z., & Chen, H.-r. (2014). Carbon-fiber and aluminum-honeycomb sandwich composites with and without Kevlar-fiber interfacial toughening. *Composites Part A: Applied Science and Manufacturing*, 67, 102-110.
- Shir Mohammadi, M., & Nairn, J. A. (2017). Balsa sandwich composite fracture study: Comparison of laminated to solid balsa core materials and debonding from thick balsa core materials. *Composites Part B: Engineering*, 122, 165-172. doi:10.1016/j.compositesb.2017.04.018
- Siddiqui, F., & Kardomateas, G. (2019). Extended higher-order sandwich panel theory for plates with arbitrary aspect ratios. *Journal of mechanics of materials and structures*, 14(4), 449-459.
- Siddiqui, F. K. (2015). *Extended higher order theory for sandwich plates of arbitrary aspect ratio*. Georgia Institute of Technology,
- Somnic, J., & Jo, B. W. (2022). Status and challenges in homogenization methods for lattice materials. *Materials*, 15(2), 605.
- Sorohan, S., Constantinescu, D. M., Sandu, M., & Sandu, A. G. (2018). On the homogenization of hexagonal honeycombs under axial and shear loading. Part II: Comparison of free skin and rigid skin effects on effective core properties. *Mechanics of Materials*, 119, 92-108.
- State, C.W. (2013). *Composite Materials Handbook Volume 6. Structural Sandwich Composites*: SAE International.
- Stocchi, A., Colabella, L., Cisilino, A., & Álvarez, V. (2014). Manufacturing and testing of a sandwich panel honeycomb core reinforced with natural-fiber fabrics. *Materials & Design*, 55, 394-403.
- Sugiyama, K., Matsuzaki, R., Ueda, M., Todoroki, A., & Hirano, Y. (2018). 3D printing of composite sandwich structures using continuous carbon fiber and fiber tension. *Composites Part A: Applied Science and Manufacturing*, 113, 114-121. doi:https://doi.org/10.1016/j.compositesa.2018.07.029
- Tan, X., & Soh, A. (2007). Multi-objective optimization of the sandwich panels with prismatic cores using genetic algorithms. *International Journal of Solids and Structures*, 44(17), 5466-5480.
- Tessler, A., Di Sciuva, M., & Gherlone, M. (2010). A consistent refinement of first-order shear deformation theory for laminated composite and sandwich plates using improved zigzag kinematics. *Journal of mechanics of materials and structures*, 5(2), 341-367.
- Thai, H.-T., & Choi, D.-H. (2013). Finite element formulation of various four unknown shear deformation theories for functionally graded plates. *Finite elements in analysis and design*, 75, 50-61.
- Thomsen, O. T. (2009). Sandwich Materials for Wind Turbine Blades — Present and Future. *Journal of Sandwich Structures & Materials*, 11(1), 7-26.

- Thomsen, O. T., & Banks, W. M. (2004). An improved model for the prediction of intra-cell buckling in CFRP sandwich panels under in-plane compressive loading. *Composite Structures*, 65(3-4), 259-268.
- Tounsi, A., Houari, M. S. A., & Benyoucef, S. (2013). A refined trigonometric shear deformation theory for thermoelastic bending of functionally graded sandwich plates. *Aerospace Science and Technology*, 24(1), 209-220.
- Vitale, J. P., Francucci, G., Xiong, J., & Stocchi, A. (2017). Failure mode maps of natural and synthetic fiber reinforced composite sandwich panels. *Composites Part A: Applied Science and Manufacturing*, 94, 217-225.
- Vlachoutsis, S. (1992). Shear correction factors for plates and shells. *International Journal for Numerical Methods in Engineering*, 33(7), 1537-1552.
- Vonach, W. K., & Rammerstorfer, F. G. (2000a). The effects of in-plane core stiffness on the wrinkling behavior of thick sandwiches. *Acta Mechanica*, 141(1-2), 1-10.
- Vonach, W. K., & Rammerstorfer, F. G. (2000b). Wrinkling of thick orthotropic sandwich plates under general loading conditions. *Archive of Applied Mechanics*, 70, 338-348.
- Vrabie, M., Chiriac, R., & Băetu, S. A. (2017). *Studies regarding the shear correction factor in the Mindlin plate theory for sandwich plates*. Paper presented at the Advanced Engineering Forum.
- Wadley, H. N. (2006). Multifunctional periodic cellular metals. *Philosophical Transactions of the Royal Society A: Mathematical, Physical and Engineering Sciences*, 364(1838), 31-68.
- Wang, A.J., & McDowell, D. (2004). In-plane stiffness and yield strength of periodic metal honeycombs. *J. Eng. Mater. Technol.*, 126(2), 137-156.
- Wang, Z., & Sobey, A. (2020). A comparative review between Genetic Algorithm use in composite optimisation and the state-of-the-art in evolutionary computation. *Composite Structures*, 233, 111739.
- Wang, R., & Wang, J. (2018). Modeling of honeycombs with laminated composite cell walls. *Composite Structures*, 184, 191-197.
- Wei, X., Li, D., & Xiong, J. (2019). Fabrication and mechanical behaviors of an all-composite sandwich structure with a hexagon honeycomb core based on the tailor-folding approach. *Composites Science and Technology*, 184, 107878.
- Wei, X., Wu, Q., Gao, Y., & Xiong, J. (2020). Bending characteristics of all-composite hexagon honeycomb sandwich beams: experimental tests and a three-dimensional failure mechanism map. *Mechanics of Materials*, 148, 103401.
- Wei, X., Wu, Q., Gao, Y., Yang, Q., & Xiong, J. (2022). Composite honeycomb sandwich columns under in-plane compression: Optimal geometrical design and three-dimensional failure mechanism maps. *European Journal of Mechanics-A/Solids*, 91, 104415.
- Xiaohui, R., Wanji, C., & Zhen, W. (2012). AC 0-type zig-zag theory and finite element for laminated composite and sandwich plates with general configurations. *Archive of Applied Mechanics*, 82, 391-406.
- Xu, X., Jiang, Y., & Pueh Lee, H. (2017). Multi-objective optimal design of sandwich panels using a genetic algorithm. *Engineering Optimization*, 49(10), 1665-1684.
- Xu, X. F., & Qiao, P. (2002). Homogenized elastic properties of honeycomb sandwich with skin effect. *International Journal of Solids and Structures*, 39(8), 2153-2188.

- Xu, X. F., Qiao, P., & Davalos, J. F. (2001). Transverse shear stiffness of composite honeycomb core with general configuration. *Journal of Engineering Mechanics*, 127(11), 1144-1151.
- Yu, K., Hu, H., Tang, H., Giunta, G., Potier-Ferry, M., & Belouettar, S. (2015). A novel two-dimensional finite element to study the instability phenomena of sandwich plates. *Computer Methods in Applied Mechanics and Engineering*, 283, 1117-1137.
- Yuan, Z. (2017). *Geometric nonlinearity effects on the behaviour of sandwich structures*. Georgia Institute of Technology.
- Yuan, Z., & Kardomateas, G. A. (2018). Nonlinear Stability Analysis of Sandwich Wide Panels—Part I: Buckling Behavior. *Journal of Applied Mechanics*, 85(8). doi:10.1115/1.4039953
- Yuan, Z., Kardomateas, G. A., & Frostig, Y. (2015). Finite element formulation based on the extended high-order sandwich panel theory. *AIAA Journal*, 53(10), 3006-3015.
- Yuan, Z., Kardomateas, G. A., & Frostig, Y. (2016). Geometric nonlinearity effects in the response of sandwich wide panels. *Journal of Applied Mechanics*, 83(9), 091008.
- Zenkert, D. (1997). *The handbook of sandwich construction: Engineering Materials Advisory Services*.
- Zhang, J., & Ashby, M. (1992). The out-of-plane properties of honeycombs. *International Journal of Mechanical Sciences*, 34(6), 475-489.

Chapter 3:

Effective stiffness matrix of laminated composite wall honeycomb core

3.1 General

Equivalent models where honeycomb cellular cores are considered as an effective homogeneous continuum are often used in the design and analysis of the honeycomb core sandwich panels. Most of the existing studies on the homogenisation of honeycomb cores focused on isotropic walls of the honeycomb core, which cannot be directly used to analyse honeycomb cores made using composite laminates. Recently, researchers (Russell et al. 2008,2011; Feng et al. 2018; Pehlivan & Baykasoğlu 2019; Chen et al. 2021; Wei et al. 2019, 2020, 2022) have considered the potential of laminated composite honeycomb cores for different lightweight sandwich structure applications. Composite honeycomb cellular core sandwich panels introduce several additional parameters, such as fibre orientations and layer sequence, compared to isotropic honeycomb cores, which need to be considered in calculating the effective stiffness properties of the core. While some models exist to calculate the equivalent properties of homogenised composite cores, they are limited to hexagonal honeycomb cores and cannot be applied in general to honeycomb cores with other shapes. This chapter aims to develop a generalised homogenisation model to determine the effective mechanical properties of the laminated composite wall honeycomb core with different shapes and to investigate the influence of fibre orientations, layer sequence, and geometry on the effective properties of the honeycomb core.

3.2 Strain-energy based homogenisation.

Amongst the most used approaches for obtaining the equivalent properties of the homogenized cores, strain energy-based approach was found to be the most applicable when more generally applicable models to be developed, thus selected in this study to develop the proposed solution for the laminated composite honeycomb core. This section describes the basic theory of strain energy-based homogenisation.

A periodic honeycomb core structure (Fig. 3.1) with a domain Ω and an external boundary Γ is replaced with a homogenous effective continuum body Ω^H with the same shape and an external boundary Γ^H .

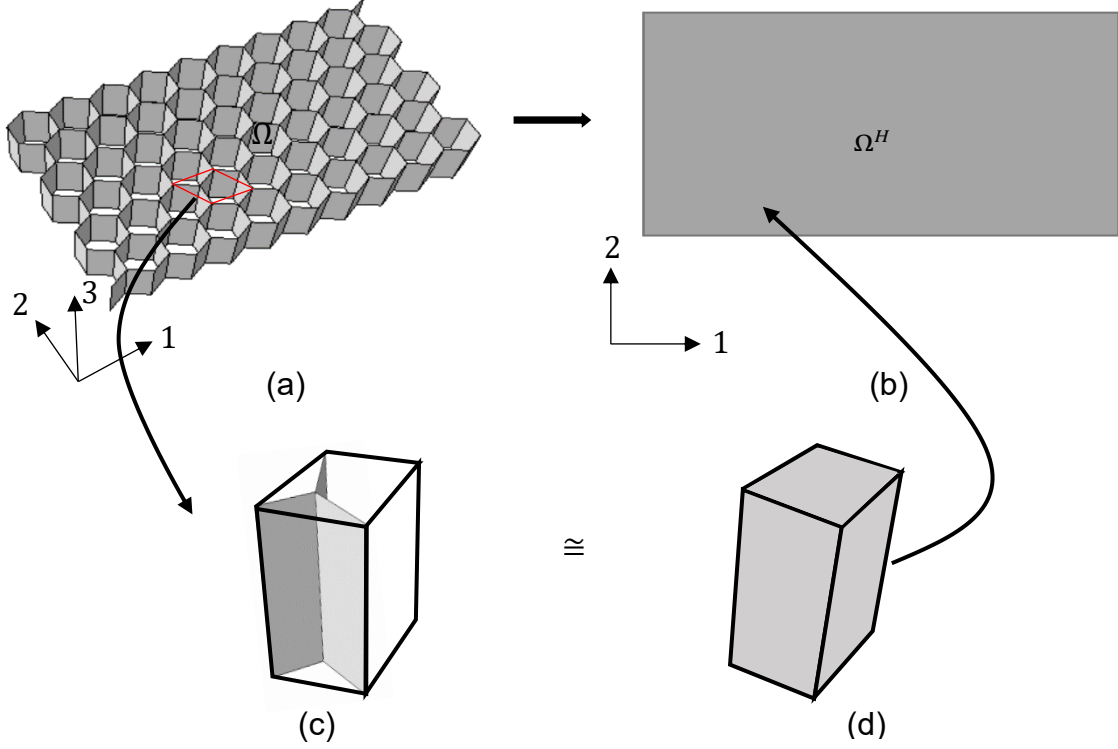


Fig. 3.1: A periodic honeycomb structure: (a) actual configuration (b) homogenous effective continuum body and RVE of (c) actual configuration and (d) effective continuum body.

In the strain energy-based homogenisation adopted in this study, both bodies are considered equivalent in terms of mechanical behaviour at the macroscopic level if the strain energy of the representative volume elements (RVEs) of both the bodies are equal under the same external loading and boundary conditions. The strain energy of both RVEs has to be equal if the volume average strains of both RVEs are equal (Bishop, & Hill 1951):

$$\varepsilon_{ij} = \frac{1}{V_{RVE}} \int_V \varepsilon_{ij}^* dV = \frac{1}{V_{RVE}} \int_V \varepsilon_{ij}^{H*} dV^H = \varepsilon_{ij}^H. \quad (3.1)$$

If the condition in Eq. (3.1) holds then equivalent strain energy between the RVEs of the honeycomb structure and the homogenised continuum can be written as in Eq. (3.2) with a linear constitutive relation for the material:

$$w(\varepsilon_{ij}) = \frac{1}{V_{RVE}} \int_V w(\varepsilon_{ij}^*) dV = \frac{1}{V_{RVE}} \int_V w^H(\varepsilon_{ij}^{H*}) dV^H = w^H(\varepsilon_{ij}^H), \quad (3.2)$$

where $w(\varepsilon_{ij})$ and $w^H(\varepsilon_{ij}^H)$ are strain energy density of the RVEs of Ω and Ω^H respectively, V_{RVE} is the volume of the RVEs, ε_{ij} and ε_{ij}^H are strain tensor components of RVEs of the honeycomb core structure and the effective homogenous continuum medium respectively. Here, Latin indices, $\{i, j, k, \dots\}$, refer to the 1, 2 or 3 directions.

If the effective continuum body is assumed to be linear elastic, then the relationship between the stress and strain components can be expressed as:

$$\sigma_{ij}^H = C_{ijkl}^H \varepsilon_{kl}^H. \quad (3.3)$$

The stiffness components C_{ijkl}^H of effective elasticity tensor for three-dimensional (3D) analysis can be expressed as in Eq. (3.4):

$$C_{ijkl}^H = \frac{\partial^2 w^H}{\partial \varepsilon_{ij}^H \partial \varepsilon_{kl}^H}. \quad (3.4)$$

Equation. (3.4) yields 21 independent components (C_{ijkl}^H) of effective elasticity tensor. Assuming the equivalent cellular core at the continuum level behaves as an orthotropic core, nine non-zero components are required to define the effective elastic stiffness tensor. Considering Eq. (3.2) - (3.4), the 9 non-zero components of C_{ijkl}^H can be expressed using Eqs. (3.5) - (3.7):

$$C_{ijkl}^H = 2w(\varepsilon_{(ij)}) \frac{1}{\varepsilon_{(ij)}^2} \text{ if: } i = j, k = l \text{ and } i = k, \quad (3.5)$$

$$C_{ijkl}^H = \frac{1}{2} w(\varepsilon_{(ij)}) \frac{1}{\varepsilon_{(ij)}^2} \text{ if: } i \neq j, k \neq l, i = k \text{ and } j = l, \quad (3.6)$$

$$C_{ijkl}^H = \left(w(\varepsilon_{(ij), \varepsilon_{(kl)}}) - w(\varepsilon_{(ij)}) - w(\varepsilon_{(kl)}) \right) \frac{1}{\varepsilon_{(ij)} \varepsilon_{(kl)}} \text{ if: } i = j, k = l \text{ and } i \neq k. \quad (3.7)$$

In Voigt's matrix notation, the effective elastic stiffness for an equivalent orthotropic continuum core can be written as:

$$\mathbf{C}^H = \begin{bmatrix} C_{1111}^H & C_{1122}^H & C_{1133}^H & 0 & 0 & 0 \\ C_{1122}^H & C_{2222}^H & C_{2233}^H & 0 & 0 & 0 \\ C_{1133}^H & C_{2233}^H & C_{3333}^H & 0 & 0 & 0 \\ 0 & 0 & 0 & C_{1212}^H & 0 & 0 \\ 0 & 0 & 0 & 0 & C_{1313}^H & 0 \\ 0 & 0 & 0 & 0 & 0 & C_{2323}^H \end{bmatrix}. \quad (3.8)$$

By assuming the equivalent continuum core as a shell, effective stiffness components for the equivalent shell of the cellular core can be derived by reducing the effective

elasticity matrix in Eq. (3.8) assuming a plane-stress condition, *i.e.*, normal stresses in direction-3 (*i.e.* through core thickness/outer plane direction, Fig. 3.1) are zero. Plane stress effective stiffness matrix \mathbf{Q}_p^H and transverse shear effective stiffness matrix \mathbf{Q}_s^H can then be written as:

$$\mathbf{Q}_p^H = \begin{bmatrix} Q_{11}^H & Q_{12}^H & 0 \\ Q_{12}^H & Q_{22}^H & 0 \\ 0 & 0 & Q_{66}^H \end{bmatrix} = \begin{bmatrix} C_{1111}^H - \frac{C_{1133}^H * C_{1133}^H}{C_{3333}^H} & C_{1122}^H - \frac{C_{1133}^H * C_{2233}^H}{C_{3333}^H} & 0 \\ C_{1122}^H - \frac{C_{1133}^H * C_{2233}^H}{C_{3333}^H} & C_{2222}^H - \frac{C_{2233}^H * C_{2233}^H}{C_{3333}^H} & 0 \\ 0 & 0 & C_{1212}^H \end{bmatrix} \quad (3.9)$$

$$\mathbf{Q}_s^H = \begin{bmatrix} Q_{44}^H & 0 \\ 0 & Q_{55}^H \end{bmatrix} = \begin{bmatrix} C_{1313}^H & 0 \\ 0 & C_{2323}^H \end{bmatrix}. \quad (3.10)$$

Effective engineering constants of the core can be calculated from the compliance matrix, which can be found from the inverse of the effective elasticity matrix:

$$(\mathbf{C}^H)^{-1} = \begin{bmatrix} \frac{1}{E_1^H} & -\frac{\nu_{21}^H}{E_2^H} & -\frac{\nu_{31}^H}{E_3^H} & 0 & 0 & 0 \\ -\frac{\nu_{12}^H}{E_1^H} & \frac{1}{E_2^H} & -\frac{\nu_{32}^H}{E_3^H} & 0 & 0 & 0 \\ -\frac{\nu_{13}^H}{E_1^H} & -\frac{\nu_{23}^H}{E_2^H} & \frac{1}{E_3^H} & 0 & 0 & 0 \\ 0 & 0 & 0 & \frac{1}{G_{12}^H} & 0 & 0 \\ 0 & 0 & 0 & 0 & \frac{1}{G_{13}^H} & 0 \\ 0 & 0 & 0 & 0 & 0 & \frac{1}{G_{23}^H} \end{bmatrix}, \quad (3.11)$$

where E_1^H, E_2^H and E_3^H are elastic moduli in 1, 2 and 3 directions, respectively. G_{12}^H is the in-plane shear modulus, and G_{13}^H and G_{23}^H are out-of-plane shear moduli. ν_{12}^H and ν_{21}^H are in-plane Poisson's ratios, and $\nu_{13}^H, \nu_{31}^H, \nu_{23}^H$ and ν_{32}^H are out-of-plane Poisson's ratios.

3.2.1 Strain energy density of the honeycomb core RVE

Section 3.2 described the concept of strain energy-based approach for the homogenisation. In the past, researchers used strain energy-based approach to derive analytical homogenisation models specifically for the hexagonal core (Becker 1998; Xu and Qiao 2002; Li et al. 2016) and for honeycomb core with different shapes with isotropic walls (Hohe & Backer 2001). However, the strain energy-based homogenisation model has not been extended for the laminated composite honeycomb core with different shapes. Therefore, in this chapter, the objective is to

develop a homogenisation model for the laminated composite honeycomb core with different shapes which considers the additional laminate parameters such as lay-up sequence, fibre orientations etc. In order to do that we incorporate the laminate theory to consider the thick and thin laminate walls of the honeycomb core and the strain energy density function is derived for the RVEs considering the plane stress condition for the laminated composite walls of the honeycomb core. A simplified methodology is also proposed to take into account of the unsymmetric laminate in the strain energy density function by defining approximate neutral axis for the laminate. This section presents the derivation of strain energy density for a RVE of the honeycomb core. In determining the strain energy for the RVE, it is necessary to use the stress-strain relationship of the composite honeycomb cell walls. Therefore, the stress-strain relationship based on classical laminate theory (CLT) is first presented briefly for completeness.

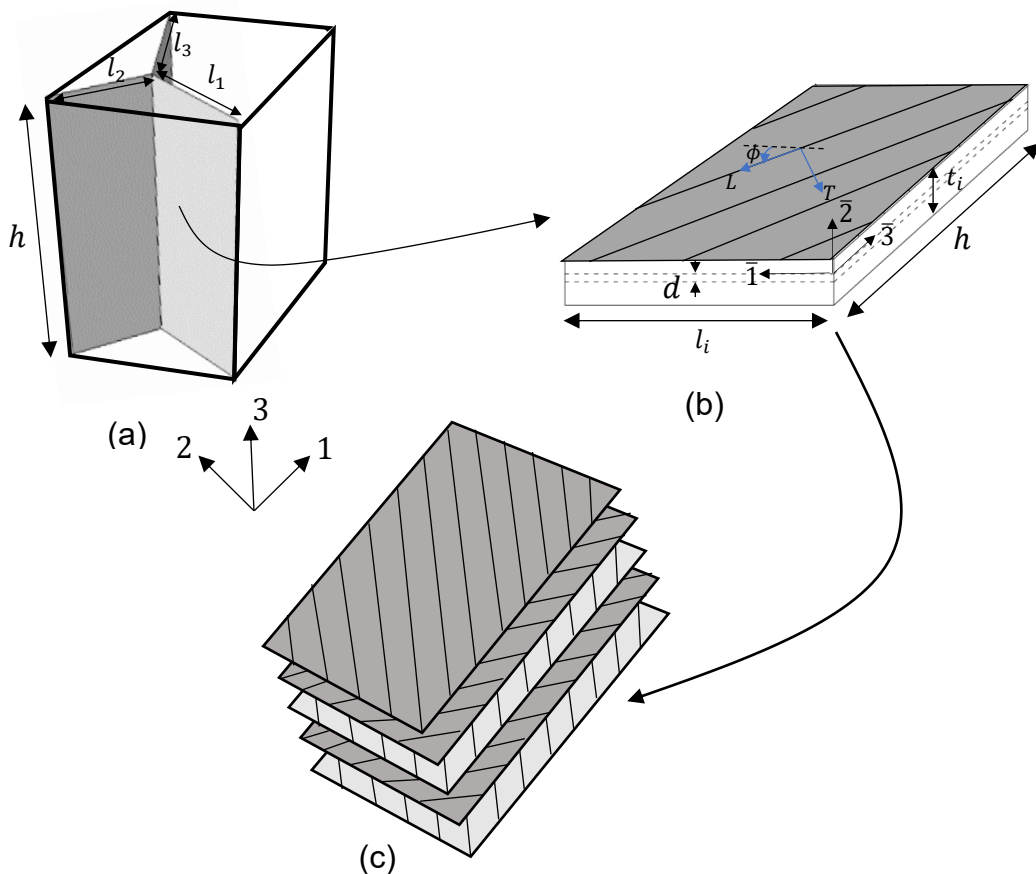


Fig. 3.2: (a) RVE of periodic honeycomb core fabricated out of (b) laminated composite walls consisting of (c) fibre layers at different orientations. The positive angle ϕ of the fibre orientation is measured counterclockwise with respect to the positive direction- $\bar{1}$.

The combined stiffness matrix (\overline{ABD}) and compliance matrix (\overline{ABD}^{-1}) of the laminated composite plate with respect to the arbitrarily chosen reference plane (in the current study, the reference plane is taken as the mid-plane of the section Fig. 3.2(b)) are respectively given by the following expressions:

$$\overline{ABD} = \begin{bmatrix} \bar{A}_{11} & \bar{A}_{13} & \bar{A}_{16} & \bar{B}_{11} & \bar{B}_{13} & \bar{B}_{16} \\ \bar{A}_{13} & \bar{A}_{33} & \bar{A}_{36} & \bar{B}_{13} & \bar{B}_{33} & \bar{B}_{36} \\ \bar{A}_{16} & \bar{A}_{36} & \bar{A}_{66} & \bar{B}_{16} & \bar{B}_{36} & \bar{B}_{66} \\ \bar{B}_{11} & \bar{B}_{13} & \bar{B}_{16} & \bar{D}_{11} & \bar{D}_{13} & \bar{D}_{16} \\ \bar{B}_{13} & \bar{B}_{33} & \bar{B}_{36} & \bar{D}_{13} & \bar{D}_{33} & \bar{D}_{36} \\ \bar{B}_{16} & \bar{B}_{36} & \bar{B}_{66} & \bar{D}_{16} & \bar{D}_{36} & \bar{D}_{66} \end{bmatrix} \quad (3.12)$$

$$\overline{ABD}^{-1} = \begin{bmatrix} \bar{a}_{11} & \bar{a}_{13} & \bar{a}_{16} & \bar{b}_{11} & \bar{b}_{13} & \bar{b}_{16} \\ \bar{a}_{13} & \bar{a}_{33} & \bar{a}_{36} & \bar{b}_{31} & \bar{b}_{33} & \bar{b}_{36} \\ \bar{a}_{16} & \bar{a}_{36} & \bar{a}_{66} & \bar{b}_{61} & \bar{b}_{63} & \bar{b}_{66} \\ \bar{b}_{11} & \bar{b}_{31} & \bar{b}_{61} & \bar{d}_{11} & \bar{d}_{13} & \bar{d}_{16} \\ \bar{b}_{13} & \bar{b}_{33} & \bar{b}_{63} & \bar{d}_{13} & \bar{d}_{33} & \bar{d}_{36} \\ \bar{b}_{16} & \bar{b}_{36} & \bar{b}_{66} & \bar{d}_{16} & \bar{d}_{36} & \bar{d}_{66} \end{bmatrix}. \quad (3.13)$$

If only a normal force \bar{F}_{11} and a moment \bar{M}_{11} (per unit length) are acting on the plate, axial strain ($\bar{\epsilon}_{11}$) and curvature ($\bar{\kappa}_{11}$) of the plate with respect to the plane $\bar{1} - \bar{3}$ can be written as:

$$\bar{\epsilon}_{11} = \bar{a}'_{11}\bar{F}_{11} + \bar{b}'_{11}\bar{M}_{11}, \quad (3.14)$$

$$\bar{\kappa}_{11} = \bar{b}'_{11}\bar{F}_{11} + \bar{d}'_{11}\bar{M}_{11}. \quad (3.15)$$

The components \bar{a}'_{11} , \bar{b}'_{11} and \bar{d}'_{11} are the elements of compliance matrix calculated with respect to the plane $\bar{1} - \bar{3}$. To find a simple solution, in the current study, the plane $\bar{1} - \bar{3}$ is assumed to be the neutral plane for bending of the plate. In doing so, the plate is assumed to be only subjected to bending about a single axis only (under cylindrical bending), and bend-twist coupling is ignored. This assumption of the neutral plane also means the coupling terms between axial, and bending can be made equal to zero, i.e. \bar{b}'_{11} should be equal to zero. Using the above condition, the following equation can be written for \bar{b}'_{11} :

$$\bar{b}'_{11} = \bar{b}_{11} + d\bar{d}_{11} = 0, \quad (3.16)$$

where d is the distance between the plane $\bar{1} - \bar{3}$ and the reference plane (Fig. 3b).

As $b'_{11} = 0$, d can be obtained from Eq. (3.16) as:

$$d = -\frac{\bar{b}_{11}}{\bar{d}_{11}}. \quad (3.17)$$

At the neutral plane, Eq. (3.14) and Eq. (3.15) can be written as:

$$\bar{\varepsilon}_{11} = \bar{a}'_{11}\bar{F}_{11} \quad (3.18)$$

$$\bar{k}_{11} = \bar{d}'_{11}\bar{M}_{11}. \quad (3.19)$$

Now the stiffness matrix components of the plate with respect to plane $\bar{1} - \bar{3}$ can be written as (Kollár & Springer, 2003):

$$\bar{A}'_{ij} = \bar{A}_{ij} \quad (3.20)$$

$$\bar{B}'_{ij} = \bar{B}_{ij} - d\bar{A}_{ij} = 0 \quad (3.21)$$

$$\bar{D}'_{ij} = \bar{D}_{ij} - 2d\bar{B}_{ij} + d^2\bar{A}_{ij}. \quad (3.22)$$

The strain energy of the RVE is calculated as the sum of the strain energy of each cell wall of the RVE under applied loading and boundary conditions. A periodic hexagonal honeycomb core shown in Fig. 3.3 is used to demonstrate this process. Use of the proposed approach to other honeycomb cores with different shapes is given at the end of this section.

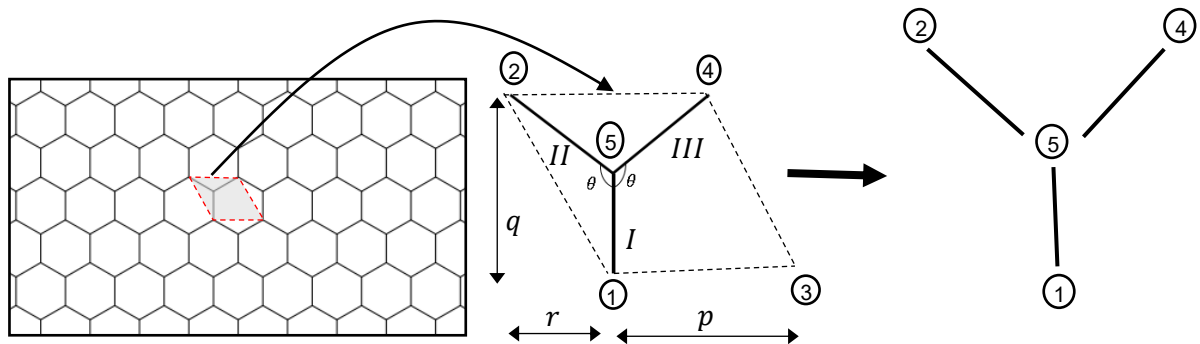


Fig. 3.3: The decomposition of the RVE into cell wall elements.

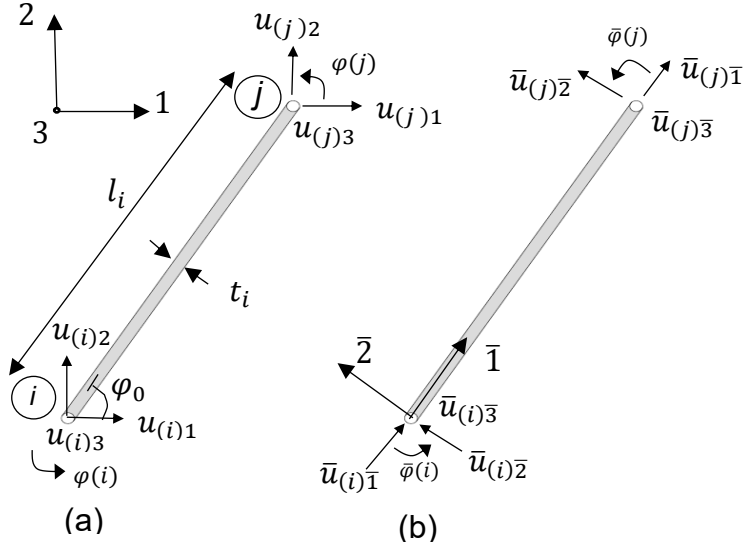


Fig. 3.4: Nodal displacements of the cell wall in (a) global (b) local coordinates.

The strain energy of each cell wall (Fig. 3.3) is calculated under plane stress conditions by solving for the nodal displacements and nodal forces based on a displacement field for the deformation of the walls. Each node of the composite cell wall element consists of four degrees of freedom, i.e. translational degrees of freedom in 1, 2, and 3 directions (or $\bar{1}$, $\bar{2}$ and $\bar{3}$ directions) and rotation about axis 3 (or $\bar{3}$) (Fig. 3.4). In Fig. 3.4, $\bar{u}_{(i)1}$, $\bar{u}_{(i)2}$ and $\bar{u}_{(i)3}$ refer to the nodal displacements of the composite cell wall in the local $\bar{1}$, $\bar{2}$ and $\bar{3}$ directions respectively and $\bar{\varphi}^{(i)}$ refers to rotation at i^{th} node about $\bar{3}$ direction. Global displacements and local displacements are related using the transformation matrix \mathbf{T} as:

$$\underline{\bar{u}} = \mathbf{T}\underline{u}, \quad (3.23)$$

where;

$$\underline{u} = \{u_{(i)1}, u_{(i)2}, u_{(i)3}, \varphi^{(i)}, u_{(j)1}, u_{(j)2}, u_{(j)3}, \varphi^{(j)}\}^T, \quad (3.24)$$

$$\underline{\bar{u}} = \{\bar{u}_{(i)1}, \bar{u}_{(i)2}, \bar{u}_{(i)3}, \bar{\varphi}^{(i)}, \bar{u}_{(j)1}, \bar{u}_{(j)2}, \bar{u}_{(j)3}, \bar{\varphi}^{(j)}\}^T, \quad (3.25)$$

and

$$T = \begin{bmatrix} \cos(\varphi_0) & -\sin(\varphi_0) & 0 & 0 & 0 & 0 & 0 & 0 \\ \sin(\varphi_0) & \cos(\varphi_0) & 0 & 0 & 0 & 0 & 0 & 0 \\ 0 & 0 & 1 & 0 & 0 & 0 & 0 & 0 \\ 0 & 0 & 0 & 1 & 0 & 0 & 0 & 0 \\ 0 & 0 & 0 & 0 & \cos(\varphi_0) & -\sin(\varphi_0) & 0 & 0 \\ 0 & 0 & 0 & 0 & \sin(\varphi_0) & \cos(\varphi_0) & 0 & 0 \\ 0 & 0 & 0 & 0 & 0 & 0 & 1 & 0 \\ 0 & 0 & 0 & 0 & 0 & 0 & 0 & 1 \end{bmatrix}. \quad (3.26)$$

The displacement field of each wall is assumed to consist of three components: (a) normal deformation due to axial force in the $\bar{1} - \bar{3}$ plane (Eqs. (3.27) to (3.29)), (b) normal deformation due to bending and transverse shear in the $\bar{1} - \bar{2}$ plane (Eqs. (3.30) to (3.32)), and (c) normal deformation due to shear in the $\bar{1} - \bar{3}$ plane (Eqs. (3.38) to (3.40)).

In the case (a), homogeneously distributed normal deformations \bar{u}_1^a , \bar{u}_2^a and \bar{u}_3^a are due to the axial force in the $\bar{1} - \bar{3}$ plane. For a wall component given in Fig. 3.4, homogeneously distributed normal deformations in $\bar{1}$, $\bar{2}$, and $\bar{3}$ directions due to an axial force in the $\bar{1} - \bar{3}$ plane can be written as:

$$\bar{u}_1^a = \bar{u}_{(i)1} + \frac{\bar{u}_{(j)1} - \bar{u}_{(i)1}}{l_i} \bar{x}_1 \quad (3.27)$$

$$\bar{u}_2^a = 0 \quad (3.28)$$

$$\bar{u}_3^a = \bar{\varepsilon}_{33} \bar{x}_3. \quad (3.29)$$

Normal deformation in the direction- $\bar{2}$ (Eq. (3.28)) is assumed to be negligible. However, this assumption does not have any effect on the strain energy of the RVE, as the plane stress assumption is used in calculating the strain energy of each wall.

In case (b), normal deformations \bar{u}_1^b , \bar{u}_2^b and \bar{u}_3^b are considered due to bending about direction- $\bar{3}$ and transverse shear in $\bar{1} - \bar{2}$ plane. For a wall component given in Fig. 3.4, homogeneously distributed normal deformations in $\bar{1}$, $\bar{2}$, and $\bar{3}$ directions due to bending and transverse shear in $\bar{1} - \bar{2}$ plane can be written as:

$$\bar{u}_1^b = -\frac{d'_{11}}{h} \left(\left(\frac{1}{2} C_1 \bar{x}_1^2 + C_2 \bar{x}_1 + C_3 \right) + \frac{\beta_s l_i^2}{12} C_1 \right) \bar{x}_2 \quad (3.30)$$

$$\bar{u}_2^b = \frac{d'_{11}}{h} \left(\frac{1}{6} C_1 \bar{x}_1^3 + \frac{1}{2} C_2 \bar{x}_1^2 + C_3 \bar{x}_1 + C_4 \right) \quad (3.31)$$

$$\bar{u}_3^b = 0, \quad (3.32)$$

where C_1, C_2, C_3 and C_4 are obtained by applying nodal displacement values at node i and j :

$$C_1 = \frac{6h}{d_{11}'l_i^2(1+\beta_s)} \left(-2 \frac{\bar{u}_{(j)2} - \bar{u}_{(i)2}}{l} + \Delta\bar{\varphi}_{(i)} + \Delta\bar{\varphi}_{(j)} \right) \quad (3.33)$$

$$C_2 = \frac{h}{d_{11}'l_i(1+\beta_s)} \left(6 \frac{\bar{u}_{(j)2} - \bar{u}_{(i)2}}{l} - (4 + \beta_s)\Delta\bar{\varphi}_{(i)} - (2 - \beta_s)\Delta\bar{\varphi}_{(j)} \right) \quad (3.34)$$

$$C_3 = \frac{h}{d_{11}'(1+\beta_s)} \left(\beta_s \frac{\bar{u}_{(j)2} - \bar{u}_{(i)2}}{l} + \frac{(2+\beta_s)}{2}\Delta\bar{\varphi}_{(i)} - \frac{\beta_s}{2}\Delta\bar{\varphi}_{(j)} \right) \quad (3.35)$$

$$C_4 = \frac{h}{d_{11}'} \bar{u}_{(i)2} \quad (3.36)$$

$$\beta_s = \frac{12}{d_{11}'\bar{S}_{eq}l_i^2} \quad (3.37)$$

The displacement functions in Eqs. (3.30) - (3.31) are derived assuming the composite honeycomb wall behaves as a Timoshenko beam. \bar{S}_{eq} is the equivalent transverse shear stiffness (Vlachoutsis, 1992) of laminated composite walls (See Appendix A.1 for the calculation of \bar{S}_{eq} of composite plate).

In case (c), normal deformations \bar{u}_1^s, \bar{u}_2^s and \bar{u}_3^s are due to shear deformation in the $\bar{1} - \bar{3}$ plane. For a wall component given in Fig. 3.4, homogeneously distributed normal deformations in $\bar{1}, \bar{2}$, and $\bar{3}$ directions due to shear deformations in $\bar{1} - \bar{3}$ plane can be written as:

$$\bar{u}_1^s = 0 \quad (3.38)$$

$$\bar{u}_2^s = 0 \quad (3.39)$$

$$\bar{u}_3^s = \bar{u}_{(i)3} + \frac{\bar{u}_{(j)3} - \bar{u}_{(i)3}}{l_i} \bar{x}_1. \quad (3.40)$$

The coordinates \bar{x}_1, \bar{x}_2 and \bar{x}_3 (Eqs. (3.27) to (3.40)) are considered in $\bar{1}, \bar{2}$ and $\bar{3}$ directions, respectively. The addition of the displacement components in each direction will give the effective displacements of the cell wall in each direction.

Assuming plane stress condition for the homogenised shell, $\bar{\sigma}_{22} = 0$, stress-strain relationship of any ply in the laminated composite wall can be written as:

$$\begin{Bmatrix} \bar{\sigma}_{11} \\ \bar{\sigma}_{33} \\ \bar{\tau}_{13} \end{Bmatrix} = \begin{bmatrix} \bar{Q}_{11} & \bar{Q}_{13} & \bar{Q}_{16} \\ \bar{Q}_{13} & \bar{Q}_{33} & \bar{Q}_{36} \\ \bar{Q}_{16} & \bar{Q}_{36} & \bar{Q}_{66} \end{bmatrix} \begin{Bmatrix} \bar{\varepsilon}_{11} \\ \bar{\varepsilon}_{33} \\ \bar{\gamma}_{13} \end{Bmatrix}, \quad (3.41)$$

$$\begin{Bmatrix} \bar{\tau}_{12} \\ \bar{\tau}_{32} \end{Bmatrix} = \begin{bmatrix} \bar{Q}_{44} & 0 \\ 0 & \bar{Q}_{55} \end{bmatrix} \begin{Bmatrix} \bar{\gamma}_{12} \\ \bar{\gamma}_{32} \end{Bmatrix}, \quad (3.42)$$

where \bar{Q}_{ij} are the components of the stiffness matrix of the ply of the laminated composite wall in $\bar{1} - \bar{3}$ coordinate system. $\bar{\varepsilon}_{11}$ and $\bar{\varepsilon}_{33}$ are in-plane normal strains in direction- $\bar{1}$ and direction- $\bar{3}$ respectively, $\bar{\gamma}_{13}$ is in-plane shear strain and $\bar{\gamma}_{12}$ and $\bar{\gamma}_{32}$ are transverse shear strains.

Strain components in Eq. (3.41) can be written as considering strain of reference plane and curvature:

$$\bar{\varepsilon}_{11} = \bar{\varepsilon}_{0,11} + \bar{x}_2 \bar{k}_{11}, \quad (3.42)$$

$$\bar{\varepsilon}_{33} = \bar{\varepsilon}_{0,33} + \bar{x}_2 \bar{k}_{33}, \quad (3.43)$$

$$\bar{\gamma}_{13} = \bar{\gamma}_{0,13} + \bar{x}_2 \bar{k}_{13}, \quad (3.44)$$

where $\bar{\varepsilon}_{0,11}$, $\bar{\varepsilon}_{0,33}$ and $\bar{\gamma}_{0,13}$ are the strains of the reference plane, \bar{k}_{11} , \bar{k}_{33} and \bar{k}_{13} are the curvatures of the cell wall, and \bar{x}_2 is the distance between the plane considered and the reference plane (i.e. the distance to the neutral plane). Strain $\bar{\varepsilon}_{11}$ can also be obtained by differentiating the effective displacements in direction- $\bar{1}$ (i.e. Eqs. (3.27), (3.30), and (3.38)) with respect to \bar{x}_1 . By comparing the components of the differential of effective displacement in direction- $\bar{1}$ and Eq. (3.42), the following relationships can be obtained:

$$\bar{\varepsilon}_{0,11} = \frac{\bar{u}_{(j)1} - \bar{u}_{(i)1}}{l_i}, \quad (3.45)$$

$$\bar{k}_{11} = -\frac{d'_{11}}{h} (C_1 \bar{x}_1 + C_2). \quad (3.46)$$

Differentiating the effective displacement in direction- $\bar{3}$ (i.e. Eqs. (3.29), (3.32), and (3.40)) with respect to \bar{x}_3 , and comparing with Eq. (3.43) the following relationship can be obtained:

$$\bar{\varepsilon}_{0,33} = \bar{\varepsilon}_{33}, \quad (3.47)$$

$$\bar{k}_{33} = 0. \quad (3.48)$$

Now, differentiating effective displacement in direction- $\bar{1}$ with respect to \bar{x}_3 and adding that to the differential of effective displacement in direction- $\bar{3}$ with respect to \bar{x}_1 , shear strain $\bar{\gamma}_{13}$ can be obtained. Comparing that with Eq. (3.44), the following relationship can be established:

$$\bar{\gamma}_{0,13} = \frac{\bar{u}_{(j)3} - \bar{u}_{(i)3}}{l_i}, \quad (3.49)$$

$$\bar{k}_{13} = 0. \quad (3.50)$$

Differentiating effective displacement in direction- $\bar{1}$ with respect to \bar{x}_2 and adding that to the differential of effective displacement in direction- $\bar{2}$ (i.e. Eqs. (3.28), (3.31), and (3.39)) with respect to \bar{x}_1 , shear strain $\bar{\gamma}_{12}$ can be obtained:

$$\bar{\gamma}_{12} = \beta_s \frac{l_i^2 d'_{11}}{12h} C_1. \quad (3.51)$$

Here we assume cylindrical bending for the composite plate, which results in zero curvatures \bar{k}_{13} and \bar{k}_{33} and transverse shear strain $\bar{\gamma}_{32}$. This assumption is made considering a thick core where h is considerably greater than l_i ($h > 3l_i$) (Zhang & Ashby, 1992).

The total strain energy of a cell wall element i (i refers to cell wall I , II and III) can be expressed as:

$$U^i = \frac{1}{2} \int_0^l \int_0^h \int_{-\frac{t}{2}+d}^{(t/2-d)} (\bar{\sigma}_{11} \bar{\varepsilon}_{11} + \bar{\sigma}_{33} \bar{\varepsilon}_{33} + \bar{\tau}_{13} \bar{\gamma}_{13} + \bar{\tau}_{12} \bar{\gamma}_{12}) d\bar{x}_2 d\bar{x}_3 d\bar{x}_1. \quad (3.52)$$

By substituting Eqs. (3.41) - (3.44) into Eq. (3.52) and simplifying using the definitions in Eqs. (3.20) - (3.22), the strain energy of the cell wall element can be derived and expressed as:

$$U^i = \frac{1}{2}(\bar{\mathbf{u}} \bar{\mathbf{K}} \bar{\mathbf{u}}^T + 2\bar{\mathbf{u}} \bar{\mathbf{G}} \bar{\mathbf{e}}_{33} + \bar{A}_{33} \bar{\mathbf{e}}_{33}^2), \quad (3.53)$$

where;

$$\bar{\mathbf{K}} = \frac{h}{l_i} \begin{bmatrix} \bar{A}_{11} & 0 & \bar{A}_{16} & 0 & -\bar{A}_{11} & 0 & -\bar{A}_{16} & 0 \\ 0 & \bar{K}_{22} & 0 & \bar{K}_{24} & 0 & \bar{K}_{26} & 0 & \bar{K}_{28} \\ \bar{A}_{16} & 0 & \bar{A}_{66} & 0 & -\bar{A}_{16} & 0 & -\bar{A}_{66} & 0 \\ 0 & \bar{K}_{42} & 0 & \bar{K}_{44} & 0 & \bar{K}_{46} & 0 & \bar{K}_{48} \\ -\bar{A}_{11} & 0 & -\bar{A}_{16} & 0 & \bar{A}_{11} & 0 & \bar{A}_{16} & 0 \\ 0 & \bar{K}_{62} & 0 & \bar{K}_{64} & 0 & \bar{K}_{66} & 0 & \bar{K}_{68} \\ \bar{A}_{16} & 0 & -\bar{A}_{66} & 0 & \bar{A}_{16} & 0 & \bar{A}_{66} & 0 \\ 0 & \bar{K}_{82} & 0 & \bar{K}_{84} & 0 & \bar{K}_{86} & 0 & \bar{K}_{88} \end{bmatrix}, \quad (3.54)$$

$$\bar{\mathbf{G}} = h[-\bar{A}_{13} \quad 0 \quad -\bar{A}_{36} \quad 0 \quad \bar{A}_{13} \quad 0 \quad \bar{A}_{36} \quad 0]^T, \quad (3.55)$$

$$\bar{K}_{22} = -\bar{K}_{26} = -\bar{K}_{62} = \bar{K}_{66} = \frac{\bar{s}_{eq} \beta^2 l_i^2 + 12 \bar{D}_{11}}{l_i^2 (\beta + 1)^2}, \quad (3.56)$$

$$\bar{K}_{24} = \bar{K}_{28} = \bar{K}_{42} = -\bar{K}_{46} = -\bar{K}_{64} = -\bar{K}_{68} = \bar{K}_{82} = -\bar{K}_{86} = \frac{\bar{s}_{eq} \beta^2 l_i^2 + 12 \bar{D}_{11}}{2 l_i (\beta + 1)^2}, \quad (3.58)$$

$$\bar{K}_{44} = \bar{K}_{88} = \frac{\bar{s}_{eq} \beta^2 l_i^2 + 4 \bar{D}_{11} ((1 + \beta^2) + 3)}{4 (\beta + 1)^2}, \quad (3.59)$$

$$\bar{K}_{48} = \bar{K}_{84} = \frac{\bar{s}_{eq} \beta^2 l_i^2 - 4 \bar{D}_{11} ((1 + \beta^2) - 3)}{4 (\beta + 1)^2}. \quad (3.60)$$

If the transverse shear deformation of the wall is neglected, then $\bar{\mathbf{K}}$ matrix can be written as:

$$\bar{\mathbf{K}} = \frac{h}{l_i} \begin{bmatrix} \bar{A}_{11} & 0 & \bar{A}_{16} & 0 & -\bar{A}_{11} & 0 & -\bar{A}_{16} & 0 \\ 0 & \frac{12}{l_i^2} \bar{D}_{11} & 0 & \frac{6}{l_i} \bar{D}_{11} & 0 & -\frac{12}{l_i^2} \bar{D}_{11} & 0 & \frac{6}{l_i} \bar{D}_{11} \\ \bar{A}_{16} & 0 & \bar{A}_{66} & 0 & -\bar{A}_{16} & 0 & -\bar{A}_{66} & 0 \\ 0 & \frac{6}{l_i} \bar{D}_{11} & 0 & 4 \bar{D}_{11} & 0 & -\frac{6}{l_i} \bar{D}_{11} & 0 & 2 \bar{D}_{11} \\ -\bar{A}_{11} & 0 & -\bar{A}_{16} & 0 & \bar{A}_{11} & 0 & \bar{A}_{16} & 0 \\ 0 & -\frac{12}{l_i^2} \bar{D}_{11} & 0 & -\frac{6}{l_i} \bar{D}_{11} & 0 & \frac{12}{l_i^2} \bar{D}_{11} & 0 & -\frac{6}{l_i} \bar{D}_{11} \\ \bar{A}_{16} & 0 & -\bar{A}_{66} & 0 & \bar{A}_{16} & 0 & \bar{A}_{66} & 0 \\ 0 & \frac{6}{l_i} \bar{D}_{11} & 0 & 2 \bar{D}_{11} & 0 & -\frac{6}{l_i} \bar{D}_{11} & 0 & 4 \bar{D}_{11} \end{bmatrix} \quad (3.61)$$

For asymmetric laminates, the elements \bar{A}_{ij} and \bar{D}_{ij} should be replaced with \bar{A}'_{ij} and \bar{D}'_{ij} according to Eqs. (3.20) - (3.22).

Strain energy density of the RVE can be expressed as volume average of the sum of the strain energy of each wall in the RVE:

$$w = \frac{1}{V_{RVE}} \sum_{i=1}^n U^i. \quad (3.62)$$

3.2.2 Solving equations to get the effective stiffness components

In order to determine the strain energy of the cell wall given in Eq. (3.53), the nodal displacement $\bar{\mathbf{u}}$ must be known. The nodal forces can be obtained by differentiating Eq. (3.53) with respect to corresponding nodal displacements. The generalised vectors of nodal forces and nodal displacements are related as given by the following expression:

$$\bar{\mathbf{F}} = \bar{\mathbf{K}}\bar{\mathbf{u}} + \bar{\mathbf{G}}\bar{\varepsilon}_{33}, \quad (3.63)$$

where;

$$\bar{\mathbf{F}} = \{\bar{F}_{(i)1} \quad \bar{F}_{(i)2} \quad \bar{F}_{(i)3} \quad \bar{M}_{(i)} \quad \bar{F}_{(j)1} \quad \bar{F}_{(j)2} \quad \bar{F}_{(j)3} \quad \bar{M}_{(j)}\}^T. \quad (3.64)$$

Using the force-displacement relationship in Eq. (3.63), nodal displacements of the cell wall are determined considering the periodic boundary conditions. Once the nodal displacements are obtained, they can be used to determine the effective stiffness matrix components defined in Eqs (3.5) – (3.7). The procedure for obtaining effective stiffness matrix components, C_{ijkl}^H is presented in 5 steps:

Step 1: In step 1, a suitable RVE for the honeycomb core (e.g., as in Fig. 3.3) is selected.

Step 2: For the selected RVE, nine reference strain states of the RVE are selected at a time to obtain nine independent C_{ijkl}^H components of effective elasticity tensor as:

$$\varepsilon_{ij} = \delta \quad \text{if: } i = j, k = l \text{ and } i = k, \quad (3.65)$$

$$\varepsilon_{ij} = \delta \quad \text{if: } i \neq j, k \neq l, i = k \text{ and } j = l, \quad (3.66)$$

$$\varepsilon_{ij} = \delta \text{ and } \varepsilon_{kl} = \delta \quad \text{if: } i = j, k = l \text{ and } i \neq k. \quad (3.67)$$

The volume average strain components defined in Eq. (3.1) can be redefined using Gauss's theorem as an integration around the boundary surfaces Γ of the RVE (Hohe & Becker 2001, Xia et al. 2003) as follows:

$$\varepsilon_{ij} = \frac{1}{2V_{RVE}} \int_{\Gamma} (u_i n_j + u_j n_i) d\Gamma. \quad (3.68)$$

and for the RVE considered in Fig. 3.3, average strain components (see Appendix A.2) can be defined using Eqs. (3.69) – (3.74):

$$\varepsilon_{11} = \frac{u_{(3)1} - u_{(1)1}}{p}, \quad (3.69)$$

$$\varepsilon_{22} = \frac{u_{(2)2} - u_{(1)2}}{q} + \frac{r}{p} \frac{u_{(3)2} - u_{(1)2}}{q}, \quad (3.70)$$

$$\varepsilon_{33} = \bar{\varepsilon}_{33}, \quad (3.71)$$

$$\varepsilon_{12} = \frac{1}{2} \left(\frac{u_{(3)2} - u_{(1)2}}{p} + \frac{u_{(2)1} - u_{(1)1}}{q} + \frac{r}{p} \frac{u_{(3)1} - u_{(1)1}}{q} \right), \quad (3.72)$$

$$\varepsilon_{13} = \frac{1}{2} \frac{u_{(3)3} - u_{(1)3}}{p}, \quad (3.73)$$

$$\varepsilon_{23} = \frac{1}{2} \left(\frac{u_{(2)3} - u_{(1)3}}{q} + \frac{r}{p} \frac{u_{(3)3} - u_{(1)3}}{q} \right). \quad (3.74)$$

Step 3: Determine the nodal displacements of each cell wall element with respect to local coordinates considering the periodic boundary conditions and the equilibrium conditions of the nodal forces. For the RVE in Fig. 3.3, periodic boundary conditions (Hohe & Becker 2001) in Eqs. (3.75) – (3.80) are applied to ensure compatibility of displacements with adjacent elements:

$$\varphi(1) = \varphi(2), \quad (3.75)$$

$$\varphi(3) = \varphi(4) \quad (3.76)$$

$$\varphi(1) = \varphi(3), \quad (3.77)$$

$$u_{(3)1} - u_{(1)1} = u_{(4)1} - u_{(2)1}, \quad (3.78)$$

$$u_{(3)2} - u_{(1)2} = u_{(4)2} - u_{(2)2}, \quad (3.79)$$

$$u_{(3)3} - u_{(1)3} = u_{(4)3} - u_{(2)3}. \quad (3.80)$$

Resultant forces of all corner nodes, at internal nodes and at all pairs of corresponding nodes i and $i + 1$ on surfaces of RVE should be zero, since there are no external forces acting which gives Eqs. (3.81) - (3.85):

$$F_{(1)1} + F_{(2)1} + F_{(3)1} = 0, \quad (3.81)$$

$$F_{(1)2} + F_{(2)2} + F_{(3)3} = 0, \quad (3.82)$$

$$F_{(1)3} + F_{(2)3} + F_{(3)3} = 0, \quad (3.83)$$

$$M_{(1)} + M_{(2)} + M_{(3)} = 0, \quad (3.84)$$

$$F_{(5)1} = F_{(5)2} = F_{(5)3} = M_{(5)} = 0. \quad (3.85)$$

RVE is not allowed to undergo any rigid body motions. Therefore, we can write Eq. (3.86):

$$u_{(1)1} = u_{(1)2} = u_{(1)3} = u_{(3)2} = 0. \quad (3.86)$$

Step 4: Calculate the strain energy of each wall (Eq. (3.53)) and then the strain energy density of the RVE (Eq. (3.62)) by adding the strain energy of all the walls together.

Step 5: Apply Eqs. (3.5) - (3.7) to find the stiffness components of the effective elasticity tensor C^H :

The above procedure could be implemented using simple program(MATLAB (Version 2022b) program is given in Appendix A.4), thus, it can be solved for different material and geometry configurations with little effort.

3.3 Force-equilibrium based approach

The previous section explains a methodology based on strain energy to derive equivalent stiffness properties for any type of honeycomb cellular cores. Force equilibrium approach is also commonly used for determining the effective stiffness properties (Gibson & Asby 1997; Master & Evans 1996; Balawi & Abot 2008; Malek & Gibson 2015; Mukherjee & Adhikari 2021), but they are not applicable in general and can be only applied with certain limitations (e.g. the shape of the hexagonal). It is considered important to compare the results of the methodology derived in the previous section based on strain energy with a methodology based on force equilibrium to evaluate the effectiveness of the strain-energy based approach against

other existing approaches (i.e. force-equilibrium approach). Therefore, in this section, a methodology for a composite hexagonal honeycomb core is developed using the force-equilibrium approach, and the results are compared with the predictions from the previously presented strain-energy based approach. It should be noted that the force-equilibrium based approach presented in this section can only be applied to hexagonal honeycomb cores, while the strain-energy based approach developed in the previous section can be applied in general to all types of honeycomb cores.

The force-equilibrium approach considers the force-equilibrium of the walls to determine the deformation of the walls under applied uniform external stress, and then the applied stress is divided by the average strain of the RVE to get the effective elastic modulus by dividing the stress by the average strain. Wang & Wang (2018) recently proposed an analytical model for the effective elastic properties of the laminated composite hexagonal core. While, for the examples produced in their study, their model performed well, their model produces a value of 1 for the effective in-plane Poisson's ratios of a regular hexagonal honeycomb core. This results in singularities when calculating Q_{11}^H and Q_{22}^H . Therefore, their model cannot be used directly to determine Q_{11}^H and Q_{22}^H . Recently Mukherjee & Adhikari (2021) also proposed an analytical model to determine the effective elastic properties of a hexagonal honeycomb core with isotropic walls. Their model, which is the most accurate up to date for hexagonal isotropic honeycomb cores, together with CLT to determine cell wall properties, are used in this section to derive equations for the effective in-plane stiffness properties (Q_{11}^H , Q_{22}^H and Q_{66}^H) of the laminated composite wall hexagonal core.

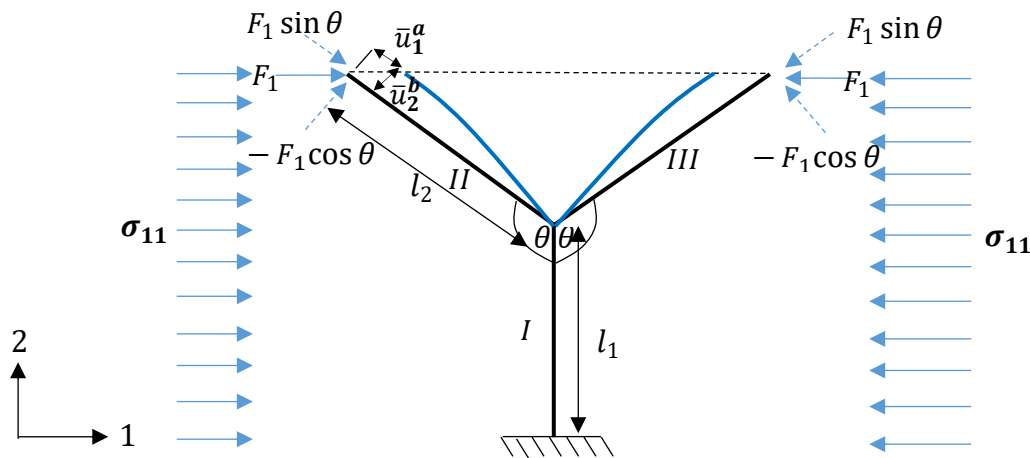


Fig. 3.5: Schematic of deformation pattern of the unit cell under the application of uniform stress field σ_{11} in direction-1.

A RVE of the hexagonal core considered for calculating the effective elastic modulus in direction-1 is given in Fig. 3.5. A uniform stress field σ_{11} is applied to the RVE in direction-1, as shown in Fig. 3.5, to derive the expression of the equivalent elastic modulus in direction-1. Applied stress field results in a force F_1 being applied at the end points of walls *II* and *III* on the unit cell. The magnitude of the force F_1 is given by:

$$F_1 = \sigma_{11} l_1 (l_1 - l_2 \cos \theta). \quad (3.87)$$

Deformation \bar{u}_2^b of the inclined member *II* due to bending can be written as:

$$\bar{u}_2^b = \frac{-F_1 \cos \theta}{\bar{K}_{55}^{II}}. \quad (3.88)$$

Deformation \bar{u}_1^a of the inclined wall *II* due to axial forces can be written as:

$$\bar{u}_1^a = \frac{F_1 \sin \theta}{\bar{K}_{44}^{II}}. \quad (3.89)$$

In Eqs. (3.88) and (3.89), \bar{K}_{55}^{II} and \bar{K}_{44}^{II} are elements of the Euler-Bernoulli beam stiffness matrix of the inclined wall *II* with length l_2 . Considering the symmetry of elements *II* and *III* ($l_2 = l_3$), the total deflection in the 1-direction can be obtained as:

$$u_1 = 2(\bar{u}_1^a \sin \theta - \bar{u}_2^b \cos \theta) = 2F_1 \left(\frac{\cos^2 \theta}{\bar{K}_{55}^{II}} + \frac{\sin^2 \theta}{\bar{K}_{44}^{II}} \right) = 2F_1 \frac{\cos^2 \theta}{k_{55}^I} \left(1 + \tan^2 \theta \frac{\bar{K}_{55}^{II}}{\bar{K}_{44}^{II}} \right). \quad (3.90)$$

Hence, the strain in 1- direction is obtained as:

$$\epsilon_{11} = \frac{u_1}{2l_2 \sin \theta} = \frac{2F_1 \frac{\cos^2 \theta}{\bar{K}_{55}^{II}} \left(1 + \tan^2 \theta \frac{\bar{K}_{55}^{II}}{\bar{K}_{44}^{II}} \right)}{2l_2 \sin \theta}. \quad (3.91)$$

From the normal stress and strain in direction-1, the effective elastic modulus of the honeycomb core in direction-1 can be obtained as:

$$E_1^H = \frac{\sigma_{11}}{\varepsilon_{11}} = \frac{\bar{K}_{55}^{II} l_2 \sin \theta}{h(l_1 - l_2 \cos \theta) \cos^2 \theta \left(1 + \tan^2 \theta \frac{\bar{K}_{55}^{II}}{\bar{K}_{44}^{II}}\right)}. \quad (3.92)$$

If the cell walls of the hexagonal core are made of laminated composite/multi-layered material, then the stretching modulus and bending modulus of the wall could be different, and deformations have to be calculated based on the corresponding modulus (Min et al. 2020). Therefore, the stiffness terms k_{44}^{II} and k_{55}^{II} in Eq. (3.88) and Eq. (3.89) should be calculated based on the equivalent elastic modulus of the wall for stretching (\bar{E}_1^s) and bending (\bar{E}_1^b), respectively. These can be calculated and are given as follows:

$$K_{44}^{II} = \left(\frac{\bar{E}_1^s A}{l_2}\right) = \left(\frac{h}{l_2 \bar{a}_{11}^{II}}\right) \quad (3.93)$$

$$\bar{K}_{55}^{II} = \left(\frac{12 \bar{E}_1^b I}{l_2^3}\right) = \left(\frac{12h}{l_2^3 \bar{a}_{11}^{II}}\right) \quad (3.94)$$

Substituting Eqs. (3.93) and (3.94) into Eq. (3.92), we will get the equation for the effective modulus E_1^H of the laminated composite wall hexagonal core as:

$$E_1^H = \frac{12 \sin \theta}{\left(\frac{l_1}{l_2} - \cos \theta\right) \cos^2 \theta (l_2^3 \bar{a}_{11}^{II} + 12 l_1 \bar{a}_{11}^{II} \tan^2 \theta)}. \quad (3.95)$$

Similarly, other equations for in-plane effective elastic properties E_2^H , ν_{12}^H and G_{12}^H can be derived as (refer to Mukherjee & Adhikari 2021):

$$E_2^H = \frac{\bar{K}_{55}^{II} \left(\frac{l_1}{l_2} - \cos \theta\right)}{h \sin^3 \theta \left(1 + \cot^2 \theta \frac{\bar{K}_{55}^{II}}{\bar{K}_{44}^{II}} + 2 \operatorname{cosec}^2 \theta \frac{\bar{K}_{55}^{II}}{\bar{K}_{44}^{II}}\right)} \quad (3.96)$$

$$E_2^H = \frac{12 \left(\frac{l_1}{l_2} - \cos \theta\right)}{\sin^3 \theta (l_2^3 \bar{a}_{11}^{II} + 12 l_2 \bar{a}_{11}^{II} \cot^2 \theta + 24 l_1 \bar{a}_{11}^{II} \operatorname{cosec}^2 \theta)} \quad (3.97)$$

$$\nu_{12}^H = -\frac{\sin^2 \theta \left(1 - \frac{\bar{K}_{55}^{II}}{\bar{K}_{44}^{II}}\right)}{\left(\frac{l_1}{l_2} - \cos \theta\right) \cos \theta \left(1 + \tan^2 \theta \frac{\bar{K}_{55}^{II}}{\bar{K}_{44}^{II}}\right)} \quad (3.98)$$

$$\nu_{21}^H = -\frac{\sin^2 \theta (l_2^3 \bar{a}_{11}^{II} - 12 l_2 \bar{a}_{11}^{II})}{\left(\frac{l_1}{l_2} - \cos \theta\right) \cos \theta (l_2^3 \bar{a}_{11}^{II} + 12 l_2 \bar{a}_{11}^{II} \tan^2 \theta)} \quad (3.99)$$

$$G_{12}^H = \frac{\left(\frac{l_1}{l_2} - \cos\theta\right)}{h \sin\theta \left(\frac{l_1^2}{2l_2 \bar{k}_{65}^{II}} + \left(\frac{4k_{66}^I}{\bar{k}_{55}^I \bar{k}_{66}^I - (\bar{k}_{56}^I)^2} \right) \left(\frac{l_1}{2}\right) + \frac{\left(\sin\theta - \left(\frac{l_1}{l_2} - \cos\theta\right) \cot\theta\right)^2}{\bar{k}_{44}^{II}} \right)} \quad (3.101)$$

$$G_{12}^H = \frac{156 \left(\frac{l_1}{l_2} - \cos\theta\right)}{\sin\theta \left(13l_1^2 l_2 \bar{a}_{11}^{II} + 2l_1^3 \bar{a}_{11}^I + 156l_2 \left(\sin\theta - \left(\frac{l_1}{l_2} - \cos\theta\right) \cot\theta\right)^2 \bar{a}_{11}^{II} \right)}. \quad (3.102)$$

3.4 Prediction of effective stiffness properties

3.4.1 Effective properties of laminated composite wall honeycomb core

To validate the proposed strain-energy based model in section 3.2, the proposed model is used to calculate the effective stiffness properties of an equivalent shell of hexagonal core (Fig. 3.3). Results are obtained with and without considering the transverse shear deformation of the walls. Results are then compared with the effective stiffness properties obtained from FE analysis. Predictions for the effective stiffness component are then compared with the effective stiffness values obtained from FE analysis of the RVEs with prescribed boundary conditions. Investigation presented in the current chapter is a theoretical investigation, and the proposed model is validated against FE results as both the FE methodology and the proposed analytical approach are based on similar idealisations. Knowing FE models are able to accurately capture behaviour of honeycomb core structures with idealized honeycomb geometries, comparison with FE results provide a good validation for the proposed analytical model for similar idealized honeycomb geometries. In real structures, such idealized geometry and material assumption may not be correct, thus experimental results may vary from the theoretical predictions based on idealized geometries. However, the aim of such comparisons will be to identify how much effect non-idealized geometric and material parameters (imperfections) will have on the predicted behaviour. However, that is beyond the scope of the current study as objective of this chapter is to develop an analytical homogenisation model to facilitate the preliminary design of the laminated composite honeycomb core considering different materials and geometric parameters. In addition, the results from the proposed strain-energy based model are compared against results from the force-equilibrium based model derived based on Mukherjee & Adhikari (2021) in section 3.3, and the homogenisation models proposed by Wang & Wang (2018) and

Krishnamurthy & Saether (2019) for the laminated composite wall hexagonal core. Elastic properties of different FRP materials used for the laminated composite wall hexagonal core with respect to principal axes of the lamina are given in Table 3.1. Thicknesses of the hexagonal core walls assumed to be equal (Fig. 3.2) and different composite fibre lay-ups were considered for the core walls as given in Table 3.2. Each ply thickness of the fibre lay-up is assumed to be equal. The core walls' lengths are taken as: $l_1 = l_2 = l_3 = 50\text{mm}$ (Fig. 3.3), while the height of the core (h) is taken as 150mm. The thickness of the core walls for all core configurations was selected to have a relative core density (ρ^*) of 0.072.

Table 3.1: Mechanical properties of composite wall material.

Material	E_L (Nmm^{-2})	E_T (Nmm^{-2})	G_{LT} (Nmm^{-2})	ν_{LT} (1)
E-glass/Epoxy(G)	38600	8270	4140	0.26
Boron/Epoxy(B)	204000	18500	5590	0.23

Table 3.2: Material configurations of the laminated composite walls.

Composite wall	Layer arrangement (Material properties for G and B are given in Table 1)	Fibre orientation ($^\circ$)
1	G/G/G/G/G	45/-45/0/-45/45
2	G/G/G/G/G	0/0/90/0/0
3	G/G/G/G/G	90/0/0/0/90
4	G/G/G/G/G	0/45/90/45/0
5	G/G/G/G/G	45/0/90/0/45
6	G/G/G/G/G	45/-45/45/-45/45
7	B/G/G/G/B	45/-45/0/-45/45
8	G/B/G/B /G	0/0/90/0/0
9	B/G/G/G/B	0/0/90/0/0
10	G/B/G/B/G	90/0/0/0/90
11	G/G/B /G/G	0/45/90/45/0
12	G/G/G/G/B	45/0/90/0/45
13	B/G/G/B /G	0/0/90/0/0
14	G/G/G/G/B	45/-45/0/-45/45

RVEs of the regular hexagonal cores (Fig. 3.6) are modelled using the commercial FE software ABAQUS (version 2021). The S4 shell element is used with a mesh size of 10mm selected based on a mesh convergence study. The composite shell option available in ABAQUS is used for modelling composite walls, with the material properties of each layer assigned based on the properties given in Table 3.1, and the local material direction of each layer is assigned based on material configurations given in Table 3.2. Prescribed displacement boundary conditions similar to Catapano & Montemurro (2014) and Grediac (1993) are applied according to Table 3.4 to get the effective properties for equivalent shell analysis. Effective properties are calculated based on the total strain energy extracted from the analysis of the RVE under applied boundary conditions. Average strain components of RVE are calculated based on the characteristic dimensions of RVE (Fig. 3.6(a)) and applied displacements. Table 3.3 illustrates the application of boundary conditions and deformed shape of the honeycomb RVE for a typical material configuration in the FE analysis.

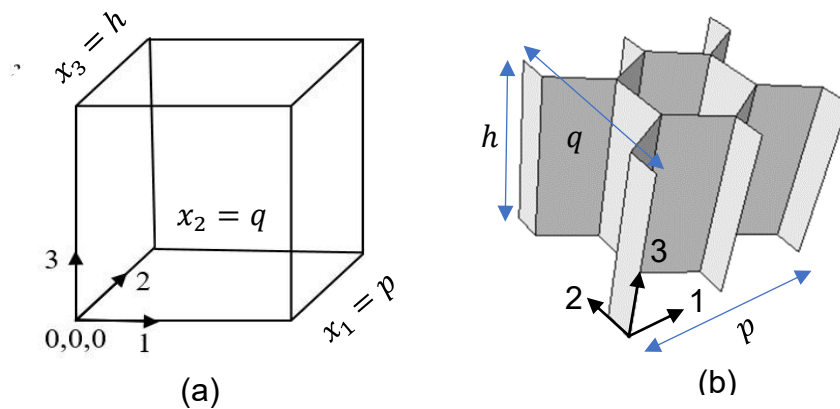
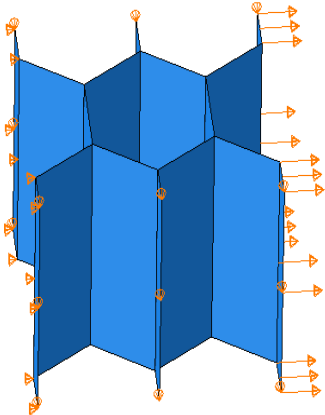
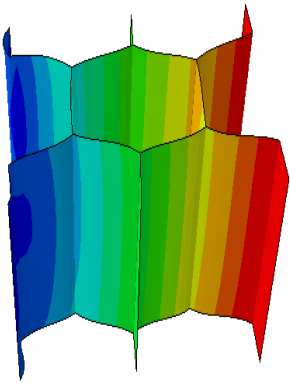
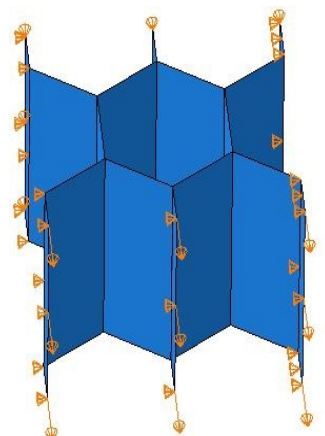
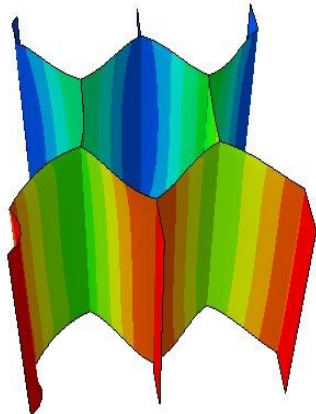
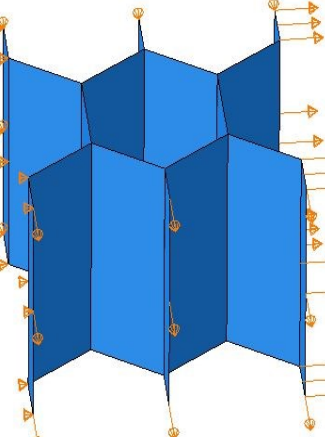
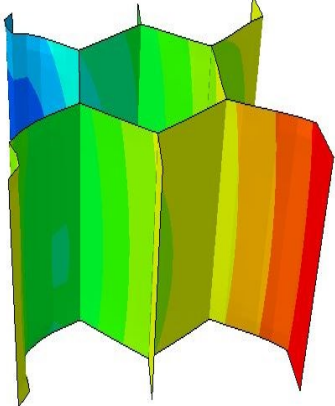


Fig. 3.6: (a) Boundaries of typical RVE for application of boundary conditions (b) RVE of hexagonal core for the FE models.

Table 3.3: Boundary conditions, deformed shapes, and the total strain energy of the hexagonal core RVE with material configuration 1.

Effective properties	Boundary conditions	Deformed shape	Total strain energy (Nmm)

Q_{11}^H			20951.1
Q_{22}^H			27936
Q_{12}^H			96749

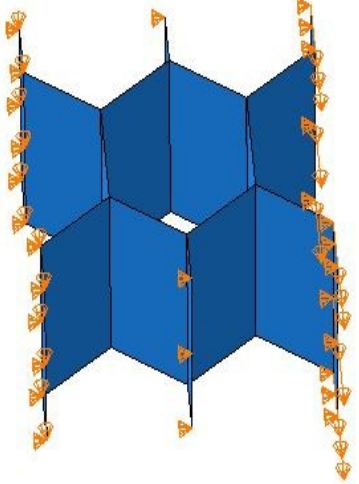
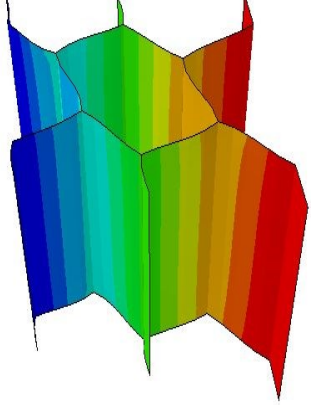
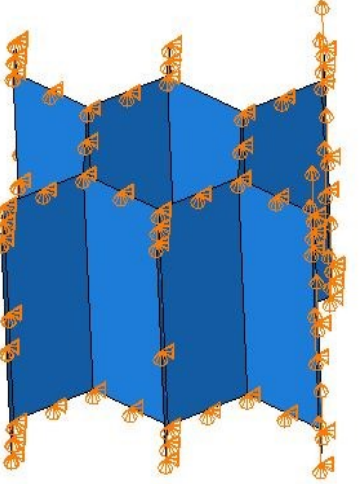
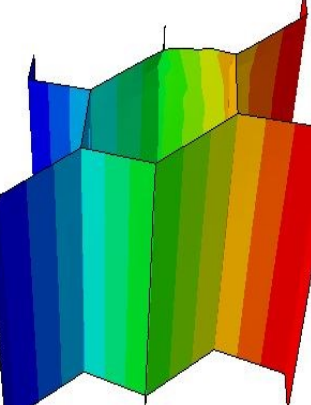
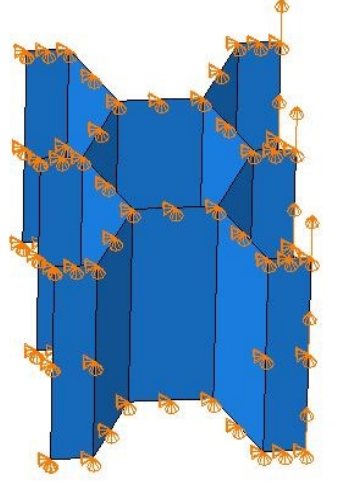
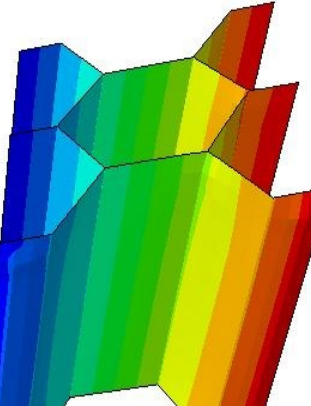
Q_{66}^H			160.6
Q_{44}^H			21801.7
Q_{55}^H			29224.4

Table 3.4: Boundary conditions applied to RVEs to get the effective shell stiffness.

Effective properties	At $x_1 = 0$ $\forall x_2, x_3$	At $x_1 = p$ $\forall x_2, x_3$	At $x_2 = 0$ $\forall x_1, x_3$	At $x_2 = q$ $\forall x_1, x_3$	At $x_3 = 0$ $\forall x_1, x_2$	At $x_3 = h$ $\forall x_1, x_2$
Q_{11}^H	$u_1 = 0$ All other degrees of freedom are set to free	$u_1 = 1$ All other degrees of freedom are set to free	$u_2 = 0$ All other degrees of freedom are set to free	$u_2 = 0$ All other degrees of freedom are set to free	All degrees of freedom are set to free.	All degrees of freedom are set to free.
Q_{22}^H	$u_1 = 0$ All other degrees of freedom are set to free	$u_1 = 0$ All other degrees of freedom are set to free	$u_2 = 0$ All other degrees of freedom are set to free	$u_2 = 1$ All other degrees of freedom are set to free	All degrees of freedom are set to free.	All degrees of freedom are set to free.
Q_{12}^H	$u_1 = 0$ All other degrees of freedom are set to free	$u_1 = 1$ All other degrees of freedom are set to free	$u_2 = 0$ All other degrees of freedom are set to free	$u_2 = 1$ All other degrees of freedom are set to free	All degrees of freedom are set to free.	All degrees of freedom are set to free.
Q_{66}^H	$u_1 = u_2 = 0$ All other degrees of freedom are set to free	$u_1 = 0, u_2 = 1$ All other degrees of freedom are set to free	$u_1 = 0$ All other degrees of freedom are set to free	$u_1 = 0$ All other degrees of freedom are set to free	All degrees of freedom are set to free.	All degrees of freedom are set to free.
Q_{44}^H	$u_1 = u_2 = u_3 = 0$ All other degrees of freedom are set to free	$u_1 = u_2 = 0$ $u_3 = 1$ All other degrees of freedom are set to free	$u_1 = u_2 = 0$ All other degrees of freedom are set to free	$u_1 = u_2 = 0$ All other degrees of freedom are set to free	$u_1 = u_2 = 0$ All other degrees of freedom are set to free	$u_1 = u_2 = 0$ All other degrees of freedom are set to free
Q_{55}^H	$u_1 = u_2 = 0$ All other degrees of freedom are set to free	$u_1 = u_2 = 0$ All other degrees of freedom are set to free	$u_1 = u_2 = u_3 = 0$ All other degrees of freedom are set to free	$u_1 = u_2 = 0$ $u_3 = 1$ All other degrees of freedom are set to free	$u_1 = u_2 = 0$ All other degrees of freedom are set to free	$u_1 = u_2 = 0$ All other degrees of freedom are set to free

Table 3.5: Effective stiffness Q_{11}^H for the regular laminated composite wall hexagonal core.

Composite wall	Proposed (without transverse shear) (1) (Nmm^{-2})	Proposed (with transverse shear) (2) (Nmm^{-2})	Modified Mukherjee & Adhikari (2021) (3) (Nmm^{-2})	Wang & Wang (2018) (4*) (Nmm^{-2})	Krishna murthy & Saether (2019) (5*) (Nmm^{-2})	FE (Nmm^{-2})	Difference % (Proposed- FE)/FE%				
							(1)	(2)	(3)	(4)	(5)
1	324.71	324.67	324.01	328.19	337.29	322.63	0.64	0.63	0.43	1.72	4.54
2	595.17	594.94	595.09	603.47	504.35	591.66	0.59	0.55	0.58	1.99	-14.76
3	482.53	482.48	482.50	485.56	855.58	477.88	0.97	0.96	0.97	1.61	79.04
4	403.27	403.10	403.07	410.41	262.71	398.85	1.11	1.07	1.06	2.90	-34.13
5	401.50	401.42	400.81	405.95	412.37	399.82	0.42	0.40	0.25	1.53	3.14
6	228.00	227.95	227.29	231.29	168.11	226.96	0.46	0.43	0.14	1.91	-25.93
7	385.23	384.83	380.09	394.99	153.08	380.83	1.15	1.05	-0.19	3.72	-59.80
8	1793.80	1792.90	1793.70	1811.54	2427.61	1785.94	0.44	0.39	0.43	1.43	35.93
9	1807.10	1803.60	1807.00	1843.09	1073.37	1760.67	2.64	2.44	2.63	4.68	-39.04
10	1681.60	1681.10	1681.50	1691.27	3154.21	1662.92	1.12	1.09	1.12	1.70	89.68
11	448.45	448.29	448.27	455.55	323.90	445.37	0.69	0.66	0.65	2.29	-27.27
12	439.45	439.36	436.84	411.11	275.58	435.58	0.89	0.87	0.29	-5.62	-36.73
13	1799.70	1797.80	1799.60	1824.87	1481.23	1715.09	4.93	4.82	4.93	6.40	-13.64
14	360.14	360.08	357.53	330.84	209.00	356.44	1.04	1.02	0.30	-7.18	-41.36

* Poisson's ratio calculated in (1) is used

Table 3.6: Effective stiffness Q_{22}^H for the regular laminated composite wall hexagonal core.

Composite wall	Proposed (without transverse shear) (1) (Nmm^{-2})	Proposed (with transverse shear) (2) (Nmm^{-2})	Modified Mukherjee & Adhikari (2021) (3) (Nmm^{-2})	Wang & Wang (2018) (4 [†]) (Nmm^{-2})	Krishna murthy & Saether (2019) (5 [†]) (Nmm^{-2})	FE (Nmm^{-2})	Difference % (Proposed- FE)/FE%				
							(1)	(2)	(3)	(4)	(5)
1	324.71	324.67	324.01	328.19	337.29	322.61	0.65	0.64	0.43	1.73	4.55
2	595.17	594.94	595.09	603.47	504.35	591.64	0.60	0.56	0.58	2.00	-14.75
3	482.53	482.48	482.50	485.56	855.58	477.85	0.98	0.97	0.97	1.61	79.05
4	403.27	403.10	403.07	410.41	262.71	398.84	1.11	1.07	1.06	2.90	-34.13
5	401.50	401.42	400.81	405.95	412.37	399.84	0.42	0.40	0.24	1.53	3.13
6	228.00	227.95	227.29	231.29	168.11	226.96	0.46	0.44	0.14	1.91	-25.93
7	385.23	384.83	380.09	394.99	153.08	380.92	1.13	1.03	-0.22	3.69	-59.81
8	1793.80	1792.90	1793.70	1811.54	2427.61	1785.82	0.45	0.40	0.44	1.44	35.94
9	1807.10	1803.60	1807.00	1843.09	1073.37	1760.67	2.64	2.44	2.63	4.68	-39.04
10	1681.60	1681.10	1681.50	1691.27	3154.21	1662.83	1.13	1.10	1.12	1.71	89.69
11	448.45	448.29	448.27	455.55	323.90	445.36	0.69	0.66	0.65	2.29	-27.27
12	439.45	439.36	436.84	411.11	275.58	435.60	0.88	0.86	-2.00	-5.62	-36.73
13	1799.70	1797.80	1799.60	1824.87	1481.23	1714.91	4.94	4.83	4.94	6.41	-13.63
14	360.14	360.08	357.53	330.84	209.00	356.38	1.06	1.04	0.32	-7.17	-41.35

[†] Poisson's ratio calculated in (1) is used.

Table 3.7: Effective stiffness Q_{12}^H for the regular laminated composite wall hexagonal core.

Composite wall	Proposed (without transverse shear)	Proposed (with transverse shear)	Modified Mukherjee & Adhikari (2021)	Wang & Wang (2018) (4 [‡])	Krishna murthy & Saether (2019) (5 [‡])	FE (Nmm^{-2})	Difference%(Proposed- FE)/FE%				
	(1) (Nmm^{-2})	(2) (Nmm^{-2})	(3) (Nmm^{-2})	(4) (Nmm^{-2})	(5) (Nmm^{-2})		(1)	(2)	(3)	(4)	(5)
1	319.85	319.9	320.56	323.27	332.24	319.03	0.26	0.27	0.48	1.33	4.14
2	584.25	584.47	584.32	592.39	495.10	584.02	0.04	0.08	0.05	1.43	-15.23
3	478.29	478.34	478.32	481.30	848.07	474.61	0.77	0.79	0.78	1.41	78.69
4	393.65	393.82	393.85	400.61	256.44	392.19	0.37	0.41	0.42	2.15	-34.61
5	395.42	395.5	396.12	399.80	406.13	395.67	-0.06	-0.04	0.11	1.04	2.64
6	223.19	223.23	223.9	226.41	164.56	223.49	-0.14	-0.12	0.18	1.31	-26.37
7	370.15	370.55	375.29	379.53	147.09	372.85	-0.72	-0.62	0.66	1.79	-60.55
8	1773.1	1774.0	1773.2	1790.72	2399.72	1772.24	0.05	0.10	0.05	1.04	35.41
9	1759.8	1763.3	1759.9	1794.84	1045.27	1732.95	1.55	1.75	1.56	3.57	-39.68
10	1667.6	1668.1	1667.7	1677.25	3128.06	1653.49	0.85	0.88	0.86	1.44	89.18
11	438.8	438.96	438.99	445.75	316.93	438.49	0.07	0.11	0.11	1.66	-27.72
12	428.81	428.9	431.42	401.15	268.91	430.08	-0.30	-0.27	0.31	-6.73	-37.48
13	1767.2	1769.1	1767.3	1791.91	1454.48	1694.91	4.26	4.38	4.27	5.72	-14.19
14	350.77	350.84	353.38	322.23	203.56	351.42	-0.18	-0.17	0.56	-8.31	-42.07

[‡] Poisson's ratio calculated in (1) is used.

Table 3.8: Effective stiffness Q_{66}^H for the regular laminated composite wall hexagonal core.

Composite wall	Proposed (without shear)	Proposed (with shear)	Modified Mukherjee & Adhikari (2021)	Wang & Wang (2018)	Krishna murthy & Saether (2019)	FE (Nmm^{-2})	Difference % (Proposed- FE)/FE%				
	(1) (Nmm^{-2})	(2) (Nmm^{-2})	(3) (Nmm^{-2})	(4) (Nmm^{-2})	(5) (Nmm^{-2})		(1)	(2)	(3)	(4)	(5)
1	2.43	2.38	1.73	4.88	2.51	2.47	-1.79	-3.68	-30.21	97.03	1.25
2	5.46	5.23	5.38	10.97	4.59	5.37	1.71	-2.55	0.27	104.35	-14.61
3	2.12	2.07	2.09	4.24	3.74	2.25	-6.06	-7.95	-6.97	88.30	65.89
4	4.81	4.64	4.61	9.68	3.10	4.75	1.38	-2.26	-2.86	103.88	-34.74
5	3.04	2.96	2.34	6.10	3.10	2.93	3.90	1.23	-19.84	108.52	5.91
6	2.40	2.36	1.69	4.83	1.75	2.39	0.41	-1.49	-29.23	101.61	-26.73
7	7.54	7.14	2.40	15.15	2.94	5.70	32.32	25.40	-57.93	166.03	-48.45
8	10.31	9.49	10.23	20.70	13.87	9.63	7.00	-1.54	6.17	114.82	43.93
9	23.65	20.19	23.53	47.62	13.87	20.25	16.82	-0.29	16.21	135.19	-31.52
10	6.97	6.49	6.94	13.96	13.02	6.72	3.73	-3.35	3.32	107.90	93.86
11	4.83	4.67	4.64	9.70	3.45	4.83	-0.08	-3.39	-3.93	100.87	-28.59
12	5.32	5.23	2.71	9.84	3.30	3.90	36.53	34.03	-30.46	152.39	-15.41
13	16.26	14.39	16.15	32.66	13.26	14.47	12.33	-0.55	11.60	125.68	-8.41
14	4.685	4.62	2.07	8.50	2.68	3.46	35.25	33.46	-40.12	145.28	-22.53

Table 3.9: Effective stiffness Q_{44}^H for the regular laminated composite wall hexagonal core.

Composite wall	Proposed (without transverse shear) (1) (Nmm^{-2})	Proposed (with transverse shear) (2) (Nmm^{-2})	Wang & Wang (2018) (4) (Nmm^{-2})	Krishna murthy & Saether (2019) (5) (Nmm^{-2})	FE (Nmm^{-2})	Difference % (Proposed- FE)/FE%			
						(1)	(2)	(4)	(5)
1	341.61	341.61	341.61	341.07	335.65	1.78	1.78	1.78	1.61
2	149.39	149.39	149.39	149.15	149.54	-0.10	-0.10	-0.10	-0.26
3	149.39	149.39	149.39	149.15	149.53	-0.10	-0.10	-0.10	-0.26
4	231.45	231.45	245.50	218.22	229.92	0.67	0.67	6.78	-5.09
5	231.42	231.42	245.50	218.22	229.91	0.66	0.66	6.78	-5.08
6	384.70	384.70	389.67	382.47	385.91	-0.31	-0.31	0.97	-0.89
7	745.01	744.95	961.64	675.07	756.43	-1.51	-1.52	27.13	-10.76
8	170.32	170.32	170.32	170.05	170.41	-0.05	-0.05	-0.051	-0.21
9	170.32	170.32	170.32	170.05	170.47	-0.09	-0.09	-0.091	-0.25
10	170.32	170.32	170.32	170.05	170.47	-0.09	-0.09	-0.089	-0.25
11	243.00	243.00	255.97	238.20	249.05	-2.43	-2.43	2.78	-4.36
12	429.05	429.03	555.51	285.57	398.00	7.80	7.80	39.59	-28.25
13	170.32	170.32	170.32	169.75	170.47	-0.09	-0.09	-0.091	-0.43
14	581.06	581.06	651.62	440.41	543.17	6.97	6.97	19.97	-18.92

Table 3.10: Effective stiffness Q_{55}^H for the regular laminated composite wall hexagonal core.

Composite wall	Proposed (without shear) (1) (Nmm^{-2})	Proposed (with shear) (2) (Nmm^{-2})	Wang & Wang (2018) (4) (Nmm^{-2})	Krishna murthy & Saether (2019) (5) (Nmm^{-2})	FE (Nmm^{-2})	Difference % (Proposed- FE)/FE%			
						(1)	(2)	(4)	(5)
1	341.61	341.61	341.61	341.07	337.46	1.23	1.23	1.23	1.07
2	149.39	149.39	149.39	149.15	149.44	-0.03	-0.03	-0.03	-0.19
3	149.39	149.39	149.39	149.15	149.44	-0.03	-0.03	-0.03	-0.19
4	231.45	231.45	245.50	218.22	228.69	1.21	1.21	7.35	-4.58
5	231.42	231.42	245.50	218.22	228.02	1.49	1.49	7.66	-4.30
6	384.70	384.70	389.67	382.47	385.24	-0.14	-0.14	1.15	-0.72
7	745.01	744.95	961.64	675.07	735.73	1.26	1.25	30.71	-8.24
8	170.32	170.32	170.32	170.05	169.84	0.28	0.28	0.28	0.12
9	170.32	170.32	170.32	170.05	170.36	-0.02	-0.02	-0.02	-0.18
10	170.32	170.32	170.32	170.05	170.36	-0.02	-0.02	-0.02	-0.18
11	243.00	243.00	255.97	238.20	246.76	-1.52	-1.52	3.73	-3.47
12	429.05	429.03	555.51	285.57	371.94	15.36	15.35	49.36	-23.22
13	170.32	170.32	170.32	169.75	170.36	-0.02	-0.02	-0.02	-0.36
14	581.06	581.06	651.62	440.41	518.36	12.09	12.09	25.71	-15.04

The proposed strain-energy-based model showed an excellent agreement with the FE results, except for predictions of Q_{66}^H for some of the composite wall material configurations considered. The maximum errors in predictions using the proposed model for Q_{11}^H , Q_{22}^H , Q_{12}^H and Q_{66}^H without the transverse shear deformation of the walls are 4.94%, 4.93% , 4.26% and 36.53%, respectively and with the transverse shear deformation of the walls are 4.83%, 4.82%, 4.38% and 34.03% respectively (Tables 3.5 – 3.8). There is no significant difference between most of results from with and without the consideration of transverse shear deformation of the walls. However, for the walls consisting of two different material combinations (configuration 7-14, Table 3.2), there are considerable differences between the results (Table 3.8), with a maximum difference of 17.11% between the two cases. Overall, the proposed model considering transverse shear deformation of the walls provides better results compared to all the other models. For all the properties except for Q_{66}^H , modified Mukherjee & Adhikari's (2021) and Wang & Wang's (2018) models also gave good agreements with the FE results agreed well with the proposed model results. However, it should be noted that Wang & Wang's (2018) model results were calculated using the Poisson's ratio calculated using the proposed model as the original equation provides the value of 1 for the Poisson's ratio, which leads to an undefined value for the effective shell stiffness properties. Predictions for Q_{66}^H from modified Mukherjee & Adhikari's (2021) and Wang & Wang's (2018) models showed a significant difference to FE results for several composite wall configurations, but former results are better in comparison to other. Results from Sather & Krishnamurthy's (2019) model are with highest error percentage and agreements with FE results are not good in comparison to other models. The major reason for the significant difference from other models is the effective modulus of laminated walls is calculated from the membrane stiffness of the wall, however, hexagonal honeycomb core walls are subjected to significant bending deformations under the in-plane loadings.

In predicting the transverse shear stiffness, the proposed strain energy-based model and FE results are in very good agreement for all the different material configurations of the core wall considered (Table 3.9 and Table 3.10). Maximum errors in predicting Q_{44}^H and Q_{55}^H out of all the combinations considered are 7.8% and 15.36%, respectively. Wang and Wang's (2018) and Sather & Krishnamurthy's (2019) models predicts the stiffness properties with more significant errors than the proposed model,

with maximum absolute errors of 39.59% and 28.25% for Q_{44}^H and 49.36% and 23.22% for Q_{55}^H , respectively.

From the different material configurations considered, the prediction for the core consisting of symmetrically laminated walls shows excellent agreement with the FE results. The prediction accuracy reduces when the laminates are not symmetric and/or not orthotropic (Table 3.4 – 3.10). When the laminate is not symmetrical, the membrane-bending coupling may exist. While for most cases, the condition given in Eq. (3.17) for considering the reference plane will eliminate this effect, for some unsymmetrical laminates, a reference plane which is also the neutral plane, may not exist within the wall thickness. In addition, when the laminate is non-orthotropic and non-isotropic, the bending-twisting coupling may also exist. As these components are not considered in the analytical models, results may deviate from the exacts when bend-twist coupling becomes stronger. However, the proposed model was shown to provide reasonable accuracy while significantly reducing the time and effort required to predict effective properties for hexagonal honeycomb cores compared to FE models.

3.4.2 Comparison of effective properties of honeycomb cores with different shapes

In this section, the performance of the proposed model in predicting the effective stiffness properties for different honeycomb core shapes with laminated walls is investigated. Also, the effective stiffness properties of different honeycomb core shapes with material configurations considered in Table 3.2 are compared. Triangular, square and mixed triangular-rhombus cores (Fig. 3.7) with the same relative core density of 0.0722 are considered. Each wall of the core has an identical thickness, and each ply thickness is assumed to be equal. Lengths of the honeycomb core walls are assumed as: $l_2 = l_3 = l_4 = 50\text{mm}$ (Fig. 3.7), while the height of the core (h) is taken as 150mm. The same approach as the hexagonal core to model the RVEs (Fig. 3.8) in ABAQUS is used, and effective stiffness properties are calculated based on the total energy extracted from the FE analysis. Figures. 3.9 – 3.14 compare the effective stiffness properties of different honeycomb core shapes under the same core density for the different material configurations of the core walls considered in this study.

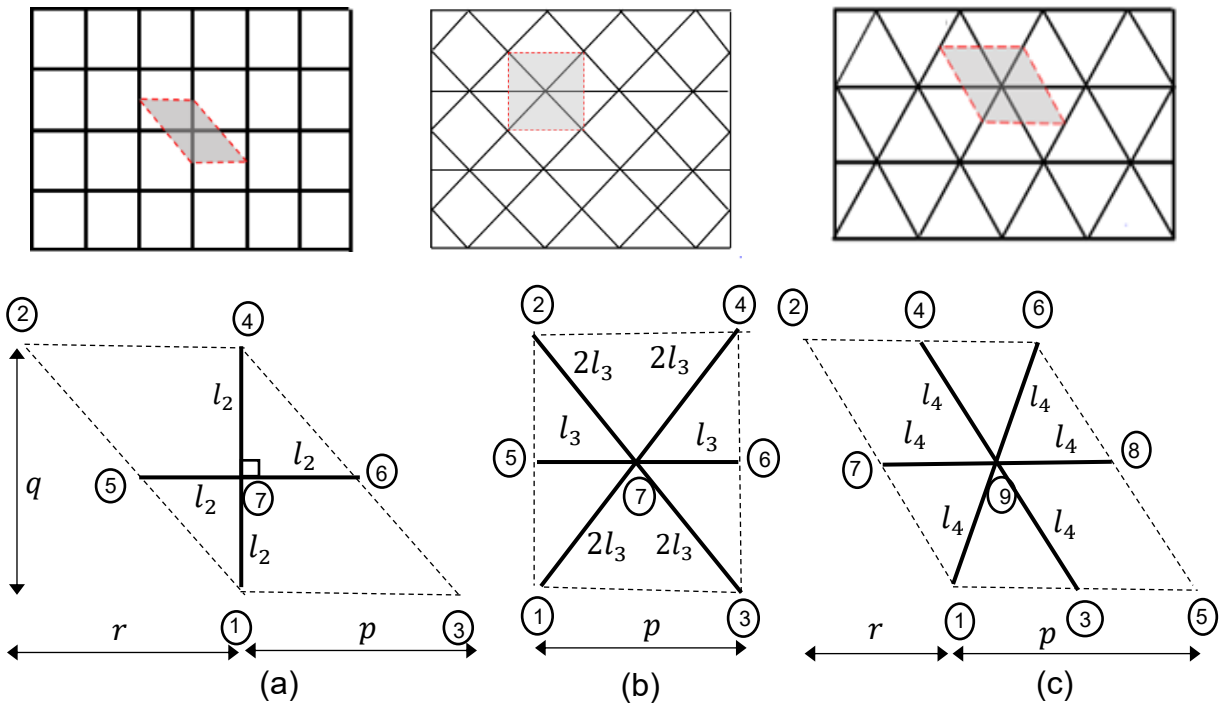


Fig. 3.7: RVEs of (a) square (b) mixed rhombus-triangular and (c) triangular honeycomb core used in the analysis of proposed models.

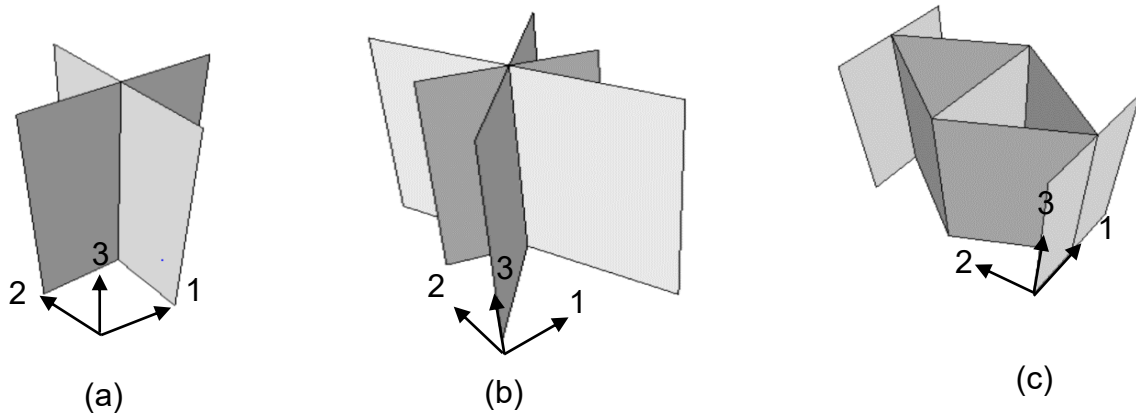
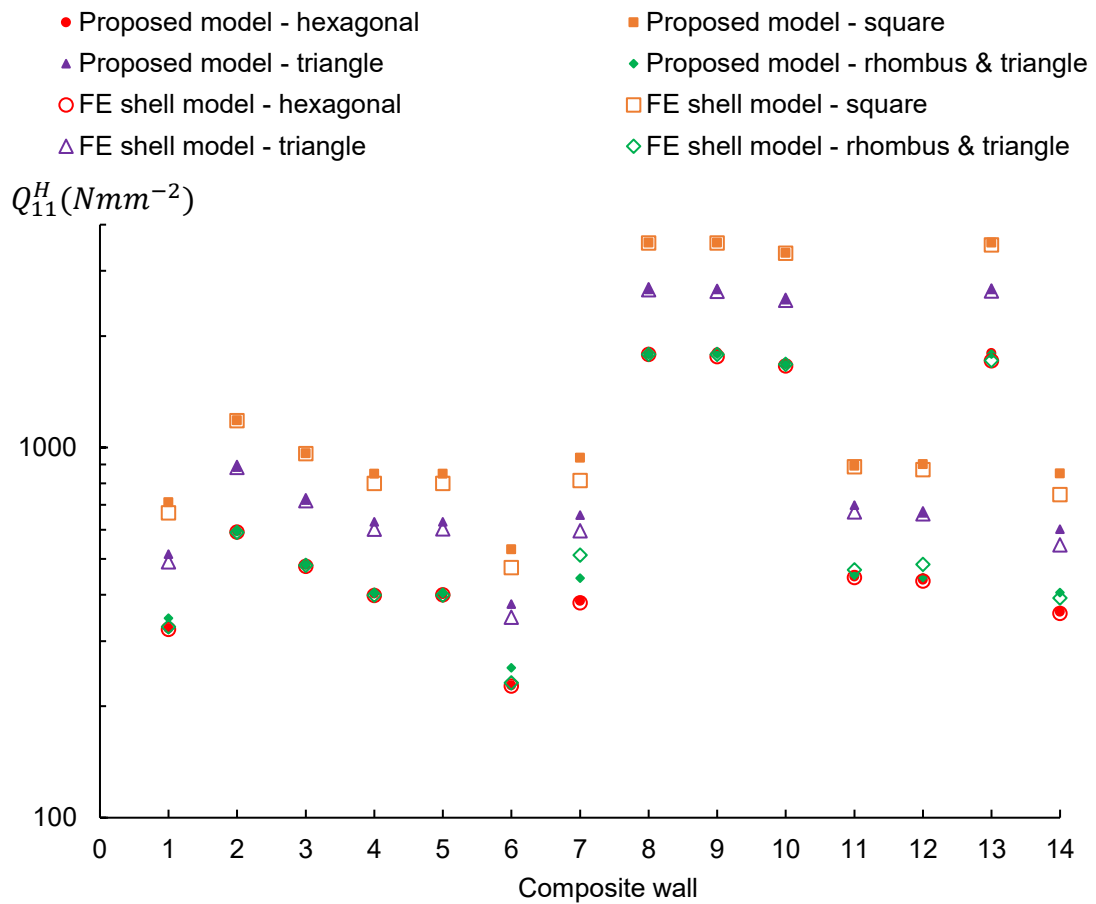
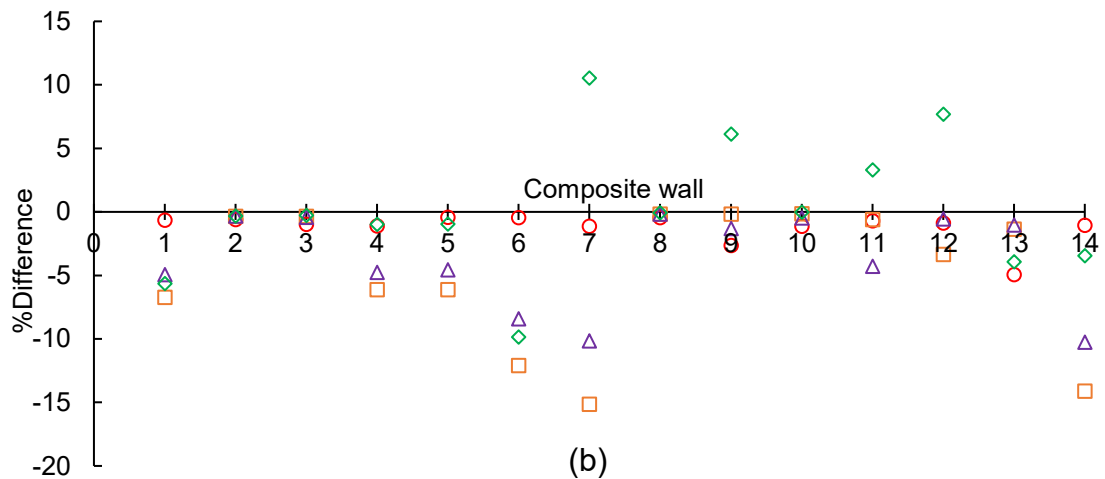


Fig. 3.8: RVEs of (a) square (b) mixed rhombus-triangular and (c) triangular honeycomb core used in FE models.

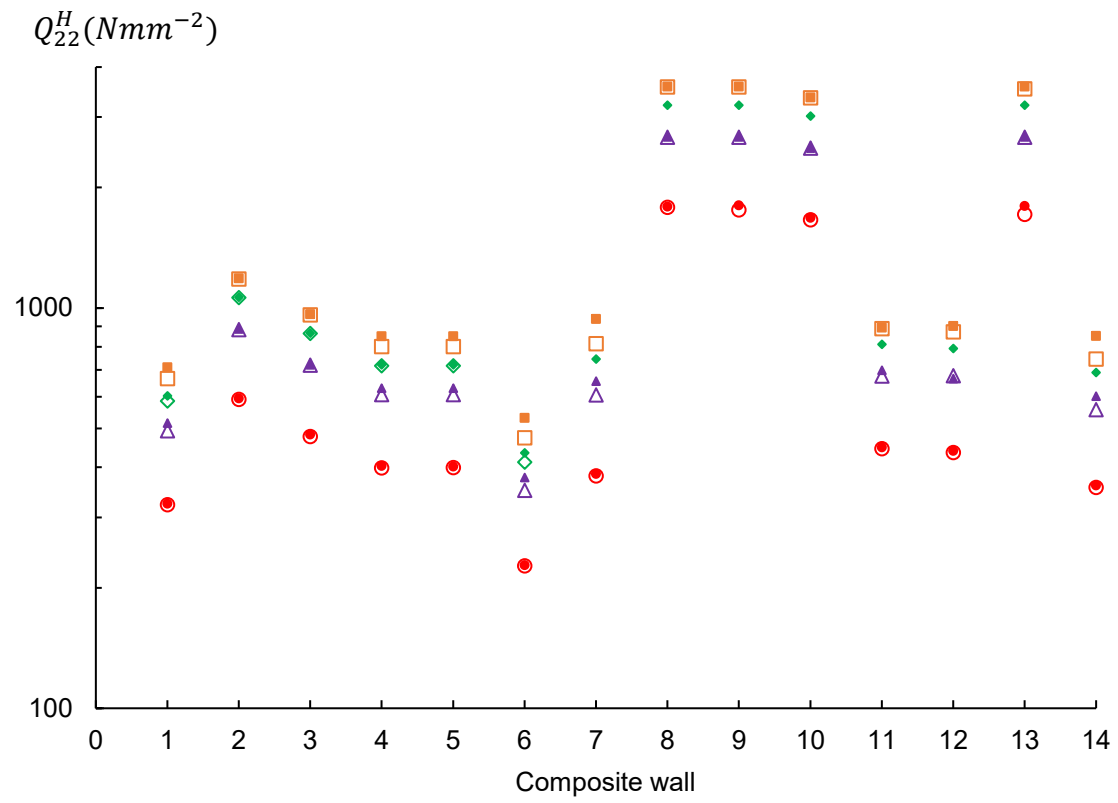


(a)

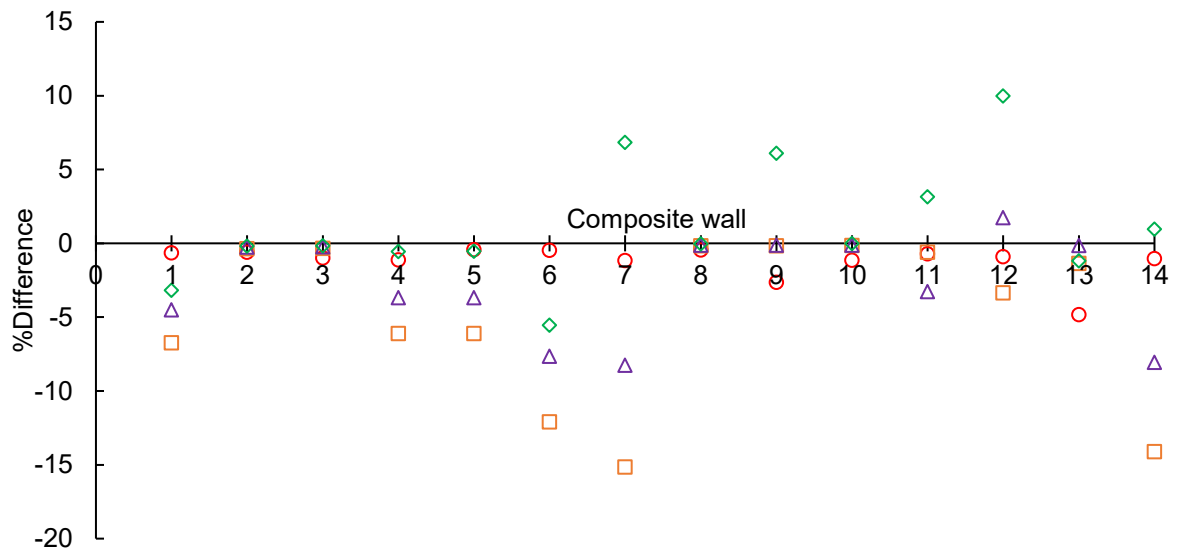


(b)

Fig. 3.9: Comparison of (a) effective stiffness Q_{11}^H of the laminated composite wall honeycomb cores and (b) percentage error of predictions relative to FE analysis.



(a)



(b)

Fig. 3.10: Comparison of (a) effective stiffness Q_{22}^H of the laminated composite wall honeycomb cores and (b) percentage error of predictions relative to FE analysis.

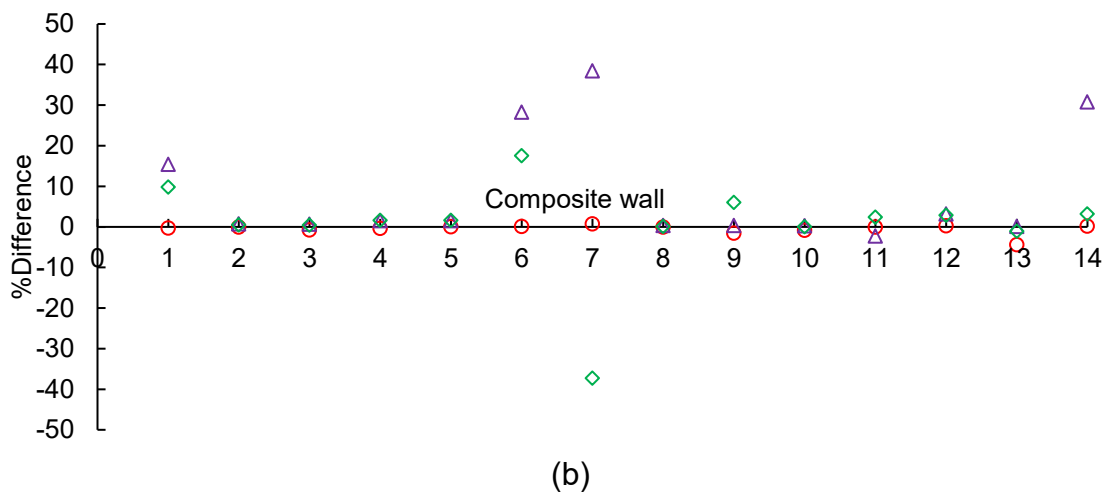
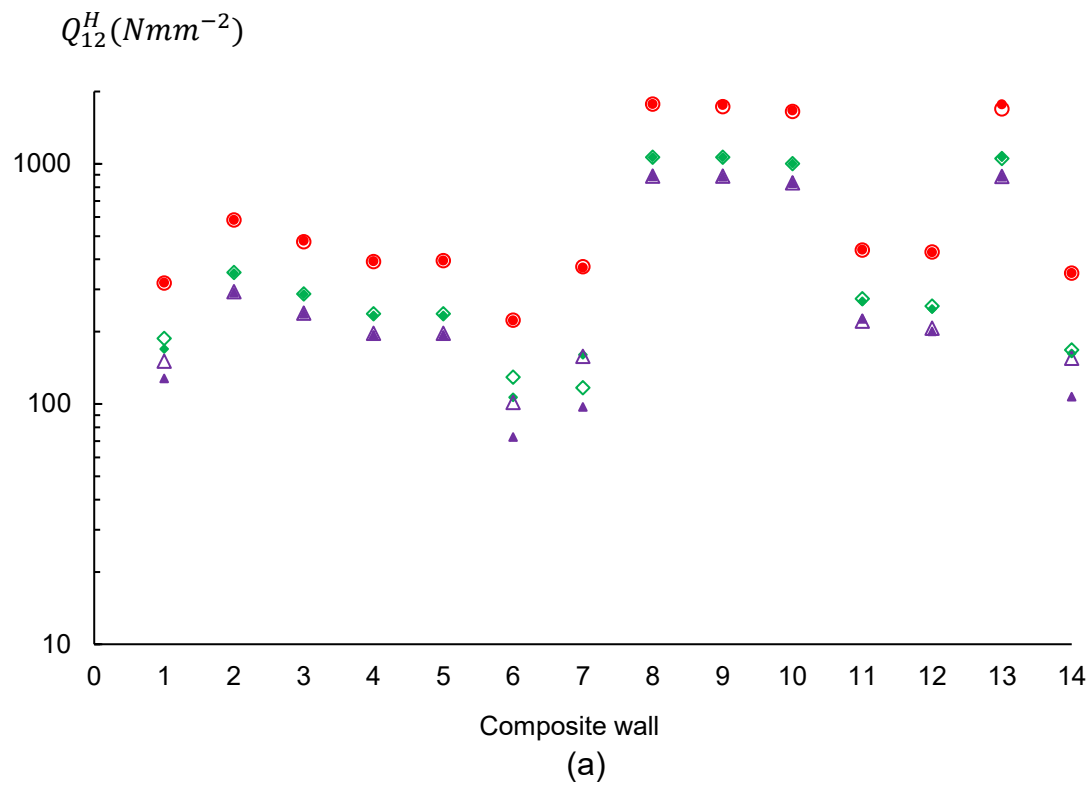


Fig. 3.11: Comparison of (a) effective stiffness Q_{12}^H of the laminated composite wall honeycomb cores and (b) percentage error of predictions relative to FE analysis.

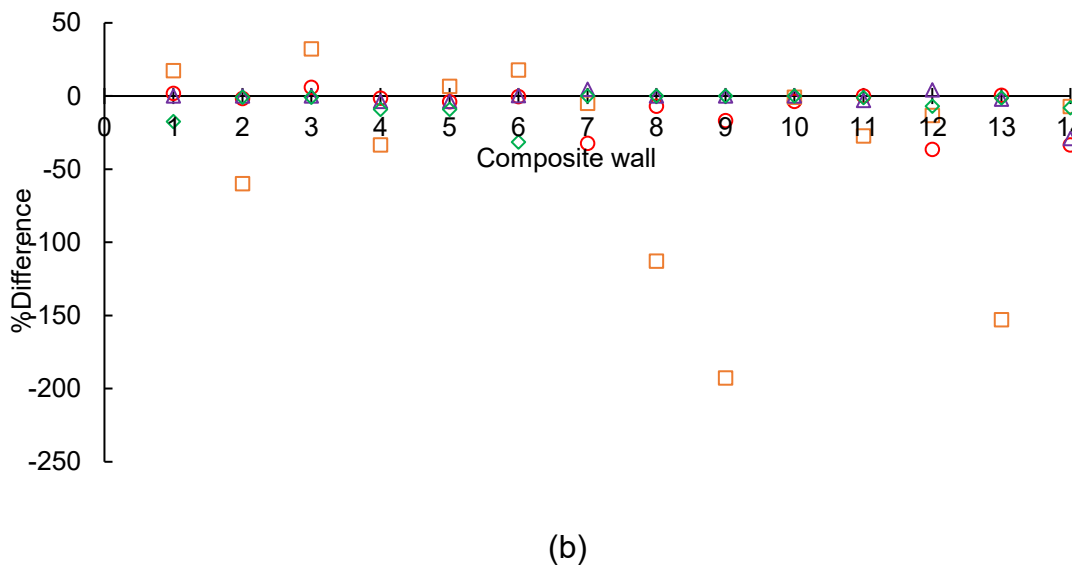
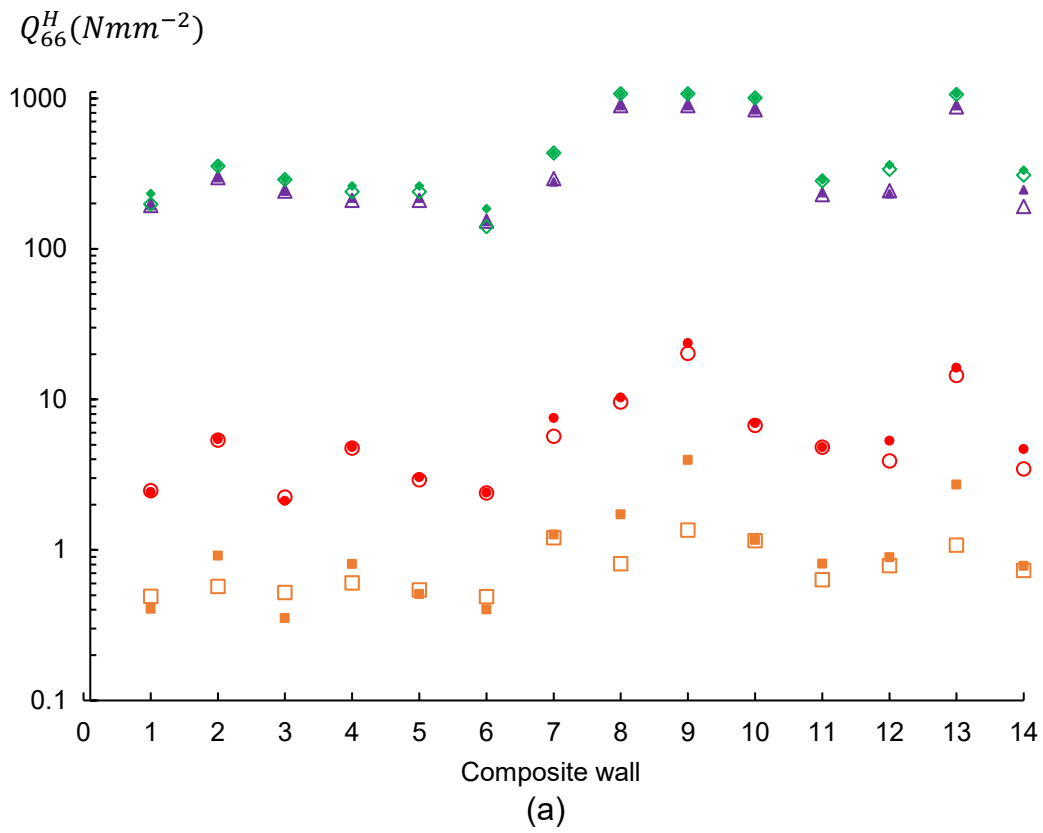


Fig. 3.12: Comparison of (a) effective stiffness Q_{66}^H of the laminated composite wall honeycomb cores and (b) percentage error of predictions relative to FE analysis.

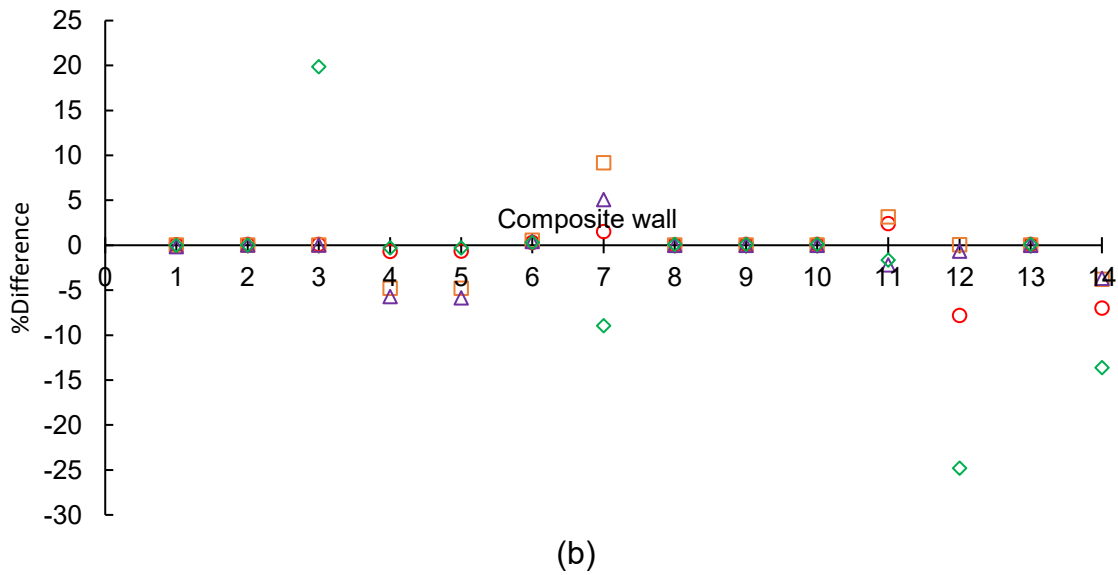
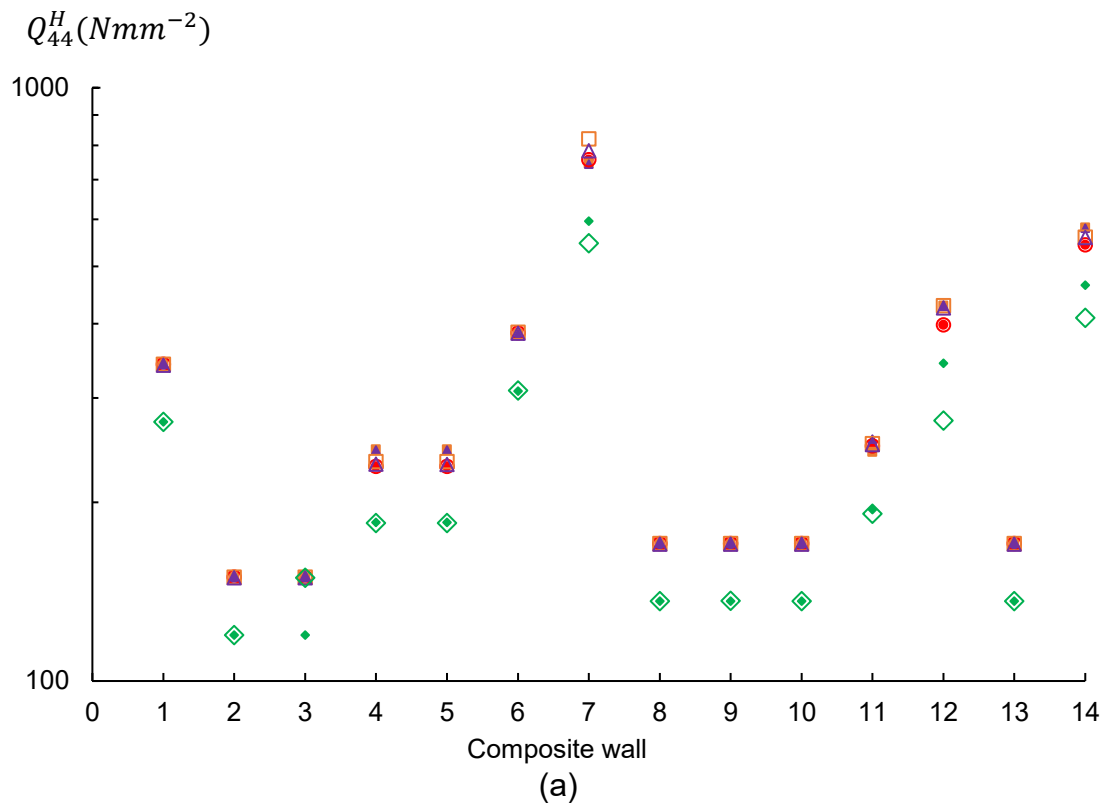


Fig. 3.13: Comparison of (a) effective stiffness Q_{44}^H of the laminated composite wall honeycomb cores and (b) percentage error of predictions relative to FE analysis.

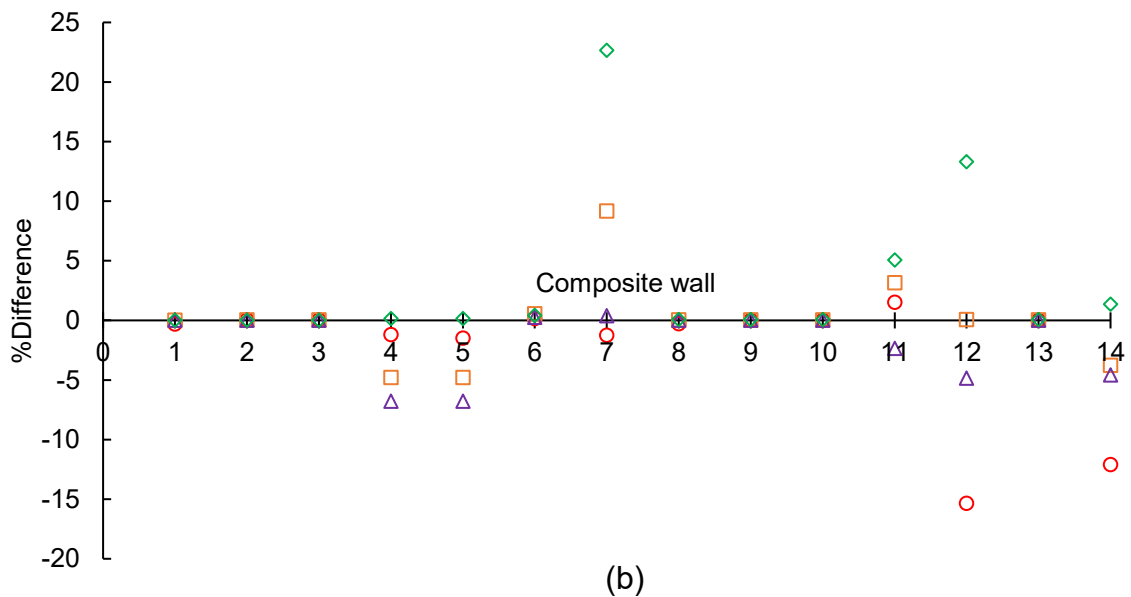
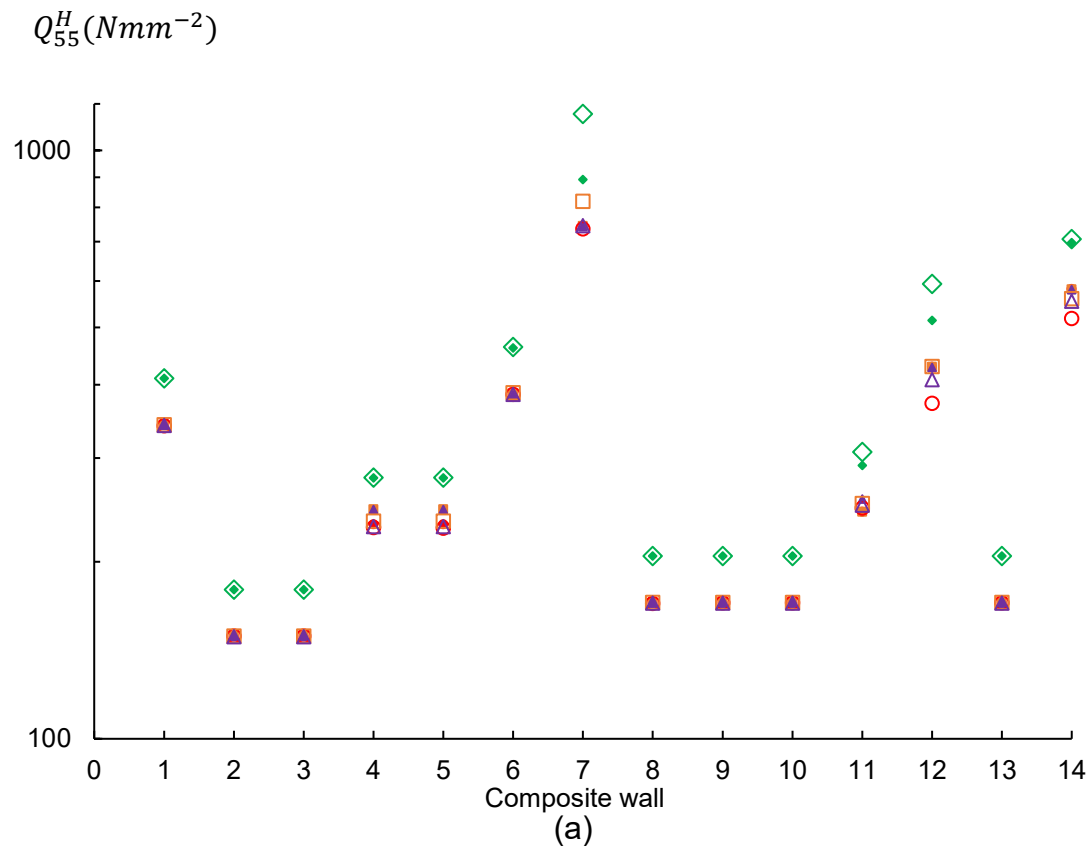


Fig. 3.14: Comparison of (a) effective stiffness Q_{55}^H of the laminated composite wall honeycomb cores and (b) percentage error of predictions relative to FE analysis.

For most of the honeycomb core shapes, the predictions from the proposed model agreed well with the FE results. However, predictions for Q_{12}^H and Q_{66}^H from the proposed model showed differences with the FE results for square core shapes (Figs. 3.11 - 3.12). Nonetheless, the actual values of the Q_{12}^H and Q_{66}^H for square cores are relatively small; thus, the overall error caused by this mismatch can be expected to be small. When stiffness values are relatively large, the proposed model predictions agreed well with the FE results.

It can be seen from Figs. 3.9 – 3.14 that, although the core density is the same, the effective stiffness properties are different for different core shapes and material configurations. Out of all the different honeycomb core shapes, the square core shows the highest in-plane normal stiffness Q_{11}^H and Q_{11}^H while having the lowest in-plane shear stiffness Q_{66}^H for all different material configurations considered. Moreover, it gives a very small negative Poisons' ratio, resulting in the negative stiffness value for Q_{12}^H (Fig. 3.11). While the hexagonal core shows the lowest in-plane normal stiffness, it shows the highest in-plane normal coupling stiffness Q_{12}^H for all the cases (Fig. 3.11) due to the high effective in-plane Poisson's ratio. The triangular core shows the highest in-plane shear stiffness out of all the honeycomb core shapes considered (Fig. 3.12). Except for the mixed rhombus-triangular core, all the other cores behave as transversely isotropic material at the effective level, whereas the mixed rhombus-triangular core shows orthotropic material behaviour.

In the case of out-of-plane shear stiffness (Figs. 3.13 - 3.14), triangular, square, and hexagonal core results in almost the same values for all the different material configurations considered. However, mixed rhombus-triangular core results in slightly higher values for Q_{44}^H and lower values for Q_{55}^H than the other core shapes. Regardless of the different honeycomb core shapes, the highest value for transverse shear stiffness is observed when the fibre layer arrangement is only with (45°/-45°) plies, and stiffness is found to reduce when the fibre layer arrangement consist of (0°/90°) plies (Figs. 3.13 - 3.14).

3.4.3 Design charts for the predictions of effective properties

While the above developed models were shown to be accurate in determining the equivalent effective stiffness properties of the laminated composite honeycomb cores, calculations may need little effort, thus may not be attractive for direct use design purposes. Therefore, simplified design plots are produced in Figs. 3.15 - 3.18

for calculating the effective properties of the honeycomb cores of different shapes with orthotropic laminate walls. The plots are produced deriving the corresponding equations following the strain-energy based homogenisation procedure in section 3.2.2. The equations are not shown here as some of the equations derived are quite long to show here. The following example demonstrated the use of design plots for obtaining the effective stiffness properties for a hexagonal core:

Examples: Consider the composite wall configuration 1 and 7 in Table 3.2 for the hexagonal core. For configuration 1 in Table 3.2, the value of the ratio $\bar{A}'_{12}{}^2/(\bar{A}'_{11}\bar{A}'_{22})$ is 0.17, while value of the ratio $\bar{D}'_{11}/(\bar{A}'_{11}l^2)$ is 2.62×10^{-4} . Using the above two values in Figs. 3.15(a)-(c), values of the ratios $(Q^H_{11}l)/\bar{A}'_{11}$, $(Q^H_{12}l)/\bar{A}'_{11}$, and $(Q^H_{66}l)/\bar{A}'_{11}$ can be obtained as approximately 0.2405, 0.2377, and 0.0018 respectively. Since value of the \bar{A}'_{11} is $6.7281 \times 10^4 \text{Nmm}^{-1}$, effective properties Q^H_{11} , Q^H_{12} , and Q^H_{66} can be calculated as 323.6Nmm^{-2} , 319.9Nmm^{-2} , and 2.42Nmm^{-2} respectively.

For configuration 7 in Table 3.2, the value of the ratio $\bar{A}'_{12}{}^2/(\bar{A}'_{11}\bar{A}'_{22})$ is 0.457, while value of the ratio $\bar{D}'_{11}/(\bar{A}'_{11}l^2)$ is 4.35×10^{-4} . Using the above two values in Figs. 3.15(a)-(c), values of the ratios $(Q^H_{11}l)/\bar{A}'_{11}$, $(Q^H_{12}l)/\bar{A}'_{11}$, and $(Q^H_{66}l)/\bar{A}'_{11}$ can be obtained as approximately 0.159, 0.152, and 0.003 respectively. Since value of the \bar{A}'_{11} is $1.2521 \times 10^5 \text{Nmm}^{-1}$, effective properties Q^H_{11} , Q^H_{12} , and Q^H_{66} can be calculated as 398Nmm^{-2} , 380Nmm^{-2} , and 7.5Nmm^{-2} respectively.

Similarly, plots Fig 3.16, Fig 3.17, and Fig 3.18 can be used for calculating the effective properties of square, triangular, and mixed rhombus-triangular core shapes, respectively.

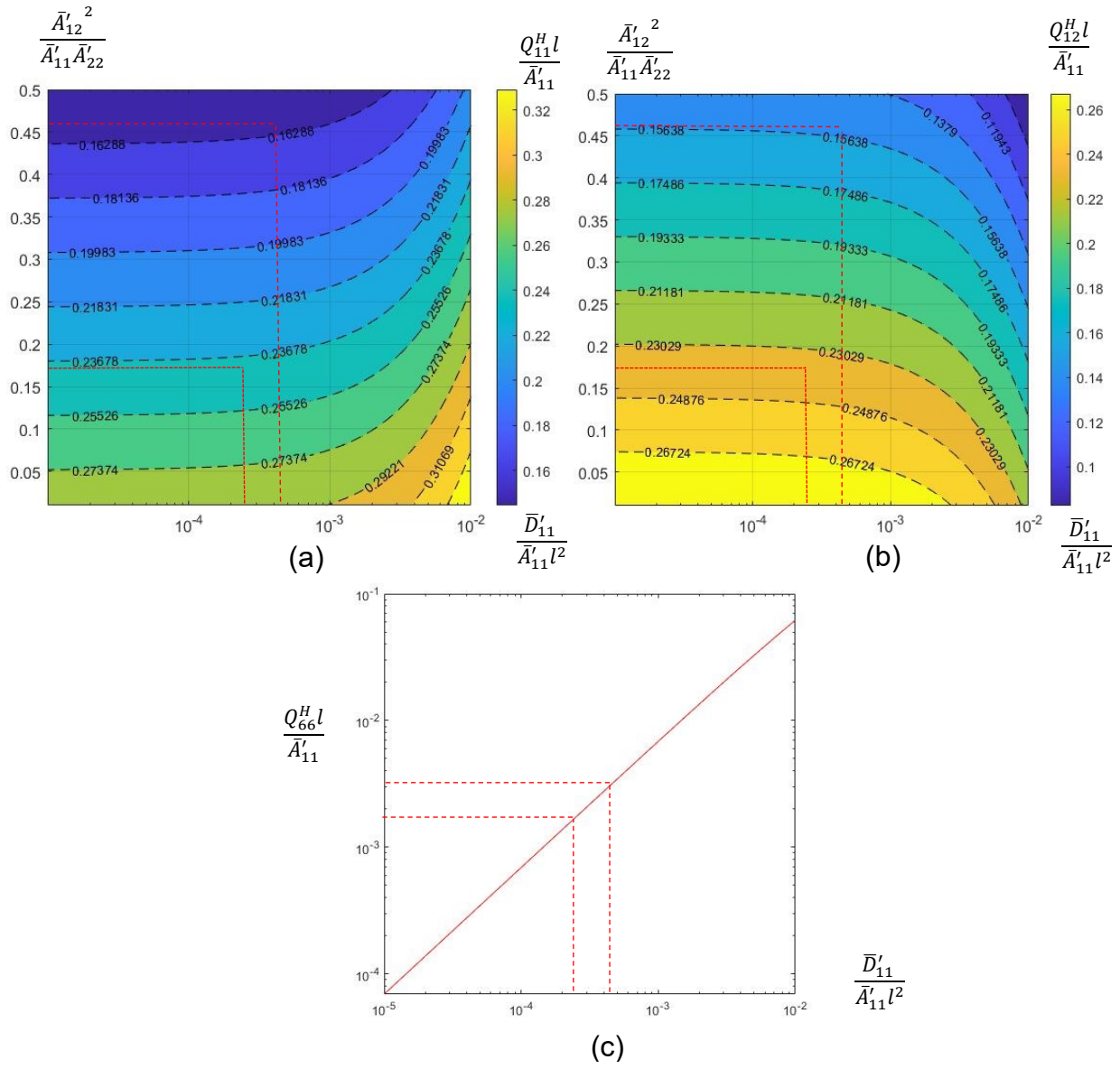


Fig. 3.15: Influence of wall stiffness parameters on (a) Q_{11}^H or Q_{22}^H (b) Q_{12}^H and (c) Q_{66}^H of the hexagonal core.

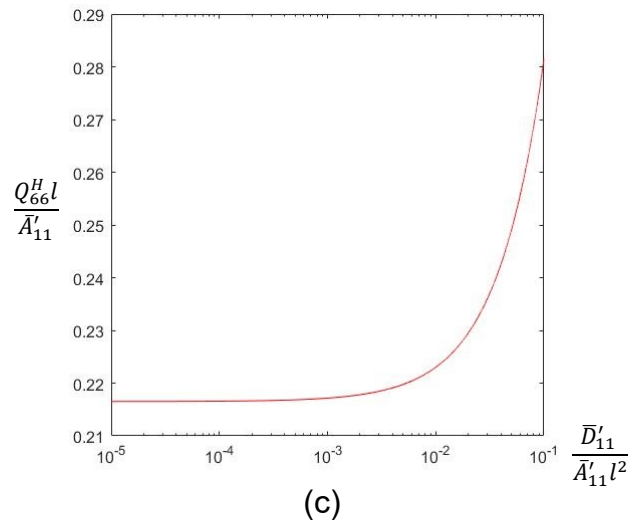
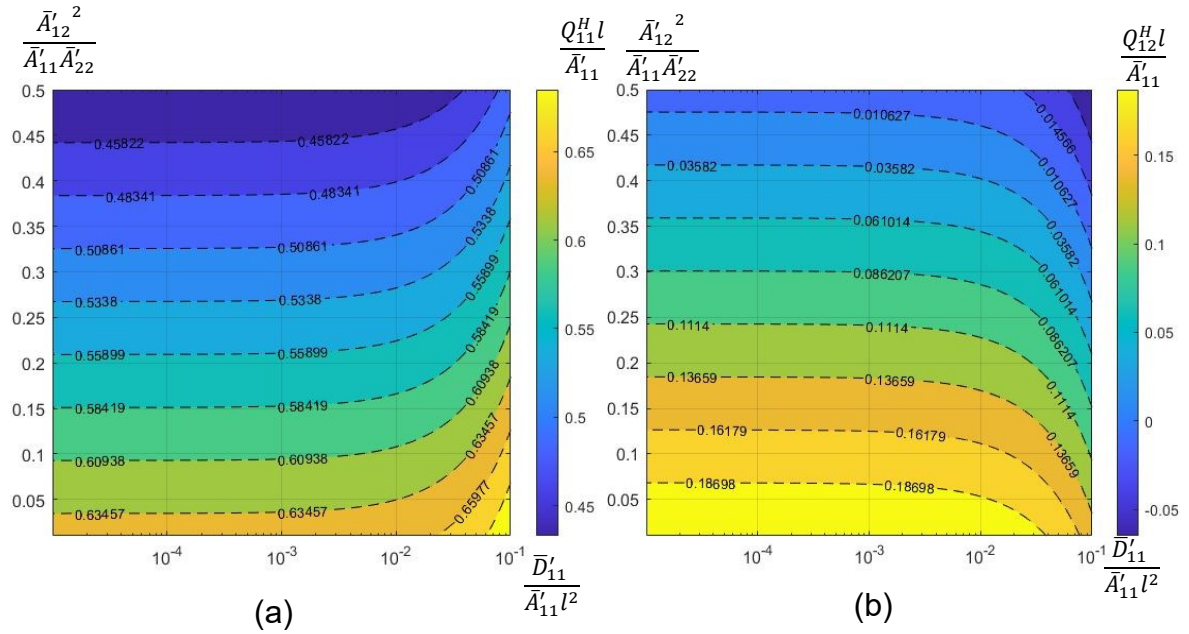


Fig. 3.16: Influence of wall stiffness parameters on (a) Q_{11}^H or Q_{22}^H (b) Q_{12}^H and (c) Q_{66}^H of the triangular core.

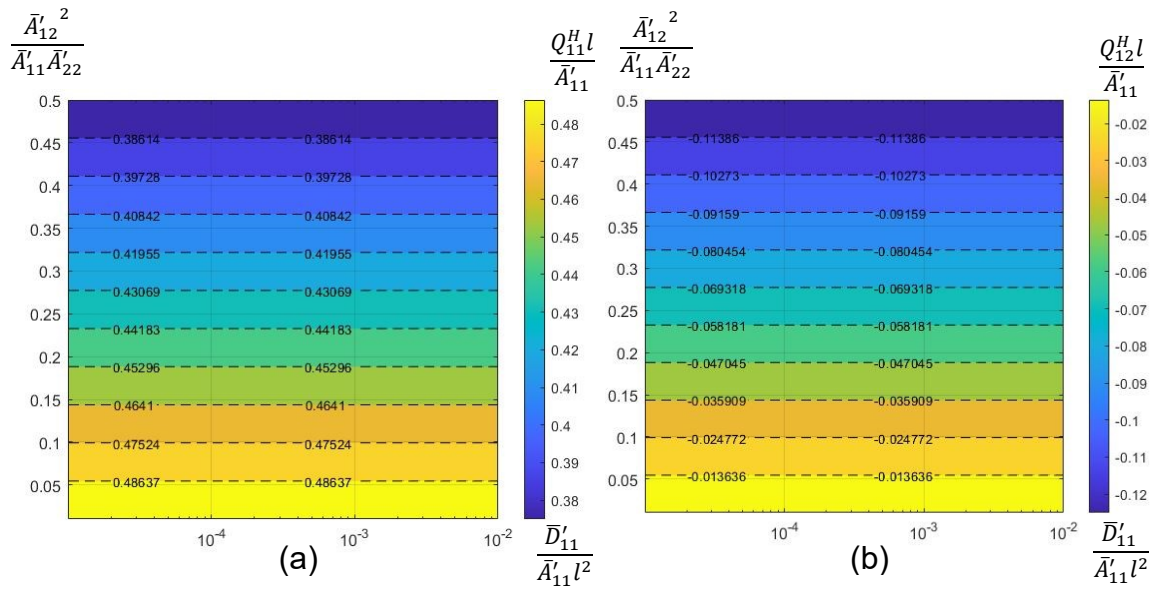


Fig. 3.17: Influence of wall stiffness parameters on (a) Q_{11}^H or Q_{22}^H (b) Q_{12}^H and (c) Q_{66}^H of the square core.

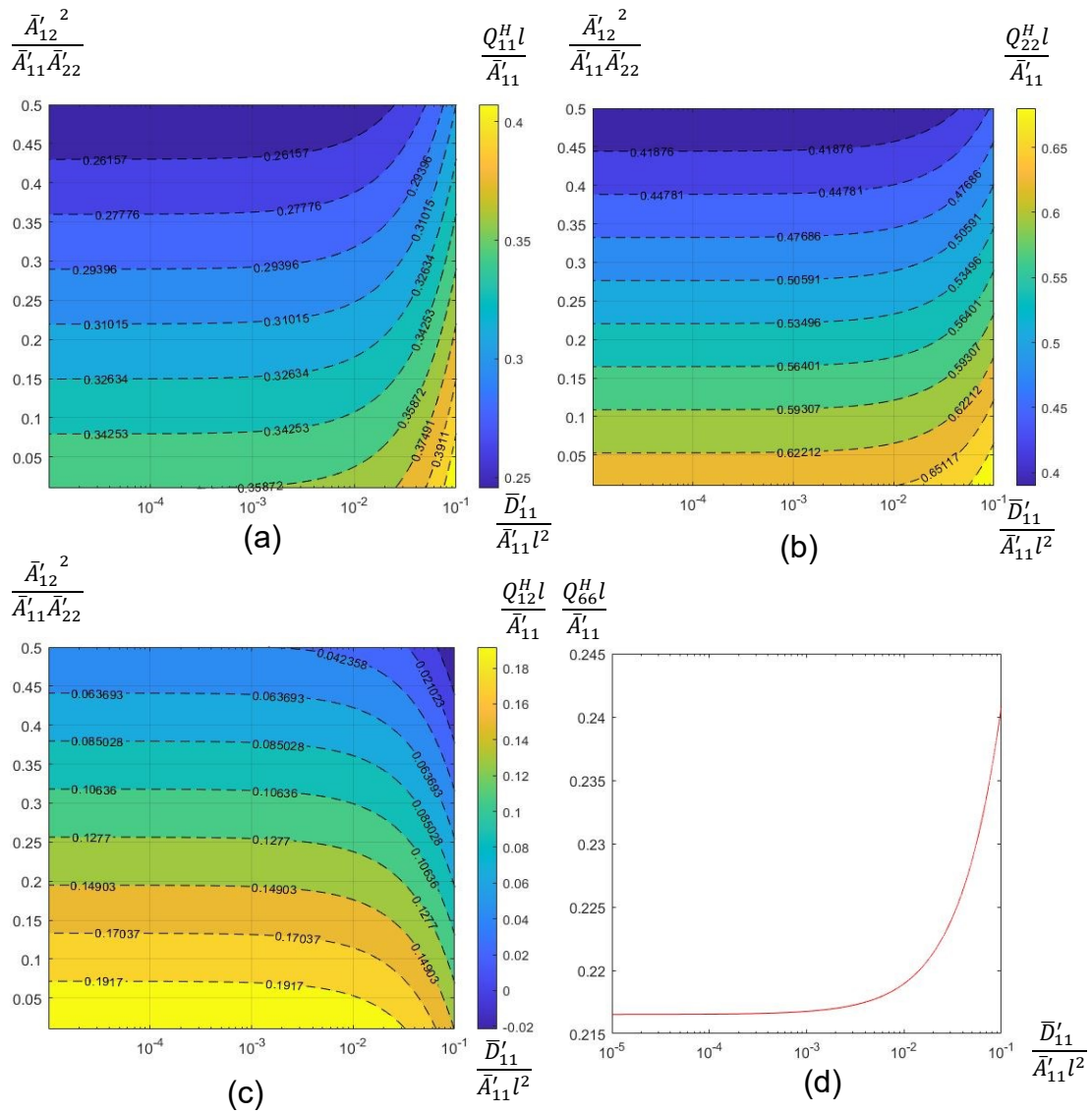


Fig. 3.18: Influence of wall stiffness parameters on (a) Q_{11}^H (b) Q_{22}^H (c) Q_{12}^H and (d) Q_{66}^H of the mixed rhombus-triangular core.

3.5 Conclusions

This chapter presented a new simplified approach to determine the effective stiffness properties of the laminated composite wall honeycomb cores, therefore providing a pathway for the designers to make better decisions on key design parameters such as honeycomb core shape and materials and layer sequences when designing honeycomb core sandwich panels to meet a desired performance. The effective stiffness values were determined by equating the strain energy of a RVE of the honeycomb core to the strain energy of an equivalent homogenised shell under the same resulting deformation for a given force.

The presented study shows that parameters such as layer sequence and fibre orientations would significantly influence the effective stiffness properties of the laminated composite honeycomb cores in addition to the core shapes. The proposed homogenisation model provides a significant advancement in the inverse design approach for the all-composite honeycomb core sandwich panels by allowing designers to consider key design parameters such as core shape, geometry, materials, and composite layer sequences and their interactions in determining optimal designs for the required performance. The proposed methodology breaks away the limitations in existing methodologies in terms of core shapes, materials and cell wall composite layer sequences and provides a unified approach to consider all the above in a single modelling approach.

To compare with existing methodologies for determining effective stiffness properties of the laminate composite wall hexagonal honeycomb core, an existing model developed based on a force-equilibrium approach for the hexagonal core with isotropic materials was also extended to determine effective stiffness properties for laminated composite hexagonal core (called modified-existing model). Predictions from the proposed model, modified-existing model, and other existing models were compared with finite element (FE) results of the hexagonal cores with different material configurations for the wall. Predictions from the proposed model were also compared with FE results for different honeycomb core shapes and cell wall composite layer sequences.

Comparisons showed that the proposed model provides accurate predictions for the effective stiffness properties of the laminated composite hexagonal core for

different composite wall layer sequences. A modified-existing model also gave good predictions for the hexagonal cores. Both models performed better than the other existing models. The proposed model also provided accurate predictions for different honeycomb core shapes. The proposed model, therefore, is superior to any other existing model in terms of its general applicability.

Simplified design plots were produced using the proposed model to calculate the effective properties of the honeycomb cores of different shapes. These plots are valuable in assisting the designers in determining the effective stiffness properties without having to go through a rigorous calculation process.

The primary purpose of calculating the effective stiffness matrix of the honeycomb core is to reduce the computation cost associated with the analysis of a 3D model of the sandwich panel with an actual discrete honeycomb core and to generalise the modelling of the sandwich panels. On the other hand, we should also have a reasonable accuracy of predictions for the responses using the equivalent models of the sandwich panels. The next chapter will investigate the modelling accuracy of the equivalent sandwich shell models using the effective stiffness values calculated for the honeycomb cores using the proposed homogenisation model.

References

- ABAQUS version 2021. Dassault Systemes Simulia Corporation. Providence, RI, USA.
- Balawi, S., & Abot, J. (2008). A refined model for the effective in-plane elastic moduli of hexagonal honeycombs. *Composite Structures*, 84(2), 147-158.
- Becker, W. (1998). The in-plane stiffnesses of a honeycomb core including the thickness effect. *Archive of Applied Mechanics*, 68(5), 334-341.
- Bishop, J., & Hill, R. (1951). XLVI. A theory of the plastic distortion of a polycrystalline aggregate under combined stresses. *The London, Edinburgh, and Dublin Philosophical Magazine and Journal of Science*, 42(327), 414-427.
- Catapano, A., & Montemurro, M. (2014). A multi-scale approach for the optimum design of sandwich plates with honeycomb core. Part I: homogenisation of core properties. *Composite Structures*, 118, 664-676.
- Chen, X., Yu, G., Wang, Z., Feng, L., & Wu, L. (2021). Enhancing out-of-plane compressive performance of carbon fiber composite honeycombs. *Composite Structures*, 255, 112984.
- Feng, Y., Qiu, H., Gao, Y., Zheng, H., & Tan, J. (2020). Creative design for sandwich structures: A review. *International Journal of Advanced Robotic Systems*, 17(3), 1729881420921327.
- Gibson, I., & Ashby, M. F. (1982). The mechanics of three-dimensional cellular materials. *Proceedings of the Royal Society of London. A. Mathematical and Physical Sciences*, 382(1782), 43-59.

- Grediac, M. (1993). A finite element study of the transverse shear in honeycomb cores. *International Journal of Solids and Structures*, 30(13), 1777-1788.
- Hohe, J., & Becker, W. (2001). An energetic homogenisation procedure for the elastic properties of general cellular sandwich cores. *Composites Part B: Engineering*, 32(3), 185-197.
- Hou, W., Shen, Y., Jiang, K., & Wang, C. (2022). Study on mechanical properties of carbon fiber honeycomb curved sandwich structure and its application in engine hood. *Composite Structures*, 286, 115302.
- Kollár, L., & Springer, G. (2003). Laminated Composites. In *Mechanics of Composite Structures* (pp. 63-88). Cambridge: Cambridge University Press.
- Krishnamurthy, T., & Saether, E. (2019). *Estimation of Effective Elastic Properties of General Multifunctional Honeycomb Structures Using a Unit Cell Method*. Paper presented at the AIAA Scitech 2019 Forum.
- Li, Y., Abbès, F., Hoang, M., Abbès, B., & Guo, Y. (2016). Analytical homogenization for in-plane shear, torsion and transverse shear of honeycomb core with skin and thickness effects. *Composite Structures*, 140, 453-462.
- Malek, S., & Gibson, L. (2015). Effective elastic properties of periodic hexagonal honeycombs. *Mechanics of Materials*, 91, 226-240.
- Masters, I., & Evans, K. (1996). Models for the elastic deformation of honeycombs. *Composite Structures*, 35(4), 403-422.
- MathWorks Inc. (2022). MATLAB version: 9.13.0 (R2022b), Natick, Massachusetts: The MathWorks Inc.
- Min, L., Fernando, D., Gilbert, B., & You, Z. (2020). Hybrid FRP-timber thin-walled Cee section columns under axial compression: Numerical modelling. *Thin-Walled Structures*, 157, 107029.
- Mukherjee, S., & Adhikari, S. (2021). A general analytical framework for the mechanics of heterogeneous hexagonal lattices. *Thin-Walled Structures*, 167, 108188.
- Pehlivan, L., & Baykasoğlu, C. (2019). An experimental study on the compressive response of CFRP honeycombs with various cell configurations. *Composites Part B: Engineering*, 162, 653-661.
- Russell, B., Deshpande, V., & Wadley, H. (2008). Quasistatic deformation and failure modes of composite square honeycombs. *Journal of mechanics of materials and structures*, 3(7), 1315-1340.
- Russell, B., Liu, T., Fleck, N., & Deshpande, V. (2011). Quasi-static three-point bending of carbon fiber sandwich beams with square honeycomb cores. *Journal of Applied Mechanics*, 78(3).
- Vlachoutsis, S. (1992). Shear correction factors for plates and shells. *International Journal for Numerical Methods in Engineering*, 33(7), 1537-1552.
- Wang, R., & Wang, J. (2018). Modeling of honeycombs with laminated composite cell walls. *Composite Structures*, 184, 191-197.
- Wei, X., Li, D., & Xiong, J. (2019). Fabrication and mechanical behaviors of an all-composite sandwich structure with a hexagon honeycomb core based on the tailor-folding approach. *Composites Science and Technology*, 184, 107878.
- Wei, X., Wang, Y., Xue, P., Zhang, T., Rouis, A., Xiao, W., & Xiong, J. (2022). Carbon Fiber Composite Honeycomb Structures and the Application for Satellite Antenna Reflector with High Precision. *Advances in Astronautics Science and Technology*, 5(4), 423-441. doi:10.1007/s42423-022-00133-5

- Wei, X., Wu, Q., Gao, Y., & Xiong, J. (2020). Bending characteristics of all-composite hexagon honeycomb sandwich beams: experimental tests and a three-dimensional failure mechanism map. *Mechanics of Materials*, 148, 103401.
- Xia, Z., Zhang, Y., & Ellyin, F. (2003). A unified periodical boundary conditions for representative volume elements of composites and applications. *International journal of solids and structures*, 40(8), 1907-1921.
- Xu, X. F., & Qiao, P. (2002). Homogenized elastic properties of honeycomb sandwich with skin effect. *International Journal of Solids and Structures*, 39(8), 2153-2188.
- Zhang, J., & Ashby, M. (1992). The out-of-plane properties of honeycombs. *International Journal of Mechanical Sciences*, 34(6), 475-489.

Chapter 4:

Equivalent model of the laminated composite honeycomb core sandwich panels

4.1 General

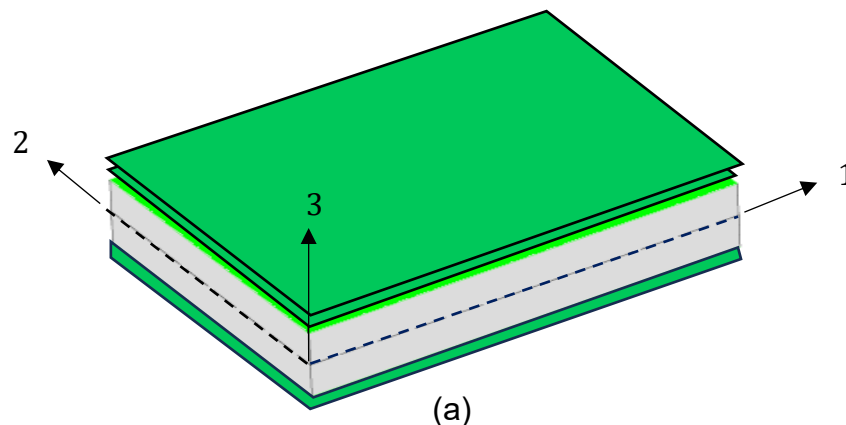
In Chapter 3, a homogenisation model was developed to predict the effective properties of the laminated composite honeycomb cellular cores. In this chapter, the effective stiffness properties of the cores are used to model the all-composite honeycomb core sandwich panels as equivalent models. Several plate and shell theories have been proposed to analyse sandwich panels as equivalent single-layer (Ferreira et al. 2005; Aydogdu 2009; Tounsi et al. 2013; Hamidi et al. 2015; Mahi and Tounsi 2015) and layer-wise (Plagianakos & Saravanos 2009; Mantari et al. 2012; Goswami & Becker 2016) models. Chapter 2 has reviewed several of those theories which differ based on their underlying assumptions, accuracy, and complexity in applications. Among the several plate theories, the classical laminate plate theory (CLT) and the first-order shear deformation theory (FSDT) are the most widely used theories for analysing composite and sandwich structures due to their computational efficiency while providing good accuracy. However, CLT has limited application for the analysis of sandwich structures due to its assumption that the cross-section remains plane and perpendicular to the reference surface after deformation, which essentially means that there are no transverse shear deformations. FSDT theory, which relaxes this assumption and considers transverse shear deformation, is often preferred in the analysis of sandwich structures because of its computational efficiency compared to higher-order theories and layer-wise theories and better accuracy in predictions compared to the CLT. Here, finite element (FE) analysis based on FSDT is used to model the sandwich panels as the equivalent single-layer plate together with effective core properties. Comparisons are being made for the predictions of the responses, such as maximum deflection and flexural stresses at the extreme plies of the face sheets under static bending and global buckling load under uniaxial compression from

the equivalent single-layer models and 3D models with actual core geometries. Also, the effects of different material configurations of the honeycomb cores on the responses of sandwich panels are evaluated. This chapter does not develop any new methodologies for the analysis using FSDT; however, comparisons between the 3D FE models of sandwich panels with actual discrete core and equivalent models based on FSDT are used to further validate the effective stiffness matrix predictions of the core and to investigate accuracy of equivalent models compared to 3D models in predicting the responses such as overall deflections and global buckling.

4.2 Equivalent model for the sandwich panels

Originally, FSDT was developed for homogeneous and isotropic thick plates by Reissner and Mindlin (Reissner 1945; Mindlin 1951). Later, several researchers (Allen 1969; Whitney 1987) extended the theory for the sandwich and composite plates and shells for theoretical analysis. As an analysis based on FSDT will be used later in this chapter, the FSDT for the sandwich panels is briefly outlined here.

Consider a section of a sandwich panel (Fig.4.1(b)) of thickness H consisting of lower and upper face sheets of thicknesses t_f^l and t_f^u respectively and a core of thickness h . The face sheets are considered to be laminated composite, and the core is represented as a homogeneous continuum based on the effective stiffness properties. It's assumed that there is a perfect bond between the face sheets and the core. The reference plane of the sandwich panel is assumed to be at the mid-height of the plate. The distance to the ply k from the reference plane is x_3^k .



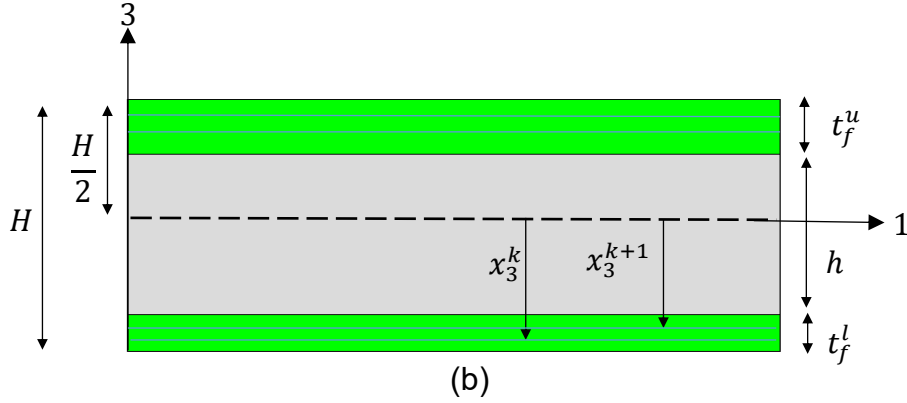


Fig.4.1: (a) A sandwich panel and (b) typical section across the 1-3 plane of the sandwich panel under consideration.

4.2.1 Displacement fields

The displacement fields of the sandwich panel according to FSDT (Fig.4.2) can be written as:

$$v_1(x_1, x_2, x_3) = v_1^o(x_1, x_2) + x_3\psi_1, \quad (4.1)$$

$$v_2(x_1, x_2, x_3) = v_2^o(x_1, x_2) + x_3\psi_2, \quad (4.2)$$

$$v_3(x_1, x_2, x_3) = v_3^o(x_1, x_2), \quad (4.3)$$

where v_1, v_2 and v_3 are the displacements at point (x_1, x_2, x_3) in 1, 2 and 3 directions respectively. v_1^o, v_2^o and v_3^o are the displacements at point (x_1, x_2) in the reference plane in 1, 2 and 3 directions respectively. ψ_1 and ψ_2 are the rotations of the cross sections originally perpendicular to axis-1 and axis-2 respectively.

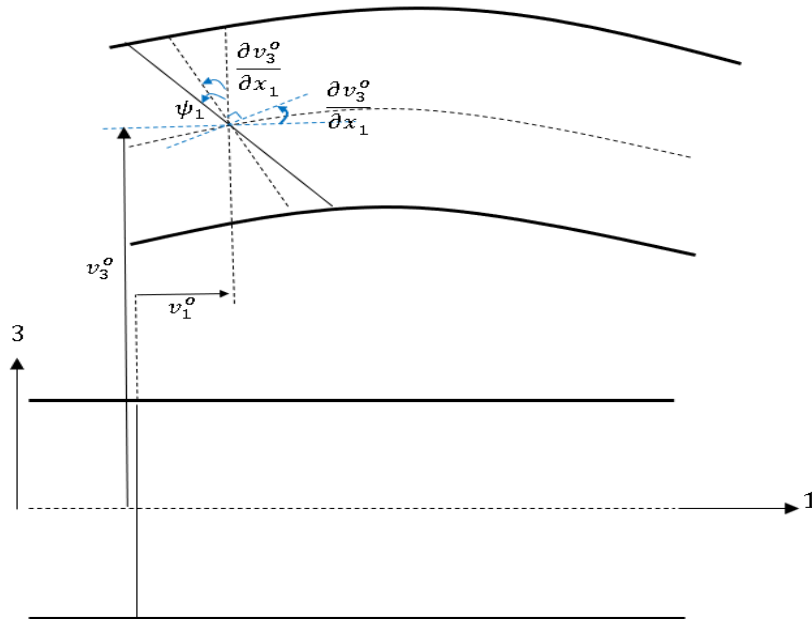


Fig.4.2: Illustration of deformation of the sandwich panel in 1-3 plane according to FSDT.

4.2.2 Stress and strain relationships

Using the displacement field defined in Eqs. (4.1) - (4.3), strains at a distance x_3 from the reference plane can be expressed as:

$$\varepsilon_{11} = \frac{\partial v_1}{\partial x_1} = \frac{\partial v_1^0}{\partial x_1} - x_3 \frac{\partial \psi_1}{\partial x_1}, \quad (4.4)$$

$$\varepsilon_{11} = \frac{\partial v_1}{\partial x_1} = \varepsilon_{11}^0 + x_3 k_{11}, \quad (4.5)$$

$$\varepsilon_{22} = \frac{\partial v_2}{\partial x_2} = \frac{\partial v_2^0}{\partial x_2} - x_3 \frac{\partial \psi_2}{\partial x_2}, \quad (4.6)$$

$$\varepsilon_{22} = \frac{\partial v_2}{\partial x_2} = \varepsilon_{22}^0 + x_3 k_{22}, \quad (4.7)$$

$$\gamma_{12} = \frac{\partial v_1}{\partial x_2} + \frac{\partial v_2}{\partial x_1} = \left(\frac{\partial v_1^0}{\partial x_2} + \frac{\partial v_2^0}{\partial x_1} \right) - x_3 \left(\frac{\partial \psi_1}{\partial x_2} + \frac{\partial \psi_2}{\partial x_1} \right), \quad (4.8)$$

$$\gamma_{12} = \gamma_{12}^0 + x_3 k_{12}, \quad (4.9)$$

$$\gamma_{13} = \psi_1 - \frac{\partial v_3^0}{\partial x_1}, \quad (4.10)$$

$$\gamma_{23} = \psi_2 - \frac{\partial v_3^0}{\partial x_2}, \quad (4.11)$$

where ε_{22} and ε_{11} are the in-plane normal strains and γ_{12} is in-plane shear strains at point (x_1, x_2, x_3) , γ_{13} and γ_{23} are the out-of-plane shear strains at point (x_1, x_2, x_3) , ε_{11}^0 and ε_{22}^0 are the in-plane normal strains at point (x_1, x_2) in the reference plane, k_{11} and k_{22} are the bending moments curvatures, and k_{12} is the twisting moment curvature. The relationship between the in-plane stresses and strains at point (x_1, x_2, x_3) of a ply- k can be written as:

$$\begin{Bmatrix} \sigma_{11}^k \\ \sigma_{22}^k \\ \tau_{12}^k \end{Bmatrix} = \begin{bmatrix} Q_{11}^k & Q_{12}^k & Q_{16}^k \\ Q_{12}^k & Q_{22}^k & Q_{26}^k \\ Q_{16}^k & Q_{26}^k & Q_{66}^k \end{bmatrix} \begin{Bmatrix} \varepsilon_{11}^k \\ \varepsilon_{22}^k \\ \gamma_{12}^k \end{Bmatrix}, \quad (4.12)$$

where Q_{ij}^k are elements of the transformed in-plane material stiffness matrix, σ_{11}^k and σ_{22}^k are the in-plane normal stresses in direction 1 and 2 respectively and τ_{12}^k is in-plane shear stress of k^{th} ply in the global coordinates system. The transverse shear stresses and strains (Eqs. 4.10 - 4.11) are assumed to be constant across the thickness of the sandwich panel and the transverse shear stresses and strains are

related using an equivalent transverse stiffness matrix calculated according to the methodology given in section 4.2.4. as:

$$\begin{Bmatrix} \tau_{13} \\ \tau_{23} \end{Bmatrix} = \begin{bmatrix} Q_{44}^E & Q_{45}^E \\ Q_{45}^E & Q_{55}^E \end{bmatrix} \begin{Bmatrix} \gamma_{13} \\ \gamma_{23} \end{Bmatrix}, \quad (4.13)$$

Q_{ij}^E are the equivalent transverse shear stiffness of the sandwich panel. Combining Eq. (4.12) and (4.13), following equation can be obtained:

$$\begin{Bmatrix} \sigma_p \\ \tau_s \end{Bmatrix} = \begin{bmatrix} Q_p & 0 \\ 0 & Q_s \end{bmatrix} \begin{Bmatrix} \varepsilon_p \\ \gamma_s \end{Bmatrix}, \quad (4.14)$$

where;

$$\sigma_p = \begin{Bmatrix} \sigma_{11}^k \\ \sigma_{22}^k \\ \tau_{12}^k \end{Bmatrix}, \quad (4.15)$$

$$\tau_s = \begin{Bmatrix} \tau_{13} \\ \tau_{23} \end{Bmatrix}, \quad (4.16)$$

$$\varepsilon_p = \begin{Bmatrix} \varepsilon_{11} \\ \varepsilon_{22} \\ \gamma_{12} \end{Bmatrix}, \quad (4.17)$$

$$\gamma_s = \begin{Bmatrix} \gamma_{13} \\ \gamma_{23} \end{Bmatrix}, \quad (4.18)$$

$$Q_p = \begin{bmatrix} Q_{11}^k & Q_{12}^k & Q_{16}^k \\ Q_{12}^k & Q_{22}^k & Q_{26}^k \\ Q_{16}^k & Q_{26}^k & Q_{66}^k \end{bmatrix}, \quad (4.19)$$

$$\text{and } Q_s = \begin{bmatrix} Q_{44}^E & Q_{45}^E \\ Q_{45}^E & Q_{55}^E \end{bmatrix}, \quad (4.20)$$

4.2.3 Stress resultants

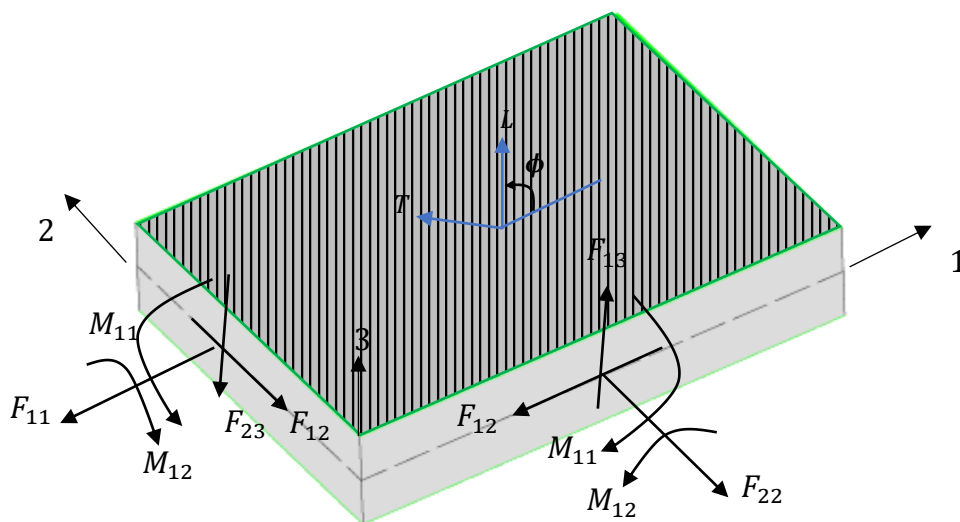


Fig.4.3: Forces and moments acting on the sandwich panel.

Forces and moments due to the stress resultants of the sandwich panel in Fig. 4.3 can be written as in Eq. (4.21) to (4.23) using the stress-strain relationships defined in Eq. (4.14).

$$\mathbf{F}_p = \int_{-\frac{H}{2}}^{\frac{H}{2}} \boldsymbol{\sigma}_p dx_3, \quad (4.21)$$

$$\mathbf{M}_p = \int_{-\frac{H}{2}}^{\frac{H}{2}} x_3 \boldsymbol{\sigma}_p dx_3, \quad (4.22)$$

and

$$\mathbf{F}_s = \int_{-\frac{H}{2}}^{\frac{H}{2}} \boldsymbol{\tau}_s dx_3, \quad (4.23)$$

where \mathbf{F}_p , \mathbf{M}_p and \mathbf{F}_s are the vector of in-plane forces, the moments, and the transverse shear forces of unit length respectively. They can be written as:

$$\mathbf{F}_p = \begin{Bmatrix} F_{11} \\ F_{22} \\ F_{12} \end{Bmatrix}, \quad (4.24) \quad \mathbf{M}_p = \begin{Bmatrix} M_{11} \\ M_{22} \\ M_{12} \end{Bmatrix}, \quad (4.25) \quad \text{and} \quad \mathbf{F}_s = \begin{Bmatrix} F_{13} \\ F_{23} \end{Bmatrix}. \quad (4.26)$$

Using the definition in Eq. (4.21) to Eq. (4.23), force resultants can be expressed in terms of the resultant section stiffness, strain vector, and curvature vector as:

$$\begin{Bmatrix} \mathbf{F}_p \\ \mathbf{M}_p \\ \mathbf{F}_s \end{Bmatrix} = \begin{bmatrix} \mathbf{A} & \mathbf{B} & \mathbf{0} \\ \mathbf{B} & \mathbf{D} & \mathbf{0} \\ \mathbf{0} & \mathbf{0} & \mathbf{S} \end{bmatrix} \begin{Bmatrix} \boldsymbol{\varepsilon}_p^0 \\ \mathbf{k} \\ \boldsymbol{\gamma}_s \end{Bmatrix}, \quad (4.27)$$

where;

$$\boldsymbol{\varepsilon}_p^0 = \begin{Bmatrix} \varepsilon_{11}^0 \\ \varepsilon_{22}^0 \\ \varepsilon_{12}^0 \end{Bmatrix}, \quad (4.28) \quad \mathbf{k} = \begin{Bmatrix} k_{11} \\ k_{22} \\ k_{12} \end{Bmatrix}, \quad (4.29)$$

$$\mathbf{A} = \int_z \mathbf{Q}_p dz = \sum_{k=1}^n \mathbf{Q}_p (x_3^{k+1} - x_3^k), \quad (4.30)$$

$$\mathbf{B} = \int_z z \mathbf{Q}_p dz = \frac{1}{2} \sum_{k=1}^n \mathbf{Q}_p [(x_3^{k+1})^2 - (x_3^k)^2], \quad (4.31)$$

$$\mathbf{D} = \int_z z^2 \mathbf{Q}_p dz = \frac{1}{3} \sum_{k=1}^n \mathbf{Q}_p [(x_3^{k+1})^3 - (x_3^k)^3], \quad (4.32)$$

and

$$S = HQ_s. \quad (4.33)$$

4.2.4 Equivalent transverse shear stiffness

In order to apply the FSDT to analyse the sandwich panels, it is essential to accurately estimate the equivalent transverse shear stiffness. In the case of a plate with homogenous isotropic material which has parabolic shear strain distribution (Fig 4.4(a)), a unique shear correction factor of $5/6$ has been commonly used to calculate the equivalent transverse shear stiffness (Timoshenko & Woinowsky 1959). However, in the case of a sandwich panel, based on combination of materials and the thickness of each layer, different discontinuities in the shear strain gradient may exist (Fig. 4.4(b)), which could result in different effective shear correction factors (Carlsson & Kardomateas 2011). Several studies have been carried out to propose the shear correction factor for FSDT of sandwich panels (Vlachoutsis 1992; Birman & Bert 2002; Huang & Kardomateas 2002; Hadaviniai et al. 2006; Vrabie, Chiriac & Băetu 2017). Researchers have used different approaches and assumptions to calculate the shear correction factor of the sandwich panels. Birman & Bert (2002) reviewed the different methodologies to calculate the equivalent transverse shear stiffness of the sandwich panels and recommended the use of shear correction factor of 1 as an initial approximation considering, only the transverse shear stiffness of the core. However, the accuracy of the result is compromised when the face sheets are moderately thick and core becomes stiff (Carlsson & Kardomateas 2011). Vlachoutis (1992) proposed a methodology to estimate the shear correction factor for a sandwich and composite plates based on the principle of equivalent shear strain energy of actual structure and equivalent structure under cylindrical bending. The methodology used in ABAQUS (version 2021) (briefly presented in this section below) is also based on the same principle; however, both differ in the following:

- In the methodology used in ABAQUS, the in-plane normal stress is defined using the elements of the compliance matrix of the section (Eq 4.36), whereas Vlachoutis (1992) considered only dominant bending stiffness term of the section to define in-plane normal stress.

- The neutral surface for the bending is defined such that the dominant membrane and bending coupling stiffness term becomes zero in Vlachoutis (1992). However, the methodology in ABAQUS applies shear stress boundary conditions (shear stress at top and bottom fibre should be zero and shear stress at the interface between adjacent plies should be equal) to find the position of the reference surface.

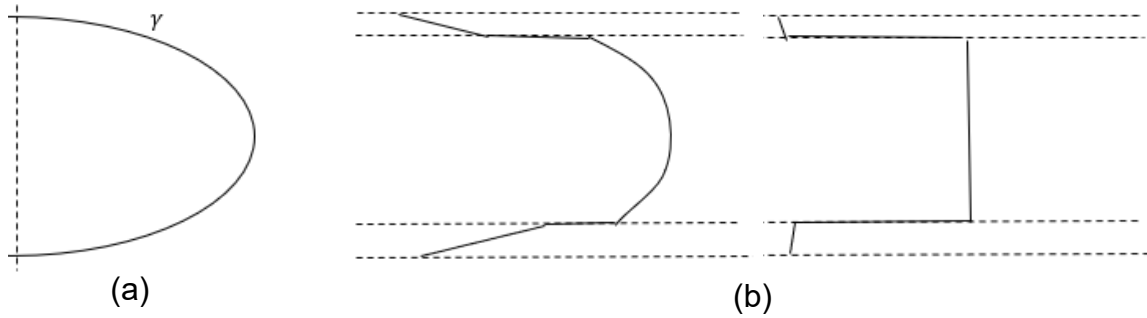


Fig.4.4: Typical transverse shear strain variation in (a) homogenous isotropic plate and (b) sandwich panels.

Here ABAQUS is used for FE analysis and the methodology adopted in the ABAQUS to calculate the equivalent transverse shear stiffness is presented below. Consider a sandwich panel in Fig. 4.3, only under a cylindrical bending moment $M_{11} \neq 0$ and transverse shear $F_{13} \neq 0$ without gradient in the direction-2. All the other forces and moments are assumed to be zero: $F_{11} = F_{22} = F_{12} = 0$, $M_{22} = M_{12} = 0$ and the derivatives with respect to x_2 are assumed to be zero for all the response variables. Although this is not true for asymmetric panels, it is used as a simplifying assumption to obtain the equivalent transverse shear stiffness. Under the assumptions above, the stress equilibrium within the section in the direction-1 can be written as:

$$\frac{\partial \sigma_{11}}{\partial x_1} + \frac{\partial \tau_{13}}{\partial x_3} = 0. \quad (4.34)$$

From the moment equilibrium about the axis-2, we can write:

$$F_{13} + \frac{\partial M_{11}}{\partial x_1} = 0. \quad (4.35)$$

For linear elastic condition, in plane stress σ_{11} in the k^{th} layer can be written as:

$$\begin{aligned} \sigma_{11}^k = & Q_{11}^k(\varepsilon_{11}^0 + (x_3 - x_3^0)k_{11}) + Q_{12}^k(\varepsilon_{22}^0 + (x_3 - x_3^0)k_{22}) + \\ & Q_{16}^k(\varepsilon_{12}^0 + (x_3 - x_3^0)k_{12}), \end{aligned} \quad (4.36)$$

where the reference surface is considered at unknown distance x_3^0 from the mid-plane for the calculation of equivalent transverse shear stiffness.

The bending moment M_{11} and in-plane strains and curvature in Eq. (4.36) can be related using the elements of compliance matrix as:

$$\begin{Bmatrix} \varepsilon_{11}^0 \\ \varepsilon_{22}^0 \\ \varepsilon_{12}^0 \\ k_{11} \\ k_{22} \\ k_{12} \end{Bmatrix} = \begin{Bmatrix} b_{11} \\ b_{21} \\ b_{61} \\ d_{11} \\ d_{21} \\ d_{16} \end{Bmatrix} M_{11}. \quad (4.37)$$

The compliance matrix can be obtained by inverting section stiffness matrix as given in Eq. (4.38):

$$ABD^{-1} = \begin{bmatrix} a_{11} & a_{12} & a_{16} & b_{11} & b_{12} & b_{16} \\ a_{21} & a_{22} & a_{26} & b_{21} & b_{22} & b_{26} \\ a_{31} & a_{32} & a_{66} & b_{31} & b_{32} & b_{66} \\ b_{11} & b_{12} & b_{16} & d_{11} & d_{12} & d_{16} \\ b_{21} & b_{22} & b_{26} & d_{21} & d_{22} & d_{26} \\ b_{31} & b_{32} & b_{66} & d_{31} & d_{32} & d_{66} \end{bmatrix}. \quad (4.38)$$

Substituting Eq. (4.37) into Eq. (4.36):

$$\sigma_{11} = (B_1^k + (x_3 - x_3^0)B_2^k)M_{11}, \quad (4.39)$$

where;

$$B_1^k = Q_{11}^k b_{11} + Q_{12}^k b_{21} + Q_{16}^k b_{61}. \quad (4.40)$$

$$B_2^k = Q_{11}^k d_{11} + Q_{12}^k d_{21} + Q_{16}^k d_{16}. \quad (4.41)$$

Substituting the σ_{11} in Eq. (4.34) with Eq. (4.39), yields Eq. (4.42) which describes the relationship between the transverse shear stress through the thickness of the plate and resultant shear force in the section.

$$\frac{\partial \tau_{13}}{\partial z} = (B_1^k + (x_3 - x_3^0) B_2^k) F_{13} \quad (4.42)$$

Integrating Eq. (4.42) through the plate thickness and applying the boundary conditions ($\tau_{13} = 0$ at top and bottom of the panel and $\tau_{13}^k = \tau_{13}^{k+1}$) give the transverse shear stress distribution in ply k:

$$\tau_{13}^k = \left[B_1^k (x_3 - x_3^0) + \left(\frac{1}{2} \left((x_3)^2 - (x_3^k)^2 \right) - x_3^0 (x_3 - x_3^k) \right) B_2^k + B_0^k \right] F_{13}, \quad (4.43)$$

and the distance to the reference plane can be found as:

$$x_3^0 = \frac{\sum_{k=1}^n (x_3^{k+1} - x_3^k) \left[\frac{1}{2} (x_3^{k+1} + x_3^k) B_2^k - B_1^k \right]}{\sum_{k=1}^n (x_3^{k+1} - x_3^k) \left[\frac{1}{2} (x_3^{k+1} + x_3^k) B_2^k - B_1^k \right] B_2^k} \quad (4.44)$$

where;

$$B_0^k = \sum_{i=1}^{k-1} (x_3^{i+1} - x_3^i) \left[B_1^i - \left(\frac{1}{2} (x_3^{i+1} + x_3^i) - x_3^0 \right) B_2^i \right]. \quad (4.45)$$

Similar procedure can be followed to obtain the equation for shear stress distribution τ_{23} through the plate thickness. The equivalent transverse shear stiffness of the section can be obtained by matching the total transverse shear strain energy of each ply using the shear stress distribution in Eq. (4.43) to the total transverse shear energy of the equivalent section:

$$\frac{1}{2H} \{F_{13} \quad F_{23}\} \begin{bmatrix} Q_{44}^E & Q_{45}^E \\ Q_{45}^E & Q_{55}^E \end{bmatrix}^{-1} \begin{Bmatrix} F_{13} \\ F_{23} \end{Bmatrix} = \frac{1}{2} \sum_{k=1}^N \int_{x_3^k}^{x_3^{k+1}} \{ \tau_{13}^k \quad \tau_{23}^k \} \begin{bmatrix} Q_{44}^k & Q_{45}^k \\ Q_{45}^k & Q_{55}^k \end{bmatrix}^{-1} \begin{Bmatrix} \tau_{13}^k \\ \tau_{23}^k \end{Bmatrix} dx_3 \quad (4.46)$$

4.3 Analysis of the sandwich panels

The sandwich panels are analysed using equivalent plate models with homogenised core and 3D models with actual discrete core geometry using ABAQUS software. The effective stiffness properties of the hexagonal honeycomb core used in the analysis are derived using the strain energy-based homogenisation approach presented in Chapter 3. The dimensions and core density of the hexagonal core used in this analysis are the same as in section 3.4.2. The material configurations of the honeycomb core defined in Tables 3.1 and 3.2 are again considered here. However, only the first 6 combinations of material lay-ups in Table 3.2 are considered for the analysis. Equivalent models of the sandwich panels are analysed using the composite shell section feature available in the ABAQUS. ABAQUS provides a number of different shell elements to model the thick shell according to FSDT. S8R element (8-node thick shell element with reduced integration) with an element size of 50mm was selected after a convergence study.

3D FE models of the sandwich panels considering actual hexagonal core geometry and two separate face sheets are used to validate the predictions of the simplified modelling technique of the sandwich panels using the equivalent models. Both the face sheets and core structures are modelled separately using composite shell sections and then assembled using tie constraints between the core and the face sheets. All the components of 3D models are modelled using the S4 shell element (4 node general purpose shell element) with an element size of 25mm after a convergence study. The fibre orientations of each ply are defined with respect to positive axis-1 for the face sheets and positive local axis- $\bar{1}$ of the core walls following the sign convention (counterclockwise positive angle). The total thickness of the sandwich panels (H) is 160mm, thickness of the core (h) is 150mm, and the thicknesses t_f^u and t_f^l of both upper and lower face sheets are equal. Face sheets have symmetric fibre sequence arrangement of [0/90/0/90/0], and each ply has equal thickness. The material properties of Carbon/Epoxy lamina of face sheets with respect to its principal axes are defined as:

$E_L = 131000MPa$, $E_T = 10300MPa$, $\nu_{LT} = 0.22$ and $G_{TL} = 6900MPa$, and the transverse shear moduli of the material are assumed to be equal to the in-plane shear modulus in the modelling. Multiple examples are considered for linear static bending and global buckling analysis of sandwich panels using equivalent models and 3D

models. The results from the equivalent models are compared with the results from the 3D models of the sandwich panels with actual core geometry.

4.3.1 Analysis for linear static bending of sandwich panels

First, simply-supported and cantilever sandwich panels under bending are considered for the analysis. The Fig. 4.5(a) shows a simply-supported sandwich panel with length of 2m and width of 1m. A uniform transverse load of $1MPa$ is applied on the upper face sheet and the sandwich panel is simply-supported at two opposite edges as shown in Fig. 4.5. The sandwich plate has length of 2m and width of 1m. The Fig. 4.4(b) shows the cantilever sandwich panel with dimensions of $1m \times 1m$. A uniform transverse load of $100N/mm$ is applied along edges at the one end of the panel and opposite end is clamped.

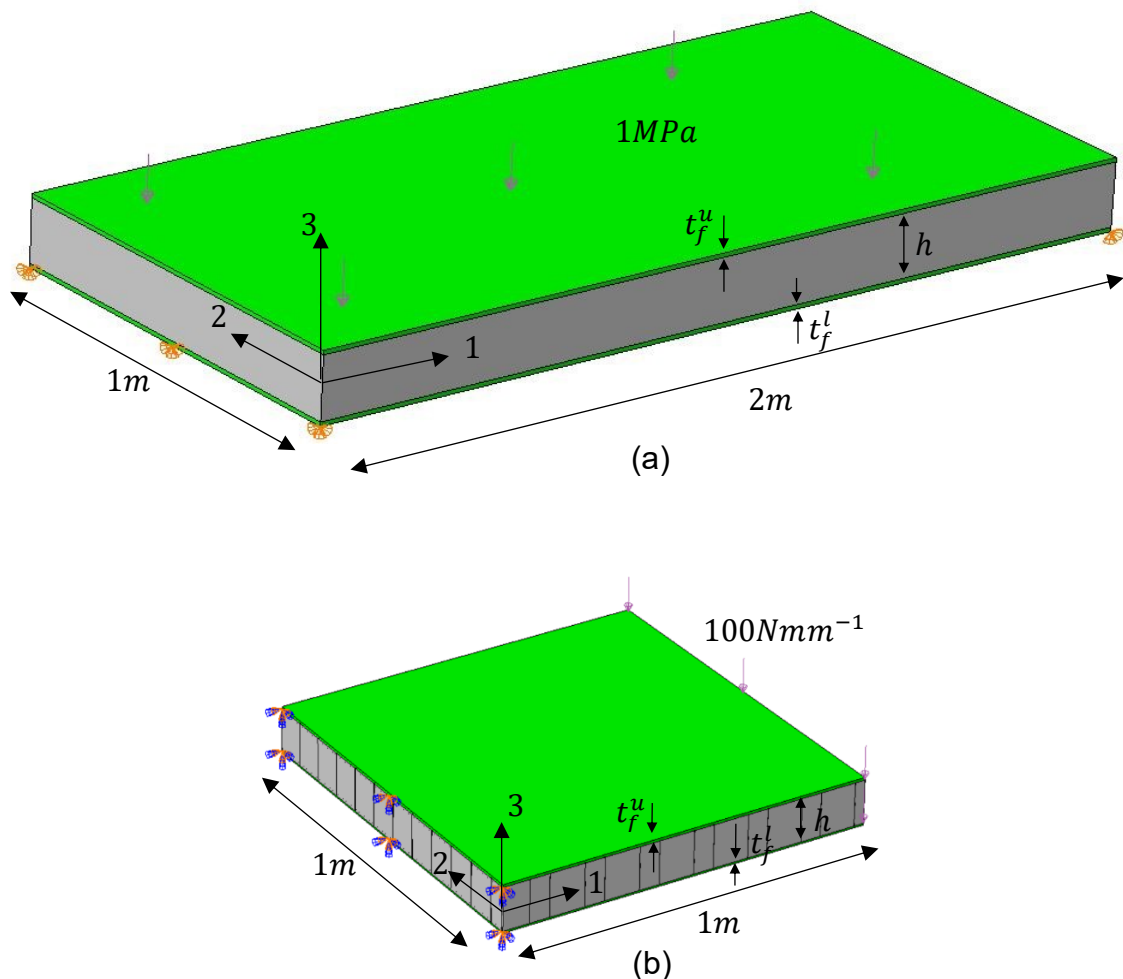


Fig.4.5: (a) Simply-supported and (b) cantilever sandwich panels considered for the analysis.

Results are obtained for the displacement in 3-direction (v_3) and in-plane normal stress (σ_{11}) along the mid-line of the sandwich panels normal to axis-2. For the equivalent models, the displacement v_3 is obtained at the reference surface as there is no through-thickness variation considered in theory, and for the 3D models, the displacement v_3 is obtained at the upper and lower surface of face sheets (Fig. 4.6 & Fig. 4.7). The displacements from both equivalent models and 3D models for the simply-supported and cantilever sandwich panels with honeycomb core having different fibre lay-ups (Table 3.2) are plotted and shown in Fig. 4.8 and Fig. 4.9. Comparisons of the maximum displacement along the mid-line are given in Table 4.1 and Table 4.2 for the simply-supported and cantilever panels respectively. The in-plane normal stress σ_{11} values are obtained at the uppermost ply and bottommost ply of the face sheets of both 3D models and equivalent models to get the variation of the compressive and tensile stress (Fig. 4.10 & Fig. 4.12). The plots for the comparisons of stresses along the length from the equivalent models and 3D models of simply-supported and cantilever sandwich panels are given in Fig. 4.11 and Fig. 4.13, respectively.

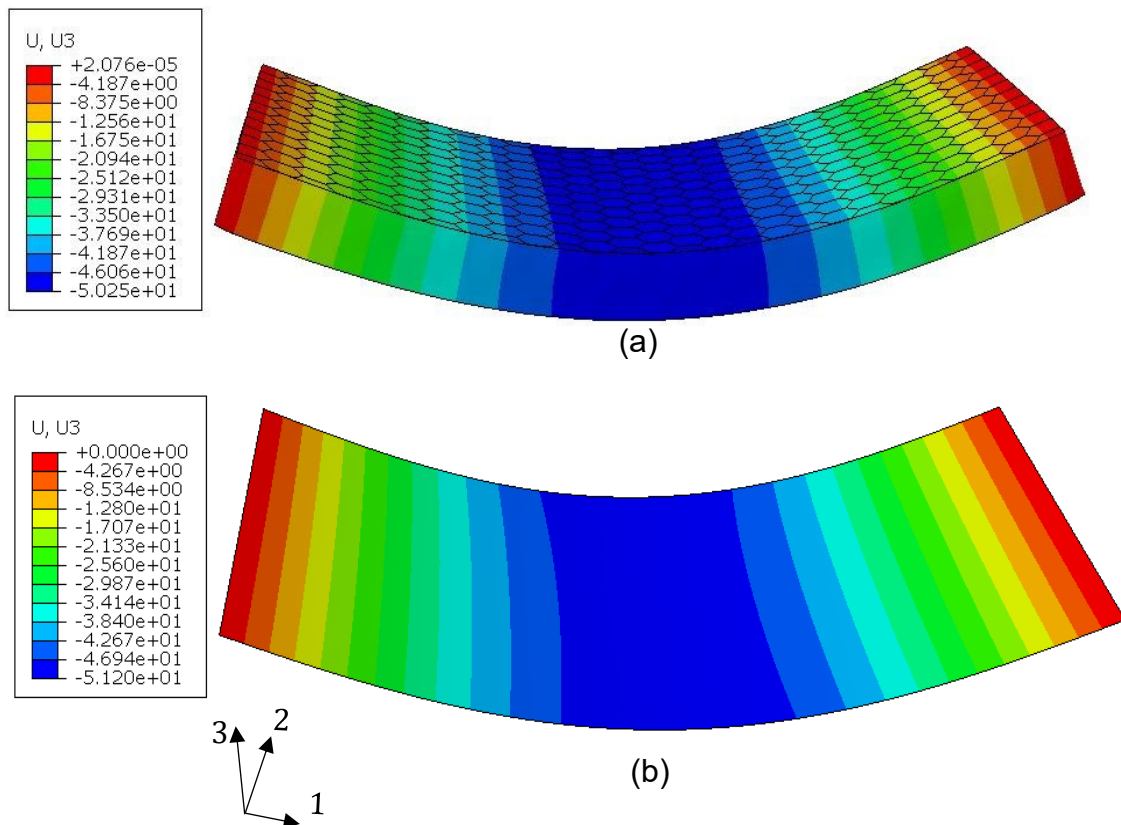


Fig.4.6: Contour maps of the displacement of (a) 3D model and (b) equivalent model of the simply-supported sandwich panel having hexagonal core of fibre lay-up [45/-45/0/-45/45].

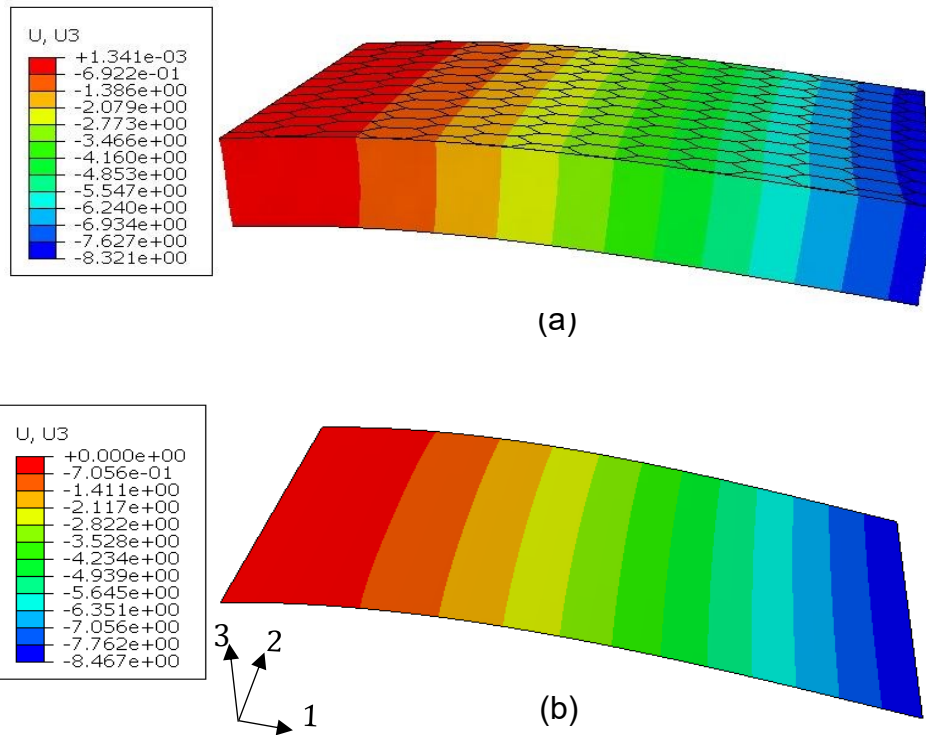


Fig.4.7: Contour maps of the displacement of (a) 3D model and (b) equivalent model of the cantilever sandwich panel having hexagonal core of fibre lay-up [45/-45/0/-45/45].

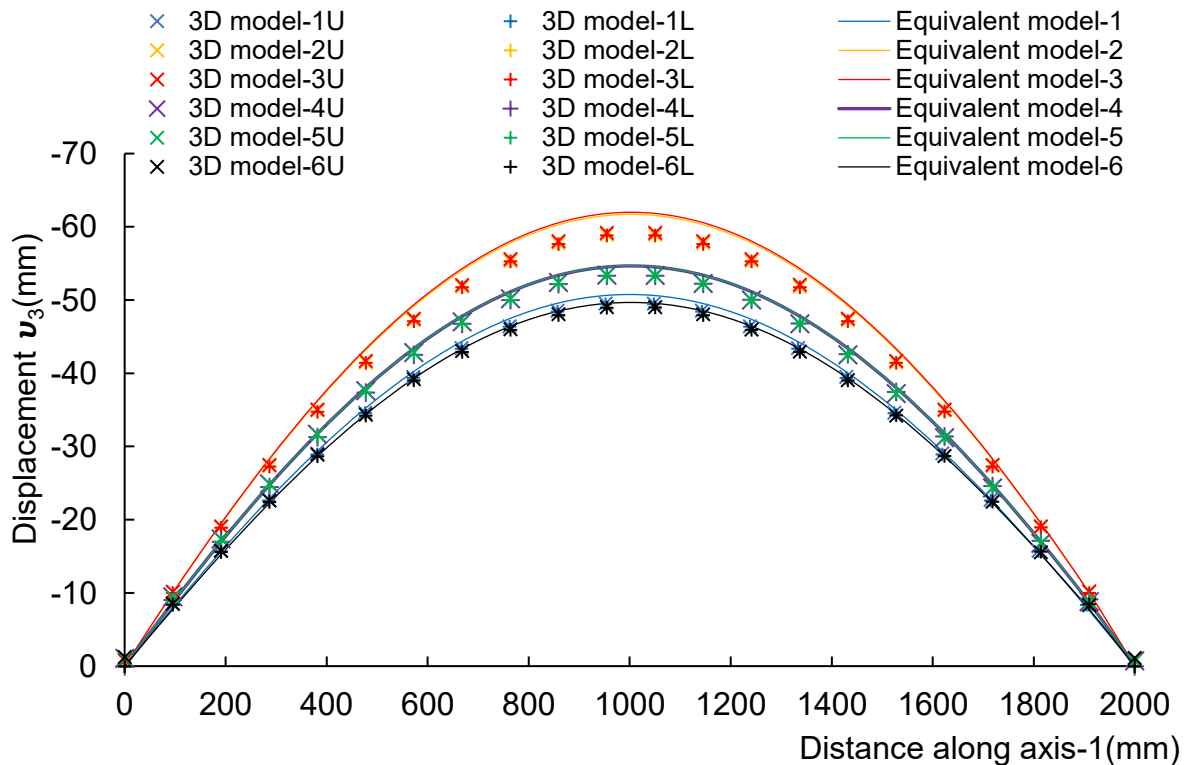


Fig.4.8: Comparison of displacement of 3D models and equivalent models of the simply-supported sandwich panels having hexagonal core of different fibre lay-up. The displacement for the 3D models were obtained at upper (U) and lower (L) face sheets.

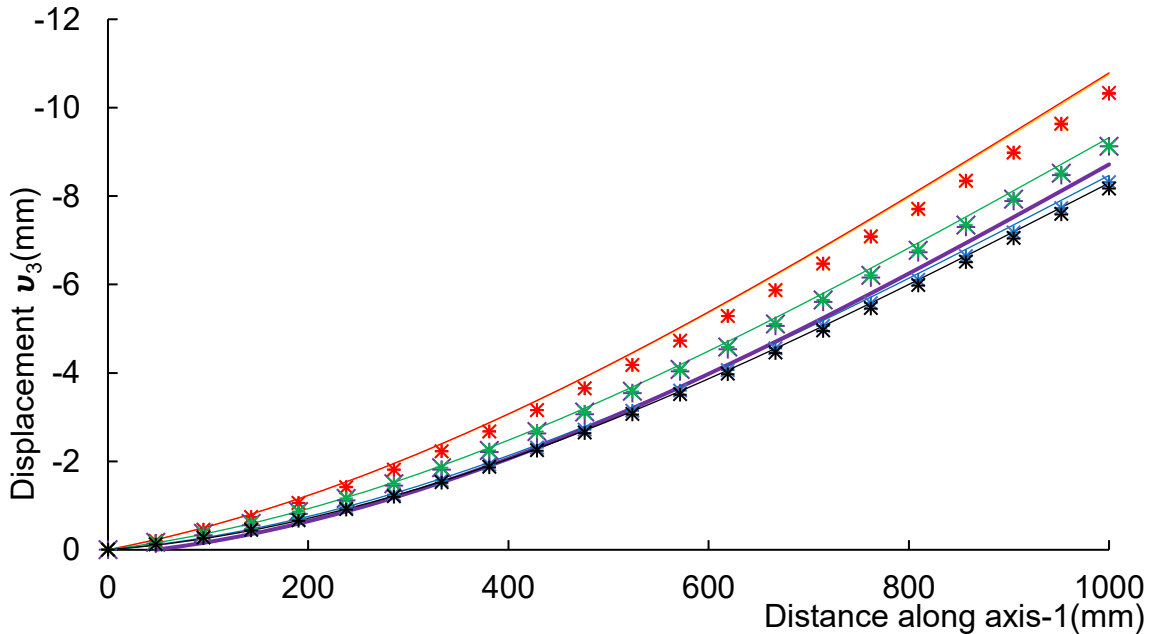


Fig.4.9: Comparison of displacement of 3D models and equivalent models of the cantilever sandwich panels having hexagonal core of different fibre lay-up. The displacement for the 3D models were obtained at upper (U) and lower (L) face sheets.

The displacements from the equivalent models showed good agreement with the displacements from the 3D models along the length for both simply-supported (Fig. 4.8) and cantilever (Fig. 4.9) sandwich panels. For all the different cases analysed, the displacements from the equivalent models are slightly higher than those from the 3D models. The maximum errors for the maximum displacement of sandwich panels having different material configurations of the core are 4.58% and 4.37% for simply-supported (Table 4.1) and cantilever (Table 4.2) sandwich panels, respectively. In both simply-supported and cantilever conditions, the change in fibre lay-up of the core walls significantly affects the displacement of the panels. As the core is mainly contributing to carry the transverse shear in the panels, the cores with the higher effective transverse shear stiffness show lower displacements compared with the cores with lower effective transverse shear stiffness. The sandwich panels having the core with fibre lay-up [45/-45/45/-45/45] give the lowest maximum displacements, which are

16.4% and 19.59% lower than the maximum displacements of sandwich panels consisting of the core with the fibre lay-up [90/0/0/0/90] for simply-supported and cantilever conditions respectively according to the 3D models. For the same cases, the equivalent models predicted 19.15% and 22.45% lower maximum displacements for the sandwich panels consisting of the core with fibre lay-up [45/-45/45/-45/45] than the sandwich panels consisting of the core with fibre lay-up [90/0/0/0/90]. The maximum displacements of sandwich panels consisting of the cores, which have the same effective transverse shear stiffness but different in-plane stiffness (E.g. fibre lay-ups 2 & 3), differ by less than 1% in both 3D and equivalent models. In general, the sandwich panels consisting of the cores with a higher percentage of angle-ply give lower displacement in comparison to the sandwich panels consisting of the cores with cross-ply due to the reason that the angle-ply laminate which has the higher in-plane shear stiffness than cross-ply laminate would positively affect the effective transverse shear stiffness of the cores. While the FSDT-based equivalent models cannot predict the variation of the displacement across the depth of the sandwich panels, the predictions from the 3D models at the lower and upper surface are almost equal mainly because of the high out-of-plane normal stiffness of the honeycombs, which makes the panel stiff in out-of-plane normal direction. This also implies that using the higher order theories, which take into account the variation of the out-of-plane normal displacement across the depth of sandwich panels, may not significantly improve the accuracy of the predictions for the displacements of honeycomb core sandwich panels. Overall, the predictions of the displacements based on the equivalent models, together with the effective stiffness properties of the core, are reasonably accurate and consistent with the predictions from 3D models.

Table 4.1: Comparison of normalised maximum displacements of simply-supported sandwich panels.

Material lay-up	Normalised maximum displacement		$\frac{(b - a)}{a}$ %
	3D model (Lower face sheet) (a)	Equivalent model (b)	
1	83.60	85.38	2.14
2	99.50	104.06	4.58
3	100.00	104.53	4.53
4	90.15	92.18	2.25
5	90.15	92.23	2.31

6	48.97	49.54	1.16
---	-------	-------	------

Table 4.2: Comparison of normalised maximum displacements of cantilever sandwich panels.

Material lay-up	Normalised maximum displacement		$\frac{(b - a)}{a} \%$
	3D model (Lower face sheet) (a)	Equivalent model (b)	
1	80.41	81.92	1.88
2	99.80	104.04	4.25
3	100.00	104.37	4.37
4	88.24	90.13	2.14
5	88.23	90.18	2.21
6	79.03	80.26	1.55

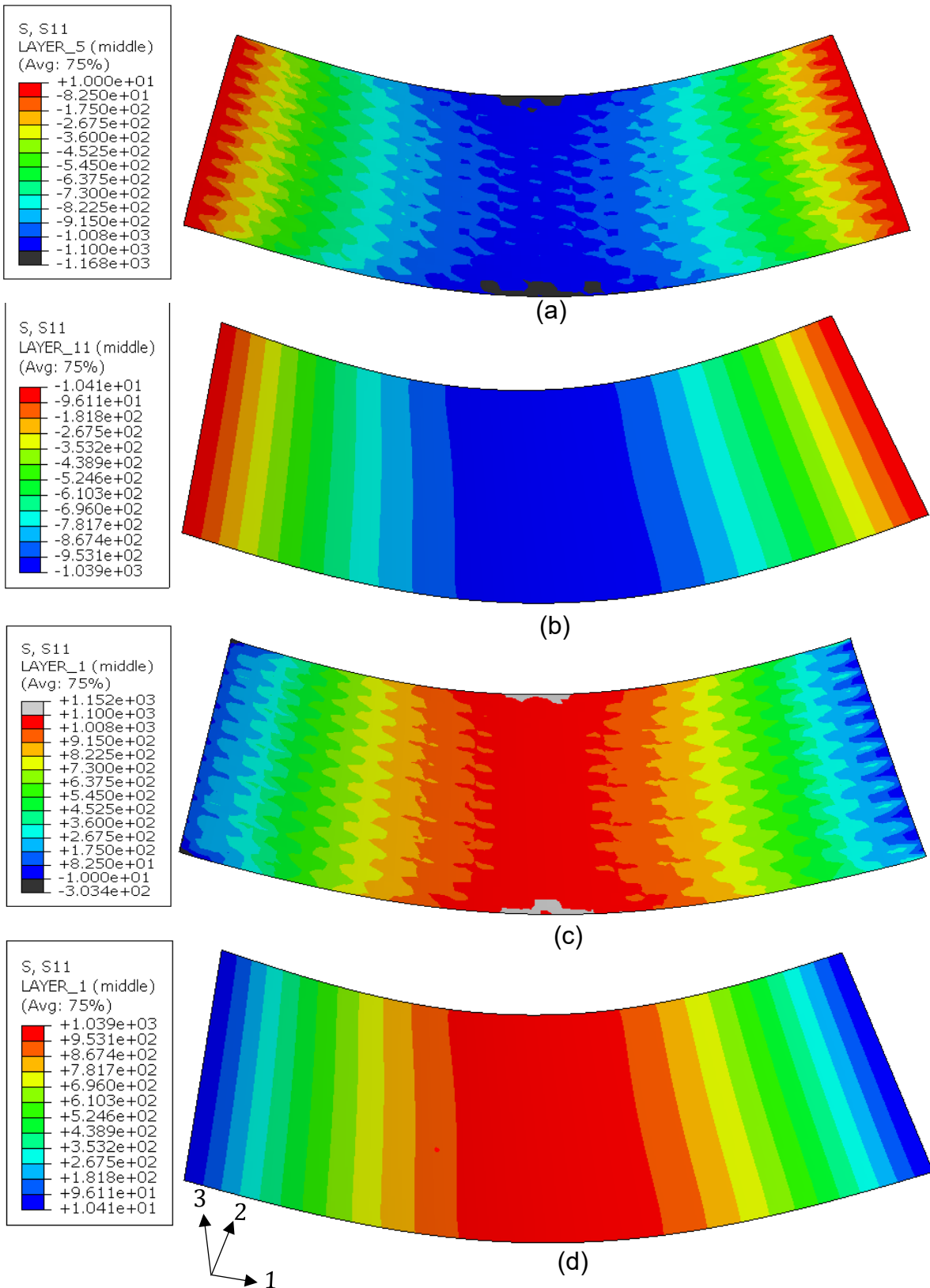
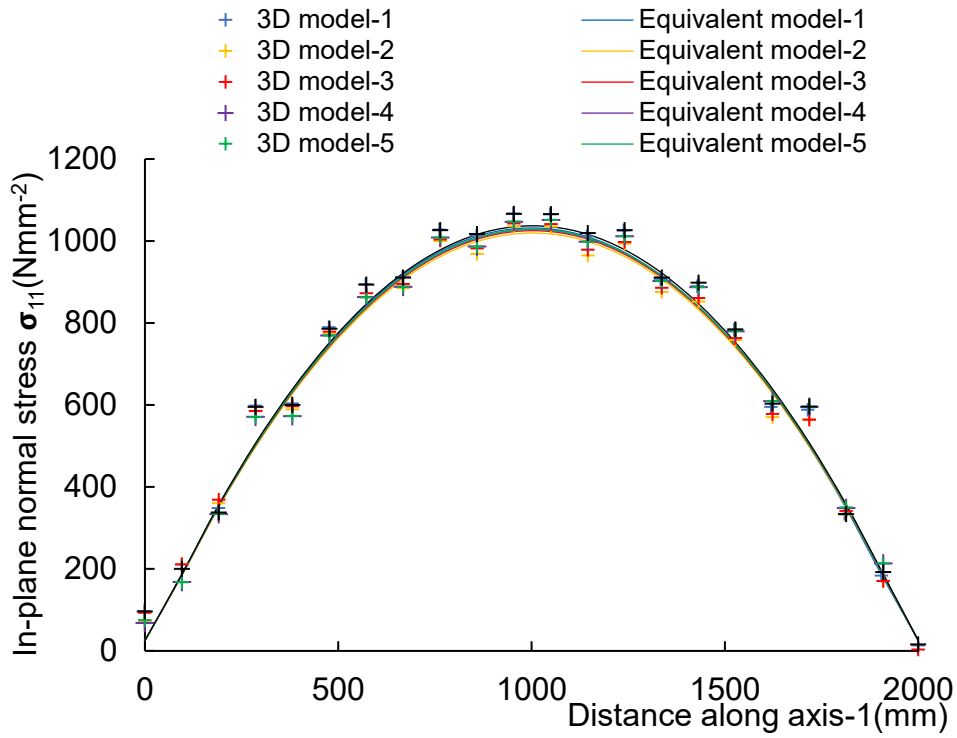
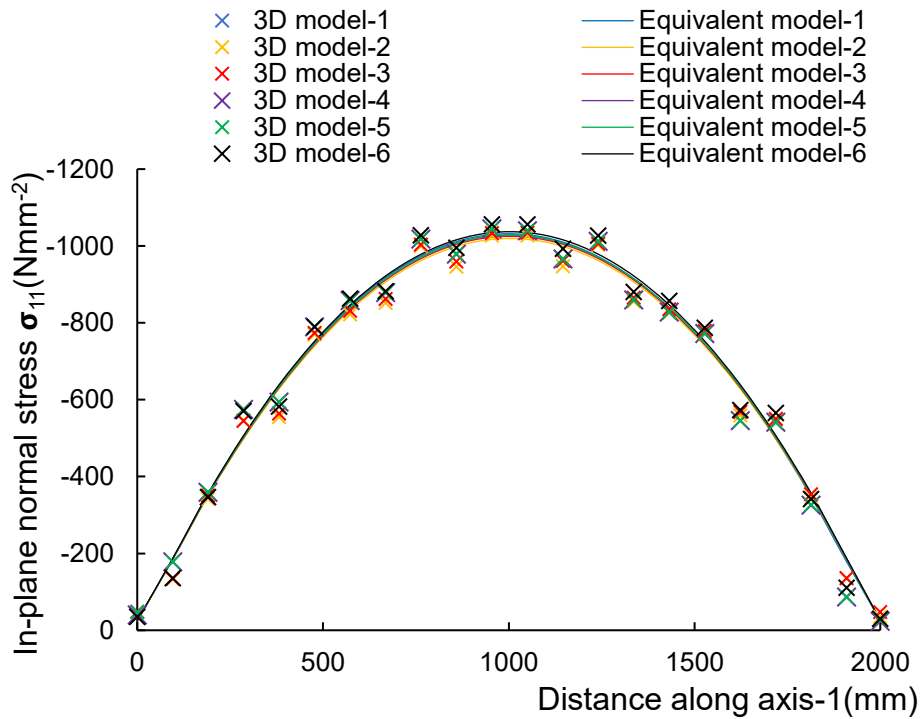


Fig.4.10: Contour maps of the in-plane normal stress σ_{11} of (a) uppermost ply of 3D model, (b) uppermost ply of equivalent model, (c) lowermost ply of 3D model, and (d) lowermost ply of equivalent model of the simply-supported sandwich panel consisting of hexagonal core with fibre lay-up [45/-45/0/-45/45].



(a)



(b)

Fig.4.11: Comparisons of in-plane normal stress σ_{11} from 3D models and equivalent models for the (a) uppermost ply and (b) lowermost ply of the simply-supported sandwich panels along axis-1 for different fibre lay-up of the hexagonal core.

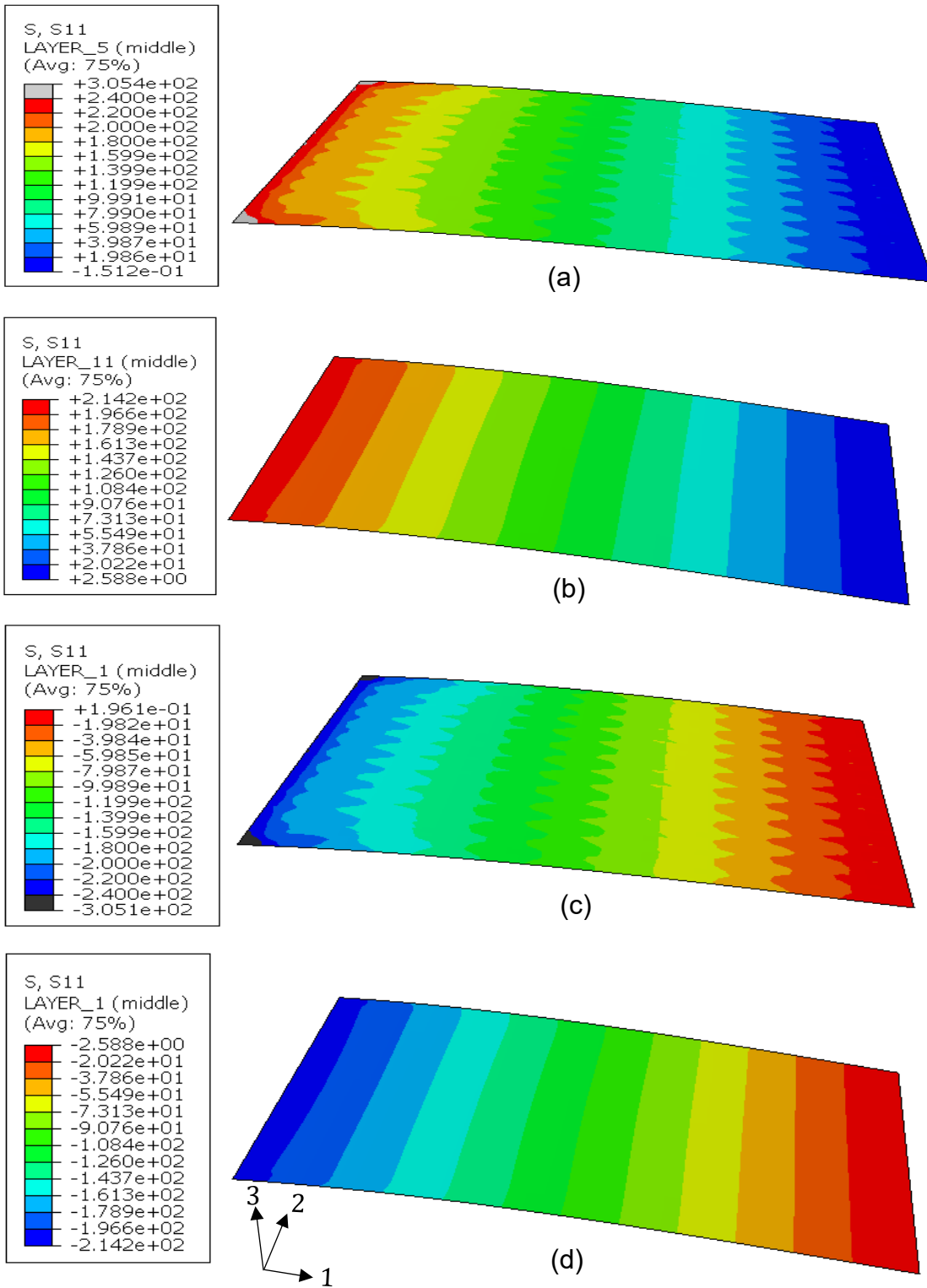
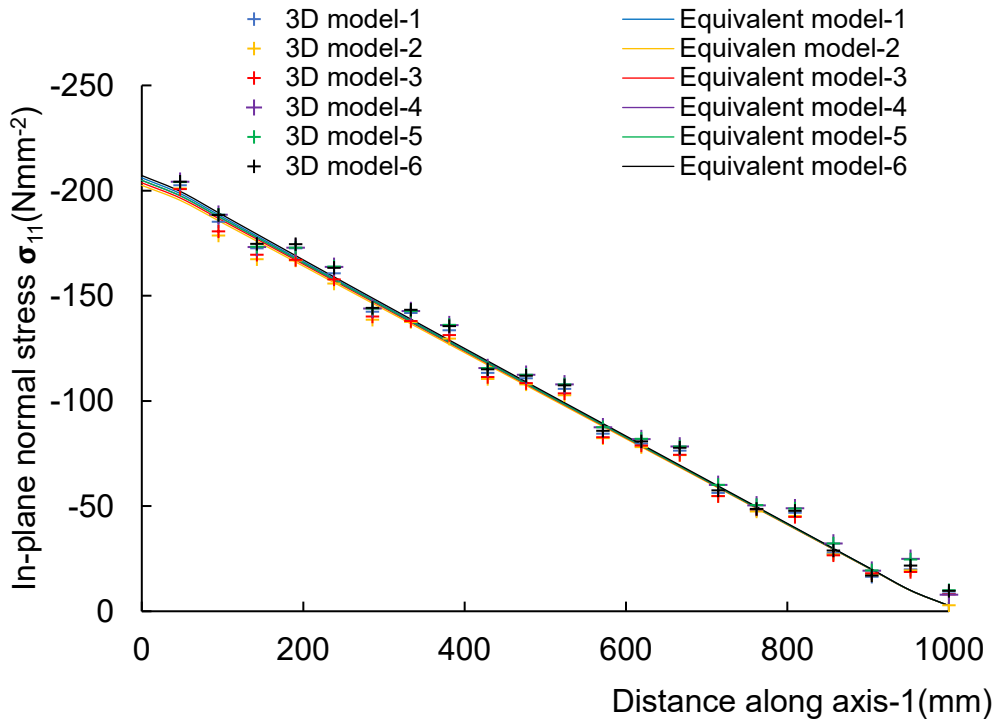
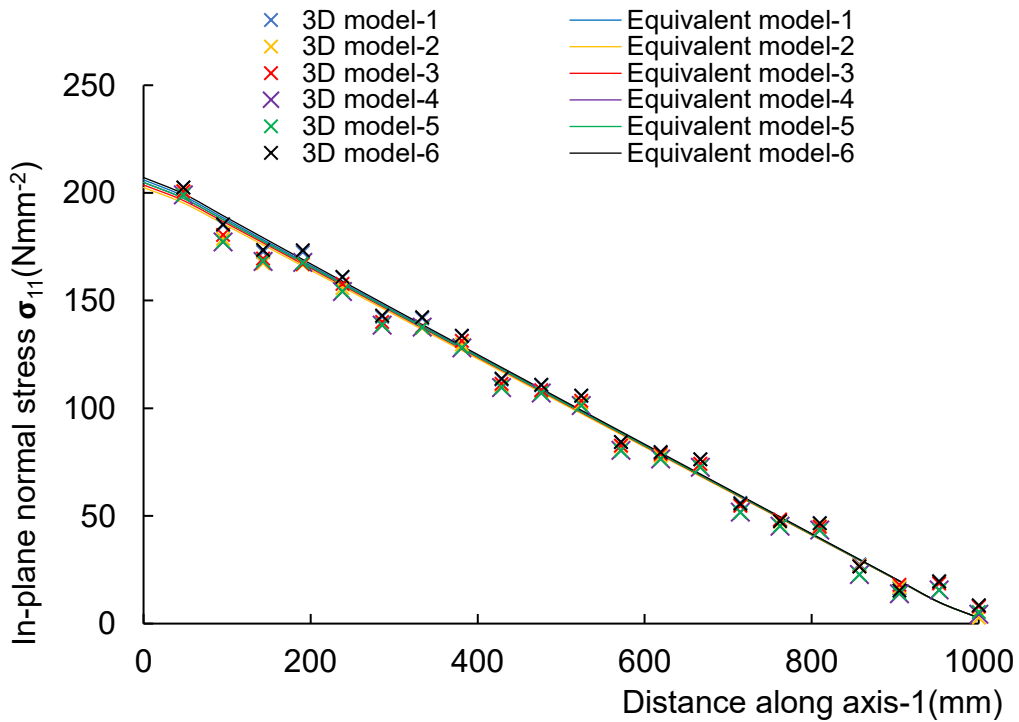


Fig.4.12: Contour maps of the in-plane normal stress σ_{11} of (a) uppermost ply of 3D model, (b) uppermost ply of equivalent model, (c) lowermost ply of 3D model, and (d) lowermost ply of equivalent model of the cantilever sandwich panel consisting of hexagonal core with fibre lay-up [45/-45/0/-45/45].



(a)



(b)

Fig.4.13: Comparisons of in-plane normal stress σ_{11} from 3D models and equivalent models for the (a) uppermost ply and (b) lowermost ply of the cantilever sandwich panels along axis-1 for different fibre lay-up of the hexagonal core.

The in-plane stresses of the face sheets are important to determine the failure of the face sheets of the sandwich panels. Figs. 4.11 and 4.13 compare the in-plane normal stresses of simply supported and cantilever panels along the midline perpendicular to 2-axis. It can be seen from Figs. 4.11 and 4.13, although the results from the 3D model fluctuate in the adjacent points due to supported and unsupported areas in the hexagonal core, overall, the stress predictions are very close to the results from the equivalent models. The predictions of in-plane normal stresses at the uppermost and lowermost plies of the sandwich panels from the equivalent models of simply-supported and cantilever panels are consistent with the predictions of 3D models. Unlike the deflections of the sandwich panels, the in-plane normal stresses in the sandwich panels do not differ significantly based on the material configurations of the core. The in-plane normal stresses of the sandwich panels having cores with the cross-ply laminates (fibre lay-ups 2 & 3) are slightly lower due to higher in-plane stiffness of the core than the sandwich panels having cores with the angle-ply laminates in both the predictions from equivalent models and 3D models. The differences between the maximum stresses at the lowermost ply and uppermost ply from the equivalent models and 3D models of simply-supported sandwich panels are less than 2% and 3.4%, respectively, considering all the different material configurations of the core. For the cantilever sandwich panels, these differences are 2.8% and 3.2%, respectively, for the stresses at 50mm away from the support. While the equivalent models are capable of predicting the in-plane stresses at the face sheets with reasonable accuracy, the equivalent models cannot predict the stresses at the individual cell walls of the core as the core is represented as a homogenised effective medium in sandwich panels. Therefore, the direct comparisons of stresses in the core between equivalent models and 3D models are not meaningful. However, the stresses in the core walls become the important responses to evaluate the local stability and material strength failure at the core, which are some of the failure modes that need to be considered in the design of the sandwich panels. As each individual wall of the core carries the stresses in the actual core structure, the stresses calculated in the homogenous core need to be related back to the individual plate to analyse the strength and stability of the cell walls of the core in the sandwich panels.

4.3.2 Influence of important parameters of sandwich panels on the accuracy of equivalent models

The prediction accuracy of FSDT-based equivalent models depends on the accuracy of estimation of the equivalent transverse shear stiffness of sandwich panels. As discussed in section 4.2.4, the estimation of the equivalent transverse shear stiffness varies depending on the combination of the material and geometric parameters of the face sheets and core of the sandwich panels. This section investigates the consistency of the methodology in section 4.2.4 for the sandwich panels in estimating the equivalent transverse shear stiffness of the sandwich panels. Because it is common to assume (Zenkert, 1997) that the transverse shear stiffness of a sandwich panel is equal to the transverse shear stiffness of the core only when the face sheet thickness is small in comparison to the sandwich panel thickness, the displacements are also calculated under this assumption for the purpose of comparison (shown as equivalent model-2 in Table 4.3-4.6). Tables 4.3 and 4.4 show the comparisons between the maximum displacements for the simply-supported sandwich panels in Fig. 4.5(a) with different face sheet thickness to sandwich thickness ratios. In this case, the thicknesses of both upper and lower face sheets are varied equally while keeping the total thickness of the sandwich panel at 160mm. Tables 4.5 and 4.6 show the comparison between the maximum displacements for the simply-supported sandwich panels in Fig.4.5 (a) with the asymmetric face sheets having different thicknesses. Here, the total thickness of the sandwich panels and the thickness of the lower face sheet remain at 160mm and 5mm, respectively, while the thickness of the upper face sheet varies only. The displacements are calculated for the sandwich panels consisting of the core with two different fibre lay-ups [45/-45/0/-45/45] and [0/0/90/0/0]. The displacements are normalised with respect to maximum displacement from 3D models in each case for the comparison.

Table 4.3: Comparison of normalised maximum displacements for different face sheet to sandwich panel thickness ratios with core fibre lay-up of [45/-45/0/-45/45].

$\frac{(t_f^l + t_f^u)}{H}$	Normalised maximum displacement			$\frac{(b - a)}{a} \%$	$\frac{(c - a)}{a} \%$
	3D model (a)	Equivalent model-1 (b)	Equivalent model-2 (c)		
0.07	100.00	101.86	104.68	1.86	4.68
0.14	62.24	63.33	66.56	1.75	6.93
0.23	49.21	50.30	55.04	2.21	11.84

0.33	42.56	43.69	50.63	2.65	18.96
0.45	38.26	39.55	49.07	3.37	28.26

Table 4.4: Comparison of normalised maximum displacements for different face sheet to sandwich panel thickness ratios with core fibre lay-up of [0/0/90/0/0].

$\frac{(t_f^l + t_f^u)}{H}$	Normalised maximum displacement			$\frac{(b-a)}{a}\%$	$\frac{(c-a)}{a}\%$
	3D model (a)	Equivalent model-1 (b)	Equivalent model-2 (c)		
0.07	100.00	104.45	109.12	4.45	9.12
0.14	68.92	72.76	78.60	5.57	14.04
0.23	57.87	61.76	70.78	6.73	22.31
0.33	51.78	55.91	69.07	7.97	33.40
0.45	47.55	51.98	70.22	9.32	47.69

Table 4.5: Comparison of normalised maximum displacements for different upper face sheet to lower face sheet thickness ratios with core fibre lay-up of [45/-45/0/-45/45].

$\frac{t_f^u}{t_f^l}$	Normalised maximum displacement			$\frac{(b-a)}{a}\%$	$\frac{(c-a)}{a}\%$
	3D model (a)	Equivalent model-1 (b)	Equivalent model-2 (c)		
1	100.00	101.86	104.68	1.86	4.68
2	81.57	83.00	86.16	1.76	5.64
3	75.88	77.31	81.38	1.89	7.26
4	73.38	74.85	80.03	2.01	9.07
5	72.03	73.52	79.97	2.07	11.03

Table 4.6: Comparison of normalised maximum displacements for different upper face sheet to lower face sheet thickness ratios with core fibre lay-up of [0/0/90/0/0].

$\frac{t_f^u}{t_f^l}$	Normalised maximum displacement			$\frac{(b-a)}{a}\%$	$\frac{(c-a)}{a}\%$
	3D model (a)	Equivalent model-1 (b)	Equivalent model-2 (c)		
1	100.00	104.45	109.12	4.45	9.12
2	84.67	88.93	94.35	5.04	11.43
3	79.70	84.01	91.12	5.41	14.33
4	77.16	81.56	90.83	5.70	17.72
5	75.40	80.03	91.68	6.15	21.59

When the face sheets to sandwich panel thickness ratio increases from 0.07 to 0.45, the errors in the predictions of maximum displacements using the equivalent models increase from 1.86% to 3.37% (Table 4.3) and 4.45% to 9.32% (Table 4.4) for the fibre lay-up [45/-45/0/-45/45] and [0/0/90/0/0] respectively of the core. When the upper face sheet to lower face sheet thickness ratio increases from 1 to 5, the errors in the predictions of displacements using the equivalent models increase from 1.86% to 2.07% (Table 4.5) and 4.45% to 6.15% (Table 4.6) for the fibre lay-up [45/-45/0/-45/45] and [0/0/90/0/0] respectively of the core. However, the equivalent models considering the transverse shear stiffness of the sandwich panels is equal to the transverse shear stiffness of the core (results from equivalent model-2 in Tables 4.3-4.6) fail to give satisfactory results when the face sheet thicknesses are not very small in comparison to the thickness of the sandwich panels. Considering all the different cases, the equivalent models of sandwich panels give reasonably accurate results for a wide range of face sheet to sandwich panel thickness ratios and asymmetric configuration of the face sheets when the transverse shear stiffness of the sandwich panels is estimated according to Eq. 4.46 in section 4.2.4.

4.3.3 Analysis for global buckling of sandwich panels

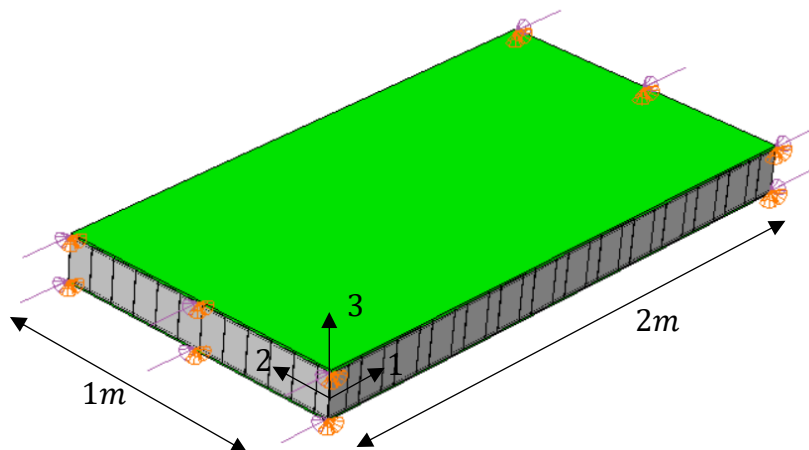


Fig.4.14: Sandwich panel under uniaxial loading for the global buckling analysis.

Linear Eigenvalue buckling analysis is conducted using 3D models and equivalent models to find the critical global buckling loads of sandwich panels under uniaxial loading (Fig. 4.14). A comparison of the results from the models is given in Table 4.7. The maximum difference between the critical global buckling load from the

equivalent models and 3D models is 6.1%, which is for the sandwich panel consisting of a core with fibre lay-up [0/0/90/0/0]. The critical global buckling load of the sandwich panel is more sensitive to the transverse shear stiffness of the core than the in-plane stiffness of the core. The cores which have higher in-plane stiffness and lower transverse shear stiffness (cores with the cross-ply laminates) provide lower critical global buckling load than cores with lower in-plane stiffness and higher transverse shear stiffness (cores with angle ply laminates). The sandwich panel having the core with fibre lay-up [90/0/0/0/90] has the lowest global buckling load, which is predicted as 8748kN and 8218kN by the 3D model and equivalent model, respectively. The sandwich panel having the core with fibre lay-up [45/-45/45/-45/45] has the highest global buckling load, which is a 21.8% and 25.4% increase from the lowest buckling load according to the 3D model and equivalent model, respectively.

Table 4.7: Comparison of global buckling loads under uniaxial compression.

Material lay-up	Critical global buckling load(kN)		$\frac{(b - a)}{a}$ %
	3D model (a)	Equivalent model (b)	
1	10517.80	10134.00	-3.65
2	8788.00	8252.00	-6.10
3	8748.00	8218.00	-6.06
4	9731.20	9341.00	-4.01
5	9731.20	9336.00	-4.06
6	10658.00	10307.00	-3.29

4.3.4 Sandwich panels with different honeycomb core shapes

Figure. 4.15 shows the comparisons of the maximum displacements v_3 of the simply-supported sandwich panels (Fig. 4.5(a)) consisting of different honeycomb core shapes such as hexagonal, triangular, and square cores with different fibre lay-up considered in the study. For all the different core shapes, the dimensions and relative core density are the same as in section 3.4.2. The calculated effective properties of the triangular and square cores in section 3.4.4 are used for the equivalent models of the sandwich panels. For all the different core shapes, a very good agreement between the result from the equivalent models and the 3D models is seen. Also, for all the different material configurations of the cores, the maximum displacements of the sandwich panels do not differ significantly between different core shapes considered because the transverse shear stiffnesses of the different core shapes are

almost equal for all the different material configurations of the cores even though the in-plane stiffnesses are different (Figs.3.9 - 3.14).

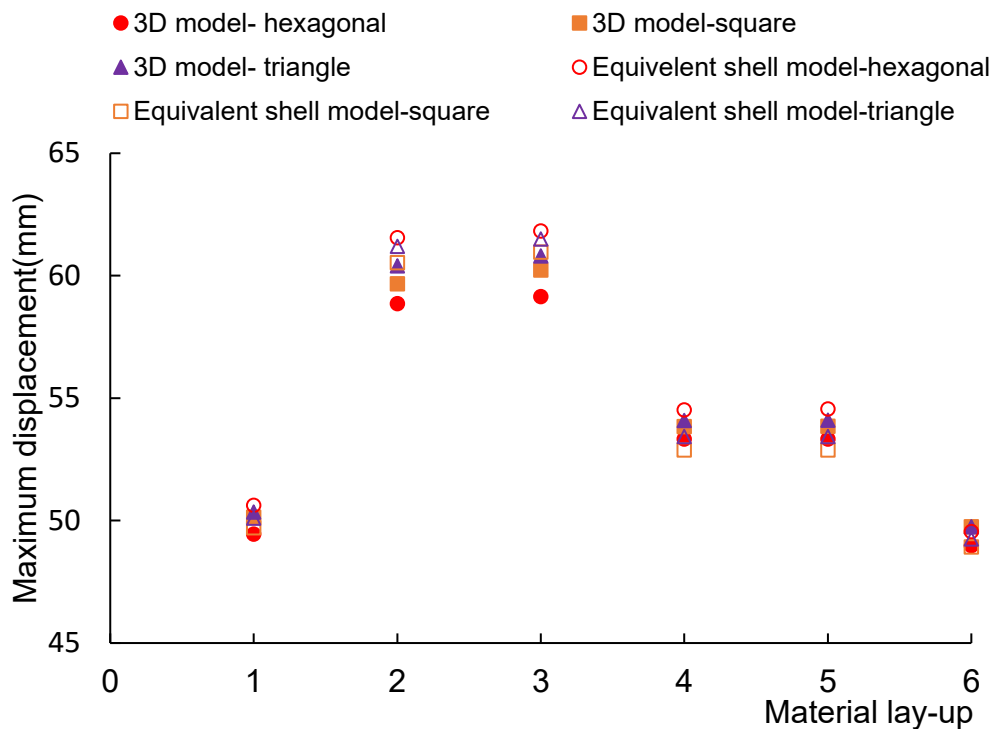


Fig.4.15: Comparison of maximum displacements of the sandwich panels with different honeycomb core shapes.

4.3.5 Comparison of the predictions with existing experimental studies

While the purpose of the inverse design is to systematically determine the preliminary design parameters considering various design variables, the comparison of the predictions from the equivalent models against the experimental data could provide insight into how accurate and justifiable the predictions of equivalent models are for informing the optimal parameters for the detailed design based on complex and costly numerical models and experiments.

Here we consider experiments conducted by Wei et al. (2020) to study three-point bending behaviour all-composite beams. Both face sheets and hexagonal core of the sandwich panels used in their experiment were manufactured using T300-3K woven CFRP/epoxy having the properties as follows: tensile and compressive elastic moduli in principal directions are $E_L^t = E_T^t = 54500MPa$ and $E_L^c = E_T^c = 45790MPa$ respectively, Poisson's ratio $\nu_{LT} = 0.0638$, in-plane shear moduli $G_{TL} = 3750MPa$ and compressive strength $\sigma_L^c = \sigma_T^c = 528.95MPa$. The panels have

dimension of 305mm×84mm×16.18mm. Thickness of each face sheet is $t_f = 0.59\text{mm}$. Thickness of the inclined walls of the hexagonal core is $t = 0.43\text{mm}$ and other wall has double the thickness of the inclined walls. Length of the core walls is $l = 8\text{mm}$. For both face sheets and core, all the plies of laminate were arranged in same orientation (0/90).

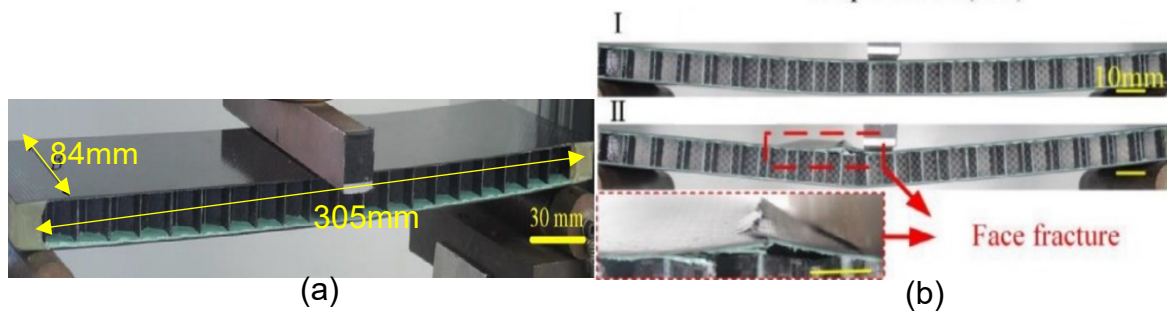


Fig.4.16: (a) All-CFRP sandwich panel under three-point loading and (b) failure due to face fracture (Wei et al. 2020).

Figure 4.17 shows comparison of load-displacement behaviour from the experiments (Wei et al. 2020) and the equivalent models. The failure loads from the experiments varies between 3953N and 4285N while the maximum displacement at failure varies between 8.9mm and 10.9mm among the three different specimen. For the same scenario, the equivalent model of the sandwich panel consisting of the core with (0/90) plies predicts the maximum load of 5740N and maximum displacement of 12.7mm at the face sheet failure stress of 526Mpa. The equivalent model of sandwich panel consisting of core with (45/-45) plies gives the maximum load of 5460N and maximum displacement of 11mm when the face sheet reaches the failure stress. The equivalent model consisting of (45/-45) plies for the core yields a lower failure load due to the core's reduced effective in-plane stiffness. Additionally, it exhibits lower deflection, attributed to the core's larger transverse shear stiffness, in contrast to the equivalent model with a (0/90) core. Unfortunately, experimental studies are very limited for all-composite honeycomb cores, and there are no adequate experimental results for the all-composite sandwich panels to investigate the influence of core and face sheets material configurations on the behaviour of sandwich panels. Discrepancies in failure load and maximum displacement between experiments and equivalent models may stem from various factors. Differences in laminate material properties obtained through testing may not precisely mirror those used in panel fabrication. Additionally, the equivalent model analysis does not consider nonlinear

effects present in the experiments, potentially resulting in stiffness and strength loss under loading. While visible face sheet fractures were evident in experiments, initiation of other, less apparent local failure modes may have occurred concurrently, their interaction potentially contributing to stiffness and strength degradation, phenomena not captured by the equivalent model. However, conducting experiments and employing complex 3D numerical models to assess the influence of various materials and geometric configurations on different failure modes and stiffness of sandwich panels is impractical due to the associated costs and time constraints. Therefore, inverse design offers a systematic and efficient approach to consider a large number of parameters and select optimal ones for target performance criteria. Despite this, the equivalent model approach remains valuable in the context of inverse design for sandwich panels.

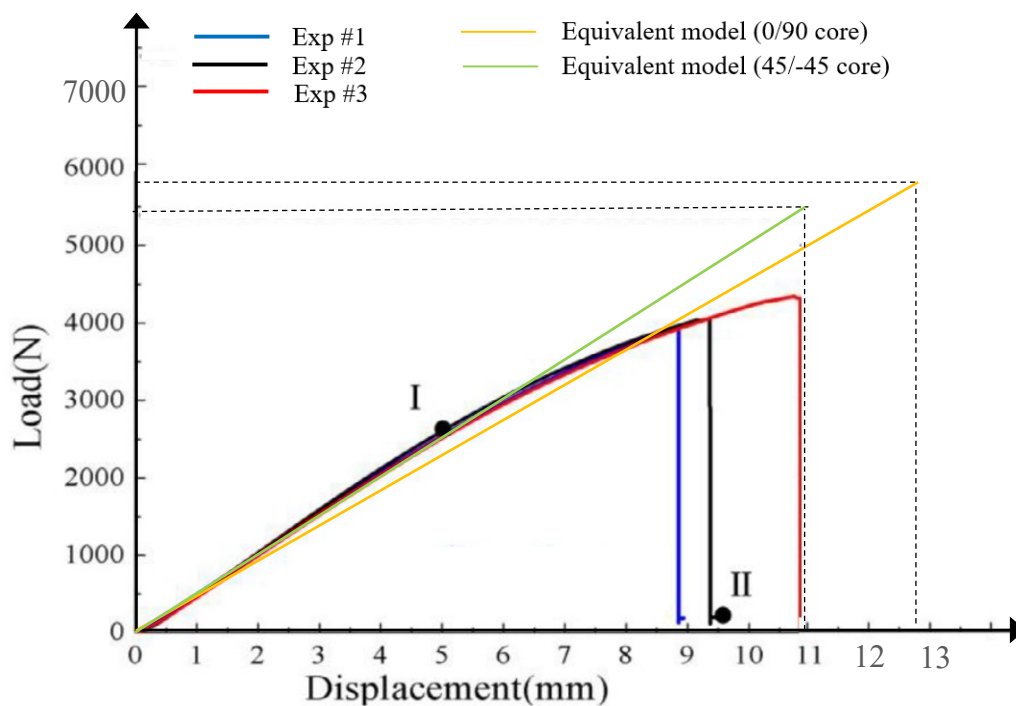


Fig.4.17: Comparisons of load-displacement behaviour from the 3-point bending experiments of Wei et al. (2020) and the equivalent models.

4.4 Conclusions

This chapter presents an investigation of the effectiveness of the equivalent models in predicting the responses of sandwich panels against the 3D models with actual core structures. The sandwich panels consisting of hexagonal honeycomb

cores with different material configurations were analysed for the deflections and in-plane normal stresses under static bending, and the global critical buckling load under uniaxial compression using the equivalent models based on FSDT and predictions were compared against results from the 3D models with actual core structure. The analysis showed that FSDT-based equivalent models, together with effective properties of cores, could predict global responses of the sandwich panels to a reasonable accuracy. The accuracy of predicting the responses using FSDT depends on the accuracy of the estimation of equivalent transverse shear stiffness. The methodology assuming the shear strain energy equivalence under cylindrical bending used in the study performs consistently over a wide range of parameters, and predictions are in good agreement with 3D models. Although FSDT-based analysis was implemented using FE software in this study, results could be obtained to the same accuracy using analytical or semi-analytical approaches based on FSDT together with the methodology used for the equivalent transverse shear stiffness estimation in this study. While the significant time saving from modelling and analysis of equivalent models based on FSDT makes this approach more suitable for the inverse design of the sandwich panels compared to other complex models, there are certain limitations in using FSDT for the sandwich panel analysis. Because the equivalent models based on FSDT represent the sandwich panels as single-layer plates with homogenised core properties, these models are not capable of predicting the local failures such as cell wall buckling of the core and local buckling of face sheets, which are some of the important failure modes governing the performance of sandwich panels. On the other hand, 3D models of the sandwich panels could be used to predict every important response governing the design of the sandwich panels with linear and non-linear analysis techniques; however, this would require significant computational time and effort.

Therefore, detailed models or more complex models are not suitable for the inverse design of the sandwich panels as this would require several repetitive evaluations of the domain of design variables. Nevertheless, it is necessary to have an approach to predict the local failures of all-composite honeycomb sandwich panels.

4.5 References

ABAQUS version 2021. Dassault Systemes Simulia Corporation. Providence, RI, USA.

- Balawi, S., & Abot, J. (2008). A refined model for the effective in-plane elastic moduli of hexagonal honeycombs. *Composite Structures*, 84(2), 147-158.
- Bishop, J., & Hill, R. (1951). XLVI. A theory of the plastic distortion of a polycrystalline aggregate under combined stresses. *The London, Edinburgh, and Dublin Philosophical Magazine and Journal of Science*, 42(327), 414-427.
- Catapano, A., & Montemurro, M. (2014). A multi-scale approach for the optimum design of sandwich plates with honeycomb core. Part I: homogenisation of core properties. *Composite Structures*, 118, 664-676.
- Chen, X., Yu, G., Wang, Z., Feng, L., & Wu, L. (2021). Enhancing out-of-plane compressive performance of carbon fiber composite honeycombs. *Composite Structures*, 255, 112984.
- Feng, Y., Qiu, H., Gao, Y., Zheng, H., & Tan, J. (2020). Creative design for sandwich structures: A review. *International Journal of Advanced Robotic Systems*, 17(3), 1729881420921327.
- Gibson, I., & Ashby, M. F. (1982). The mechanics of three-dimensional cellular materials. *Proceedings of the Royal Society of London. A. Mathematical and Physical Sciences*, 382(1782), 43-59.
- Grediac, M. (1993). A finite element study of the transverse shear in honeycomb cores. *International Journal of Solids and Structures*, 30(13), 1777-1788.
- Hohe, J., & Becker, W. (2001). An energetic homogenisation procedure for the elastic properties of general cellular sandwich cores. *Composites Part B: Engineering*, 32(3), 185-197.
- Hou, W., Shen, Y., Jiang, K., & Wang, C. (2022). Study on mechanical properties of carbon fiber honeycomb curved sandwich structure and its application in engine hood. *Composite Structures*, 286, 115302.
- Kollár, L., & Springer, G. (2003). Laminated Composites. In *Mechanics of Composite Structures* (pp. 63-88). Cambridge: Cambridge University Press.
- Krishnamurthy, T., & Saether, E. (2019). *Estimation of Effective Elastic Properties of General Multifunctional Honeycomb Structures Using a Unit Cell Method*. Paper presented at the AIAA Scitech 2019 Forum.
- Malek, S., & Gibson, L. (2015). Effective elastic properties of periodic hexagonal honeycombs. *Mechanics of Materials*, 91, 226-240.
- Masters, I., & Evans, K. (1996). Models for the elastic deformation of honeycombs. *Composite Structures*, 35(4), 403-422.
- MathWorks Inc. (2022). MATLAB version: 9.13.0 (R2022b), Natick, Massachusetts: The MathWorks Inc.
- Min, L., Fernando, D., Gilbert, B., & You, Z. (2020). Hybrid FRP-timber thin-walled Cee section columns under axial compression: Numerical modelling. *Thin-Walled Structures*, 157, 107029.
- Mukherjee, S., & Adhikari, S. (2021). A general analytical framework for the mechanics of heterogeneous hexagonal lattices. *Thin-Walled Structures*, 167, 108188.
- Pehlivan, L., & Baykasoğlu, C. (2019). An experimental study on the compressive response of CFRP honeycombs with various cell configurations. *Composites Part B: Engineering*, 162, 653-661.
- Russell, B., Deshpande, V., & Wadley, H. (2008). Quasistatic deformation and failure modes of composite square honeycombs. *Journal of mechanics of materials and structures*, 3(7), 1315-1340.

- Russell, B., Liu, T., Fleck, N., & Deshpande, V. (2011). Quasi-static three-point bending of carbon fiber sandwich beams with square honeycomb cores. *Journal of Applied Mechanics*, 78(3).
- Vlachoutsis, S. (1992). Shear correction factors for plates and shells. *International Journal for Numerical Methods in Engineering*, 33(7), 1537-1552.
- Wang, R., & Wang, J. (2018). Modeling of honeycombs with laminated composite cell walls. *Composite Structures*, 184, 191-197.
- Wei, X., Li, D., & Xiong, J. (2019). Fabrication and mechanical behaviors of an all-composite sandwich structure with a hexagon honeycomb core based on the tailor-folding approach. *Composites Science and Technology*, 184, 107878.
- Wei, X., Wang, Y., Xue, P., Zhang, T., Rouis, A., Xiao, W., & Xiong, J. (2022). Carbon Fiber Composite Honeycomb Structures and the Application for Satellite Antenna Reflector with High Precision. *Advances in Astronautics Science and Technology*, 5(4), 423-441. doi:10.1007/s42423-022-00133-5
- Wei, X., Wu, Q., Gao, Y., & Xiong, J. (2020). Bending characteristics of all-composite hexagon honeycomb sandwich beams: experimental tests and a three-dimensional failure mechanism map. *Mechanics of Materials*, 148, 103401.
- Xia, Z., Zhang, Y., & Ellyin, F. (2003). A unified periodical boundary conditions for representative volume elements of composites and applications. *International journal of solids and structures*, 40(8), 1907-1921.
- Zenkert, D. (1997). *The handbook of sandwich construction*: Engineering Materials Advisory Services.
- Zhang, J., & Ashby, M. (1992). The out-of-plane properties of honeycombs. *International Journal of Mechanical Sciences*, 34(6), 475-489.

Chapter 5:

Local buckling of laminated composite honeycomb core in sandwich panels

5.1 General

In Chapter 4, a FSDT-based equivalent model of the honeycomb core sandwich panels was developed to predict the global responses of the sandwich panels. The study illustrated that the equivalent model of all-composite sandwich panels, where the honeycomb core is represented as a homogenous continuum with effective stiffness, is capable of predicting the global responses such as maximum deflection, rupture of face sheets, and global buckling accurately. However, the equivalent models cannot predict the local failures such as local buckling of core walls and face sheets. Local buckling of the honeycomb core walls is related to the responses at the local level (stresses at each wall) which cannot be calculated directly based on the effective stiffness of the core. The stresses at the local level depend on the geometry and material parameters of the core, thus it's necessary to have relationships relating the macro-level responses of the core at the continuum level to the local responses. As the transverse shear force is predominantly carried by the core, the shear buckling of the core wall is one of the important failure modes to be considered in the design of honeycomb core sandwich panels. In the past, researchers (Banerjee et al. 2010; Kim & Christensen 2000; López Jiménez & Triantafyllidis 2013; Pan et al. 2006, 2008; Shi & Tong 1994; Qiu et al. 2020; Zhang & Ashby 1992) have investigated the shear buckling behaviour of honeycomb cores. However, most of the studies are limited to cores of certain geometric shapes (mainly limited to hexagonal honeycomb core) and made using isotropic materials. In addition, those studies considered shear loading in two major directions separately and failed to consider the effects of resulting shear. The shear buckling strength of the honeycomb core depends on the effective direction of shear loading when the honeycomb core is subjected to combined transverse shear in two different directions (Cote et al. 2006), an aspect not considered in the existing models. In order to carryout inverse design of sandwich panels, in addition to the

equivalent stiffness models, it is also necessary to develop accurate yet simple models to predict shear buckling failures of honeycomb core sandwich panels.

This chapter presents a simplified approach to predict the critical shear buckling load of the composite honeycomb cores, considering various geometries and material configurations. The predictions of the buckling loads for the honeycomb cores with different materials and geometric configurations using the proposed approach are verified using the results from the finite element (FE) analysis of RVEs of the honeycomb cores.

5.2 Shear buckling of the core walls

Consider a typical periodic honeycomb core structure built using laminated composite plates having different fibre layer sequences (Fig. 3.2). In sandwich panels subjected to flexural loadings, the transverse shear forces are predominantly carried by the honeycomb core. While it is possible that honeycomb core cell walls may also carry compression forces, considering core depth is typically much larger than the thickness of the cell walls, such compressive forces can be taken as negligible compared to transverse shear forces acting on the cell walls (Zenkert 1997). Therefore, only transverse shear forces acting on cell walls are considered in this study. Similar to the assumptions made in existing studies (Shi & Tong 1994; Zhang & Ashby 1992), this study also assumes that transverse shear stresses are constant across the depth of the core. This can also be understood from the linear static bending analysis in section 4.1.1. Figure. 5.1(a) shows the shear strain variation of the honeycomb core walls of the simply supported sandwich panel considered in the analysis of section 4.1.1, and Fig. 5.1(b) shows the variation of the shear strain of core walls at lower (L), middle (M) and upper (U) points of the core walls along the midline of the honeycomb core structure having fibre lay-up of [45/-45/0/-45/45]. From Fig. 5.1(b), it can be seen that the shear strains along the height of the core walls remain relatively constant.

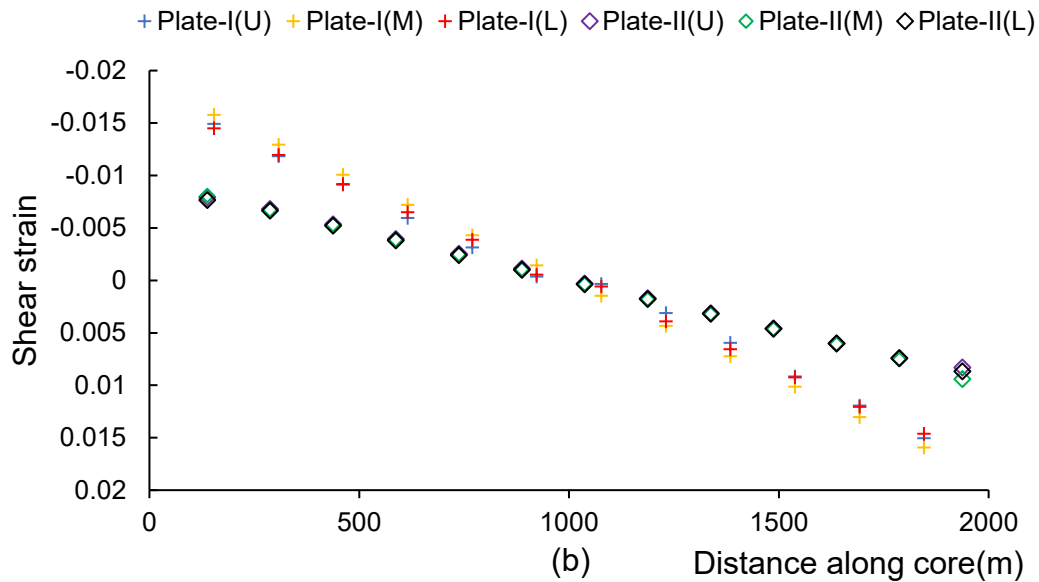
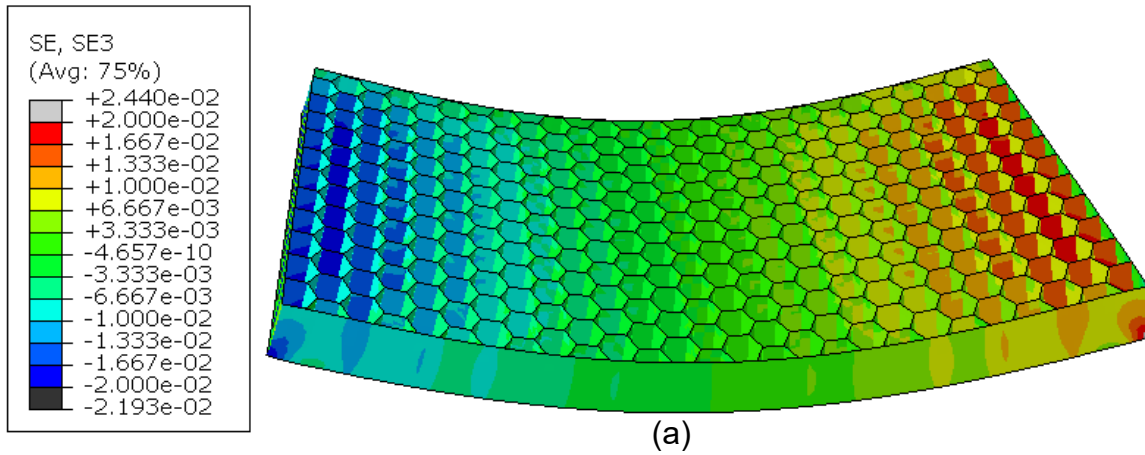


Fig. 5.1: (a) Contour map of the shear strain of the hexagonal core with fibre lay-up $[45/-45/0/-45/45]$ and (b) variation of the shear strain at lower (L), middle (M) and upper (U) points of the core walls.

5.2.1 Relationship between the shear strain of each plate and the global transverse shear strain of the core

The RVE of honeycomb cores were represented to be a homogeneous continuum core to analyse the global behaviour of sandwich panels (in Chapters 3 and 4). For the study presented in this chapter, it is necessary to relate back the shear responses of the homogenous core to the individual plate of the actual discrete core to identify the local buckling behaviour of the individual plate. To illustrate the proposed approach, a RVE of the hexagonal core shown in Fig. 5.2(a) subjected to certain global transverse shear strain is considered. Then, each plate of the selected RVE of the hexagonal core (Fig. 5.2(a)), which is subjected to certain in-plane shear strain, is

approximated to be under a constant shear strain according to the assumption discussed in the previous section. Under this assumption, each node of the RVE (Fig. 5.2(a)) is considered to be subjected to a normal displacement in direction-3 or $\bar{3}$ due to the applied transverse shear load on the RVE of the core. Fibre orientations of the composite core wall (Fig. 5.2(b)) are defined such that the anti-clockwise angle (ϕ) is positive with respect to positive local direction- $\bar{1}$. The positive local direction- $\bar{1}$ is defined for the plate-I, plate-II and plate-III, from node 1 to 5, node 5 to 2 and node 5 to 4 respectively (Fig. 5.2(a)). The positive direction- $\bar{3}$ of the core wall is always defined in the positive global direction-3. Considering the sign convention assumed here, the positive shear strain of each plate is expressed as:

$$\bar{\gamma}_{13}^I = \frac{\bar{u}_{(5)3} - \bar{u}_{(1)3}}{l_1} = \frac{u_{(5)3} - u_{(1)3}}{l_1}, \quad (5.1)$$

$$\bar{\gamma}_{13}^{II} = \frac{\bar{u}_{(2)3} - \bar{u}_{(5)3}}{l_2} = \frac{u_{(2)3} - u_{(5)3}}{l_2}, \quad (5.2)$$

$$\bar{\gamma}_{13}^{III} = \frac{\bar{u}_{(4)3} - \bar{u}_{(5)3}}{l_3} = \frac{u_{(4)3} - u_{(5)3}}{l_3} \quad (5.3)$$

where, $\bar{u}_{(i)3}$ and $u_{(i)3}$ are displacement at node i in global 3 and local $\bar{3}$ directions respectively.

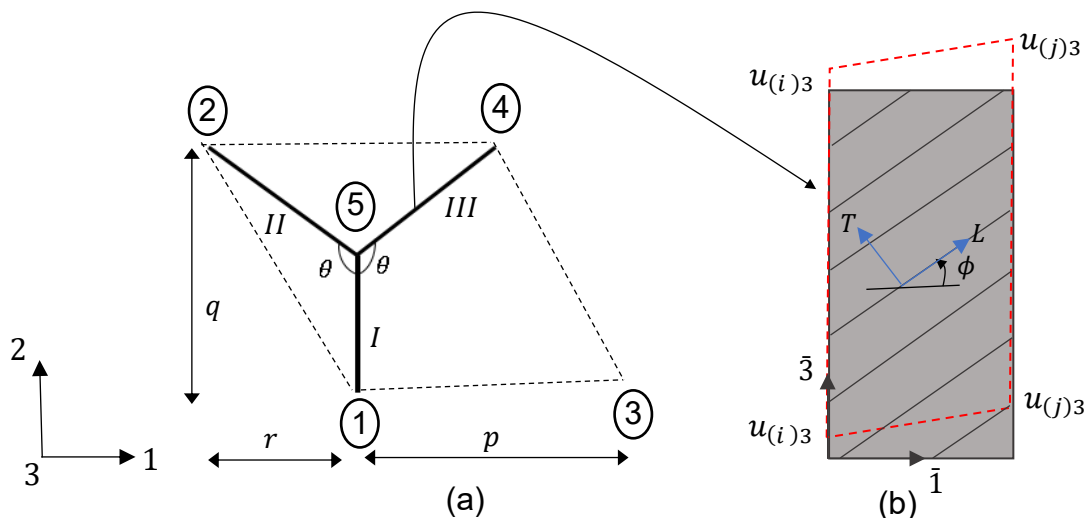


Fig. 5.2: (a) RVE of hexagonal core with the nodal numbers and characteristic dimensions, (b) deformed shape of the plate under positive shear strain. The positive angle ϕ of the fibre orientation is measured counterclockwise with respect to the positive $\bar{1}$ direction.

The relationship between a laminated composite plate's shear load and shear strain can also be written using the classical laminate theory (CLT). Considering the assumption that the core is subjected to only the transverse shear strain, we may also assume that in-plane normal strains $\bar{\epsilon}_{11}$ and $\bar{\epsilon}_{33}$ of the plates are equal to zero, ignoring the shear-extensional coupling. Therefore, the relationship between the in-plane shear strain to the shear force of the plate $-i$ (*refers to I, II and III*) can be simplified as:

$$\bar{\gamma}_{13}^i = \frac{\bar{F}_{13}^i}{\bar{A}_{66}^i}, \quad (5.4)$$

where \bar{F}_{13}^i and \bar{A}_{66}^i are in-plane shear load and the section in-plane shear stiffness of plate- i respectively.

In order to find the relationship between the applied global shear strain on the hexagonal core to shear strain at each plate, first, it's necessary to solve for the displacement at each node, taking into account the periodic nature of the honeycomb core. Considering the periodic boundary conditions and force equilibrium of the RVE, nodal displacements can be solved to get the strain at each plate due to the applied global strain. Applying the periodic boundary condition to the RVE in Fig. 5.2, we can write:

$$u_{(3)1} - u_{(1)1} = u_{(4)1} - u_{(2)1}. \quad (5.5)$$

RVE does not undergo any rigid body motions, therefore, we can write:

$$u_{(1)3} = 0. \quad (5.6)$$

We can define the average global shear strains of the RVE using the same definition of Eq. (3.68):

$$\gamma_{13} = \frac{u_{(3)3} - u_{(1)3}}{p}, \quad (5.7)$$

$$\gamma_{23} = \frac{u_{(2)3} - u_{(1)3}}{q} + \frac{r}{p} \frac{u_{(3)3} - u_{(1)3}}{q}, \quad (5.8)$$

The average global shear strain γ_{13} and γ_{23} of the hexagonal core RVE are illustrated in Fig. 5.3.

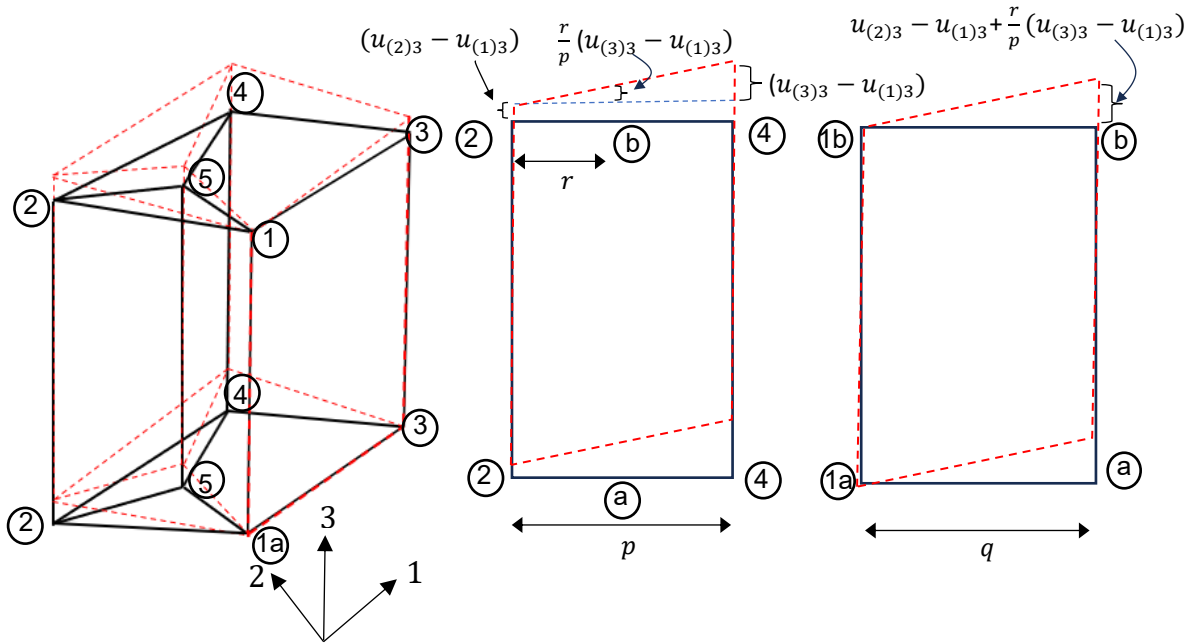


Fig. 5.3: Illustration of the global transverse shear strains of typical honeycomb RVE.

In addition to the conditions in Eqs. (5.5) – (5.8), we can also write additional equations considering the force equilibrium conditions of the RVE. Considering the force equilibrium of the RVE in Fig. 5.2(b), sum of the forces in all four corner nodes should be zero in the periodic honeycomb core. This can be explained considering the periodicity of the RVE in Fig. 5.4.

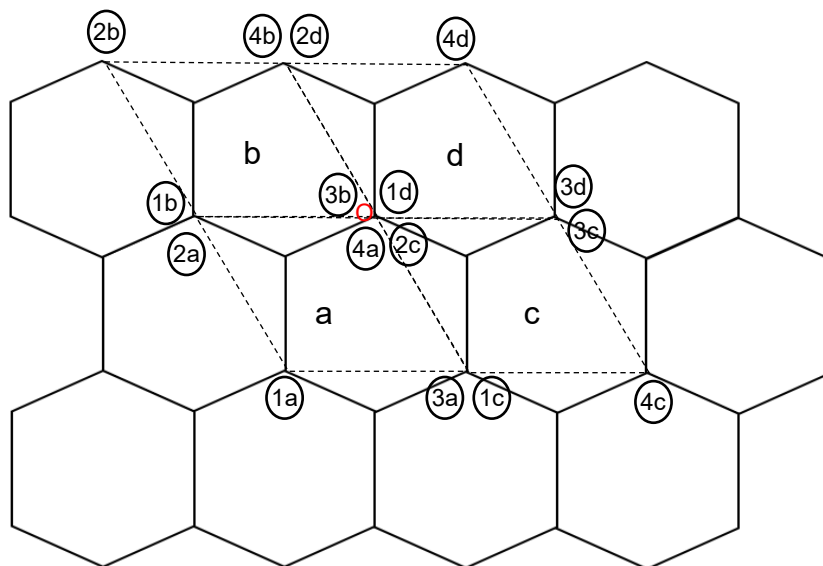


Fig. 5.4: Repetition of the RVEs to form the periodic honeycomb core.

Considering the adjacent RVEs a, b, c and d in Fig.5.4, the resultant force at point O should be zero:

$$F_{(4a)13} + F_{(2c)13} + F_{(1d)13} = 0, \quad (5.9)$$

where $F_{(i)13}$ is the shear force at node i . Considering the repetitiveness of the RVEs, it is possible to write:

$$F_{(1d)13} = F_{(1a)13} \quad \text{and} \quad F_{(2c)13} = F_{(2a)13}. \quad (5.10)$$

From Eqs. (5.10), the Eq. (5.9) can be equivalently written for the RVE of the hexagonal core in the Fig. (5.2) as:

$$F_{(1)13} + F_{(2)13} + F_{(4)13} = 0. \quad (5.11)$$

Resultant force at the internal node-(5) of the hexagonal RVE (Fig. (5.2)) also should be zero, which gives:

$$F_{(5)13} = 0. \quad (5.12)$$

For the hexagonal RVE considered (Fig. (5.2)), Eq. (5.12) is not an independent equation because by considering the local equilibrium of each plate, Eq. (5.11) can be shown to equal to Eq. (5.12).

The general procedure to formulate the required equations to solve for the displacements of the RVE was presented until now. Considering the Eqs. (5.4) - (5.12), the nodal displacements can be found in terms of geometric and stiffness parameters of the RVE and substituting the results into Eqs. (5.1) - (5.3), the relationships between the applied global shear strains γ_{13} and γ_{23} of the hexagonal RVE to the shear strain of each plate $\bar{\gamma}_{13}^i$ of the RVE can be derived as:

$$\bar{\gamma}_{13}^I = \frac{\gamma_{23}(\bar{A}_{66}^{II} + \bar{A}_{66}^{III})(l_1 - l_2 \cos\theta) + \gamma_{13}(\bar{A}_{66}^{III} - \bar{A}_{66}^{II})l_2 \sin\theta}{\bar{A}_{66}^I l_2 + (\bar{A}_{66}^{II} + \bar{A}_{66}^{III})l_1}, \quad (5.13)$$

$$\bar{\gamma}_{13}^{II} = \frac{\gamma_{23}(l_1 - l_2 \cos\theta)\bar{A}_{66}^I - \gamma_{13}(l_2 \bar{A}_{66}^I + 2l_1 \bar{A}_{66}^{III})\sin\theta}{\bar{A}_{66}^I l_2 + (\bar{A}_{66}^{II} + \bar{A}_{66}^{III})l_1}, \quad (5.14)$$

$$\bar{\gamma}_{13}^{III} = \frac{\gamma_{23}((l_1 - l_2 \cos\theta)\bar{A}_{66}^I + \gamma_{13}(l_2 \bar{A}_{66}^I + 2l_1 \bar{A}_{66}^{III})\sin\theta)}{\bar{A}_{66}^I l_2 + (\bar{A}_{66}^{II} + \bar{A}_{66}^{III})l_1}. \quad (5.15)$$

By considering the ratio between the applied shear strain γ_{13}/γ_{23} as k , the shear strain $\bar{\gamma}_{13}^i$ of the plate- i can be expressed as:

$$\bar{\gamma}_{13}^i = \gamma_{13} f^i, \quad (5.16)$$

where;

$$f^I = \frac{k(\bar{A}_{66}^I + \bar{A}_{66}^{III})(l_1 - l_2 \cos\theta) + (\bar{A}_{66}^{III} - \bar{A}_{66}^I)l_2 \sin\theta}{\bar{A}_{66}^I l_2 + (\bar{A}_{66}^I + \bar{A}_{66}^{III})l_1}, \quad (5.17)$$

$$f^{II} = \frac{k(l_1 - l_2 \cos\theta)\bar{A}_{66}^I - (l_2 \bar{A}_{66}^I + 2l_1 \bar{A}_{66}^{III}) \sin\theta}{\bar{A}_{66}^I l_2 + (\bar{A}_{66}^I + \bar{A}_{66}^{III})l_1}, \quad (5.18)$$

$$f^{III} = \frac{k((l_1 - l_2 \cos\theta)\bar{A}_{66}^I + (l_2 \bar{A}_{66}^I + 2l_1 \bar{A}_{66}^{III}) \sin\theta)}{\bar{A}_{66}^I l_2 + (\bar{A}_{66}^I + \bar{A}_{66}^{III})l_1}. \quad (5.19)$$

Substituting Eq. (5.16) with Eq. (5.4), we can write the following relationship for the shear strain γ_{13} of the RVE:

$$\gamma_{13} = \frac{\bar{F}_{13}^i}{\bar{A}_{66}^i f^i}. \quad (5.20)$$

The critical shear buckling load of the honeycomb core is defined as the minimum shear load which requires for any wall of the RVE to buckle, therefore, the condition to determine the critical shear strain of the hexagonal core can be written from Eq.(5.20) as:

$$\gamma_{cr} = \min \left\{ \left| \frac{\bar{F}_{cr}^I}{\bar{A}_{66}^I f^I} \right|, \left| \frac{\bar{F}_{cr}^{II}}{\bar{A}_{66}^I f^{II}} \right|, \left| \frac{\bar{F}_{cr}^{III}}{\bar{A}_{66}^I f^{III}} \right| \right\}, \quad (5.21)$$

where \bar{F}_{cr}^i is the critical shear buckling load of plate- i .

5.2.2 Critical shear buckling load of the composite plate

To find the critical shear strain of the hexagonal core using Eq. (5.21), it is necessary to solve for the critical shear buckling load of the composite wall. Closed-form solutions for buckling problem may only be obtained for certain boundary and loading conditions. However, for the case of shear loading condition and with complex laminates where the coupling terms exist ($\bar{D}_{16} \neq 0$, $\bar{D}_{36} \neq 0$), closed-form solutions may not be obtained, and only approximate solutions may be possible. For many of the approximate solutions, the formulation of the buckling problems is carried out using

the principle of minimum energy and approximate solutions are obtained using the Rayleigh-Ritz method (Leissa, 2005). The accuracy and computational efficiency of the Rayleigh-Ritz method in predicting the critical buckling load greatly depend on the choice of appropriate displacement function of the plate. Moreno-Garcia et al. (2016) provides a detailed overview of the various admissible function types commonly used in the Rayleigh-Ritz method, including trigonometric functions, characteristic functions, and orthogonal polynomials. Here, we will also use the Rayleigh-Ritz method based solution to calculate the critical shear buckling load of the composite wall. Consider a plate (which is the composite wall) subjected to in-plane shear having rotationally restrained along the long edges ($h > 3l$) and simply supported along short edges (Fig. 5.5). For a long plate under in-plane shear load, the function in Eq. (5.22) can be used to approximately describe the out-of-plane displacement due to buckling (Qiao & Huo 2011). The function consists of a term R, which takes into account the degree of rotational restraint at the boundaries of the plate.

$$\bar{u}_2(\bar{x}_1, \bar{x}_3) = A_m \left[(1 - R) \sin\left(\frac{\pi \bar{x}_1}{l_i}\right) + R \left(1 - \cos\left(\frac{2\pi \bar{x}_1}{l_i}\right)\right) \right] \sin\left(\frac{\pi(\bar{x}_3 - \alpha \bar{x}_1)}{ml_i}\right), \quad (5.22)$$

where $\bar{u}_2(\bar{x}_1, \bar{x}_3)$ is the out-of-plane displacement of the plate- i in direction- $\bar{2}$, A_m , m and α are the amplitude of the wave, ratio of the half wave length to l_i and skew angle of the wave respectively and \bar{x}_1 and \bar{x}_3 are coordinates in directions- $\bar{1}$ and direction- $\bar{3}$ respectively. The function consists of a weighted term R, which takes into account the degree of rotational restraint of the plate. When R becomes zero, then the displacement function represents the simply-supported boundaries for all the edges and when R becomes 1, then the displacement function implies the clamped longer edges. R could be determined considering the boundary conditions along the rotationally restrained edges.

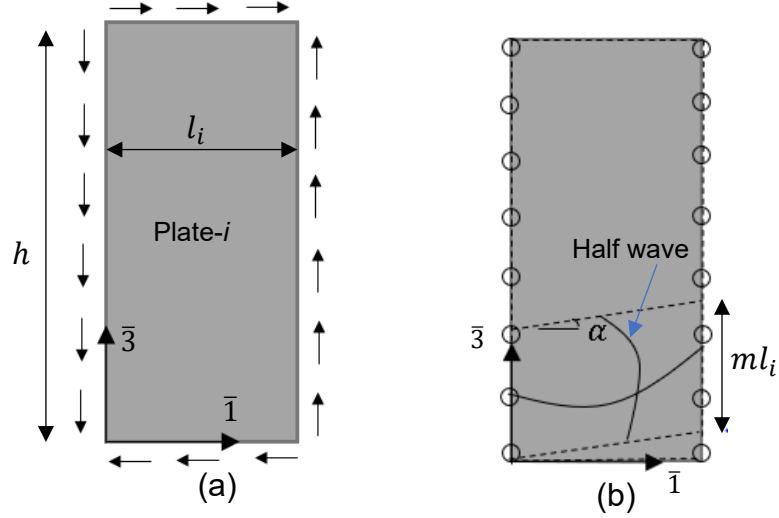


Fig. 5.5: (a) Composite plate subjected to in-plane shear (b) rotationally restrained plate along longer edges.

The boundary conditions along the rotationally restrained edges of the plate can be written as (Qiao & Huo 2011):

$$\bar{u}_2(0, \bar{x}_3) = 0, \quad \bar{u}_2(l_i, \bar{x}_3) = 0, \quad (5.23)$$

$$M_{11}(0, \bar{x}_3) = -\bar{D}_{16} \left(\frac{\partial^2 \bar{u}_2}{\partial \bar{x}_1 \partial \bar{x}_3} \right)_{\bar{x}_1=0} - \bar{D}_{13} \left(\frac{\partial^2 \bar{u}_2}{\partial \bar{x}_3^2} \right)_{\bar{x}_1=0} - \bar{D}_{11} \left(\frac{\partial^2 \bar{u}_2}{\partial \bar{x}_1^2} \right)_{\bar{x}_1=0} = -k_1 \left(\frac{\partial \bar{u}_2}{\partial \bar{x}_1} \right)_{\bar{x}_1=0}, \quad (5.24)$$

$$M_{11}(l_i, \bar{x}_3) = -\bar{D}_{16} \left(\frac{\partial^2 \bar{u}_2}{\partial \bar{x}_1 \partial \bar{x}_3} \right)_{\bar{x}_1=l_i} - \bar{D}_{13} \left(\frac{\partial^2 \bar{u}_2}{\partial \bar{x}_3^2} \right)_{\bar{x}_1=l_i} - \bar{D}_{11} \left(\frac{\partial^2 \bar{u}_2}{\partial \bar{x}_1^2} \right)_{\bar{x}_1=l_i} = k_1 \left(\frac{\partial \bar{u}_2}{\partial \bar{x}_1} \right)_{\bar{x}_1=l_i}, \quad (5.25)$$

where \bar{D}_{ij} is the element of the plate bending stiffness matrix defined with respect to the $(\bar{1}, \bar{2}, \bar{3})$ coordinate system and k_1 is the stiffness of the edge rotational restraint due to unbuckled adjacent plate or plates. Simplifying the Eqs. (5.24) - (5.25) under the assumption of cylindrical bending (Qiao & Huo 2011) and with the substitution of Eq. (5.22), we will get:

$$R = \frac{1}{1 + \frac{4\pi \bar{D}_{11}}{lk_1}}, \quad (5.26)$$

where k_1 is the stiffness of the rotational restrain of longer edges due to unbuckled adjacent plate or plates. When $k_1 = 0 \rightarrow R = 0$, then simply supported conditions exist along all edges. The Rayleigh-Ritz method based solution for the buckling problem can be conveniently formulated using principle of minimum energy. Now total potential energy of the plate (Fig. 5.5) in equilibrium at the buckled state can be written as sum of strain energy due to bending (U_b), strain energy stored in the rotational spring (U_r) and the work done (V):

$$\Pi = U_b + U_r + V, \quad (5.27)$$

where;

$$U_b = \frac{1}{2} \iint \bar{D}_{11} \left(\frac{\partial^2 \bar{u}_2}{\partial \bar{x}_1^2} \right)^2 + 2\bar{D}_{13} \frac{\partial^2 \bar{u}_2}{\partial \bar{x}_1^2} \frac{\partial^2 \bar{u}_2}{\partial \bar{x}_3^2} + \bar{D}_{33} \left(\frac{\partial^2 \bar{u}_2}{\partial \bar{x}_3^2} \right)^2 + 4\bar{D}_{16} \frac{\partial^2 \bar{u}_2}{\partial \bar{x}_1^2} \frac{\partial^2 \bar{u}_2}{\partial \bar{x}_1 \partial \bar{x}_3} + 4\bar{D}_{36} \frac{\partial^2 \bar{u}_2}{\partial \bar{x}_3^2} \frac{\partial^2 \bar{u}_2}{\partial \bar{x}_1 \partial \bar{x}_3} + 4\bar{D}_{66} \left(\frac{\partial^2 \bar{u}_2}{\partial \bar{x}_1 \partial \bar{x}_3} \right)^2 d\bar{x}_1 d\bar{x}_3, \quad (5.28)$$

$$U_r = \frac{1}{2} \int k_1 \left(\frac{\partial \bar{u}_2}{\partial \bar{x}_1} \right)_{\bar{x}_1=0}^2 + k_1 \left(\frac{\partial \bar{u}_2}{\partial \bar{x}_1} \right)_{\bar{x}_1=l_i}^2 d\bar{x}_3, \quad (5.29)$$

$$V = \iint \bar{F}_{13} \frac{\partial \bar{u}_2}{\partial \bar{x}_1} \frac{\partial \bar{u}_2}{\partial \bar{x}_3} d\bar{x}_1 d\bar{x}_3. \quad (5.30)$$

Substituting the displacement function (Eq. (5.22)) into Eq. (5.28) and then getting the first variation of total potential energy of the plate gives the condition for the minimum energy:

$$\delta \Pi = \delta U_b + \delta U_r + \delta V = 0. \quad (5.31)$$

By simplifying Eq. (5.31), the shear buckling load of the plate can be determined as:

$$\bar{F}_{13} = \frac{\pi^2}{l^2} \left[\left(\frac{\alpha^3}{2m^2} + \frac{m^2}{2\alpha} + 3\alpha \right) \bar{D}_{11} + \frac{\bar{D}_{33}}{2m^2\alpha} + \left(\frac{\alpha}{m^2} + \frac{1}{\alpha} \right) \bar{D}_{13} - \left(\frac{2\alpha^2}{m^2} + \frac{6\pi^2}{l^2} \right) \bar{D}_{16} - \frac{2\bar{D}_{36}}{m^2} + \left(\frac{2\alpha}{m^2} + \frac{2}{\alpha} \right) \bar{D}_{66} \right] + \frac{3\pi^3 R^2}{2l^2 \alpha (3\pi + R_n)} \left[(6\alpha^2 + 26m^2) \bar{D}_{11} + 2\bar{D}_{13} - 12\alpha \bar{D}_{16} + 4\bar{D}_{66} + \frac{4k_1 m^2 l (-1+R)^2}{\pi^2 R^2} \right], \quad (5.32)$$

where;

$$R_n = 32R - 6\pi R - 32R^2 + 12\pi R^2. \quad (5.33)$$

In order to find the minimum critical shear buckling load \bar{F}_{cr} , Eq. (5.32) has to be minimised with respect to two unknowns α and m . A numerical solution procedure is implemented using MATLAB 'fmincon' function to get the critical skew angle α_{cr} and critical aspect ratio m_{cr} . The upper and lower limits for the α and m are defined as $[0, \pi/2]$ and $[0, h/l_i]$ respectively for positive shear load and $[-\pi/2, 0]$ and $[0, h/l_i]$ respectively for the negative shear load acting on the plate. Plate may subject to positive or negative shear depending on the applied global shear strain and the plate position in the RVE.

5.2.3 Determination of rotational stiffness

Depending on the shear load carried by each plate, core walls may not buckle simultaneously. Therefore, when one or more plates buckle (referred to as 'critical plate/plates' hereafter) at a time, other adjacent non-buckled plate or plates (referred to as 'restraining plate/plates' hereafter) restrain the rotation of the critical plate (or plates). Therefore, the boundary of the critical plate should be considered to lie between simply-supported (i.e. no restrain against the rotation at the boundaries) and fixed-supported (i.e. fully clamped against the rotation at the boundaries) for more accurate predictions. The effect of the rotational restraint provided by the restraining plates at the boundaries of the critical plates against buckling should be considered. The critical plates and restraining plates of the RVE could be identified based on the predictions of shear buckling strain for each plate, considering all the edges of plates are simply-supported in Eq. (5.21). Rotational stiffness provided by the restraining plates can be conservatively written in the following form assuming cylindrical bending (Kollár 2003):

$$k_1 = \frac{c(\bar{D}_{11})_{rs}}{l} \frac{1}{r_a}, \quad (5.34)$$

where c can be conservatively assumed to be equal to 2 when the restraining plate is subjected to the equal and opposite moment, $(\bar{D}_{11})_{rs}$ is the bending stiffness of the restraining plate and r is the amplification factor depending on the loading on the restraining plate. The factor r is defined as (Kollár 2003):

$$r_a = \frac{1}{1 - \frac{(\bar{F}_{13})_{rs}^{ss}}{(\bar{F}_{cr})_{rs}^{ss}}}, \quad (5.35)$$

the ratio $(\bar{F}_{13})_{rs}^{SS}/(\bar{F}_{cr})_{rs}^{SS}$ being defined as follows:

$$\frac{(\bar{F}_{13})_{rs}^{SS}}{(\bar{F}_{cr})_{rs}^{SS}} = \frac{\bar{A}_{66}(\bar{\gamma}_{13})_{rs}^{SS}}{\bar{A}_{66}(\bar{\gamma}_{cr})_{rs}^{SS}} = \frac{(\bar{\gamma}_{13})_{rs}^{SS}}{(\bar{\gamma}_{cr})_{rs}^{SS}}, \quad (5.36)$$

where $(\bar{F}_{cr})_{rs}^{SS}$ is the critical shear buckling load of restraining plate with all boundaries simply-supported and $(\bar{F}_{13})_{rs}^{SS}$ is the shear load carried by the restraining plate at the time of buckling of the critical plate considering simply supported boundaries. Two examples are presented in the following to illustrate the calculation of rotational stiffness k_1 for the critical plate of the RVE (Fig. 5.2):

1. If plate-II and plate-III (critical plates) buckle simultaneously before plate-I (restraining plate), then plate-I will restrain the rotation of plate-II and plate-III.

Rotational stiffness provided by the plate-I can be determined as follows:

$$k_1 = \frac{1}{2} \frac{2(\bar{D}_{11})_{p1}}{l_1} \frac{1}{r_{p1}}, \quad (5.37)$$

where $(\bar{D}_{11})_{p1}$ and r_{p1} are the bending stiffness and amplification factor of the plate-I.

2. If plate-III (critical plate) only buckles first, then plate-I and plate-II (restraining plates) together will restrain the rotation of plate-I. Rotational stiffness provided by the restraining plates can be determined as follows:

$$k_1 = \frac{2(\bar{D}_{11})_{p2}}{l_2} \frac{1}{r_{p2}} + \frac{2(\bar{D}_{11})_{p3}}{l_3} \frac{1}{r_{p3}}. \quad (5.38)$$

Similar way, other scenarios can be considered by identifying the critical plate and restraining plates of the RVE. Once we determine the rotational stiffness of the critical plate, then critical shear buckling shear strain of the honeycomb can be calculated as illustrated using flowchart in Fig.5.6.

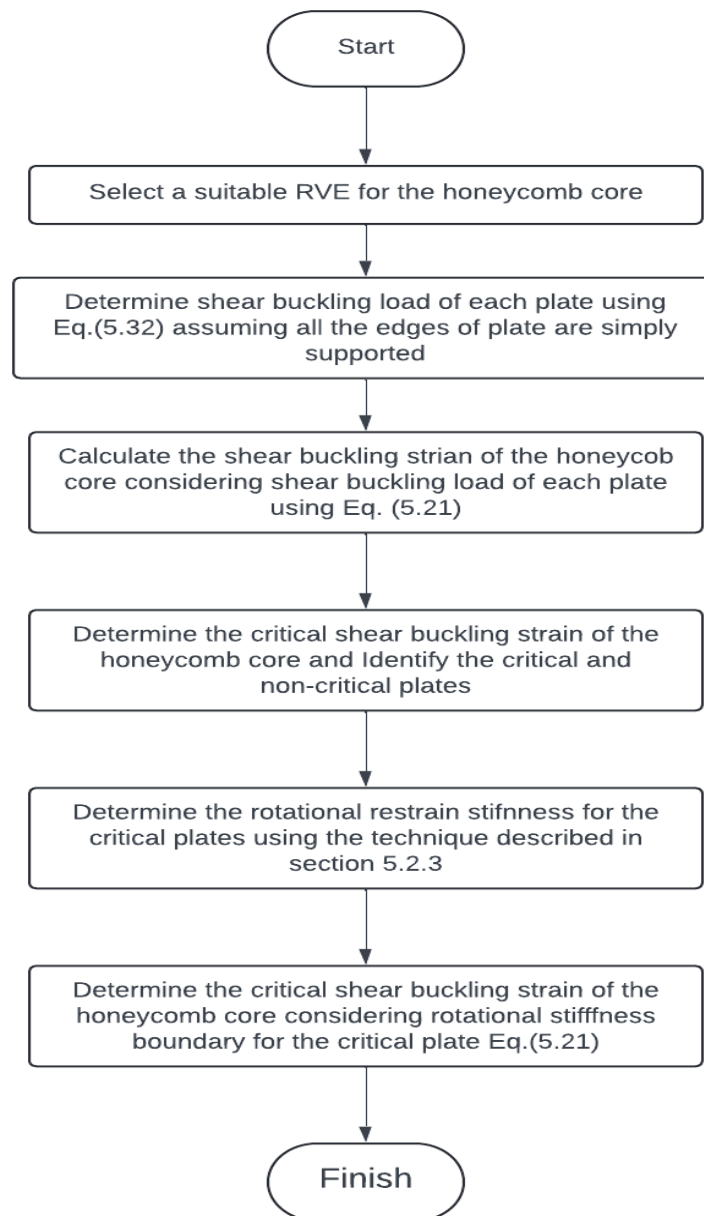


Fig. 5.6: Flowchart for the calculation of critical shear buckling strain of a honeycomb core.

5.3 Theoretical analysis

5.3.1 Hexagonal core with identical plates

For simplicity, it is assumed that all the plates in the RVE (Fig. 5.7) have an identical fibre layer arrangement, length (l) and thickness (t). Typical deformed configurations of regular hexagonal core ($\theta = 120^\circ$) in Fig. 5.6 illustrate the

displacements of each plate under different global shear strains of the RVE. For a RVE subjected to the shear strain of γ_{13} (Fig. 5.7(a)), only the plate-II and plate-III carry the load, and the plate-I does not take any shear load. Plate-III and plate-II are subject to positive shear and negative shear, respectively. Since the magnitudes of the shear strains are equal, both plates will buckle simultaneously if the plates are identical and without any bend-twist coupling. This is not true when plates are fabricated using angle-ply laminates consisting of bend-twist coupling. In such a case, shear buckling loads for the plates will be different depending on the fibre orientations and the direction of shear in the plate due to applied global strain. When the RVE is subjected to a shear strain γ_{23} (Fig. 5.7(b)), all the plates experience positive shear and plate-I is subjected to the largest shear strain. Therefore, plate-I will buckle first because the material and geometric parameters are identical for all three plates. Similarly, when the RVE is subjected to combined shear of $\gamma_{13}/\gamma_{23} = 1$, plate-III will buckle first.

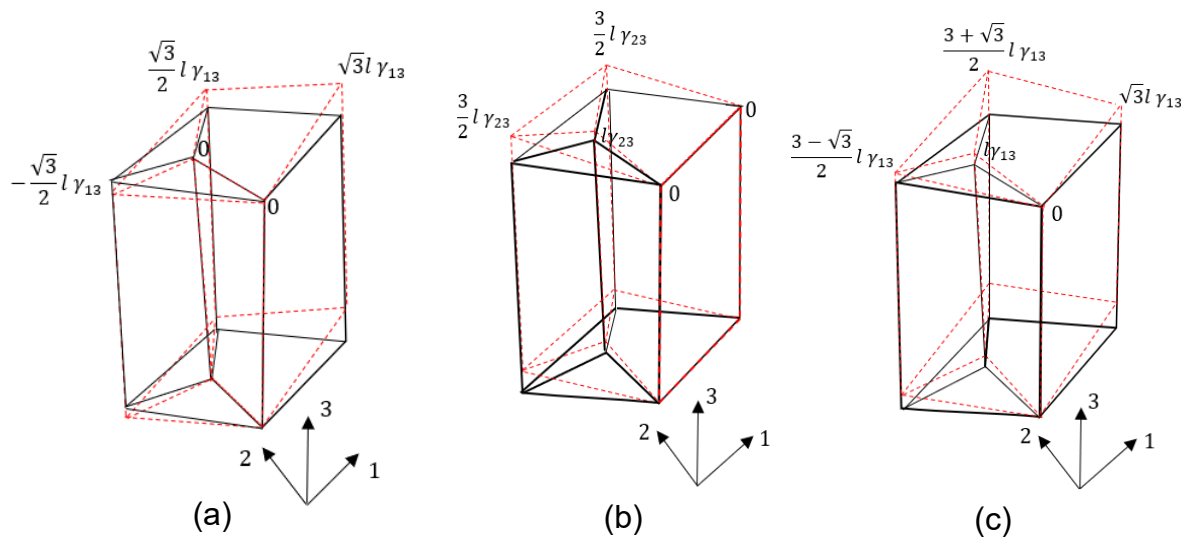


Fig. 5.7: Deformed configuration of hexagonal RVE with identical composite plates under the shear load (a) γ_{13} (b) γ_{23} and (c) $\gamma_{13}/\gamma_{23} = 1$.

It can be noted that depending on applied shear strain ratio on the RVE, the critical plate of RVE may be different which can be easily identified using a phase failure map. As all plates are identical in this case, the magnitude of the term $\bar{F}_{cr}^i/\bar{A}_{66}^i$ (Eq. (5.20)) is equal for all three plates if the plates are perfectly orthotropic laminates. Then Eq. (5.21) can be simplified to a form in Eq. (5.39) to plot the phase failure map in Fig 5.8.

$$\gamma_{cr} = \min \left\{ \left| \frac{\bar{F}_{cr}^I}{k\bar{A}_{66}^I} \right|, \left| \frac{2\bar{F}_{cr}^{II}}{\bar{A}_{66}^{II}(k-\sqrt{3})} \right|, \left| \frac{2\bar{F}_{cr}^{III}}{\bar{A}_{66}^{III}(k+\sqrt{3})} \right| \right\}. \quad (5.39)$$

From the phase failure map in Fig. 5.8, we can identify that if:

- $k > \sqrt{3}$ or $k < -\sqrt{3}$, then plate-I buckles first,
- $k = 0$, then plate-II and plate-III buckle simultaneously before plate-I,
- $k = \sqrt{3}$, then plate-I and plate-II buckle simultaneously before plate-III,
- $k = -\sqrt{3}$, then plate-I and plate-III buckle simultaneously before plate-II,
- $0 < k < \sqrt{3}$, then only plate-II buckles first, and
- $-\sqrt{3} < k < 0$, then plate-III buckles first.

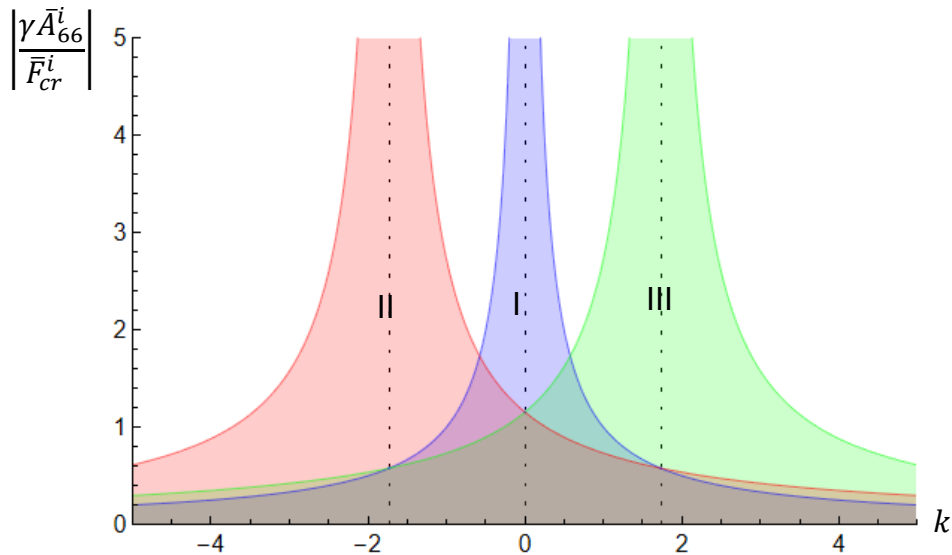


Fig. 5.8: Failure phase map of the hexagonal core with identical orthotropic plates.

The failure map in Fig. 5.8 shows a coloured region for each plate where the plate is safe against the buckling under the applied shear load. The common intersecting region of all three plates shows a feasible design region where the honeycomb core is safe against shear buckling.

5.3.2 Hexagonal core with non-identical plates

If plate-II and plate-III have an identical fibre layer arrangement, length (l) and thickness (t), and plate-I has a double thickness ($2t$), same length and symmetric fibre

layout of plate-I and plate II, then deformed configurations of RVE of regular hexagonal core ($\theta = 120^\circ$) for different shear strain conditions can be plotted as in Fig. 5.9. The plate-II and plate-III will buckle simultaneously under both the shear strains γ_{13} and γ_{13} . However, when RVE is subjected to γ_{23} , both plates experience positive shear in contrast to the γ_{13} (Figs. 5.9(a) - (b)). Like in the RVE with identical plates, in this case also, Plate-III buckles first under combined shear $\gamma_{13}/\gamma_{13} = 1$; however, the ratios of the shear strains between the plates are different to those in the RVE with identical plates. It can also be identified from Fig. 5.7 that nodal points of the deform configurations are coplanar in the hexagonal RVE with identical plates. However, in the case where Plate-I is different to the Plate II and Plate-III, the nodal points of the deform configurations are not coplanar (Fig.9(b) - (c)), which is not compatible with the deformation of the face sheets in the sandwich panels. Therefore, the honeycomb core with non-identical plates is subjected to bending due to a skin effect (Grediac 1993) of the sandwich panel. This effect is minimal if the bending rigidity of the face sheets (typically thin face sheets) is very small in comparison to the bending rigidity of the core (typically for a thick core).

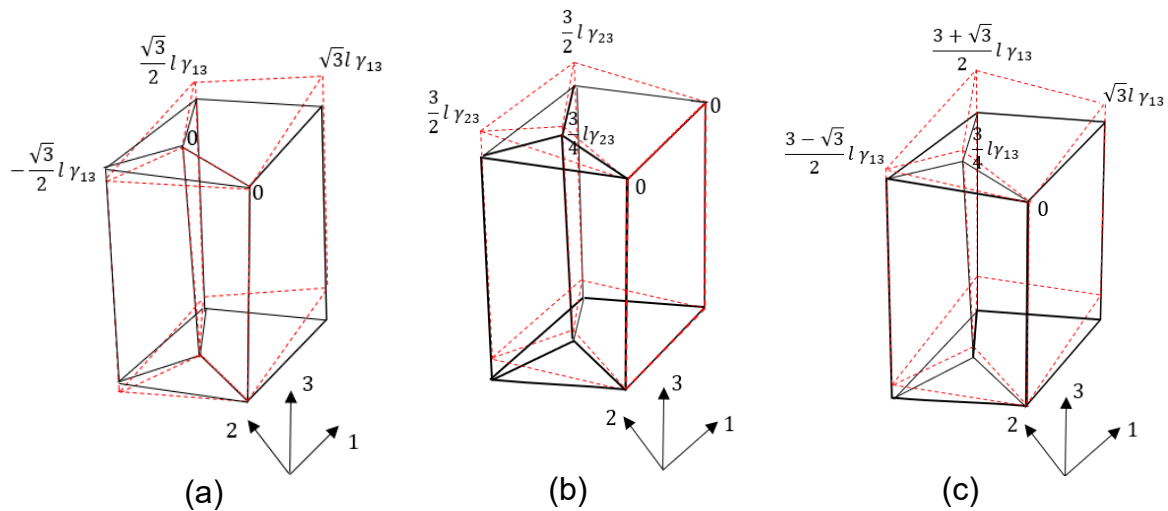


Fig. 5.9: Deformed configuration of hexagonal RVE with non-identical composite plates under the shear load (a) γ_{13} (b) γ_{23} and (c) $\gamma_{13}/\gamma_{23} = 1$.

For the regular hexagonal core, the critical shear strain γ_{cr} of the core for the shear buckling can be derived from Eq. (5.21) as:

$$\gamma_{cr} = \min \left\{ \left| \frac{2\bar{F}_{cr}^I}{\bar{A}_{66}^I 3k} \right|, \left| \frac{4\bar{F}_{cr}^{II}}{\bar{A}_{66}^{II} (3k - 2\sqrt{3})} \right|, \left| \frac{4\bar{F}_{cr}^{III}}{\bar{A}_{66}^{III} (3k + 2\sqrt{3})} \right| \right\}. \quad (5.40)$$

Here, for the purpose of plotting the failure phase map (Fig. 5.10), additionally, we also assume that $\bar{F}_{cr}^I = 8\bar{F}_{cr}^{II}$. This is true when the RVE consists of plates having all the plies arranged in the same orientation. However, this may or may not be true for the other fibre lay-up of the plates. Subjected to the condition above, the failure phase map can be used as a theoretical guidance to identify the critical plates and the critical shear strain.

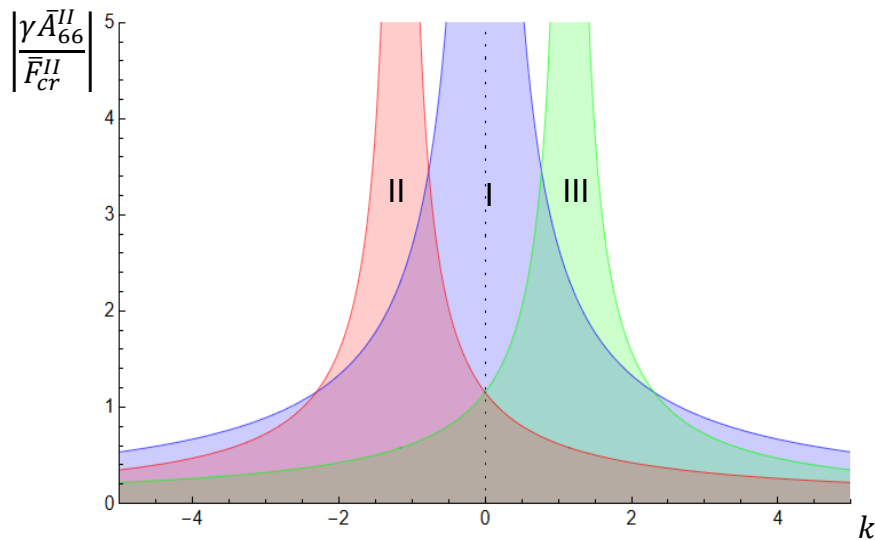
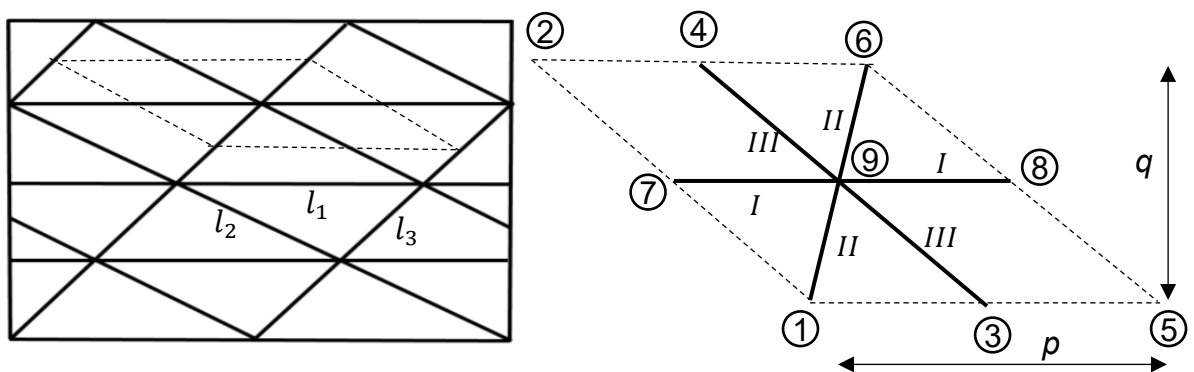
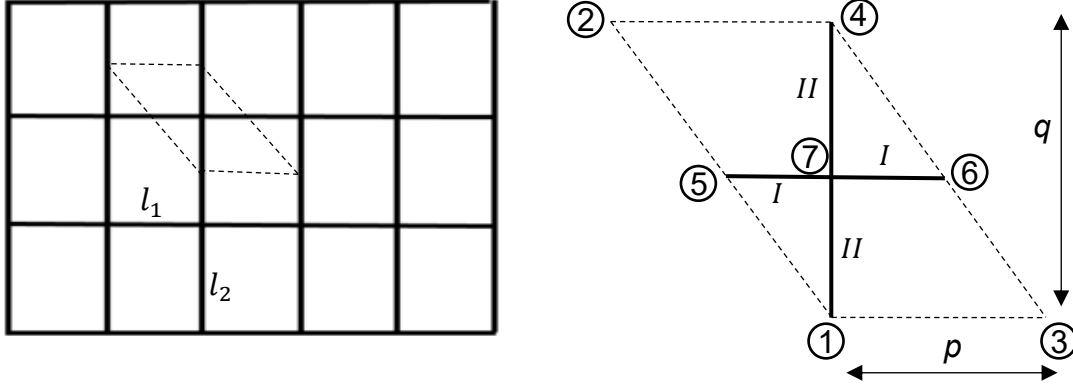


Fig. 5.10: Failure phase map of the hexagonal core with non-identical orthotropic plates. Plate-I has double thickness of plate-II and plate-III.

5.4 Shear buckling of honeycomb core with different shapes



(a)



(b)

Fig. 5.11: RVEs of (a) triangular core (b) rectangular core.

Following the same procedure as in section 5.2.1, we can derive the equations for the critical shear strain of the honeycomb cores with different shapes. For rectangular and triangular cores, RVEs in Fig. 5.11 are used to analyse and to obtain the required equations for the critical shear strain of the cores. For the triangular core, positive direction - $\bar{1}$ is defined for the plates-I, plates-II, and plates-III from nodes 7 to 9 (or 9-8), 1 to 9 (or 9-6) and 3 to 9 (or 9-4) respectively (Fig. 5.11(a)). For the rectangular core, positive direction $\bar{1}$ is defined for the plates-I and plates-II from nodes 5 to 7 (or 7-6) and 1 to 7 (or 7-4) respectively (Fig. 5.11(b)).

For the triangular core in Fig. 5.11(a) with all members having identical laminate, strain at each plate can be derived as:

$$\bar{\gamma}_{13}^I = \gamma_{13}, \quad (5.41)$$

$$\bar{\gamma}_{13}^{II} = \frac{\gamma_{13}(l_1 + l_3 \cos(\theta + \beta) + kl_2 \sin\beta)}{l_2}, \quad (5.42)$$

$$\bar{\gamma}_{13}^{III} = \frac{\gamma_{13}(l_3 \cos(\theta + \beta) + kl_2 \sin\beta)}{l_3}, \quad (5.43)$$

where;

$$\theta = \cos^{-1} \left(\frac{(l_2^2 + l_3^2) - l_1^2}{2l_2l_3} \right) \text{ and} \quad (5.44)$$

$$\beta = \cos^{-1} \left(\frac{(l_1^2 + l_2^2) - l_3^2}{2l_1l_2} \right). \quad (5.45)$$

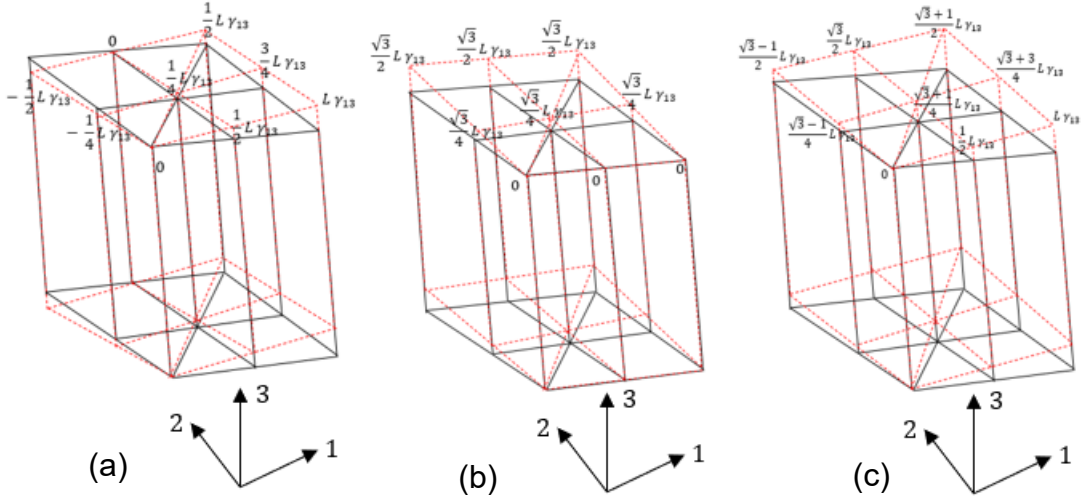


Fig. 5.12: Deformed configuration of triangular RVE with identical composite plates under the shear load (a) γ_{13} (b) γ_{23} and (c) $\gamma_{13}/\gamma_{23} = 1$.

Figure 5.12 illustrates the deformed configuration of an equilateral triangular core consisting of identical plates. In the presence of the γ_{13} global shear condition, all plates carry the shear load. However, plate-I emerges as the critical plate since it bears the largest shear load among the three plates in the RVE. Under the γ_{23} global shear condition, both plate-II and plate-III carry equal shear loads, while plate-I carries none, leading to the simultaneous buckling of both plates, especially if they are made of orthotropic laminates. In combined shear conditions, plate-II carries the largest shear load among the three plates, thus determining the core's shear buckling strength. Critical shear buckling strains under various shear strain conditions can be predicted using a phase failure map (illustrated in Fig. 5.13).

For an equilateral triangular core with identical laminates for all the plates, the critical shear strain of core γ_{cr} can be written as:

$$\gamma_{cr} = \min \left\{ \left| \frac{\bar{F}_{cr}^I}{\bar{A}_{66}^I} \right|, \left| \frac{2\bar{F}_{cr}^{II}}{\bar{A}_{66}^{II}(1+\sqrt{3}k)} \right|, \left| \frac{2\bar{F}_{cr}^{III}}{\bar{A}_{66}^{III}(-1+\sqrt{3})} \right| \right\}. \quad (5.46)$$

The failure phase map in Fig. 5.11 can be plotted using the Eq. (5.46).

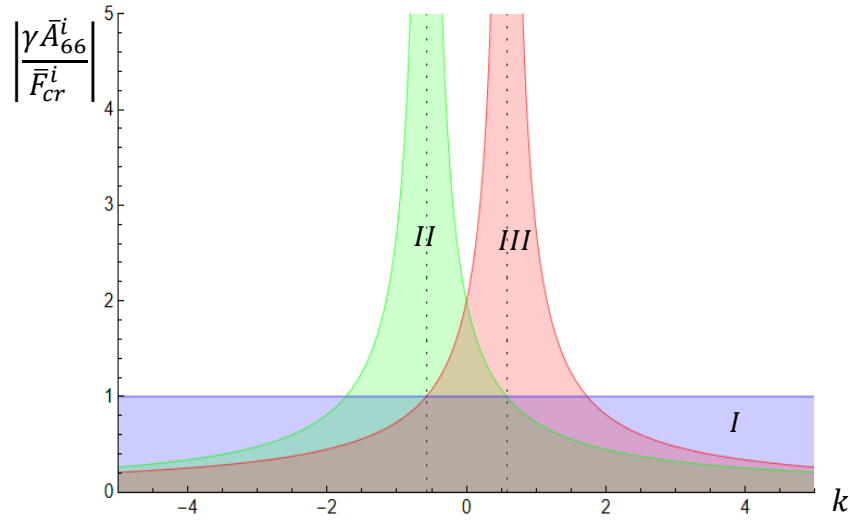


Fig. 5.13: Failure phase map of the triangular core with identical orthotropic plates.

From the failure map in Fig.13, it can be identified that if,

- $-\frac{1}{\sqrt{3}} < k < \frac{1}{\sqrt{3}}$, then the plate-I buckles first,
- $k = \frac{1}{\sqrt{3}}$, then plate-I and plate-II buckle simultaneously,
- $k = -\frac{1}{\sqrt{3}}$, then plate-I and plate-III buckle simultaneously,
- $k > \frac{1}{\sqrt{3}}$, then plate-II buckles first, and
- $k < -\frac{1}{\sqrt{3}}$, then only plate-III buckles first.

For rectangular honeycomb core (Fig. 5.11(b)), regardless of length and stiffness ratio of the plates, the applied shear strain in each direction is equal to shear strain at each plate when the plates are orthotropic.

$$\bar{\gamma}_{13}^I = \gamma_{13}, \quad (5.47)$$

$$\bar{\gamma}_{13}^{II} = k\gamma_{13}. \quad (5.48)$$

This can be understood from the Fig. 5.14 which illustrates the deformed configuration of a square core under different shear strain conditions.

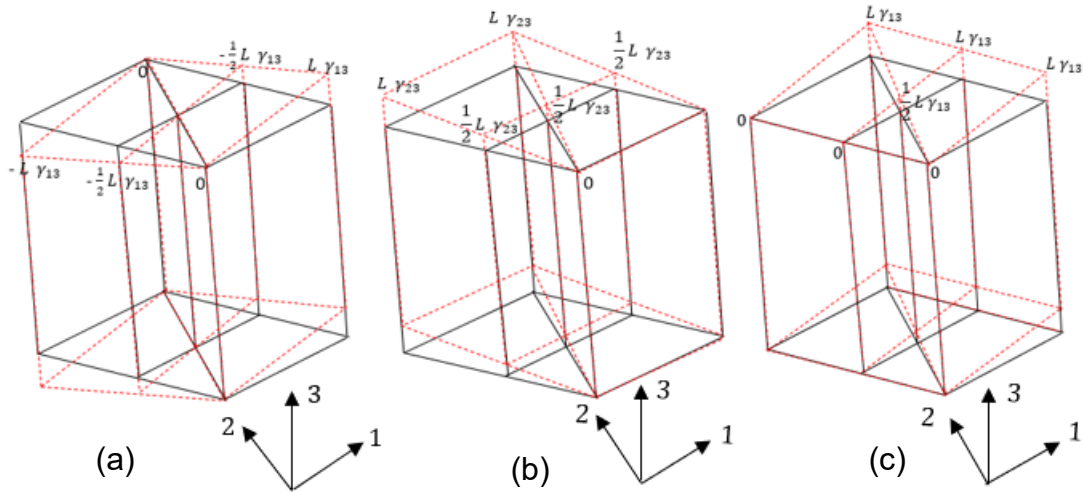


Fig. 5.14: Deformed configuration of square RVE with identical composite plates under the shear load (a) γ_{13} (b) γ_{23} and (c) $\gamma_{13}/\gamma_{23} = 1$.

5.5 Validation of the proposed approach

In order to validate the proposed semi-analytical approach, results are compared with the predictions from the linear buckling analysis of the RVEs carried out using ABAQUS software. RVEs of the hexagonal core are modelled with S4 shell elements and material properties are assigned using composite shell section feature available in ABAQUS. The fibre orientation of each lamina is defined according to positive local direction of each plate considered in this study. The element size of 5mm was selected following a mesh convergence study. Prescribed displacement boundary conditions are used to apply the shear load on models. Shear loads are applied to represent the following average global shear strain conditions on the RVEs: (a) γ_{13} , (b) γ_{23} , and (c) $\gamma_{13}/\gamma_{23} = 1$ (Fig. 5.15). Critical shear buckling strains and the critical plate of the RVEs are determined for positive and negative shear loading under above different scenarios.

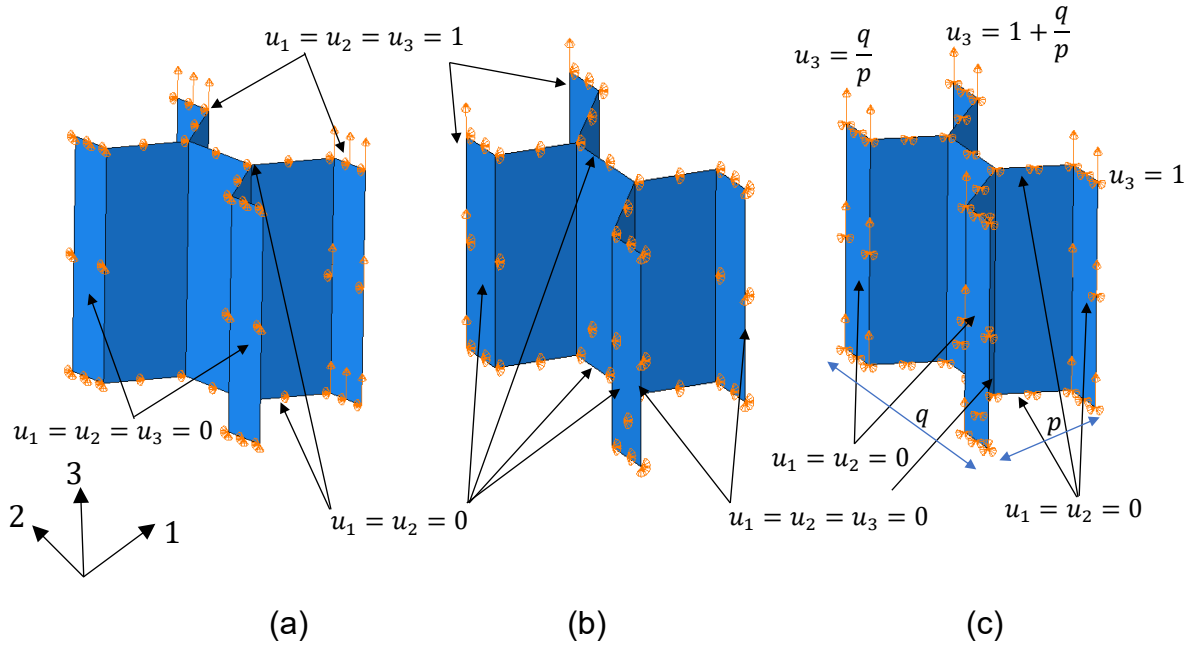


Fig. 5.15: FE models analysed for the shear load (a) γ_{13} (b) γ_{23} and (c) $\gamma_{13}/\gamma_{23} = 1$.

Elastic properties of E-glass/Epoxy used for composite wall honeycomb cores with respect to principal axes of the lamina in the analysis are $\bar{E}_L = 38600Nmm^{-2}$, $\bar{E}_T = 8270Nmm^{-2}$, $\bar{G}_{LT} = 4140Nmm^{-2}$, and $\bar{\nu}_{LT} = 0.26$. The hexagonal core wall lengths are equal and taken as $l = 50mm$, while the height of the core (h) is $150mm$. The thickness of plate-I of the hexagonal core (Fig. 5.2) is double the thickness of the inclined plates (Plate II and III). In this study hexagonal core having two different relative core densities (ρ^*) 0.0722 and 0.036 are considered for the analysis. The thicknesses of plates are chosen to satisfy the requirement of the relative core density(ρ^*). Fibre lay-ups and orientations defined in Table 5.1 for the inclined plates are assigned with respect to the local axes of the plates and fibre layer sequence and orientations of the plate-I are assumed to be symmetrical lay-up of the inclined plates. Each ply of the laminate has an equal thickness.

Table 5.1: Material configurations of the core walls.

Material lay-up	Fibre orientation ($^\circ$)
1	0/0/90/0/0
2	0/90/90/90/0
3	90/0/0/0/90
4	45/-45/0/-45/45
5	45/-45/90/-45/45

5.5.1 Predictions of the shear buckling for the hexagonal core

The proposed approach is used to predict the critical shear buckling load of the hexagonal core, assuming the boundaries of core walls are simply-supported (SS) and rotationally restrained (RR) along longer edges. Predicted results for the hexagonal core with different material configurations are then compared with results from the FE analysis to validate the proposed approach. Tables 5.2-5.7 show the comparison of the results for the hexagonal core with relative core density (ρ^*) 0.072 and Tables 5.8 – 5.13 show the comparisons for the relative core density (ρ^*) 0.036. Both positive and negative critical strains of the hexagonal core have been calculated and compared against the FE results. For the buckling under negative shear strains of the hexagonal core, the absolute values of critical shear strains are shown in the Tables.

Table 5.2: Critical shear strain of the hexagonal core ($\rho^* = 0.072$) under $\gamma_{13} = \gamma$ (positive) and $\gamma_{23} = 0$.

Fibre lay-up	Critical shear buckling strain			Error%		Critical plate	
	Proposed-SS(a)	Proposed-RR(b)	FE(c)	$\frac{(a-c)}{c}$ %	$\frac{(b-c)}{c}$ %	Proposed	FE
1	0.06476	0.08574	0.09076	-28.6	-5.5	II& III	II&III
2	0.06226	0.08064	0.09007	-30.9	-10.5	II& III	II&III
3	0.04234	0.06087	0.06813	-37.9	-10.7	II& III	II&III
4	0.01884	0.02797	0.03014	-37.5	-7.2	III	III
5	0.01867	0.02703	0.03000	37.8	-9.9	III	III
6	0.01636	0.02388	0.02852	-42.7	-16.3	III	III

Table 5.3: Critical shear strain of the hexagonal core ($\rho^* = 0.072$) under $\gamma_{13} = \gamma$ (negative) and $\gamma_{23} = 0$.

Fibre lay-up	Critical shear buckling strain			Error %		Critical plate	
	Proposed-SS(a)	Proposed-RR(b)	FE(c)	$\frac{(a-c)}{c}$ %	$\frac{(b-c)}{c}$ %	Proposed	FE
1	0.06476	0.08574	0.09076	-28.6	-5.5	II& III	II&III

2	0.06226	0.08064	0.09007	-30.9	-10.5	II& III	II&III
3	0.04234	0.06087	0.06813	-37.9	-10.7	II& III	II&III
4	0.01884	0.02797	0.03014	-37.5	-7.2	II	II
5	0.01867	0.02703	0.03000	-37.8	-9.9	II	II
6	0.01636	0.02388	0.02852	-42.7	-16.3	II	II

Table 5.4: Critical shear strain of the hexagonal core ($\rho^* = 0.072$) under $\gamma_{13} = 0$ and $\gamma_{23} = \gamma$ (positive).

Fibre lay-up	Critical shear buckling strain			Error %		Critical plate	
	Proposed-SS(a)	Proposed-RR(b)	FE(c)	$\frac{(a-c)}{c} \%$	$\frac{(b-c)}{c} \%$	Proposed	FE
1	0.07478	0.09513	0.10400	-28.1	-8.5	II& III	II&III
2	0.07189	0.08900	0.10333	-30.4	-13.9	II& III	II&III
3	0.04889	0.06837	0.07827	-37.5	-12.6	II& III	II&III
4	0.02175	0.02881	0.03387	-35.8	-14.9	II&III	II&III
5	0.02155	0.02802	0.03347	-35.6	-16.3	II&III	II&III
6	0.01889	0.02436	0.03367	-43.9	-27.6	II&III	II&III

Table 5.5: Critical shear strain of the hexagonal core ($\rho^* = 0.072$) under $\gamma_{13} = 0$ and $\gamma_{23} = \gamma$ (negative).

Fibre lay-up	Critical shear buckling strain			Error %		Critical plate	
	Proposed-SS(a)	Proposed-RR(b)	FE(c)	$\frac{(a-c)}{c} \%$	$\frac{(b-c)}{c} \%$	Proposed	FE
1	0.07478	0.09513	0.10400	-28.1	-8.5	II& III	II&III
2	0.07189	0.08900	0.10333	-30.4	-13.9	II& III	II&III
3	0.04889	0.06837	0.07827	-37.5	-12.6	II& III	II&III
4	0.03924	0.04944	0.05467	-28.2	-9.6	II&III	II&III
5	0.03900	0.04738	0.05400	-27.8	-12.3	II&III	II&III
6	0.03440	0.04247	0.04200	-18.1	1.1	II&III	II&III

Table 5.6: Critical shear strain of the hexagonal core ($\rho^* = 0.072$) under $\gamma_{13} = \gamma$ and $\gamma_{23} = \gamma$ (positive).

Fibre	Critical shear buckling strain	Error %	Critical plate
-------	--------------------------------	---------	----------------

lay-up	Proposed- SS(a)	Proposed- RR(b)	FE(c)	$\frac{(a-c)}{c}\%$	$\frac{(b-c)}{c}\%$	Proposed	FE
1	0.03471	0.05036	0.04885	-28.9	3.1	III	III
2	0.03336	0.04760	0.04792	-30.4	-0.7	III	III
3	0.02269	0.03512	0.03614	-37.2	-2.8	III	III
4	0.01010	0.01494	0.01570	-35.7	-4.8	III	III
5	0.01000	0.01445	0.01547	-35.4	-6.6	III	III
6	0.00877	0.01275	0.01467	-40.2	-13.0	III	III

Table 5.7: Critical shear strain of the hexagonal core ($\rho^* = 0.072$) under $\gamma_{13} = \gamma$ (negative) and $\gamma_{23} = \gamma$ (negative).

Fibre lay-up	Critical shear buckling strain			Error %		Critical plate	
	Proposed- SS(a)	Proposed- RR(b)	FE(c)	$\frac{(a-c)}{c}\%$	$\frac{(b-c)}{c}\%$	Proposed	FE
1	0.03471	0.05036	0.04885	-28.9	3.1	III	III
2	0.03336	0.04760	0.04792	-30.4	-0.7	III	III
3	0.02269	0.03512	0.03614	-37.2	-2.8	III	III
4	0.01821	0.02579	0.02552	-28.6	1.1	III	III
5	0.01810	0.02499	0.02506	-27.8	-0.3	III	III
6	0.01597	0.02225	0.02079	-23.2	7.0	III	III

Table 5.8: Critical shear strain of the hexagonal core ($\rho^* = 0.036$) under $\gamma_{13} = \gamma$ (positive) and $\gamma_{23} = 0$.

Fibre lay-up	Critical shear buckling strain			Error %		Critical plate	
	Proposed- SS(a)	Proposed- RR(b)	FE(c)	$\frac{(a-c)}{c}\%$	$\frac{(b-c)}{c}\%$	Proposed	FE
1	0.01619	0.02344	0.02575	-37.1	-9.0	II& III	II&III
2	0.01557	0.02216	0.02540	-38.7	-12.8	II& III	II&III
3	0.01059	0.01592	0.01848	-42.7	-13.8	II& III	II&III
4	0.00471	0.00714	0.00820	-42.6	-12.9	III	III
5	0.00467	0.00695	0.00814	-42.7	-14.6	III	III
6	0.00409	0.00613	0.00774	-47.1	-20.8	III	III

Table 5.9: Critical shear strain of the hexagonal core ($\rho^* = 0.036$) under $\gamma_{13} = \gamma$ (negative) and $\gamma_{23} = 0$.

Fibre lay-up	Critical shear buckling strain			Error %		Critical plate	
	Proposed-SS(a)	Proposed-RR(b)	FE(c)	$\frac{(a-c)}{c}\%$	$\frac{(b-c)}{c}\%$	Proposed	FE
1	0.01619	0.02344	0.02575	-37.1	-9.0	II& III	II&III
2	0.01557	0.02216	0.02540	-38.7	-12.8	II& III	II&III
3	0.01059	0.01592	0.01848	-42.7	-13.8	II& III	II&III
4	0.00471	0.00714	0.00820	-42.6	-12.9	II	II
5	0.00467	0.00695	0.00814	-42.7	-14.6	II	II
6	0.00409	0.00613	0.00774	-47.1	-20.8	II	II

Table 5.10: Critical shear strain of the hexagonal core ($\rho^* = 0.036$) under $\gamma_{13} = 0$ and $\gamma_{23} = \gamma$ (positive).

Fibre lay-up	Critical shear buckling strain			Error %		Critical plate	
	Proposed-SS(a)	Proposed-RR(b)	FE(c)	$\frac{(a-c)}{c}\%$	$\frac{(b-c)}{c}\%$	Proposed	FE
1	0.01870	0.02578	0.02967	-37.0	-13.1	II& III	II&III
2	0.01797	0.02425	0.02900	-38.0	-16.4	II& III	II&III
3	0.01222	0.01809	0.02133	-42.7	-15.2	II& III	II&III
4	0.00588	0.00806	0.00920	-36.0	-12.4	II&III	II&III
5	0.00583	0.00777	0.00907	-35.7	-14.3	II&III	II&III
6	0.00505	0.00679	0.00913	-44.7	-25.6	II&III	II&III

Table 5.11: Critical shear strain of the hexagonal core ($\rho^* = 0.036$) under $\gamma_{13} = 0$ and $\gamma_{23} = \gamma$ (negative).

Fibre lay-up	Critical shear buckling strain			Error %		Critical plate	
	Proposed-SS(a)	Proposed-RR(b)	FE(c)	$\frac{(a-c)}{c}\%$	$\frac{(b-c)}{c}\%$	Proposed	FE
1	0.01870	0.02578	0.02967	-37.0	-13.1	II& III	II&III
2	0.01797	0.02425	0.02900	-38.0	-16.4	II& III	II&III
3	0.01222	0.01809	0.02133	-42.7	-15.2	II& III	II&III
4	0.01061	0.01373	0.01520	-30.2	-9.7	II&III	II&III
5	0.01055	0.01326	0.01500	-29.7	-11.6	II&III	II&III

6	0.00860	0.01062	0.01160	-25.9	-8.5	II&III	II&III
---	---------	---------	---------	-------	------	--------	--------

Table 5.12: Critical shear strain of the hexagonal core ($\rho^* = 0.036$) under $\gamma_{13} = \gamma$ (positive) and $\gamma_{23} = \gamma$ (positive).

Fibre lay-up	Critical shear buckling strain			Error %		Critical plate	
	Proposed-SS(a)	Proposed-RR(b)	FE(c)	$\frac{(a-c)}{c}\%$	$\frac{(b-c)}{c}\%$	Proposed	FE
1	0.00868	0.01259	0.01374	-36.9	-8.4	III	III
2	0.00834	0.01190	0.01339	-37.7	-11.2	III	III
3	0.00567	0.00878	0.00970	-41.5	-9.5	III	III
4	0.00252	0.00374	0.00427	-40.9	-12.6	III	III
5	0.00250	0.00361	0.00416	-39.8	-13.1	III	III
6	0.00219	0.00319	0.00393	-44.2	-18.8	III	III

Table 5.13: Critical shear strain of the hexagonal core ($\rho^* = 0.036$) under $\gamma_{13} = \gamma$ (negative) and $\gamma_{23} = \gamma$ (negative).

Fibre lay-up	Critical shear buckling strain			Error %		Critical plate	
	Proposed-SS(a)	Proposed-RR(b)	FE(c)	$\frac{(a-c)}{c}\%$	$\frac{(b-c)}{c}\%$	Proposed	FE
1	0.00868	0.01259	0.01374	-36.9	-8.4	III	III
2	0.00834	0.01190	0.01339	-37.7	-11.2	III	III
3	0.00567	0.00878	0.00970	-41.5	-9.5	III	III
4	0.00455	0.00645	0.00704	-35.4	-8.5	III	III
5	0.00453	0.00625	0.00693	-34.7	-9.8	III	III
6	0.00399	0.00556	0.00577	-30.9	-3.7	III	III

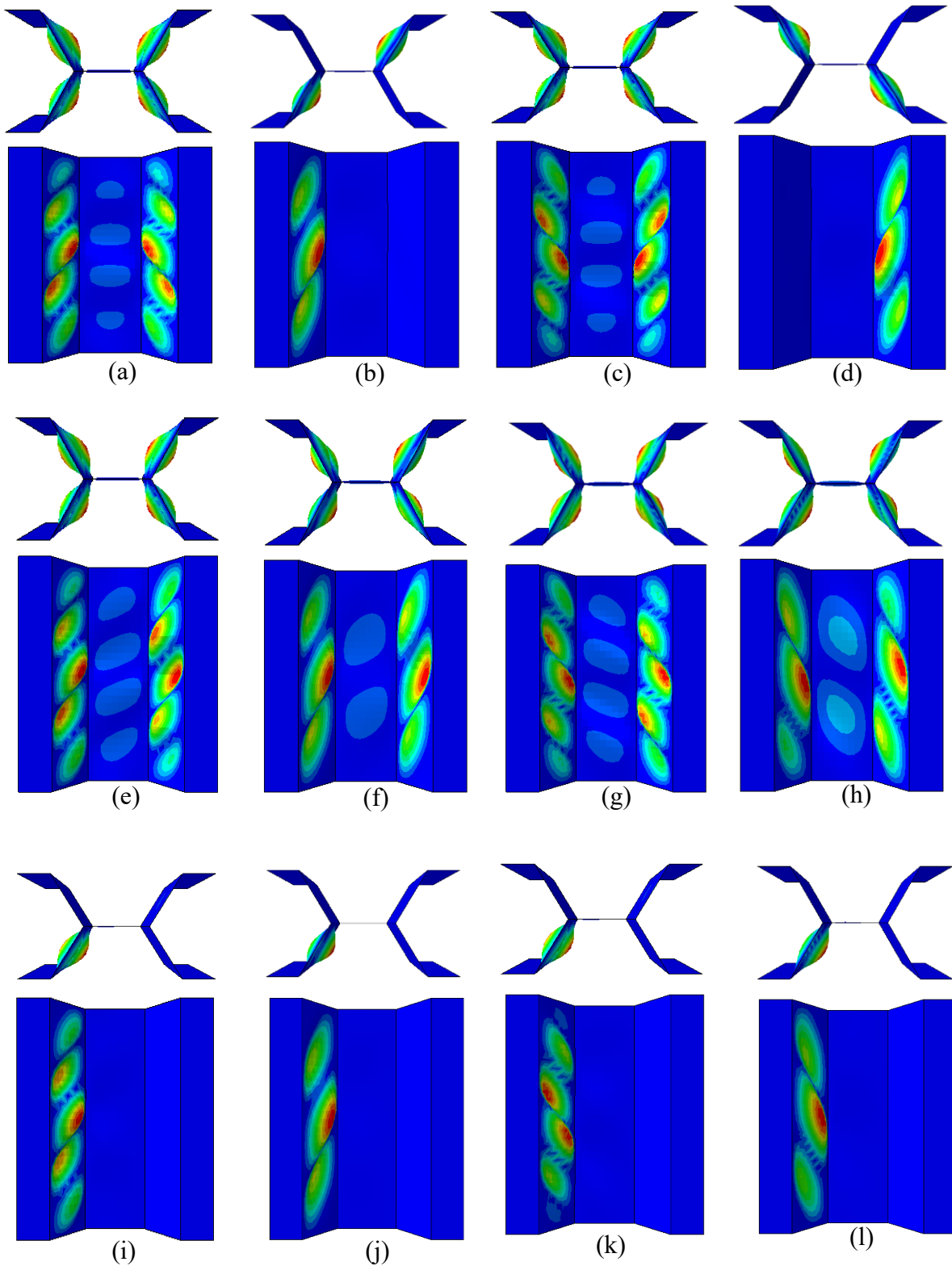


Fig. 5.16: Top view and side view of critical buckling mode shapes for the shear load (a-b) γ_{13} (positive shear), (c-d) γ_{13} (negative shear), (e-f) γ_{23} (positive shear), (g-h) γ_{23} (negative shear), (i-j) $\gamma_{13}/\gamma_{23} = 1$ (positive shear), and (k-l) $\gamma_{13}/\gamma_{23} = 1$ (negative shear). The critical buckling mode shapes are shown for the hexagonal core RVEs with (0/0/90/0/0) and (45/-45/0/-45/45) laminates and relative core density of 0.072. 1st and 3rd critical mode shapes of each row are for (0/0/90/0/0) laminate and 2nd and 4th are for (45/-45/0/-45/45) laminate.

It can be seen from Tables 5.2 – 5.13 that the predictions using the proposed approach give conservative results for all the different cases under the assumption that all the edges of the plates are simply-supported. The error percentage varies from -29% to -47 %, considering two different core densities. On the other hand, except for a few cases of fibre lay-up 6, the predictions are much closer to FE results under the assumption that longer edges of the plates are rotationally restrained. The fibre lay-up 6 is unbalanced and symmetric laminate, causing extensional-shear and bend-twist coupling. Although bend-twist coupling is accounted for in the Eq. (5.32), the extensional-shear coupling is not considered in the shear buckling Eq. (5.32) of the composite plate. The presence of extensional and shear coupling in the laminate tends to underestimate or overestimate the critical strain depending on whether the normal stress caused is tensile or compressive, respectively. In all other fibre lay-ups, the absolute error is less than 16% (Tables 5.2 – 5.13) for all the different load cases and core densities. For the shear load of γ_{13} , the same absolute values of critical shear strains are obtained regardless of the positive and negative direction of applied shear load on the RVE of the hexagonal core for all the different material configurations (Tables 5.2-5.3 & Tables 5.8-5.9). Under this shear loading on the RVE, only inclined plates (Plate II and Plate III) carry the shear load, and one of the inclined plates is under positive shear and the other is under negative shear (Figs. 5.16(a)-(d)). For the cross-ply laminates (fibre lay-up 1-3 in Table 5.1) RVE, both inclined plates buckle simultaneously since the magnitudes of critical shear strains are equal. However, for the RVE having angle-ply laminates (Fibre lay-up 4-6 in Table 5.1), the magnitudes of critical shear strains for the buckling of the inclined plates (plate II and plate III) are different due to effect of bend-twist coupling, therefore only one of the inclined plates which has the lowest critical shear buckling load buckles. When the direction of the shear load on the RVE is changed (positive to negative or vice-versa), other inclined plate buckles at the same absolute critical strain. Therefore, the change in the direction (positive to negative or vice-versa), of the applied shear loading γ_{13} does not change the critical shear buckling strain of the hexagonal core.

For the shear strain of γ_{23} on the RVE, critical shear buckling strain of the hexagonal core with specific fibre lay-up changes depending on the positive and negative direction of the applied shear load (Tables 5.4 - 5.5 & Tables 5.9 - 5.10). Under γ_{23} loading, for all the material configurations and for both negative and positive

shear loading, plate-II and plate-III buckle simultaneously (Figs. 5.16 (e)-(h)), and all the plates experience the strain in the same direction. Therefore, the change in the direction of the applied shear load (positive to negative or vice-versa) on the RVE gives different critical strains for the hexagonal cores with angle-ply laminates due to the effect of bend-twist coupling. However, for the hexagonal core with cross-ply laminates, the same magnitudes of the critical strains are obtained regardless of the direction of loading on the RVE. The difference between the critical shear strains for the positive and negative shear loading on the RVE with the angle-ply laminates is significant (the critical strain for negative shear is approximately 1.7 times the critical strain for the positive shear). Therefore, neglecting bend-twist coupling of laminates will under or overestimate the results for critical shear strain under γ_{23} loading.

Comparing the critical shear strains of the hexagonal core under shear loadings γ_{13} and γ_{23} , a slightly higher results are obtained for the shear load γ_{23} for all fibre lay-ups (Table 5.1) in positive shear and for the cross-ply laminates in negative shear. However, the critical strains of the hexagonal core under negative γ_{23} loading are significantly higher than for negative γ_{13} loading for the angle-ply laminates. In the combined shear loading where γ_{13} and γ_{23} are equal, the buckling behaviour is similar to γ_{23} loading in terms of the impact of the positive and negative shear loading on the hexagonal core. However, here only one of the inclined plates (Plate-III) buckles (Figs. 5.16 (i) - (l)).

5.5.2 Influence of important parameters

In the previous section, the predictions using the proposed approach were validated using the results from FE. In this section the proposed approach is used to study the influence of important parameters on the critical shear buckling strain. The Fig. 5.17 shows the variation of the critical strains against the walls' length ratio of the hexagonal core with constant relative core density of 0.072. The length of plate-II and plate-III are varied while length of the plate-I remains still at 50mm. The requirement of constant core density is maintained by selecting the suitable thickness for plates. All other conditions such as the thickness ratio of plates and material lay-up are kept the same as in the previous analysis.

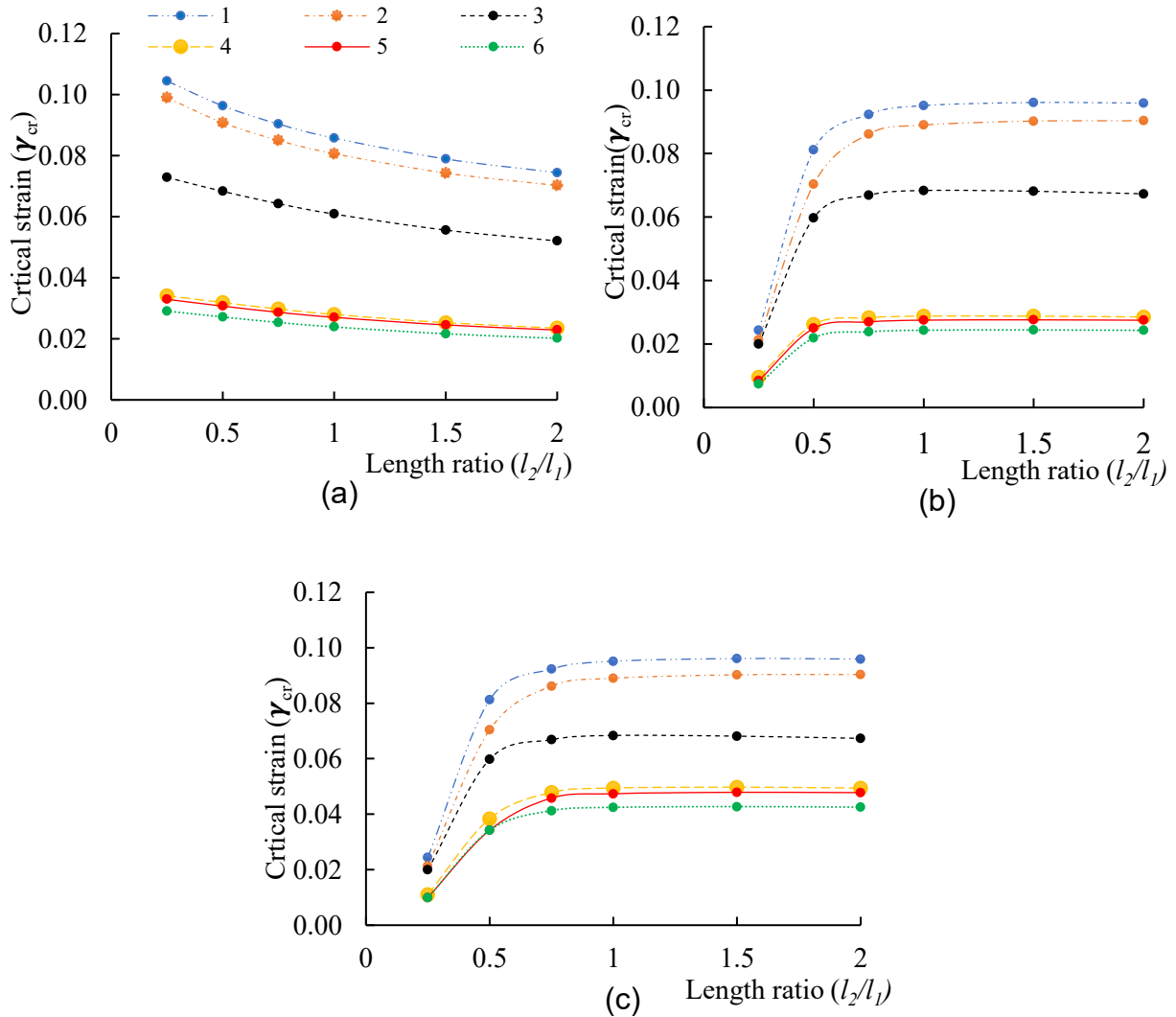
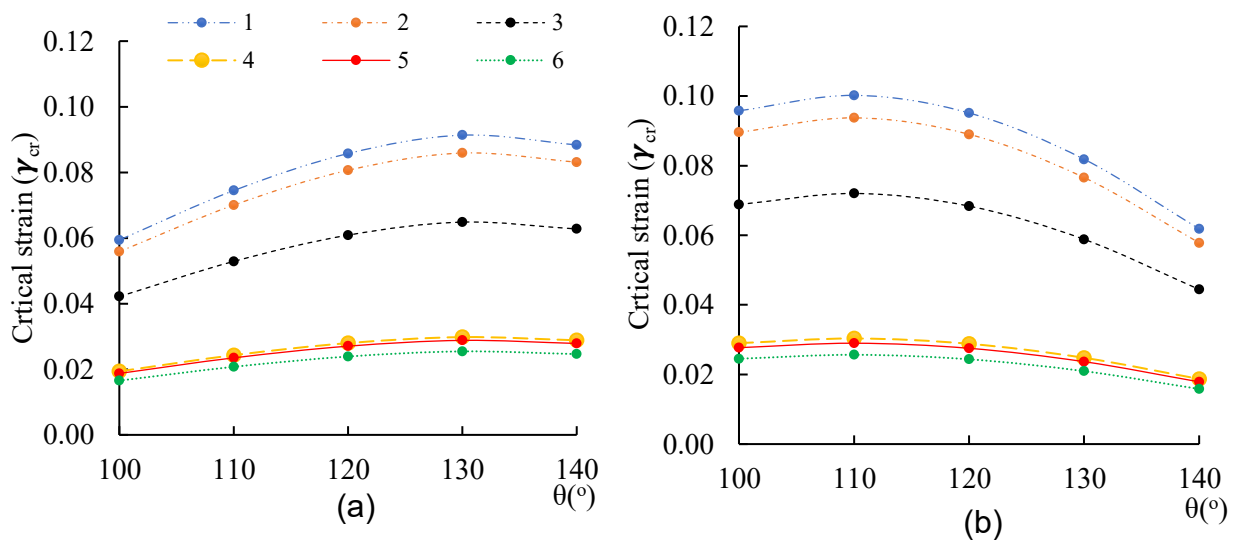


Fig. 5.17: Variation of the critical shear buckling strain with different length ratio between plate-I and plate-II for the shear load (a) γ_{13} (positive and negative shear), (b) γ_{23} (positive shear) and (c) γ_{23} (negative shear).

Figure. 5.17(a) shows the variation of the critical strains with different length ratios between plate-I and plate-II under γ_{13} shear loading. Increasing the length ratio of plates reduces the critical strain of the RVE. Increasing the length of the plate-II and plate-III under constant core density leads to the reduction of the thickness of the inclined plates leading to the monotonic reduction of the buckling load as the plate-I does not contribute to any load sharing due to its orientation in the core. On the other hand, different trends can be seen in the variations of the critical strains under the γ_{23} loading on the RVE (Figs. 5.17(b)-(c)). Under γ_{23} loading, shear load on the hexagonal core is carried by all three plates; therefore, changing the length ratio leads to a

transition of critical strain dependency between the plate-I and the inclined plates (plate-II and plate-III). At the lower length ratio, the plate-I buckles first and governs the critical strain of the core. As the length ratio increases, both inclined plates buckle before the plate-I, and the critical strain is almost constant with the variation of the length ratio. For the cross-ply laminates, the transition of buckling from the plate-I to inclined plates happens at a length ratio of 0.75 for both positive and negative shear on the RVE. For the angle-ply laminates, the transition happens at a length ratio of 0.5 for the positive shear and 0.75 for the negative shear.

Figure. 5.18 shows the variation of the critical strain with the change of angle between the plates while the relative core density remains constant at 0.072. The maximum critical shear strains of the hexagonal core are obtained at around 130° and 110° for the shear strains γ_{13} and γ_{23} respectively, regardless of positive or negative shear and the material configuration of the plates. It can be noted that although the thickness of each plate at these angles are lower than the thickness when the angle is 120° , the ratios in Eq. (5.21) become maximum at 130° and 110° for the respective shear loading.



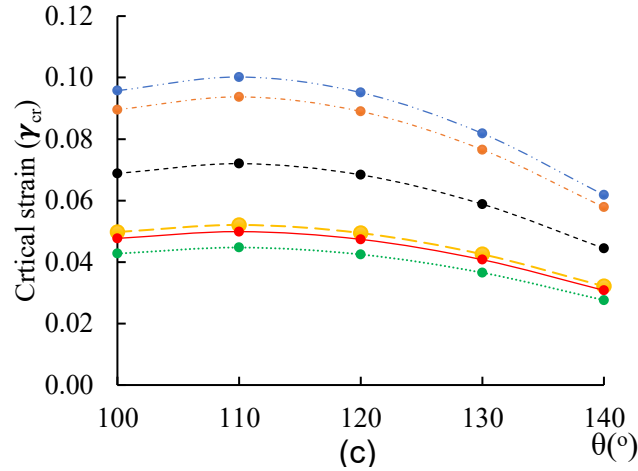
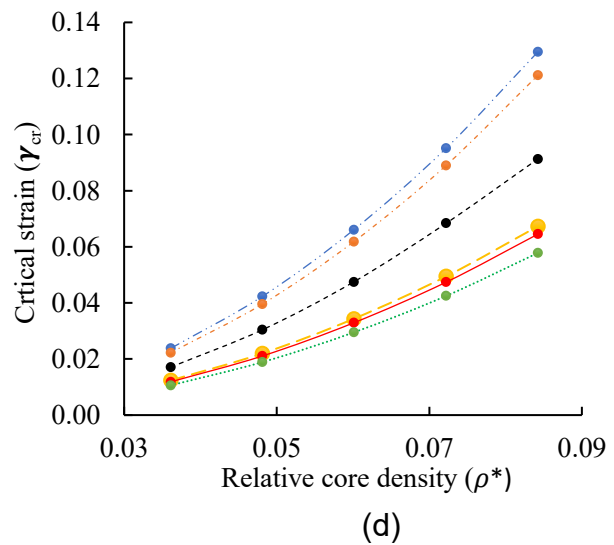
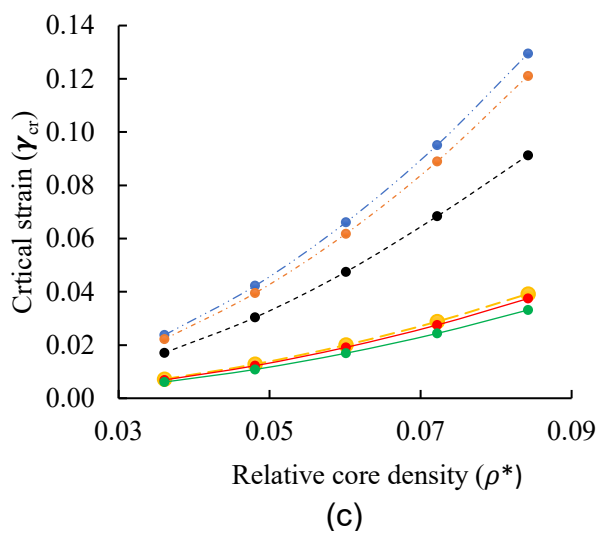
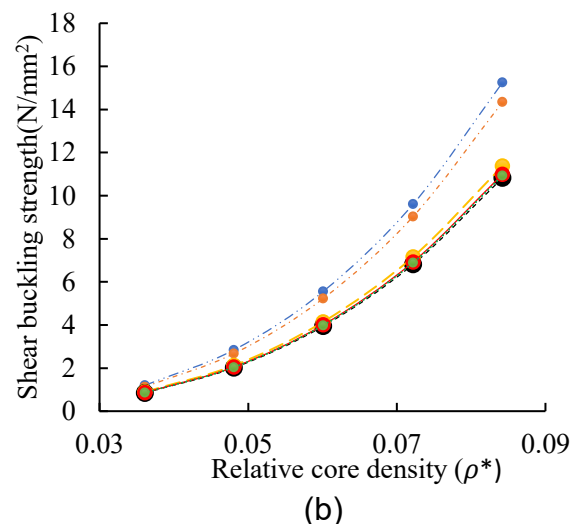
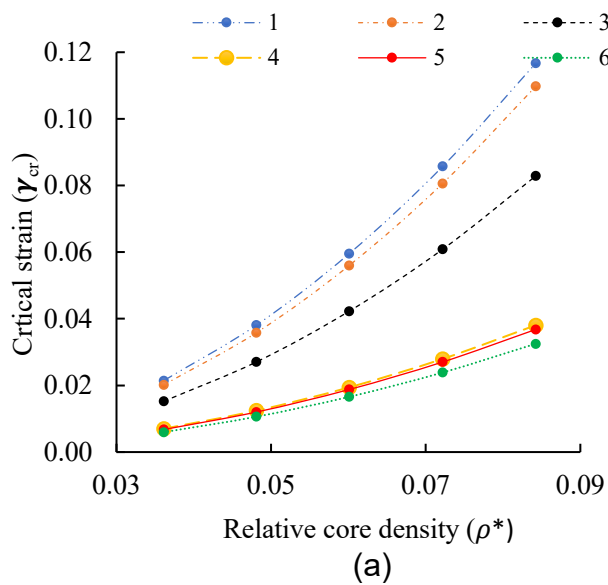


Fig. 5.18: Variation of the critical shear buckling strain with the angle θ between the plates for the shear load (a) γ_{13} (positive and negative shear), (b) γ_{23} (positive shear) and (c) γ_{13} (negative shear).

Figure. 5.19 shows the variation of the critical strain and shear buckling strength of the hexagonal core with relative core density. The shear buckling strength of the hexagonal core is calculated by multiplying the critical strain with the effective shear stiffness obtained from the proposed homogenisation approach in Chapter 3. The relative core density is varied by changing the thicknesses of the plates while keeping the length of each wall constant at 50mm. However, it can be deduced from Eq. (5.21) that even if the length of plates is changed (without changing the thickness) to vary the relative core density, the same effect on the critical shear strain could be obtained as long as the length ratio of the plates remains constant and the core depth to length ratio is adequate to consider as long plate. The Fig. 5.19(a) - (b) shows the critical shear buckling strain and corresponding shear buckling strength for the positive and negative shear strain γ_{13} with the change of core density. Although the effective stiffnesses of the hexagonal core with angle-ply laminates are higher than the effective stiffness of the hexagonal core with cross-ply laminates (Figs. 5.19(g) - (h)), the buckling strength of the hexagonal core with cross-ply laminates are higher than angle-ply laminates for the positive and negative shear strain γ_{13} (Fig. 5.19(b)) and positive shear strain γ_{23} (Fig. 5.19(d)). For negative shear strain γ_{23} , the hexagonal core with angle-ply laminates shows higher shear buckling strength than the cross-ply laminates (Fig. 5.19(f)). It can be seen from Figs. 5.19(a) - (f), the shear buckling strength for the γ_{13} loading is always lower than the shear buckling strength for γ_{23} loading. Therefore,

for the uniaxial bending, it is always efficient to orient the plate-I along the longitudinal axis of the beam and to use angle-ply laminates considering the direction of the shear. However, for the plates subjected to combined shear, using the angle-ply laminates for the core is beneficial if the design is governed by the stiffness (e.g. deflection). If the buckling strength governs the design, then material configurations and geometry of the hexagonal core need to be designed for the specific loadings for optimal performance.



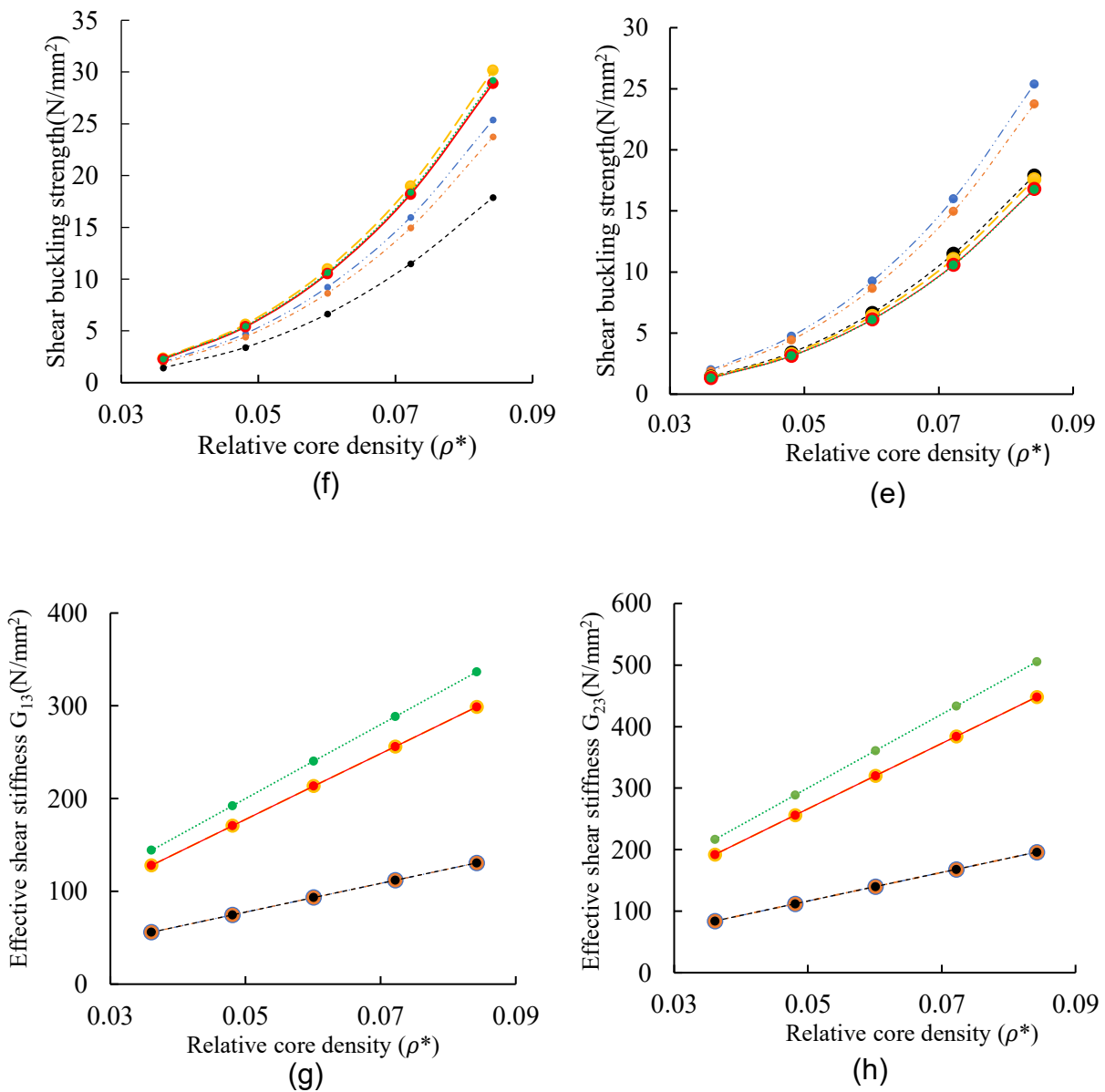


Fig. 5.19: Variation of the critical shear buckling strain and shear buckling strength for the shear load (a-b) γ_{13} (positive and negative shear), (c-d) γ_{23} (positive shear) and (e-f) γ_{13} (negative shear) and variation of the effective shear stiffness (g) G_{13} and (h) G_{23} with the relative core density of the honeycomb. Shear buckling strength of the honeycomb core is calculated by multiplying the critical strain by the effective shear stiffness of the core.

As discussed earlier, the presence of bend-twist coupling in the angle ply laminates positively and negatively influences the shear buckling strength of the honeycomb core. Figure. 5.20 shows comparisons of the critical strains obtained for the hexagonal core without considering the bend-twist coupling (orthotropic solution $\bar{D}_{16} = 0$ and $\bar{D}_{36} = 0$) with the predictions considering the effect of bend-twist coupling

for the material lay-up [45/-45/0/-45/45] in Table 5.1. The ratio of $\bar{D}_{16}/\bar{D}_{66}$ is varied by changing the ratio of thickness of 45/-45 plies to 0-ply while the laminate remains still symmetric and balanced, and the relative core density of the hexagonal core is 0.072. For the γ_{13} loading, the critical strain is overestimated with an orthotropic buckling solution (Fig. 5.20(a)). Maximum error is found to be approx. 60% (Fig.5.20(b)) when the thickness of the 0-ply approaches zero. On the other hand, predictions with and without the bend-twist coupling converge to the same results as the percentage of 45/-45 plies approaches zero. For the γ_{23} loading, the critical shear strain of the honeycomb core is overestimated by a maximum of 56% and underestimated by 25% for the positive and negative shear, respectively. When the thicknesses of each ply of laminate are equal (honeycomb cores considered in Table 5.2 - 5.3), the error percentages are 41%, 36% and -20% for positive and negative γ_{13} , positive γ_{23} and negative γ_{23} , respectively.

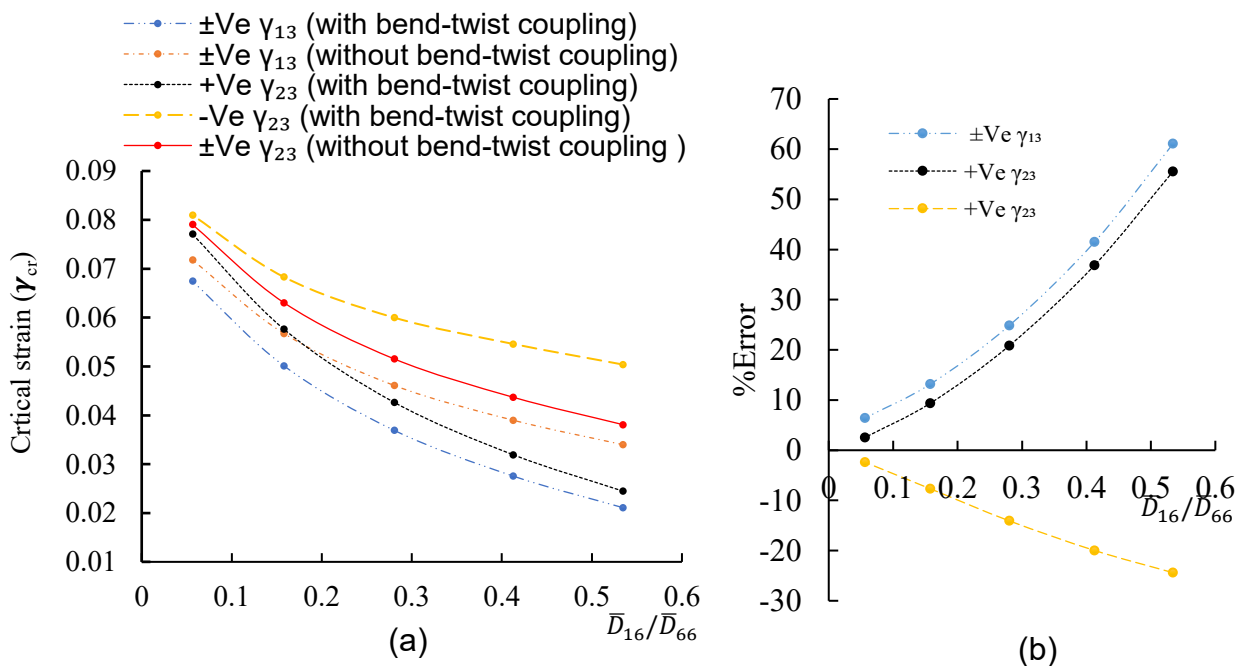


Fig. 5.20: Comparison of (a) the predictions for the critical shear strains and (b) percentage of difference in predictions between with and without bend-twist coupling. Thickness of (45/-45) plies and 0-ply of angle ply laminate (45/-45/0/-45/45) in Table 1 were varied without changing the total thickness of the laminate (constant relative core density) to vary the influence of bend-twist coupling.

5.5.3 Comparisons between different honeycomb core shapes

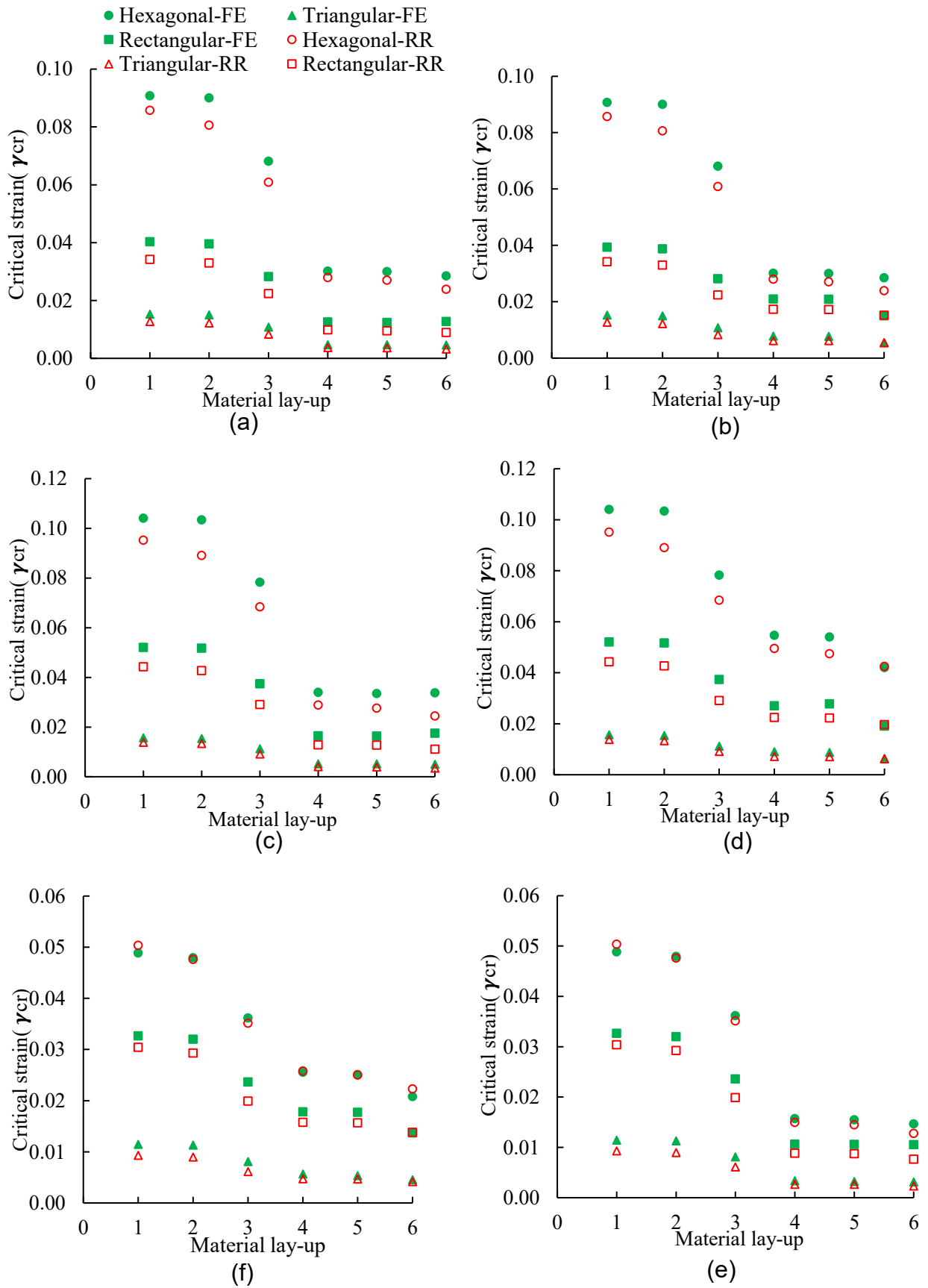


Fig. 5.21: Comparison of critical shear strain between honeycomb cores with different shapes for the shear load (a) γ_{13} (positive shear), (b) γ_{13} (negative shear), (c) γ_{23} (positive shear), (d) γ_{23} (negative shear), (e) $\gamma_{13}/\gamma_{23} = 1$ (positive shear) and (f) $\gamma_{13}/\gamma_{23} = 1$ (negative shear).

Table 5.14: Comparison of maximum of critical shear buckling strain of different honeycomb core shapes.

Fibre lay-up	Strain condition	Maximum critical shear buckling strain ($\times 10^{-3}$)		
		Hexagonal	Triangular	Rectangular
		Proposed FE	Proposed FE	Proposed FE
Cross-ply	$\pm Ve \gamma_{13}$	85.74 90.76	34.18 40.28	12.70 15.29
	$\pm Ve \gamma_{23}$	95.13 104.00	44.12 52.00	13.83 15.67
	$\pm Ve \gamma_{23} / \gamma_{13}$	48.85 50.36	30.38 32.64	9.29 11.41
Angle-ply	$+Ve \gamma_{13}$	27.97 30.14	9.85 12.52	3.73 4.70
	$-Ve \gamma_{13}$	27.97 30.14	17.35 20.96	6.21 7.85
	$+Ve \gamma_{23}$	28.81 33.87	12.74 16.40	3.98 5.20
	$-Ve \gamma_{23}$	49.44 54.67	22.40 27.00	7.15 9.00
	$+Ve \gamma_{23} / \gamma_{13}$	14.94 15.70	8.80 10.64	2.66 3.34
	$-Ve \gamma_{23} / \gamma_{13}$	25.52 25.79	15.72 17.80	4.71 5.66

Figure. 5.21 shows the comparison of critical shear buckling strains of different core shapes with an equal relative core density of 0.072. Here, plates' lengths of equilateral triangular core and rectangular core are selected such that the characteristics dimensions p and q of the honeycomb RVEs are equal to the hexagonal core considered in this study, which are 86.6mm and 75mm, respectively. The hexagonal core has the highest critical buckling strains (Table 5.14) for all the different load cases compared to triangular and rectangular cores (Figs. 5.21(a)-(f)). The superior performance of the hexagonal core in comparison to other core shapes is mainly due its geometric configuration and the loading conditions considered. However, under the combined shear condition, the relative reduction in the shear buckling capacity of the hexagonal core is higher than the other core shapes. It can be noted that for the same relative core density and for selected plate lengths, rectangular and triangular cores have lower plate thickness than the hexagonal core. By selecting larger plates' length l for the triangular and rectangular cores, one may consider higher thickness for plates keeping the core density constant. However, it

can be deduced from Eq. (5.21) that the critical strain of the sufficiently thick core does not vary with the length of the plate as long as the core density and length ratio between the plates remain constant.

5.6 Conclusions

A new simplified semi-analytical approach to predict the critical shear buckling load of the composite honeycomb cores was presented. The proposed approach is more general than the existing approaches and can be used to predict shear buckling loads of different honeycomb core shapes and material configurations. In the proposed model, using simply-supported boundaries for all the edges of the plates leads to the conservative prediction of the critical buckling load, while using boundary conditions of two edges simply-supported and the other two restrained against rotations leads to close predictions of critical shear buckling strains to the FE results. The hexagonal honeycomb core with the cross-ply laminates and the angle-ply laminates were investigated, while the cores with the cross-ply laminates provided the same critical shear buckling strains regardless of the positive and negative shear, the angle-ply laminates positively and negatively influenced the critical shear buckling load depending on the direction of applied shear loads on the core. As the bend-twist coupling exists in the angle-ply laminates, neglecting bend-twist terms may over or underestimate the results significantly. Comparing different core shapes, for the load cases considered in this study, the hexagonal core showed superior performance. The shear buckling strength of honeycomb cores can be optimised not only by changing material configurations but also changing the geometric parameters of the core. Because the proposed approach can be easily implemented and efficient compared to FE in predicting the shear buckling failure of the sandwich panels, it would be instrumental in selecting the honeycomb core shapes and material configurations of the core for the optimal design of sandwich panels.

5.7 References

Allen, H. G. (1969). *Analysis and Design of Structural Sandwich Panels*: Pergamon.
ABAQUS version 2021. Dassault Systemes Simulia Corporation. Providence, RI, USA.

- Banerjee, S., Battley, M., & Bhattacharyya, D. (2010). Shear strength optimization of reinforced honeycomb core materials. *Mechanics of Advanced Materials and Structures*, 17(7), 542-552.
- Cote, F., Deshpande, V., & Fleck, N. (2006). The shear response of metallic square honeycombs. *Journal of Mechanics of Materials and Structures*, 1(7), 1281-1299.
- Grediac, M. (1993). A finite element study of the transverse shear in honeycomb cores. *International Journal of Solids and Structures*, 30(13), 1777-1788.
- Jiménez, F. L., & Triantafyllidis, N. (2013). Buckling of rectangular and hexagonal honeycomb under combined axial compression and transverse shear. *International Journal of Solids and Structures*, 50(24), 3934-3946.
- Kim, B., & Christensen, R. M. (2000). Basic two-dimensional core types for sandwich structures. *International Journal of Mechanical Sciences*, 42(4), 657-676.
- Kollár, L. P. (2003). Local buckling of fiber reinforced plastic composite structural members with open and closed cross sections. *Journal of Structural Engineering*, 129(11), 1503-1513.
- Leissa, A.W. 2005. The historical bases of the Rayleigh and Ritz methods. *Journal of Sound and Vibration*. 287. 961-978. 10.1016/j.jsv.2004.12.021.
- MathWorks Inc. (2022). MATLAB version: 9.13.0 (R2022b), Natick, Massachusetts: The MathWorks Inc.
- Moreno-García, P., dos Santos, J. V. A., & Lopes, H. (2018). A review and study on Ritz method admissible functions with emphasis on buckling and free vibration of isotropic and anisotropic beams and plates. *Archives of Computational Methods in Engineering*, 25(3), 785-815.
- Pan, S. D., Wu, L. Z., Sun, Y. G., Zhou, Z. G., & Qu, J. L. (2006). Longitudinal shear strength and failure process of honeycomb cores. *Composite Structures*, 72(1), 42-46.
- Pan, S. D., Wu, L. Z., & Sun, Y. G. (2008). Transverse shear modulus and strength of honeycomb cores. *Composite Structures*, 84(4), 369-374.
- Qiao, P., & Huo, X. (2011). Explicit local buckling analysis of rotationally-restrained orthotropic plates under uniform shear. *Composite structures*, 93(11), 2785-2794.
- Qiu, C., Guan, Z., Guo, X., & Li, Z. (2020). Buckling of honeycomb structures under out-of-plane loads. *Journal of Sandwich Structures & Materials*, 22(3), 797-821.
- Shi, G., & Tong, P. (1994). Local buckling of honeycomb sandwich plates under action of transverse shear forces. *AIAA Journal*, 32(7), 1520-1524.
- Zhang, J., & Ashby, M.F. (1992). The out-of-plane properties honeycombs. *International journal of mechanical sciences*, 34(6), 475-489.
- Zenkert, D. (1997). *The handbook of sandwich construction: Engineering Materials Advisory Services*.

Chapter 6:

Local buckling of face sheets in sandwich panels

6.1 General

In Chapter 5, a novel approach to predict the local shear buckling of the honeycomb cores was presented. Another critical failure to consider in design of sandwich panels is the local buckling of face sheets (Allen 1969; Zenkert 1997). Face sheets of the honeycomb core sandwich panels can experience mainly two types of local buckling failures, namely, wrinkling and intracellular buckling, depending on the geometric and material configurations. Several researchers have investigated the wrinkling of thick and thin sandwich panels consisting of isotropic cores (Hoff & Maunters 1945; Plantema 1966; Allen 1969; Niu & Talreja 1999; Birman 2004) or orthotropic cores (Vonach & Rammerstorfer 2000; Pozorski et al. 2021). Wrinkling failure is a buckling failure of the face sheets, which is a short-wave buckling that occurs over multiple cells of the core, while intracellular buckling is a short-wave buckling occurring within a single cell of the core. Analytical (Hoff & Maunters 1945; Plantema 1966; Allen 1969; Birman 2004; Pozorski et al. 2021) and semi-analytical (Niu & Talreja 1999; Pozorski et al. 2021) solutions for the wrinkling failure have been presented for different loading conditions. As the methodologies and equations for the wrinkling failure were developed based on the assumptions that face sheets are supported by homogenous elastic foundations, those solutions cannot be used to predict the intracellular buckling of face sheets which occurs within a cell of the core. Existing analytical solutions (Norris 1964; Blass 1984; Thomsen & Banks 2004) for the intracellular buckling of sandwich panels were developed under several simplified assumptions related to geometry and boundary conditions. Therefore, it's found to underpredict the intracellular buckling loads significantly. Considering the research carried out up to now on the local buckling of face sheets, very few studies are available on the intracellular buckling of sandwich panels. Therefore, the objective of this chapter is to develop a semi-analytical approach to accurately predict the intracellular buckling load of the cellular core sandwich panel. The proposed solution

methodology is developed considering the geometry of the cell, boundary, and different loading conditions. The proposed semi-analytical approach is verified using the FE results of the sandwich panels. Existing methodologies are also used to calculate the intracellular buckling loads, and comparisons have been made between different methodologies.

6.2 Intracellular buckling of sandwich panels

Consider a sandwich panel consisting of composite face sheets and a honeycomb core subjected to biaxial compressive forces at the lower and upper face sheets. It's assumed that each cell of the face sheet is subjected to uniform and equal compressive force before the bifurcation point (Fig. 6.1(a)). As the interest is in the intracellular buckling load of the sandwich panel, a cell as shown in Fig. 6.1(b) is selected for the buckling analysis of plate considering the boundaries are rotationally restrained due to the core walls attached to the edges.

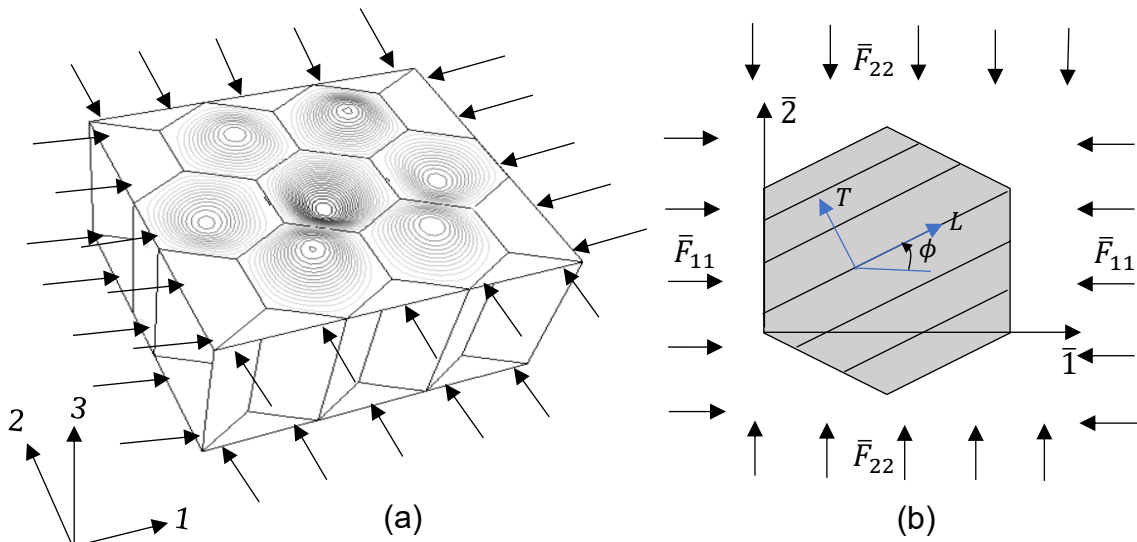


Fig.6.1: (a) A sandwich panel with intracellular buckling and (b) typical hexagonal cell of factsheet subjected to uniform biaxial compressive force.

6.2.1 Admissible displacement function

As this is a buckling problem of a non-rectangular shape plate (e.g. Fig. 6.1(b)) with combined loading conditions and with the laminates having the coupling terms, a closed-form solution may not be possible. Therefore, Rayleigh-Ritz method is adopted to get an approximate solution. In the past, the studies on the intracellular buckling of the sandwich panels (Norris 1964; Blass 1984; Thomsen & Banks 2004), restricted support conditions of the cell to classical conditions such as simply-supported or

clamped. However, considering the intracellular buckling of honeycomb core sandwich panels, the edges of each cell may not be simplified to classical support conditions for more accurate predictions. The degree of restraint offered by the core walls to the cell edges could vary between null restraint, representing the simply-supported condition, and full restraint, representing a clamped condition. Since the accuracy and computational efficiency of Rayleigh-Ritz method in predicting the critical buckling load greatly depends on the choice of appropriate displacement function of the plate, it's critical to choose a suitable function to satisfy the edge restraint conditions. Such edge restraint conditions can be accounted for by considering the displacement of such a plate as a weighted superposition of the displacement function for simply-supported edges and that of clamped edges (Yang & Wang, 2017), with the contribution of each depending on the degree of edge rotational restraint at the boundaries. For a rectangular plate (Fig. 6.2), a compatible displacement function can be written of the form (Chai (1994)):

$$\bar{v}_3(\bar{x}_1, \bar{x}_2) = \sum_{m,n}^{M,N} A_{mn} X_m(\bar{x}_1) Y_n(\bar{x}_2), \quad (6.1)$$

where, X_m and Y_n are suitable functions, which satisfy the geometric boundary conditions of the plate on the edges perpendicular to the $\bar{1}$ and $\bar{2}$ axis respectively, and A_{mn} are the unknown coefficients of the function and $\bar{v}_3(\bar{x}_1, \bar{x}_2)$ is the out-of-plane normal displacement at coordinate (\bar{x}_1, \bar{x}_2) .

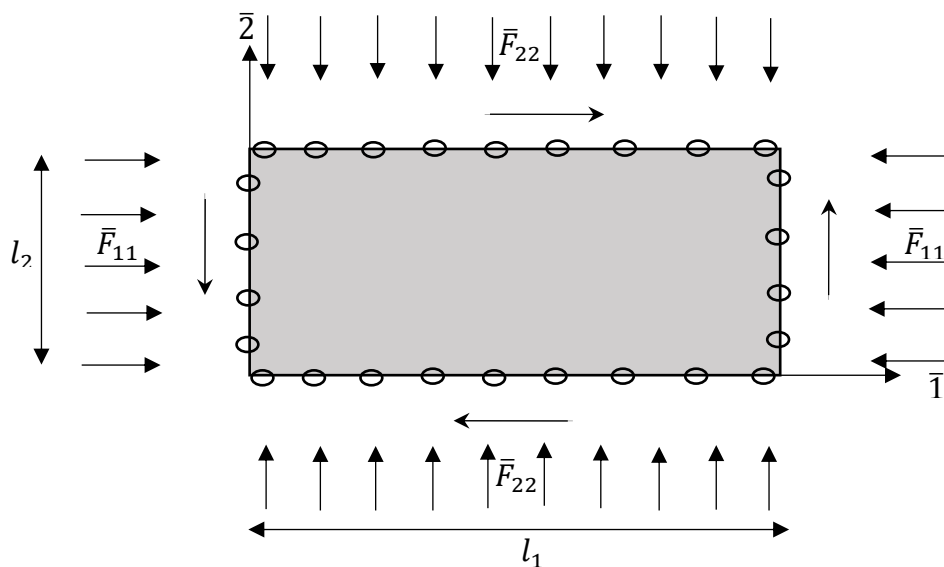


Fig.6.2: Rectangular plate of all edges rotationally restrained subjected to biaxial compression.

Extending the Eq. (6.1), Qio & Shan (2007) defined a function for the out-of-plane displacement as in Eq. (6.2) for the buckling problem of a rectangular plate (Fig. (6.2)) with all edges rotationally restrained:

$$\bar{v}_3(\bar{x}_1, \bar{x}_2) = \sum_{m,n}^{M,N} A_{mn} \left[(1 - R_1) \sin\left(\frac{m\pi\bar{x}_1}{l_1}\right) + R_1 \left(1 - \cos\left(\frac{2m\pi\bar{x}_1}{l_1}\right)\right) \right] \left[(1 - R_2) \sin\left(\frac{n\pi\bar{x}_2}{l_2}\right) + R_2 \left(1 - \cos\left(\frac{2n\pi\bar{x}_2}{l_2}\right)\right) \right], \quad (6.2)$$

where;

$$X_m(\bar{x}_1) = \left[(1 - R_1) \sin\left(\frac{m\pi\bar{x}_1}{l_1}\right) + R_1 \left(1 - \cos\left(\frac{2m\pi\bar{x}_1}{l_1}\right)\right) \right] \quad (6.3)$$

$$Y_n(\bar{x}_2) = \left[(1 - R_2) \sin\left(\frac{n\pi\bar{x}_2}{l_2}\right) + R_2 \left(1 - \cos\left(\frac{2n\pi\bar{x}_2}{l_2}\right)\right) \right] \quad (6.4)$$

R_1 and R_2 are the degree of rotational restraints along the edges parallel to $\bar{1}$ and $\bar{2}$ axis respectively. The expressions for the R_1 and R_2 can be derived from satisfaction of the required boundary conditions along the edges of the plate. The boundary conditions along rotationally restrained edges parallel to the axis- $\bar{1}$ can be written as:

$$\bar{v}_3(0, \bar{x}_2) = 0, \quad (6.5)$$

$$\bar{v}_3(l_1, \bar{x}_2) = 0, \quad (6.6)$$

$$\bar{M}_{11}(0, \bar{x}_2) = -\bar{D}_{11}^f \left(\frac{\partial^2 \bar{v}_3}{\partial \bar{x}_1^2}\right)_{\bar{x}_1=0} - \bar{D}_{12}^f \left(\frac{\partial^2 \bar{v}_3}{\partial \bar{x}_2^2}\right)_{\bar{x}_1=0} - \bar{D}_{16}^f \left(\frac{\partial^2 \bar{v}_3}{\partial \bar{x}_1 \partial \bar{x}_2}\right)_{\bar{x}_1=0} = -k_1 \left(\frac{\partial \bar{v}_3}{\partial \bar{x}_1}\right)_{\bar{x}_1=0}, \quad (6.7)$$

$$\bar{M}_{11}(l_1, \bar{x}_2) = -\bar{D}_{11}^f \left(\frac{\partial^2 \bar{v}_3}{\partial \bar{x}_1^2}\right)_{\bar{x}_1=l_1} - \bar{D}_{12}^f \left(\frac{\partial^2 \bar{v}_3}{\partial \bar{x}_2^2}\right)_{\bar{x}_1=l_1} - \bar{D}_{16}^f \left(\frac{\partial^2 \bar{v}_3}{\partial \bar{x}_1 \partial \bar{x}_2}\right)_{\bar{x}_1=l_1} = k_1 \left(\frac{\partial \bar{v}_3}{\partial \bar{x}_1}\right)_{\bar{x}_1=l_1} \quad (6.8)$$

Similarly, the boundary conditions along rotationally restrained edges parallel to the axis- $\bar{2}$ can be written as:

$$\bar{v}_3(\bar{x}_1, 0) = 0, \quad (6.9)$$

$$\bar{v}_3(\bar{x}_1, l_2) = 0, \quad (6.10)$$

$$\bar{M}_{22}(\bar{x}_1, 0) = -\bar{D}_{22}^f \left(\frac{\partial^2 \bar{v}_3}{\partial \bar{x}_2^2} \right)_{\bar{x}_2=0} - \bar{D}_{12}^f \left(\frac{\partial^2 \bar{v}_3}{\partial \bar{x}_1^2} \right)_{\bar{x}_2=0} - \bar{D}_{16}^f \left(\frac{\partial^2 \bar{v}_3}{\partial \bar{x}_1 \partial \bar{x}_2} \right)_{\bar{x}_2=0} = -k_2 \left(\frac{\partial \bar{v}_3}{\partial \bar{x}_2} \right)_{\bar{x}_2=0} \quad (6.11)$$

$$\bar{M}_{22}(\bar{x}_1, l_2) = -\bar{D}_{22}^f \left(\frac{\partial^2 \bar{v}_3}{\partial \bar{x}_2^2} \right)_{\bar{x}_2=l_2} - \bar{D}_{12}^f \left(\frac{\partial^2 \bar{v}_3}{\partial \bar{x}_1^2} \right)_{\bar{x}_2=l_2} - \bar{D}_{16}^f \left(\frac{\partial^2 \bar{v}_3}{\partial \bar{x}_1 \partial \bar{x}_2} \right)_{\bar{x}_2=l_2} = -k_2 \left(\frac{\partial \bar{v}_3}{\partial \bar{x}_2} \right)_{\bar{x}_2=l_2}, \quad (6.12)$$

where, \bar{D}_{ij}^f are the element of bending stiffness matrix of factsheet. Substituting Eq. (6.3) - (6.10) with Eq. (6.2) and simplifying with the conservative assumption that plate undergoes cylindrical bending in each direction (Qio & Shan 2007), we will get:

$$R_1 = \frac{1}{1 + \left(\frac{4m\pi \bar{D}_{11}^f}{k_1 l_1} \right)} \quad (6.13)$$

$$R_2 = \frac{1}{1 + \left(\frac{4n\pi \bar{D}_{22}^f}{k_2 l_2} \right)} \quad (6.14)$$

where, k_1 and k_2 are the stiffnesses of rotational restraints along the boundaries parallel to axis- $\bar{1}$ and axis- $\bar{2}$ respectively. Higginson et al. (2021) showed that the out-of-plane displacement function for the buckling problem of a curved plate may be written in form as:

$$\bar{v}_3(\bar{x}_1, \bar{x}_2) = \sum_{m,n}^{M,N} A_{mn} X_m(\bar{x}_1) Y_n(\bar{x}_1, \bar{x}_2) \quad (6.15)$$

Now, combining Eq. (6.2) and Eq. (6.15), we can write a displacement function for the buckling problem of non-rectangular plate consisting of all the boundaries with rotationally restrained conditions. We consider the function $X_m(\bar{x}_1)$ is same as in Eq. (6.2) and we define the function $Y(\bar{x}_2, \bar{x}_1)$ as:

$$Y(\bar{x}_2, \bar{x}_1) = \left[(1 - R_2) \sin \left(\frac{n\pi(\bar{x}_2 - f_1(\bar{x}_1))}{l_2(\bar{x}_1)} \right) + R_2 (1 - \cos \left(\frac{2n\pi(\bar{x}_2 - f_1(\bar{x}_1))}{l_2(\bar{x}_1)} \right)) \right] \quad (6.16)$$

with $f_1(\bar{x}_1)$ being a polynomial function approximately defines the boundaries (a-b-c) of the cell in Fig. 6.3(a). The function $l_2(\bar{x}_1)$ is the variation of distance between the boundaries in direction $\bar{2}$ which is defined to be $(f_2(\bar{x}_1) - f_2(\bar{x}_1))$. The factors R_1 and R_2 , defining the degree of the rotational restraints along the boundaries of the cell in Fig. 6.3(b), are approximated as in Eqs. (6.13) and (6.14) respectively. In Eqs. (6.13) and (6.14), the average values of the distance between boundaries in direction $\bar{1}$ and $\bar{2}$ are used. For instance, the distance l_1 in Eq. (6.13) is calculated as the average distance between the boundaries (b-a-d-e) and (b-c-f-e), and the average distance l_2 in Eq. (6.14) is calculated as the average distance between the boundaries (a-b-c) and (d-e-f). Similarly, the rotational restraints stiffnesses are also estimated to be the average rotational restraints along the boundaries as explained and illustrated in section 6.2.3. Although, these conditions will not exactly satisfy the equilibrium of moments (Eqs. (6.11) - (6.12)) at the boundaries (Fig. 6.3(b)), the assumptions are made for R_1 and R_2 in order to simplify the calculations while satisfying the boundary conditions to a certain degree.

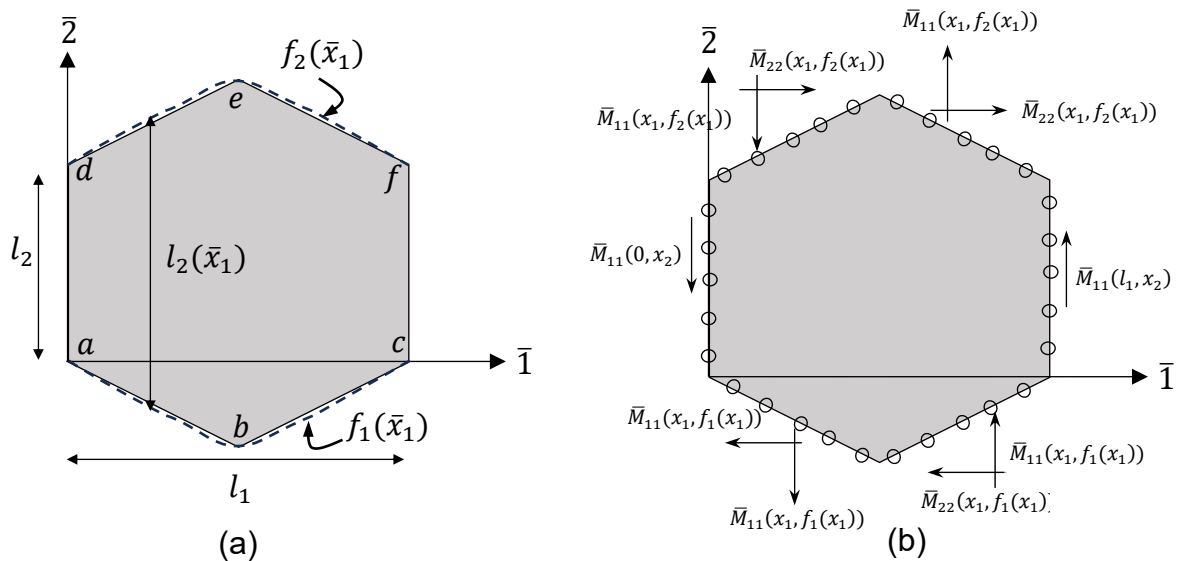


Fig.6.3: A hexagonal cell (a) with approximate boundaries defined using polynomial functions and (b) with the boundary moments at the rotationally restrained edges.

6.2.2 Minimisation of the total potential energy of the plate

The buckling problem based on the Rayleigh-Ritz method can be formulated using the principle of minimum total energy or the variational principle. It's assumed that the face sheets consist of symmetric laminate then the total potential energy (Π) of a face sheet while in equilibrium in a displaced buckling mode is the sum of strain

energy due to bending (U_b), strain energy stored in rotational springs along the boundaries (U_r) and the energy due to applied loads (V):

$$\Pi = U_b + U_r + V, \quad (6.17)$$

where, the bending energy U_b of the face sheet's cell of area A can be obtained as:

$$U_b = \iint_A \left[\bar{D}_{11}^f \left(\frac{\partial^2 \bar{v}_3}{\partial \bar{x}_1^2} \right)^2 + 2\bar{D}_{12}^f \frac{\partial^2 \bar{v}_3}{\partial \bar{x}_1^2} \frac{\partial^2 \bar{v}_3}{\partial \bar{x}_2^2} + \bar{D}_{22}^f \left(\frac{\partial^2 \bar{v}_3}{\partial \bar{x}_2^2} \right)^2 + 4\bar{D}_{16}^f \frac{\partial^2 \bar{v}_3}{\partial \bar{x}_1^2} \frac{\partial^2 \bar{v}_3}{\partial \bar{x}_1 \partial \bar{x}_2} + 4\bar{D}_{26}^f \frac{\partial^2 \bar{v}_3}{\partial \bar{x}_2^2} \frac{\partial^2 \bar{v}_3}{\partial \bar{x}_1 \partial \bar{x}_2} + 4\bar{D}_{66}^f \left(\frac{\partial^2 \bar{v}_3}{\partial \bar{x}_1 \partial \bar{x}_2} \right)^2 \right] dA, \quad (6.18)$$

the strain energy stored in rotational spring U_r along boundary Γ can be written as:

$$U_r = \frac{1}{2} \int_{\Gamma} \left[k_1 \left(\frac{\partial \bar{v}_3}{\partial \bar{x}_1} \right)_{\bar{x}_1=0}^2 + k_1 \left(\frac{\partial \bar{v}_3}{\partial \bar{x}_1} \right)_{\bar{x}_1=l_1}^2 + k_1 \left(\frac{\partial \bar{v}_3}{\partial \bar{x}_1} \right)_{\bar{x}_2=f_1(\bar{x}_1)}^2 + k_1 \left(\frac{\partial \bar{v}_3}{\partial \bar{x}_1} \right)_{\bar{x}_2=f_2(\bar{x}_1)}^2 + k_2 \left(\frac{\partial \bar{v}_3}{\partial \bar{x}_2} \right)_{\bar{x}_2=f_1(\bar{x}_1)}^2 + k_2 \left(\frac{\partial \bar{v}_3}{\partial \bar{x}_2} \right)_{\bar{x}_2=f_2(\bar{x}_1)}^2 \right] d\Gamma, \quad (6.19)$$

The work done by the uniform compressive loads on the plate can be written as:

$$V = \frac{1}{2} \iint_A \left[-\bar{F}_{11} \left(\frac{\partial \bar{v}_3}{\partial \bar{x}_1} \right)^2 - \bar{F}_{22} \left(\frac{\partial \bar{v}_3}{\partial \bar{x}_2} \right)^2 \right] dA. \quad (6.20)$$

For a plate in an equilibrium state, the total potential energy becomes minimum when the first variation of the total potential energy (Eq. (6.17)) is zero. Then, the condition for the state of minimum energy is expressed as:

$$\delta \Pi = \delta U_b + \delta U_r + \delta V = 0, \quad (6.21)$$

where, the δU_b , δU_r and δV are given by Eqs. (6.20) - (6.22):

$$\begin{aligned} \delta U_b = \iint_A \left[\bar{D}_{11}^f \left(\frac{\partial^2 \bar{v}_3}{\partial \bar{x}_1^2} \right) \left(\frac{\partial^2 \delta \bar{v}_3}{\partial \bar{x}_1^2} \right) + \bar{D}_{12}^f \left(\frac{\partial^2 \bar{v}_3}{\partial \bar{x}_1^2} \frac{\partial^2 \delta \bar{v}_3}{\partial \bar{x}_2^2} + \frac{\partial^2 \delta \bar{v}_3}{\partial \bar{x}_1^2} \frac{\partial^2 \bar{v}_3}{\partial \bar{x}_2^2} \right) + \bar{D}_{22}^f \left(\frac{\partial^2 \bar{v}_3}{\partial \bar{x}_1^2} \right) \left(\frac{\partial^2 \delta \bar{v}_3}{\partial \bar{x}_1^2} \right) + \right. \\ \left. 2\bar{D}_{16}^f \left(\frac{\partial^2 \bar{v}_3}{\partial \bar{x}_1^2} \frac{\partial^2 \delta \bar{v}_3}{\partial \bar{x}_1 \partial \bar{x}_2} + \frac{\partial^2 \delta \bar{v}_3}{\partial \bar{x}_1^2} \frac{\partial^2 \bar{v}_3}{\partial \bar{x}_1 \partial \bar{x}_2} \right) + 2\bar{D}_{26}^f \left(\frac{\partial^2 \bar{v}_3}{\partial \bar{x}_2^2} \frac{\partial^2 \delta \bar{v}_3}{\partial \bar{x}_1 \partial \bar{x}_2} + \frac{\partial^2 \delta \bar{v}_3}{\partial \bar{x}_2^2} \frac{\partial^2 \bar{v}_3}{\partial \bar{x}_1 \partial \bar{x}_2} \right) + \right. \\ \left. 4\bar{D}_{66}^f \left(\frac{\partial^2 \bar{v}_3}{\partial \bar{x}_1 \partial \bar{x}_2} \right) \left(\frac{\partial^2 \delta \bar{v}_3}{\partial \bar{x}_1 \partial \bar{x}_2} \right) \right] dA, \end{aligned} \quad (6.22)$$

$$\begin{aligned} \delta U_r = \int_{\Gamma} \left[k_1 \left(\frac{\partial \bar{v}_3}{\partial \bar{x}_1} \right)_{\bar{x}_1=0} \delta \left(\frac{\partial \bar{v}_3}{\partial \bar{x}_1} \right)_{\bar{x}_1=0} + k_1 \left(\frac{\partial \bar{v}_3}{\partial \bar{x}_1} \right)_{\bar{x}_1=l_1} \delta \left(\frac{\partial \bar{v}_3}{\partial \bar{x}_1} \right)_{\bar{x}_1=l_1} + \right. \\ \left. k_1 \left(\frac{\partial \bar{v}_3}{\partial \bar{x}_1} \right)_{\bar{x}_2=f_1(\bar{x}_1)} \delta \left(\frac{\partial \bar{v}_3}{\partial \bar{x}_1} \right)_{\bar{x}_2=f_1(\bar{x}_1)} + k_1 \left(\frac{\partial \bar{v}_3}{\partial \bar{x}_1} \right)_{\bar{x}_2=f_2(\bar{x}_1)} \delta \left(\frac{\partial \bar{v}_3}{\partial \bar{x}_1} \right)_{\bar{x}_2=f_2(\bar{x}_1)} + \right. \\ \left. k_2 \left(\frac{\partial \bar{v}_3}{\partial \bar{x}_2} \right)_{\bar{x}_2=f_1(\bar{x}_1)} \delta \left(\frac{\partial \bar{v}_3}{\partial \bar{x}_2} \right)_{\bar{x}_2=f_1(\bar{x}_1)} + k_2 \left(\frac{\partial \bar{v}_3}{\partial \bar{x}_2} \right)_{\bar{x}_2=f_1(\bar{x}_1)} \delta \left(\frac{\partial \bar{v}_3}{\partial \bar{x}_2} \right)_{\bar{x}_2=f_1(\bar{x}_1)} \right] d\Gamma, \end{aligned} \quad (6.23)$$

and

$$\delta V = \iint_A \left[-\bar{F}_{11} \left(\frac{\partial \bar{v}_3}{\partial \bar{x}_1} \right) \left(\frac{\partial \delta \bar{v}_3}{\partial \bar{x}_1} \right) - \bar{F}_{22} \left(\frac{\partial \bar{v}_3}{\partial \bar{x}_2} \right) \left(\frac{\partial \delta \bar{v}_3}{\partial \bar{x}_2} \right) \right] dA. \quad (6.24)$$

The derivation of the equation for the total potential energy of a composite plate with an arbitrary lay-up can be found in Leissa (1985), where it is shown that the strain energy of an unsymmetrical laminate consists of components corresponding to stretching and bend-stretch coupling in addition to the components of energy in Eq. (6.15). For unsymmetrical laminates, use of the reduced bending stiffness approach (Ashton, 1969) allows decoupling of the stretching and bending components and hence the same variation in total potential energy equation of symmetric plates (Eq. (6.17)) may be applied for approximate solution for the face sheet with asymmetric laminate using the reduced bending stiffness matrix.

Substituting the Eq. (6.21) with the displacement function defined in Eq. (6.15) leads to:

$$\begin{aligned} 0 = \sum_{p=1}^P \sum_{q=1}^Q \left\{ \sum_{m=1}^M \sum_{n=1}^N A_{mn} \left[\bar{D}_{11}^f I_{1(m,n)} I_{1(p,q)} + \bar{D}_{12}^f \left[I_{1(m,n)} I_{2(p,q)} + I_{2(m,n)} I_{1(p,q)} \right] + \right. \right. \\ \left. \bar{D}_{22}^f I_{1(m,n)} I_{1(p,q)} + 2\bar{D}_{16}^f \left[I_{1(m,n)} I_{3(p,q)} + I_{3(m,n)} I_{1(m,n)} \right] + \right. \\ \left. 2\bar{D}_{26}^f \left[I_{1(m,n)} I_{3(p,q)} + I_{3(m,n)} I_{1(p,q)} \right] + 4\bar{D}_{11}^f I_{3(m,n)} I_{3(p,q)} + \right. \\ \left. k_1 I_{4(m,n)} I_{4(p,q)} + k_2 I_{5(m,n)} I_{5(p,q)} - \bar{F}_{11} I_{6(m,n)} I_{6(p,q)} - \right. \\ \left. \bar{F}_{22} I_{7(m,n)} I_{7(p,q)} \right] \} \delta A_{pq}, \end{aligned} \quad (6.25)$$

where;

$$I_{1(m,n)} = \iint_A \left[2 \frac{\partial X_m}{\partial \bar{x}_1} \frac{\partial Y_n}{\partial \bar{x}_1} + Y_n \frac{\partial^2 X_m}{\partial \bar{x}_1^2} + X_m \frac{\partial^2 Y_n}{\partial \bar{x}_1^2} \right] dA, \quad (6.26)$$

$$I_{2(m,n)} = \iint_A \left[X_m \frac{\partial^2 Y_n}{\partial \bar{x}_2^2} \right] dA, \quad (6.27)$$

$$I_{3(m,n)} = \iint_A \left[\frac{\partial X_m}{\partial \bar{x}_1} \frac{\partial Y_n}{\partial \bar{x}_2} + X_m \frac{\partial^2 Y_n}{\partial \bar{x}_1 \partial \bar{x}_2} \right] dA, \quad (6.28)$$

$$I_{4(m,n)} = \int_{\Gamma} \left[\frac{\partial X_m}{\partial \bar{x}_1} \Big|_{\bar{x}_1=0} Y_n(0, \bar{x}_2) + X_m(0) \frac{\partial Y_n}{\partial \bar{x}_1} \Big|_{\bar{x}_1=0} + \frac{\partial X_m}{\partial \bar{x}_1} \Big|_{\bar{x}_1=l_1} Y_n(0, \bar{x}_2) + \right. \\ \left. + X_m(l_1) \frac{\partial Y_n}{\partial \bar{x}_1} \Big|_{\bar{x}_1=l_1} + \frac{\partial X_m}{\partial \bar{x}_1} \Big|_{\bar{x}_2=f_1(\bar{x}_1)} Y_n(0, \bar{x}_2) + X_m(0) \frac{\partial Y_n}{\partial \bar{x}_1} \Big|_{\bar{x}_2=f_1(\bar{x}_1)} + \right. \\ \left. \frac{\partial X_m}{\partial \bar{x}_1} \Big|_{\bar{x}_2=f_2(\bar{x}_2)} Y_n(0, \bar{x}_2) + X_m(0) \frac{\partial Y_n}{\partial \bar{x}_1} \Big|_{\bar{x}_2=f_2(\bar{x}_2)} \right] d\Gamma, \quad (6.29)$$

$$I_{5(m,n)} = \int_{\Gamma} \left[X_m \frac{\partial Y_n}{\partial \bar{x}_2} \Big|_{\bar{x}_2=f_1(\bar{x}_1)} + X_m \frac{\partial Y_n}{\partial \bar{x}_2} \Big|_{\bar{x}_2=f_2(\bar{x}_2)} \right] d\Gamma, \quad (6.30)$$

$$I_{6(m,n)} = \iint_A \left[\frac{\partial X_m}{\partial \bar{x}_1} Y_n + X_m \frac{\partial Y_n}{\partial \bar{x}_1} \right] dA, \quad \text{and} \quad (6.31)$$

$$I_{7(m,n)} = \iint_A \left[X_m \frac{\partial Y_n}{\partial \bar{x}_2} \right] dA. \quad (6.32)$$

Since the condition in Eq. (6.23) should be true for any arbitrary variations δA_{pq} , then for every $p, q = 1, 2, \dots$, the equation inside the curly bracket should be zero which gives:

$$\sum_{p=1}^P \sum_{q=1}^Q A_{mn} \left[\bar{D}_{11}^f I_{1(m,n)} I_{1(p,q)} + \bar{D}_{12}^f [I_{1(m,n)} I_{2(p,q)} + I_{2(m,n)} I_{2(p,q)}] + \bar{D}_{22}^f I_{1(m,n)} I_{1(p,q)} + \right. \\ \left. 2\bar{D}_{16}^f [I_{1(m,n)} I_{3(p,q)} + I_{3(m,n)} I_{1(p,q)}] + 2\bar{D}_{26}^f [I_{1(m,n)} I_{3(p,q)} + I_{3(m,n)} I_{1(p,q)}] + \right. \\ \left. 4\bar{D}_{11}^f I_{3(m,n)} I_{3(p,q)} + k_2 I_{4(m,n)} I_{4(p,q)} + k_1 I_{5(m,n)} I_{5(p,q)} - \bar{F}_{11} I_{6(m,n)} I_{6(p,q)} - \right. \\ \left. \bar{F}_{22} I_{7(m,n)} I_{7(p,q)} \right]. \quad (6.33)$$

The Eq. (6.33) will give a system of $M \times N$ linear equations which can be written in matrix form of the generalized eigenvalue problem as:

$$[\bar{K}]\{A_{mn}\} = \bar{F}_{cr}[\bar{K}_s]\{A_{mn}\}, \quad (6.34)$$

where $[\bar{K}]$ is the stiffness matrix, $[\bar{K}_s]$ is the geometric stiffness matrix, and $\{A_{mn}\}$ is a vector of the unknown coefficients. The lowest eigenvalue gives the critical buckling load \bar{F}_{cr} , with the corresponding eigenvector depicting the mode shape. By using sufficient number of terms (m, n) for the displacement function in Eq. (6.15), the convergence of the buckling solution can be achieved for Eq. (6.34) (Jones, 1998). The critical buckling load can be obtained from the minimum eigenvalue of the converged solution of the buckling problem.

Because the calculation involves complex integrations terms to calculate the total potential energy, numerical integration technique would be more efficient, and it is used to evaluate the associated energy components defined with the integrals in Eqs. (6.24) - (6.30). Considering the hexagonal profile of composite plate in Fig. 6.3(a), a coordinate transformation into natural co-ordinates (ξ, η) ranging from -1 to 1 over a rectangular profile can be undertaken through the following equations:

$$\xi = \frac{2\bar{x}_1}{l_1} - 1, \quad (6.35)$$

$$\eta = \frac{\bar{x}_2 - \frac{l_2}{2}}{\frac{l_2}{2} - f_1(\bar{x}_1)}. \quad (6.36)$$

The double integrals functions defined in Eqs. (6.26) - (6.32) can be then simplified as:

$$\iint g(\bar{x}_1, \bar{x}_2) \partial\bar{x}_1 \partial\bar{x}_2 = \iint g(\bar{x}_1(\xi, \eta), \bar{x}_2(\xi, \eta)) |J| \partial\xi \partial\eta = \sum_{i=1}^N \sum_{j=1}^N w_i w_j g(\bar{x}_1(\xi_i, \eta_j), \bar{x}_2(\xi_i, \eta_j)) |J|, \quad (6.37)$$

where;

$$J = \begin{bmatrix} \frac{\partial \bar{x}_1}{d\xi} & \frac{\partial \bar{x}_2}{d\xi} \\ \frac{\partial \bar{x}_1}{d\eta} & \frac{\partial \bar{x}_2}{d\eta} \end{bmatrix}, \quad (6.38)$$

(ξ_i, η_j) is the location of the integration point, and (w_i, w_j) are the corresponding weight factors.

6.2.3 Rotational restraint stiffness at the boundaries of the cell

Because the boundaries of a cell are connected to core walls and adjacent cells, the edges of the cell are restrained against the rotation, therefore, the boundaries of the cell may not be considered as fully simply-supported or fully clamped. Since we assume that each cell of face sheets carries equal and uniform compressive stress, all the cells face sheet may be assumed to buckle at the same time; thus, rotational restraints provided by the adjacent cells may be neglected (Bleich 1952). Therefore, we assume that rotational restraint is provided only by the core walls attached to the edges of the cells of the face sheets. In order to estimate the stiffness of rotational restraint provided by the core walls, it's important to understand the deformed shape of core walls for the critical buckling mode under axial compression and bending of a sandwich panel. Multiple FE models of the sandwich panels (Fig. 6.1(a)) were created with various core densities to understand the deformed configuration of core walls under intracellular buckling. The FE models of sandwich panels under axial compression showed both symmetric and antisymmetric modes of buckling (Fig. 6.4(a)-(d)). Although it is common to have a symmetric buckling mode shape as a critical mode when the sandwich panel is subjected to wrinkling due to axial compression (Ley et al. 1999), nevertheless, it was observed that the critical intracellular buckling load always occurs with antisymmetric mode shape (Fig. 6.4(a)-(b)). The FE models for intracellular buckling of the sandwich panels under bending were considered by applying the axial compression to the upper face sheet and tension to the bottom face sheet (Fig. 6.4(e)-(f)).

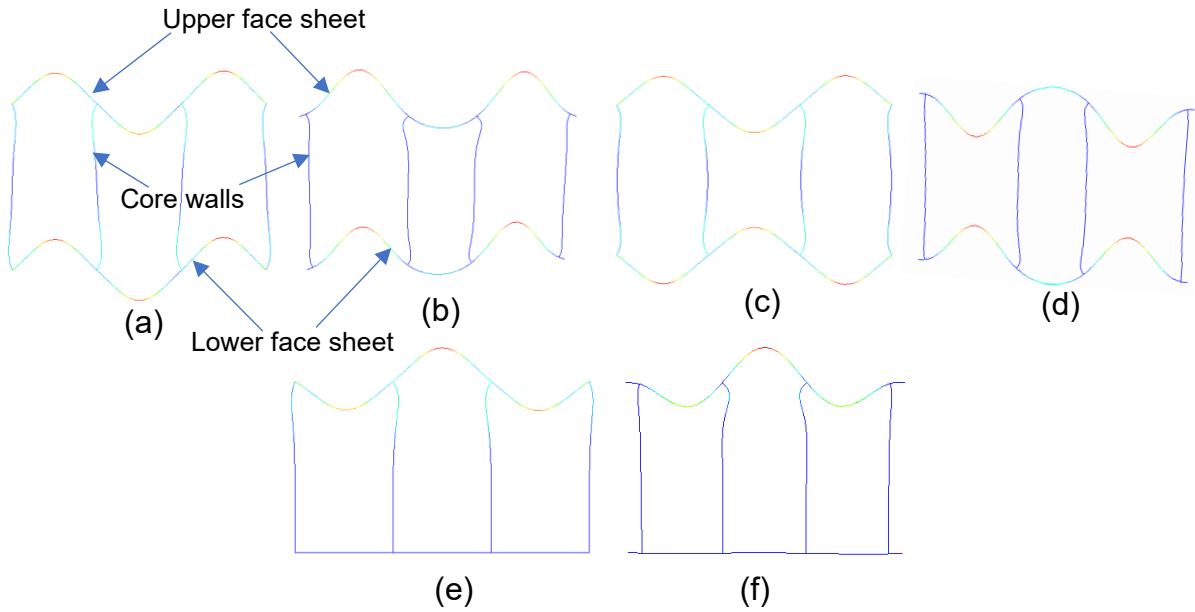


Fig.6.4: Typical section of the deformed shape of sandwich panel across (a) 1 – 3 and (b) 2 – 3 planes for anti-symmetric mode, (c) 1 – 3 and (d) 2 – 3 planes for symmetric mode under axial compression and (e) 1 – 3 and (f) 2 – 3 planes under bending.

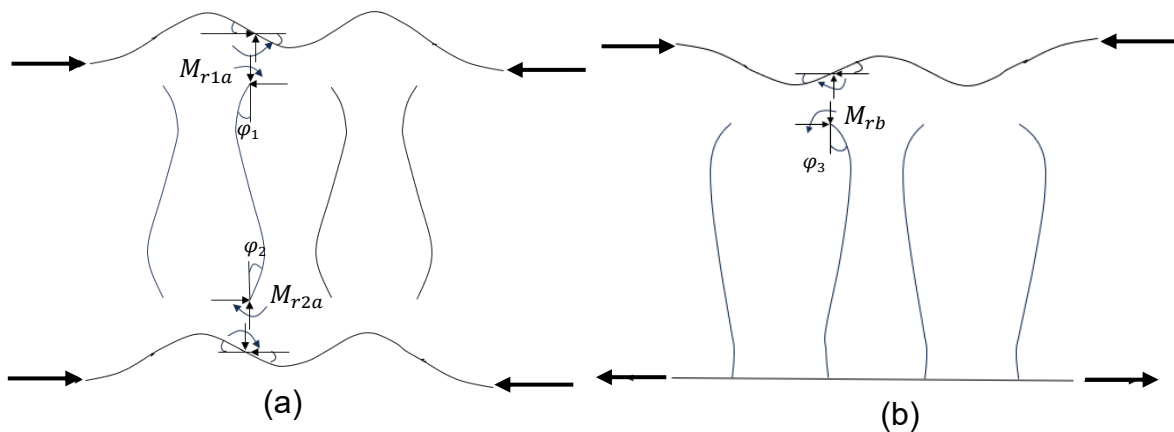


Fig.6.5: Illustration of rotational restraint provided by the core walls against buckling of face sheets under (a) axial compression and (b) bending of sandwich panel.

Based on the study in section 6.2.3, we consider the section of the sandwich panel in Fig. 6.5 for the analysis which shows the restraining moments acting on the face sheets subjected to intracellular buckling under axial compression (Fig. 6.5(a)) and bending (Fig. 6.5(b)). The restraining moments are acting along the edges of the cells due to the core walls attached to it; therefore, the core walls will experience opposite and equal moments as shown in Fig. 6.5, which may be approximately written assuming the core walls as combinations of several strips of beam elements across

the depth of the core. Considering the Fig. 6.5(a) for intracellular buckling under the axial compression, the restraining moment M_{r1a} can be written as:

$$M_{r1a} = \left(\frac{4(EI)}{h}\right) \varphi_1 + \left(\frac{2(EI)}{h}\right) \varphi_2, \quad (6.39)$$

where, EI is the flexural rigidity of a strip of the core the wall and h is the depth of the core. Assuming the sandwich panel is symmetric (both bottom and upper face sheet are equal), it's possible to take $\varphi_1 = \varphi_2$ and the moment $M_{r1a} = M_{r1a} = M_{ra}$ can be written as:

$$M_{ra} = \left(\frac{6(EI)}{h}\right) \varphi_1. \quad (6.40)$$

While a core wall is attached to two adjacent cells, only a single cell for buckling analysis is considered. Therefore, the restraining moment along boundaries of the cell can be written as:

$$M_{ra} = \frac{1}{2} \left(\frac{6(EI)}{h}\right) \varphi_1. \quad (6.41)$$

From Eq. (6.41), rotational restraint stiffnesses k_1 and k_1 for case of buckling under axial compression can be obtained as:

$$k_1 = \left(\frac{3(\overline{EI})_1}{h}\right), \quad (6.42)$$

$$k_2 = \left(\frac{3(\overline{EI})_2}{h}\right). \quad (6.43)$$

$(\overline{EI})_1$ and $(\overline{EI})_2$ are average flexural rigidity of core walls along the edges b-a-d-e (subjected to the moment \overline{M}_{11}) and a-b-c (subjected to the moment \overline{M}_{22}) respectively in Fig. 6.3(b).

Similarly, for intracellular buckling of face sheet under bending, the rotational restraint stiffnesses can be obtained as:

$$k_1 = \left(\frac{2(\overline{EI})_1}{h} \right), \quad (6.44)$$

$$k_2 = \left(\frac{2(\overline{EI})_2}{h} \right). \quad (6.45)$$

6.3 Validation of the proposed approach

In section 6.2.2, the Rayleigh-Ritz method based solution for the intracellular buckling was formulated using the variational approach. The solution procedure is implemented in MATLAB for the intracellular buckling of sandwich panels with a hexagonal core (Fig. 6.6). The intracellular buckling loads are calculated for the sandwich panels with various configurations such as different cell size, core density, thickness, and fibre lay-up face sheets and different loading conditions to validate accuracy and consistency of the proposed approach. The total thickness of the sandwich panel (H) is 160 mm, the thickness of core (h) is 150 mm, and the thicknesses t_f^u and t_f^l of both upper and lower face sheets are 5 mm. Inclined walls of the hexagonal core have fibre lay-up of $[0/90/90/90/0]$ and vertical wall has the symmetric fibre lay-up and double the thickness of the inclined walls. Each ply of the core walls is considered to be of equal thickness. Both face sheets and core walls are assumed to be fabricated out of E-glass/Epoxy, and the material properties of E-glass/Epoxy lamina with respect to its principal axes are defined as: $E_L = 38600 \text{ MPa}$, $E_T = 8270 \text{ MPa}$, $\nu_{LT} = 0.26$ and $G_{TL} = 4140 \text{ MPa}$. The fibre orientations of each ply are defined with respect to the positive 1-axis for the face sheets and positive $\bar{1}$ -axis of the core walls following the sign convention defined (counterclockwise positive angle). For the displacement function of the Rayleigh-Ritz based approach, using $n = m = 12$ was found sufficient for the convergence of solutions. The functions $f_2(\bar{x}_1)$ and $f_2(\bar{x}_1)$ are selected to be quadratic polynomials to approximate boundaries of the cell (Fig. 6.3(a)). The results from the proposed semi-analytical approach are verified against the results from the linear buckling analysis of sandwich panels consisting of multiple cells as in Fig. 6.6 using ABAQUS. Both face sheets and core are modelled using S4 shell element with a size of 10 mm. In the FE models, the compressive loads are applied along the edges of the face sheets. Additionally, the intracellular buckling loads from other existing analytical approaches discussed in section 2.4.4 of Chapter 2 are also calculated for the purpose of comparison with the results from the proposed approach.

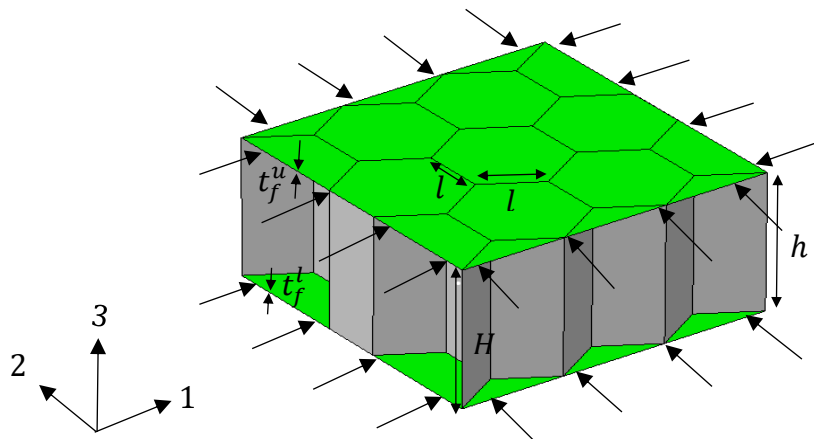


Fig.6.6: The sandwich panel considered for the intracellular buckling analysis.

6.3.1 The effect of cell size on the intracellular buckling

The cell size of face sheets (Fig. 6.6) is varied from $l = 40 \text{ mm}$ to 100 mm to validate the consistency of the proposed approach and to study the effect of boundary conditions on the intracellular buckling. In this case, the relative core density (ρ^*) is kept constant at 0.072 and both upper and lower face sheets have fibre lay-up of $[0/90/0/90/0]$. All other parameters are chosen as defined in section 4.3. Tables 6.1 - 6.6 show comparisons of the results for the intracellular buckling loads from the proposed semi-analytical approach and FE for various loading conditions. Figure. 6.7 shows a comparison of normalised buckling loads (normalised by the maximum buckling loads for direction-1 from FE) for different axial compressive loadings. The predictions from the proposed approach are also compared with analytical solutions from the existing literature (section 2.4.4) and shown in (Figs. 6.8 - 6.9).

Table 6.1: Comparison of intracellular buckling load of sandwich panels with different cell sizes under axial uniaxial compression in direction-1.

$l \text{ (mm)}$	Intracellular buckling load(N/mm)			Error %	
	Proposed-SS (a)	Proposed-RR (b)	FE(c)	$\frac{(a - c)}{c} \%$	$\frac{(b - c)}{c} \%$
40	1752	2529	2690	-34.9	-6.0
50	1121	2088	2146	-47.7	-2.7
60	779	1709	1651	-52.8	3.5
70	572	1385	1343	-57.4	3.2
80	438	1148	1125	-61.1	2.0

Table 6.2: Comparison of intracellular buckling load of sandwich panels with different cell sizes under uniaxial compression in direction-2.

l (mm)	Intracellular buckling load(N/mm)			Error %	
	Proposed-SS (a)	Proposed-RR (b)	FE(c)	$\frac{(a-c)}{c}$ %	$\frac{(b-c)}{c}$ %
40	2122	2508	2543	-16.6	-1.4
50	1358	1893	1912	-29.0	-1.0
60	943	1512	1498	-37.0	0.9
70	693	1216	1190	-41.8	2.2
80	530	995	988	-46.3	0.7

Table 6.3: Comparison of intracellular buckling load of sandwich panels with different cell sizes under biaxial compression.

l (mm)	Intracellular buckling load(N/mm)			Error %	
	Proposed-SS (a)	Proposed-RR (b)	FE(c)	$\frac{(a-c)}{c}$ %	$\frac{(b-c)}{c}$ %
40	968	1422	1431	-32.3	-0.6
50	620	1194	1103	-43.8	8.3
60	430	978	870	-50.5	12.4
70	316	788	713	-55.7	10.6
80	242	650	586	-58.7	11.0

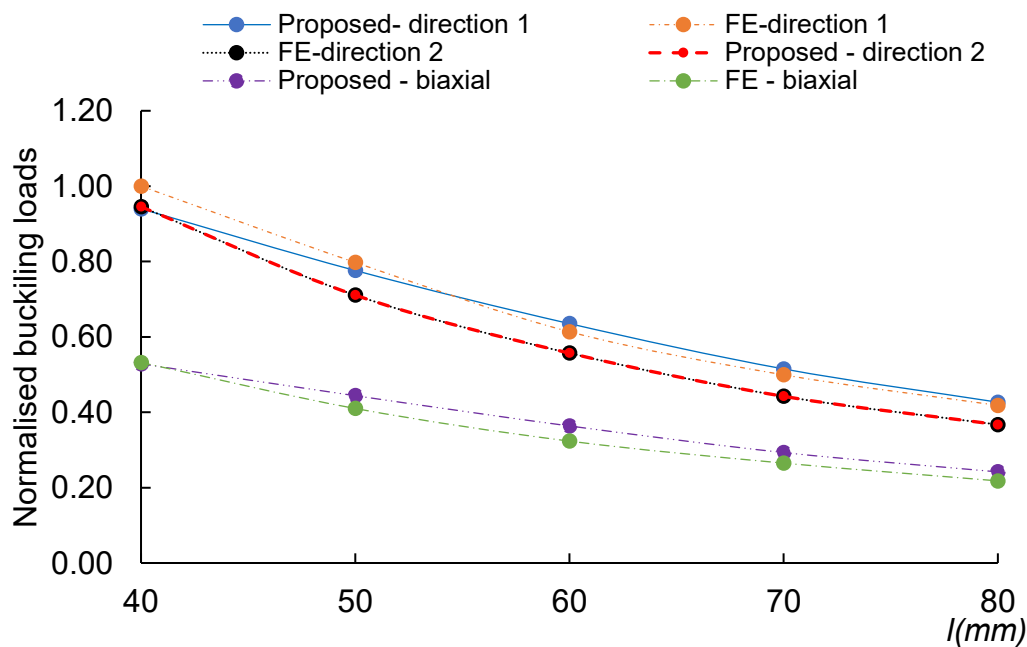


Fig. 6.7: Variation of intracellular buckling loads with cell sizes under different axial compressive loadings.

Tables 6.1 and 6.2 show the predictions of the intracellular buckling loads under uniaxial compression in direction-1 and direction-2, respectively. The predictions from the proposed approach with rotationally restrained boundaries differ by maximum of -6% and -1.4% from the FE results for the uniaxial compression in direction-1 and direction-2, respectively. The corresponding errors are much higher when the boundaries of the cell are considered to be simply-supported. As the cell size increases, the prediction errors become higher with simply-supported boundaries for the cell. That is because, with the increase in cell size under the constant relative core density, the thickness of the core wall also increases providing additional rotational restraints to the edges of the cell. Comparing the buckling loads for the uniaxial compression in direction-1 and direction-2 for different cell sizes, the intracellular buckling loads for direction-1 are always slightly higher than direction-2 (Fig. 6.7). However, the predictions considering the simply-supported boundaries for the cell show higher buckling loads for the direction-2 than direction-1. It is expected that an increase in cell size will reduce intracellular buckling load for the sandwich panel even though the rotational restraint due to the core walls increases with cell size (Fig. 6.7). These effects have been correctly reflected in the results from the proposed approach. The existing closed-form analytical solutions can only be used to predict the intracellular buckling loads under uniaxial compression. However, it may be unavoidable to have biaxial compressive loading conditions in the sandwich panels. Table 6.3 shows the comparison of the buckling loads for biaxial compression from the proposed approach and FE. The predictions using the proposed approach with rotationally restrained boundaries for the cell are within reasonable accuracy with a maximum error of 12.4%. Overall, the predictions using the proposed semi-analytical approach with the rotationally restrained boundaries for the cell agree well with the predictions from FE (Fig. 6.7) for all different cell sizes and for all different axial compressive loading conditions.

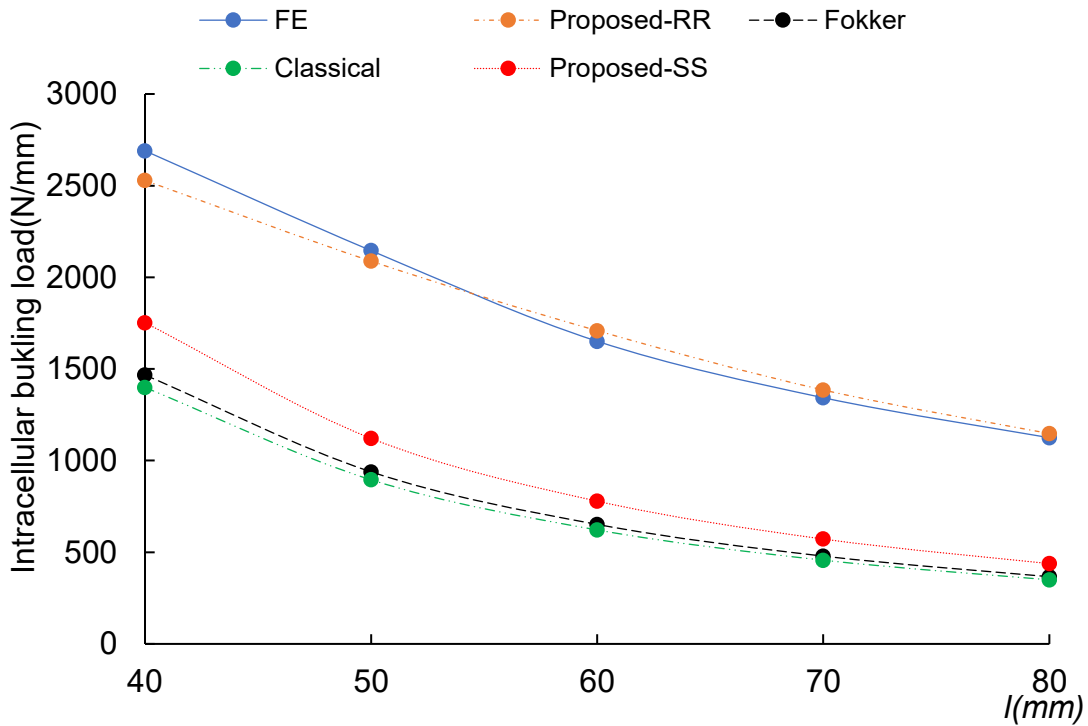


Fig. 6.8: Comparison of intracellular buckling loads of different cell sizes from various methods for the uniaxial compression in direction-1.

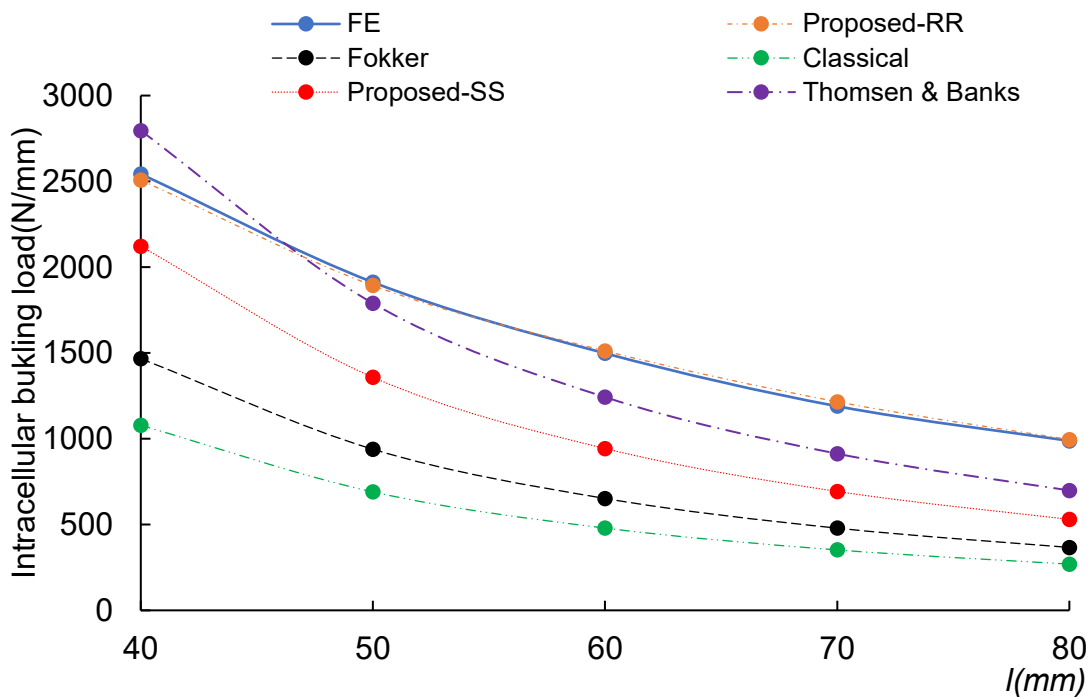


Fig. 6.9: Comparison of intracellular buckling loads of different cell sizes from various methods for the uniaxial compression in direction-2.

Figures. 6.8 and 6.9 show the comparisons of the buckling loads for uniaxial compression in direction-1 and direction-2, respectively, from various analytical

solutions and the proposed approach. From Fig. 6.8, it is clear that the classical method (Eq. (2.6)), which is based on an empirical factor and approximated geometry of the hexagonal cell with the largest inscribed circle, gives the lowest buckling loads. The Fokker formula (Eq. (2.7)), which also considers the approximated geometry of a square having side dimensions equal to the diameter of a largest inscribed circle within the cell and simply-supported boundaries, gives slightly higher buckling loads than the classical method. While the proposed approach with simply-supported boundaries for the cell gives better results than both the classical and Fokker formulas, predicted buckling loads are still significantly lower than the FE results. The proposed approach with rotationally restrained boundaries for the cell gives much closer result to the FE results. For the axial compression in direction-2, trends of the predictions from different models are similar to those in direction-1 (Fig 6.9). The classical approach gives significantly lower results than the other methods as it considers only a single bending stiffness term of the composite face sheet for the buckling load calculations. The Fokker formula provides same buckling loads regardless of the direction of the loadings, as it is analogous to the buckling equation of a simply-supported square composite plate. Since Thomsen & Banks (2004) considered an approximated geometry of rectangular profile for the cell with fixed and simply-supported boundaries for shorter and longer edges respectively (Fig. 2.9(b)), their method (Eq. (2.8)) gives better results compared to the classical and Fokker formulas. Nonetheless, the results deviate considerably from the predictions of FE analysis. The proposed approach with simply-supported conditions again provides lower predictions than the FE results, while the proposed method with rotationally restrained boundary conditions provides predictions similar to the FE results.

Tables 6.4 - 6.6 show intracellular buckling loads of the top face sheet under the bending of sandwich panels. The bending of sandwich panels is considered by applying compressive force to the upper face sheet and an equal magnitude of tensile force to the bottom face sheet. Again, assuming simply supported support conditions results in much lower predictions than the FE results and the proposed method with rotationally restrained boundaries provides results closer to the FE predictions. The intracellular buckling loads under bending (Tables 6.4 - 6.6) are found to be slightly lower than the corresponding intracellular buckling loads under axial compression (Tables 6.1 - 6.4) of the sandwich panels because of the effect of the difference in the

rotational restraints due to core walls during bending and axial compression(section 6.2.3).

Table 6.4: Comparison of intracellular buckling load of sandwich panels with different cell sizes under bending about axis-2.

$l_1(mm)$	Intracellular buckling load(N/mm)			Error %	
	Proposed-SS (a)	Proposed-RR (b)	FE(c)	$\frac{(a-c)}{c} \%$	$\frac{(b-c)}{c} \%$
40	1752	2321	2598	-32.6	-10.7
50	1121	1907	1992	-43.7	-4.2
60	779	1599	1540	-49.4	3.8
70	572	1317	1245	-54.0	5.8
80	438	1088	1020	-57.1	6.7

Table 6.5: Comparison of intracellular buckling load of sandwich panels with different cell sizes under bending about axis-1.

$l_1(mm)$	Intracellular buckling load(N/mm)			Error %	
	Proposed-SS (a)	Proposed-RR (b)	FE(c)	$\frac{(a-c)}{c} \%$	$\frac{(b-c)}{c} \%$
40	2122	2402	2444	-13.2	-1.7
50	1358	1773	1834	-26.0	-3.3
60	943	1425	1399	-32.6	1.9
70	693	1162	1115	-37.9	4.2
80	530	953	918	-42.2	3.8

Table 6.6: Comparison of intracellular buckling load of sandwich panels with different cell sizes under biaxial bending.

$l_1(mm)$	Intracellular buckling load(N/mm)			Error %	
	Proposed-SS (a)	Proposed-RR (b)	FE(c)	$\frac{(a-c)}{c} \%$	$\frac{(b-c)}{c} \%$
40	968	1298	1396	-30.6	-7.0
50	620	1085	1103	-43.8	-1.6
60	430	917	824	-47.8	11.3
70	316	752	670	-52.8	12.2
80	242	618	553	-56.2	11.7

6.3.2 The effect of core density on the intracellular buckling

The degree of rotational restraints provided by the core walls depends mainly on the bending rigidity of the core walls. Therefore, varying the core density for constant cell size can be expected to influence the intracellular buckling load. Therefore, it is necessary to investigate the effect of core density on intracellular buckling. The relative core density(ρ^*) is varied from 0.036 to 0.108 while the cell size is constant with $l = 50 \text{ mm}$ (Fig. 6.6). All other parameters are the same as defined in section 4.3. Tables 6.7 - 6.9 show the comparisons of results for intracellular buckling loads from the proposed approach and the FE under axial compression. The variation of normalised buckling loads with relative core density for different compressive loadings is shown in Fig. 6.10. The comparisons of the predictions of the intracellular buckling loads from various analytical methods available in the literature are shown in Figs. 6.11- 6.12.

Table 6.7: Comparison of intracellular buckling load of sandwich panels with different relative core density under uniaxial compression in direction-1.

ρ^*	Intracellular buckling load(N/mm)			Error %	
	Proposed-SS (a)	Proposed-RR (b)	FE(c)	$\frac{(a-c)}{c} \%$	$\frac{(b-c)}{c} \%$
0.036	1135	1349	1512	-28.7	-10.8
0.054	1135	1714	1866	-39.2	-8.1
0.072	1135	2088	2146	-47.1	-2.7
0.090	1135	2373	2334	-51.4	1.7
0.108	1135	2584	2530	-55.1	2.1

Table 6.8: Comparison of intracellular buckling load of sandwich panels with different relative core density under uniaxial compression in direction-2.

ρ^*	Intracellular buckling load(N/mm)			Error %	
	Proposed-SS (a)	Proposed-RR (b)	FE(c)	$\frac{(a-c)}{c} \%$	$\frac{(b-c)}{c} \%$
0.036	1358	1473	1489	-8.8	-1.1
0.054	1358	1657	1679	-19.1	-1.3
0.072	1358	1893	1912	-29.0	-1.0
0.090	1358	2106	2116	-35.8	-0.5
0.108	1358	2271	2250	-39.6	0.9

Table 6.9: Comparison of intracellular buckling load of sandwich panels with different relative core density under biaxial compression.

ρ^*	Intracellular buckling load(N/mm)			Error %	
	Proposed-SS (a)	Proposed-RR (b)	FE(c)	$\frac{(a-c)}{c}$ %	$\frac{(b-c)}{c}$ %
0.036	620	750	827	25.1	9.3
0.054	620	968	952	34.9	-1.6
0.072	620	1194	1103	43.8	-8.3
0.090	620	1361	1247	50.3	-9.1
0.108	620	1477	1376	55.0	-7.3

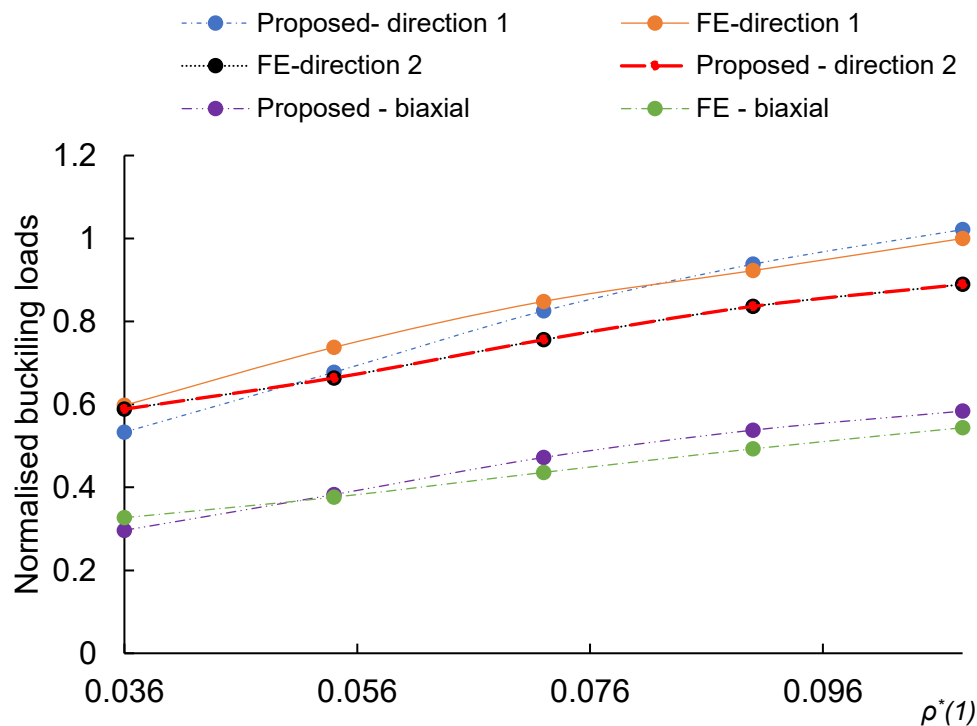


Fig. 6.10: Variation of intracellular buckling loads with relative core density under different axial compressive loadings.

It can be seen from Table 6.7, for the uniaxial compression in direction-1, the absolute errors in the predictions from the proposed methodology with rotationally restrained boundaries for the cell are less than 8.1% (except for the case of lowest core density which has an error of 10.8%). When the boundaries of the cell are simply-supported, the absolute error percentage varies from 28.7% to 55.1% as core density increases. Table 6.8 shows the predictions of the buckling loads under uniaxial compression in direction-2. An excellent agreement between results from the FE and the proposed approach with rotationally restrained boundaries can be seen. The maximum absolute error of predictions between FE and the proposed with rotationally

restrained boundaries is just 1.3%, while the error increased to 39.6% with simply supported boundaries for the cell. The intracellular buckling loads for direction-1 are higher than for direction-2, and the difference between the direction-1 and direction-2 buckling loads increases with core density; however, this increase in load is mainly due to positive influence of fibre orientation and rotationally restrained boundaries rather than positive influence of the geometry of the cell in the direction-1. This behaviour is correctly captured by the proposed approach only when boundaries of the cell are considered to be rotationally restrained. Table 6.9 shows the predictions of buckling loads under biaxial compression. The absolute errors of predictions from the proposed approach are under 9.3% when the boundaries of the cell are considered to be rotationally restrained, while the maximum error is 55% with simply supported boundaries for the cell. For all different loading conditions, the predictions for the intracellular buckling loads converge towards the simply supported solutions when the relative core density is low. It is also possible that other buckling failure modes, such as wrinkling and core wall buckling, become dominant at low core densities (Ley et al. 1999). When the core density increases from 0.036 to 0.108, the increase in the buckling loads varies between about 50-60% (Fig. 6.10), depending on the axial compression loading conditions. The buckling load for the biaxial compression is about half the buckling loads of axial compression in direction-1 at the core density of 0.036 and about 60% when the core density is 0.108. Overall, the predictions from the proposed approach with the rotationally restrained boundaries for the cell are in very good agreement with results from the FE (Fig. 6.10) for all the core densities considered.

Figures. 6.11 and 6.12 show the comparisons of the intracellular buckling loads for the sandwich panels with varying core density under axial compression in direction-1 and direction-2, respectively. As it can be seen from Figs. 6.11 - 6.12, the classical and Fokker closed-form solutions significantly underpredict the intracellular buckling loads as the core density increases. The classical solution underpredicts the buckling loads up to 2.8 and 3.3 times compared to the FE for the axial compression in direction-1 and direction-2, respectively. The Fokker formula underpredicts the buckling loads up to 2.7 and 2.4 times, respectively. The solution proposed by Thomsen & Banks (2004) is applicable only for the axial compression in direction-2, which considerably overpredicts the buckling loads at the lower core density and underpredicts the buckling loads at higher density.

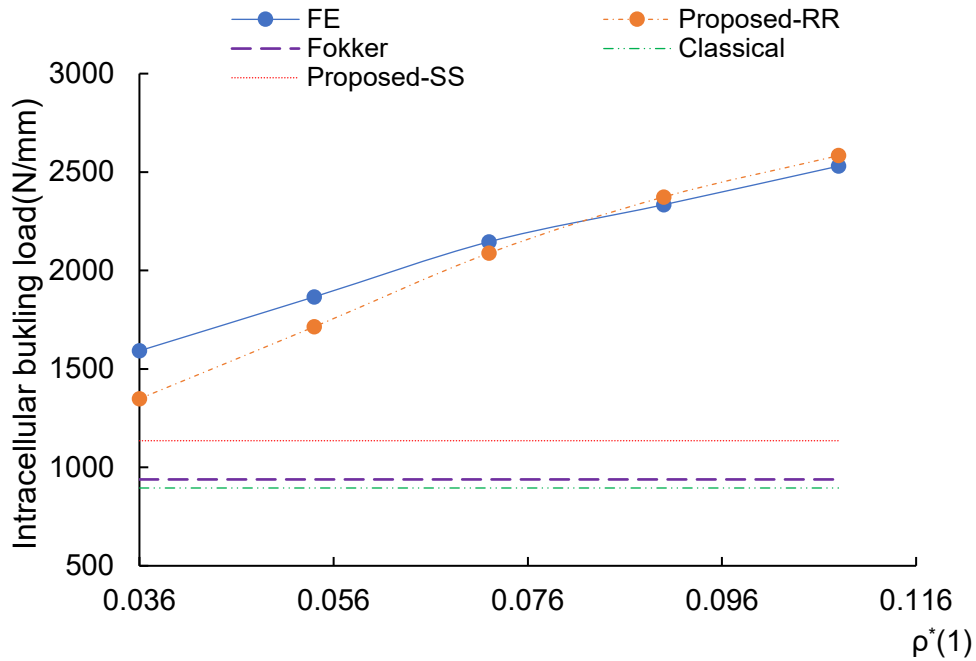


Fig. 6.11: Comparison of intracellular buckling loads for different relative core density from various analytical methods for the uniaxial compression in direction-1.

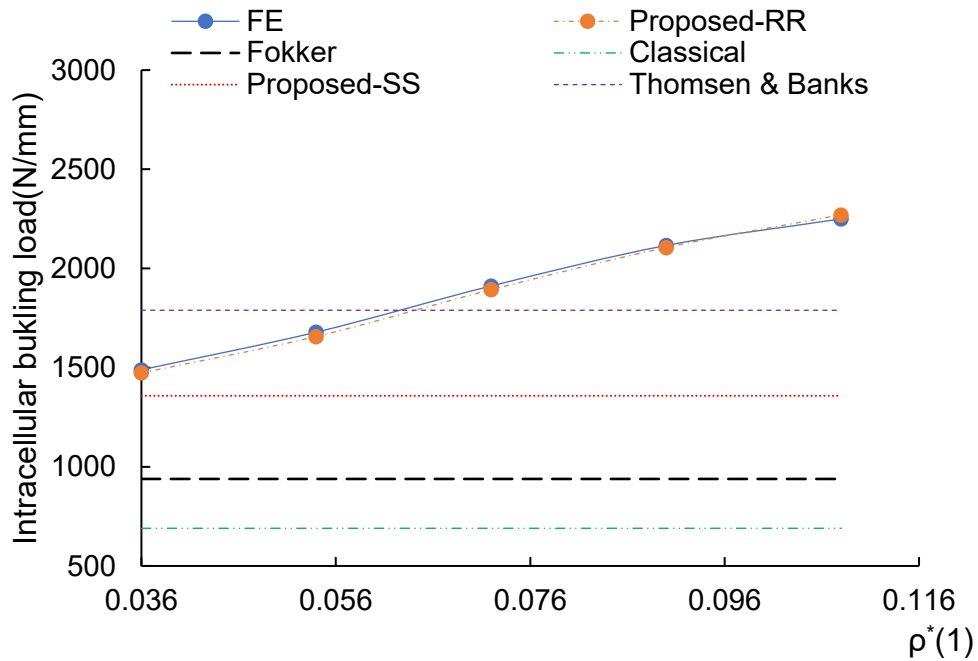


Fig.6.12: Comparisons of intracellular buckling loads for different relative core density from various analytical methods for the uniaxial compression in direction-2.

6.3.3 The effect of the face sheet fibre lay-up on the intracellular buckling

Another important variable to consider in intracellular buckling is the fibre lay-up of the face sheet. In order to investigate this, the relative core density is kept at a constant of 0.072, and the cell size is chosen to be $l = 50 \text{ mm}$ (Fig.6.6). The fibre lay-ups considered for the face sheet in this study are given in Table 6.10.

Table 6.10: *The fibre lay-ups considered for the face sheets.*

Fibre lay-up	Fibre orientation ($^{\circ}$)
1	0/90/0/90/0
2	0/90/90/90/0
3	90/0/0/0/90
4	45/-45/0/-45/45
5	45/-45/90/-45/45
6	45/-45/45/-45/45

Figure. 6.13 shows intracellular buckling loads for the uniaxial compression in direction-1 for the different fibre lay-ups in Table 6.10. It can be seen that cross-ply laminates with 0° ply as topmost and bottommost ply (fibre lay-ups 1 and 2) have the highest buckling load, while the cross-ply laminate which has 90° ply as topmost and bottommost ply gives the lowest buckling load (Fibre lay-up 3). Buckling loads of all the angle-ply laminates are close to each other and considerably lower than the cross-ply laminates with fibre lay-ups 1 and 2. Except for the proposed approach with rotationally restrained boundaries for the cell, all the other models fail to predict the buckling loads to a reasonable accuracy, and they are not consistent with the trend of the buckling loads from the FE for different fibre lay-ups. Fig. 6.14 shows the intracellular buckling loads for the uniaxial compression in direction-2. The trend is found to be opposite to that of direction-1 loading. Face sheets with angle-ply laminates show higher buckling loads than the face sheets with cross-ply laminates. Only the proposed approach with rotationally restrained boundaries and Thomsen & Banks (2004) method predict the buckling loads close to the FE results. The predictions from all other methods are significantly different from the FE. The buckling loads for biaxial compression show a similar trend as buckling under axial compression in direction-1, however, with different ratios between the buckling loads. The buckling loads for the biaxial compression have also been predicted to have reasonable accuracy using the proposed approach with rotational restrained boundaries for the cell. Although the proposed approach considering simply supported boundaries yields lower predictions for buckling loads compared to those with rotationally restrained boundaries and FE results across various loading scenarios due to boundary considerations, these predictions outperform classical and Fokker solutions due to their consideration of accurate geometry and alignment with

the trend observed in FE and the proposed approach employing rotationally restrained boundaries.

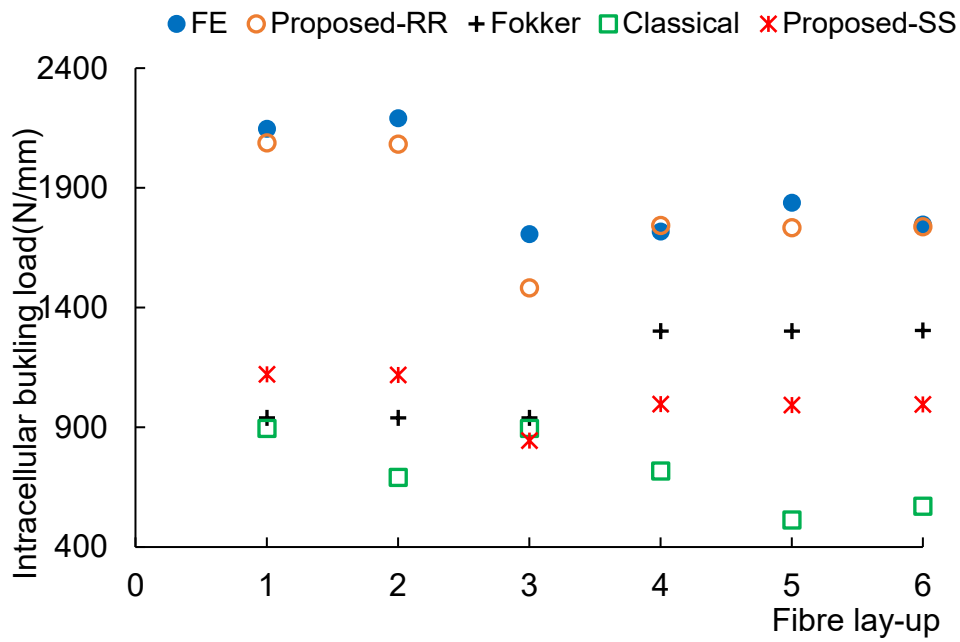


Fig.6.13: Comparisons of intracellular buckling loads for different fibre lay-up of the face sheet under uniaxial compression in direction-1.

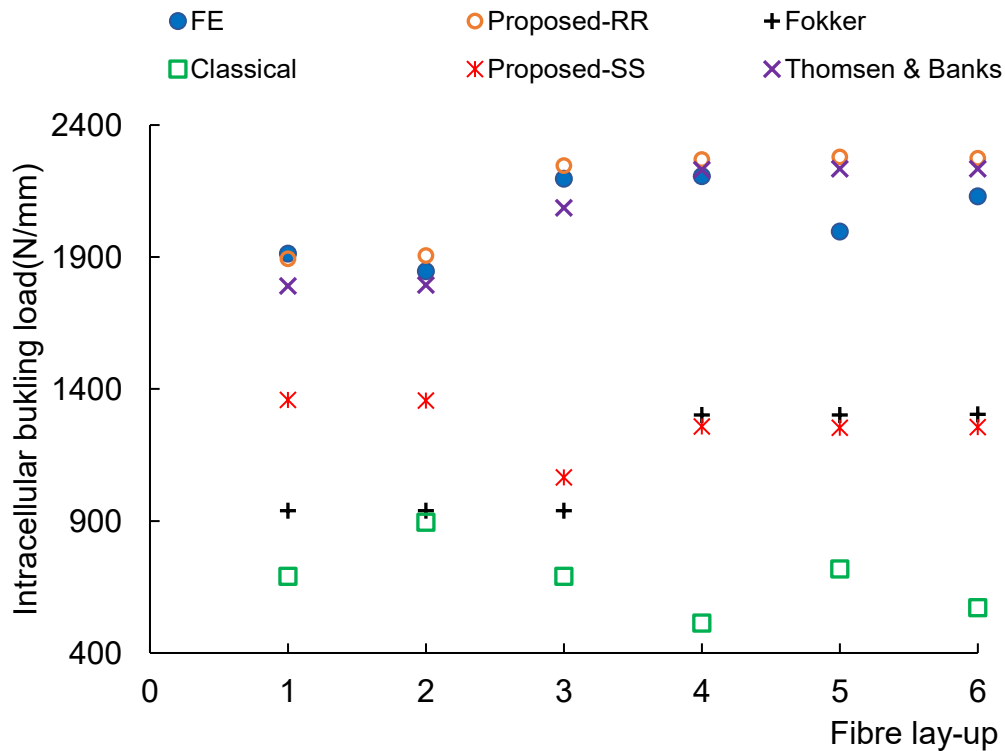


Fig.6.14: Comparisons of intracellular buckling loads for different fibre lay-up of the face sheet under uniaxial compression in direction-2.

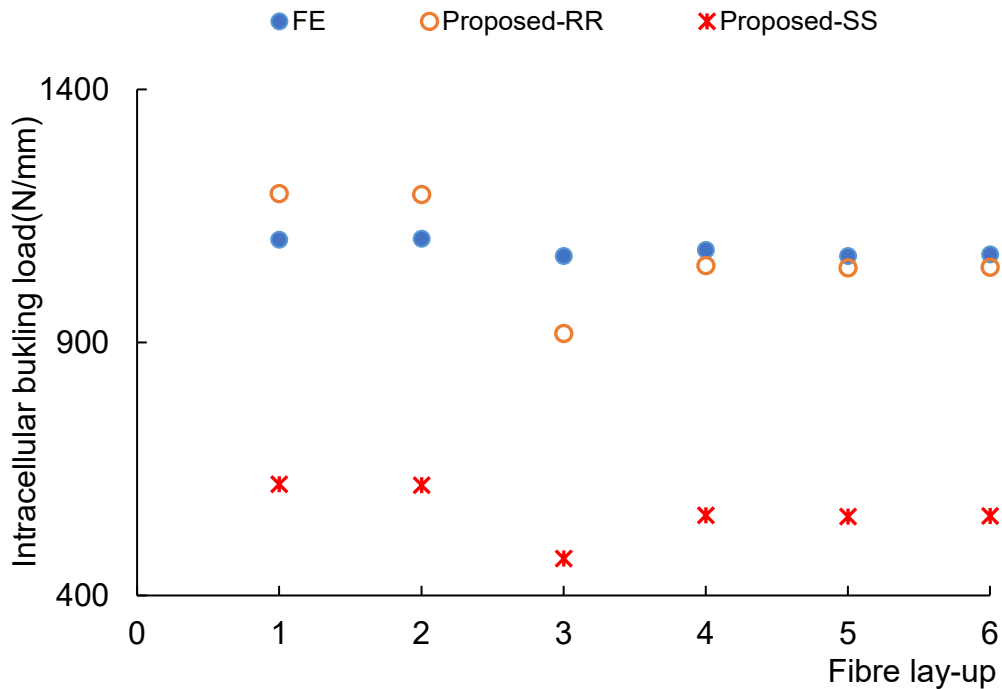


Fig.6.15: Comparisons of intracellular buckling loads for different fibre lay-up of the face sheet under biaxial compression.

6.3.4 Comparison of predictions with existing experimental studies

In this section, comparisons are conducted between predictions derived from our proposed semi-analytical approach, other existing analytical models utilized in the inverse design approach, and experimental findings from previous studies. Due to the limited availability of experimental data, conducting a comprehensive comparison across various parameters is impractical. Nonetheless, an effort is made to assess the performance of the proposed approach by comparing it to the results of uniaxial compression tests conducted on all-CFRP sandwich panels (manufactured using T300-3K woven CFRP/epoxy) by Wei et al. (2022), aimed at intracellular buckling failure in the sandwich panels.

The sandwich panels tested have dimension of 140mm×80mm×15.38mm. Material properties of T300-3K woven CFRP/epoxy are same as given section in section 4.3.5. Thickness of each face sheet is $t_f=0.19\text{mm}$. Thickness of the inclined walls of the hexagonal core is $t=0.21\text{mm}$ and other wall has double the thickness of the inclined wall. Length of the core walls is $l=8\text{mm}$. For both face sheet and core, all the plies of laminate were arranged in same orientation (0/90).

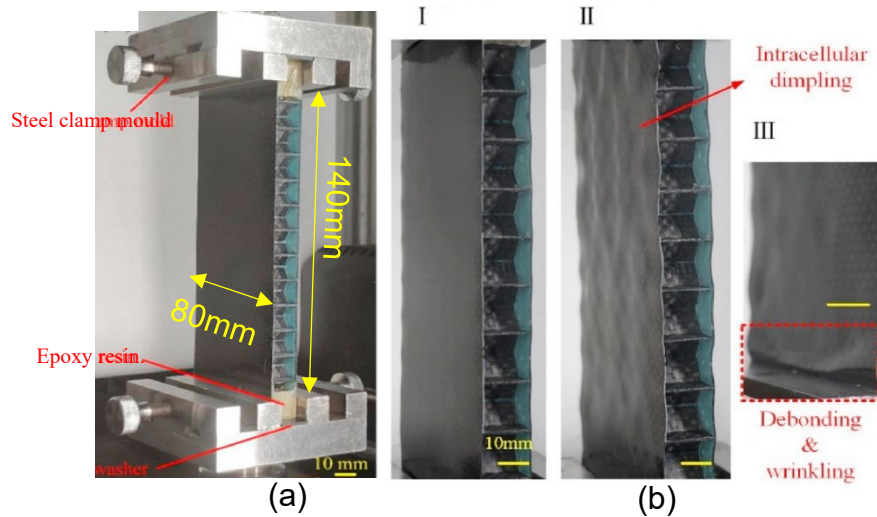


Fig.6.16: (a) All-CFRP sandwich panel tested under axial compression and (b) intracellular buckling mode of failure (Wei et al. 2022).

Since the failure in the sandwich panels tested was initiated due to intracellular buckling (Fig.6.16b), it's reasonable to consider that applied uniaxial compression at the failure is very close to intracellular buckling load of the sandwich panels. Figure 6.17 shows the comparison of the predictions for the intracellular buckling from the proposed approach and the experimental results. The failure loads from the experiments vary between 2.91kN-3.33kN between the specimens. For the same panels, the proposed model incorporating the rotational restrain boundaries predicts the intracellular buckling load to be 2.61kN which is 16% lower than average failure load from the experiments. This disparity between predictions and experiments could be attributed to the mismatch between the failure modes at maximum load. As illustrated in the tested specimens in Fig. 6.16(b), real-world structures may experience a loss of stiffness rather than immediate collapse following intracellular buckling (Thomsen & Banks, 2004), potentially carrying additional loads until collapsing due to interactions with other failure modes (i.e., intracellular buckling occurs close to position II, but panels carry further load until they collapse due to wrinkling & debonding as illustrated in Fig. 6.17). Therefore, the maximum load obtained in the experiment may not exactly represent the actual theoretical intracellular buckling loads. Nonetheless, honeycomb core sandwich panels are always designed to resist intracellular buckling occurrence (Zenkert, 1997), as such buckling could subsequently trigger other failure modes like delamination, wrinkling, etc., ultimately leading to structural collapse. Except for the proposed model with

rotational restrain boundaries, all the other predictions are much lower than experimental results which may lead to much conservative design rather than optimal or near optimal design. Consequently, the use of such conservative models could negatively impact the accuracy of inverse design solutions in detailed analyses, even when employing highly efficient search algorithms. This discordant scenario underscores the critical need for precise and robust analytical models in intracellular buckling predictions.

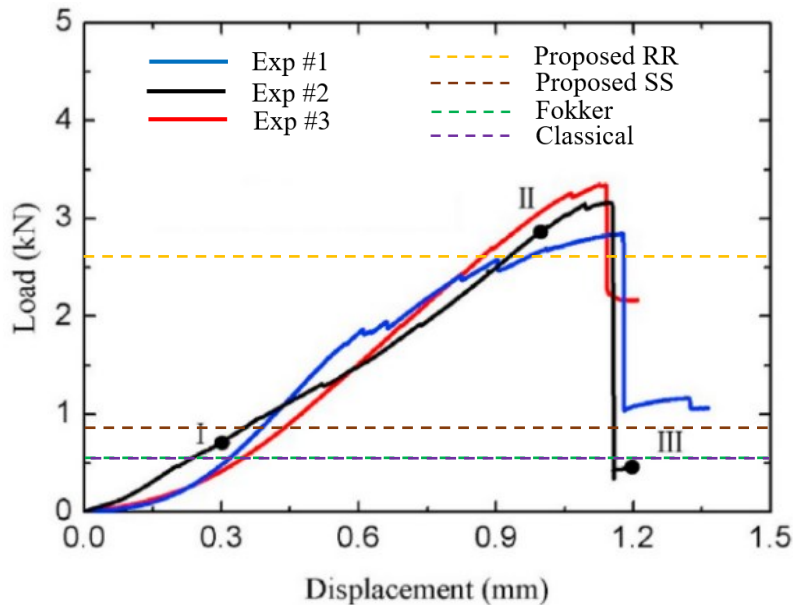


Fig.6.17: Comparison of intracellular buckling predictions with the experimental results of Wei et al. (2022).

6.4 Intracellular buckling of face sheets with different cell shapes

Previous sections validated the proposed approach for intracellular buckling of face sheets with hexagonal cells. This section will focus on extending the application of the proposed methodology for intracellular buckling of face sheets of different cell shapes. The classical and Fokker formulas (Eqs. (2.6) - (2.7)) cannot differentiate between specific geometries of the cell, although different cell shapes can result in different buckling loads. For instance, according to the classical and Fokker buckling formulas, intracellular buckling loads will be equal for the square and rhombus (rotated square with equal angles) cells. However, this is not the case, as the orientation of the geometry concerning the fibre orientation and loadings would be different, which may significantly affect the buckling loads of the cell. The proposed approach for intracellular buckling loads can be generalised to other geometries to be used for sandwich panels consisting of other cell shapes such as triangular, rhombus, etc.

Consider rhombus and triangular cells in Fig. 6.18. The displacement function in Eq. (6.3) may be manipulated for the buckling problem of the rhombus and triangular cells by selecting a suitable polynomial to define the boundaries. Suitable polynomial functions $f_1(\bar{x}_1)$ and $f_2(\bar{x}_1)$ may be selected to define the boundaries of the rhombus and triangular cells. In Eq. (6.4), $l_2(\bar{x}_1)$ should not be zero at any boundary points as it will cause a singularity in the calculations. In order avoid these numerical issues, $l_2(\bar{x}_1)$ should be defined such that $l_2(\bar{x}_1)$ at the corner points a and c (Fig.6.18) should not be zero. Equations. (6.43) and (6.44) may be used to define $l_2(\bar{x}_1)$ for the rhombus cell and triangular cell shapes respectively:

$$l_2(\bar{x}_1) = (f_2(\bar{x}_1) - f_1(\bar{x}_1)) + \delta l, \quad (6.43)$$

$$l_2(\bar{x}_1) = -f_1(\bar{x}_1) + \delta l, \quad (6.44)$$

where, δl is very small value to avoid the singularity at the corner points. Now, the buckling problems can be solved following same procedure discussed in section 6.3.

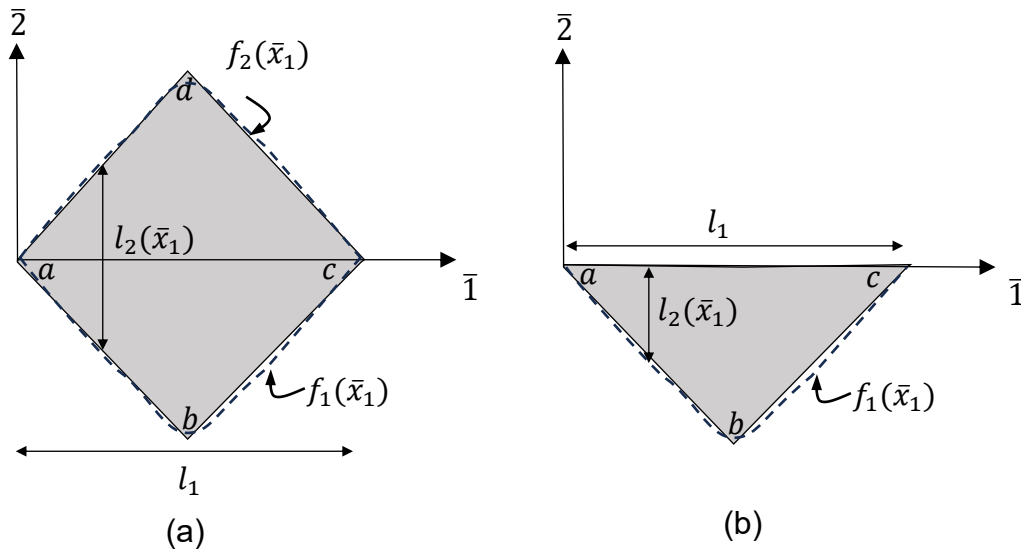


Fig. 6.18: Illustration of definition of the displacement functions for the (a) rhombus and (b) triangular cells.

6.4.1 Comparison of intracellular buckling of different cell shapes

In this section, intracellular buckling behaviour of different cell shapes is studied. Regular hexagonal, equilateral triangular, square and 45° rotated square (will be referred as 'rhombus' afterwards) shapes are considered for the study. Cell sizes of different shapes have been selected such that

1. the diameter of the largest inscribed circle within the cell of different shapes (Fig.6.19) is equal to each other ($D_1 = D_2 = D_3$) and
2. the area of the cell of different shapes is equal to each other.

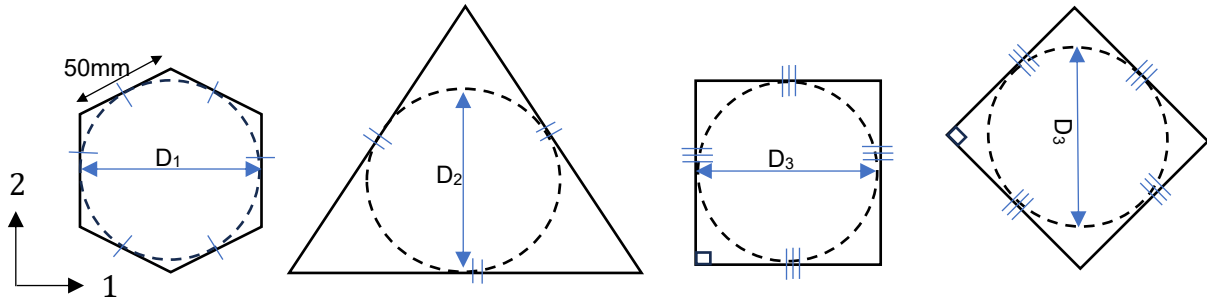


Fig. 6.19: Different cell shapes considered for the analysis of intracellular buckling.

The material properties of the honeycomb core and face sheets considered here are the same as in section 6.3. Face sheets of sandwich panels have a thickness of 5mm and fibre lay-up of $[0,90,0,90,0]$ with equal ply thickness. Except for the hexagonal core (the vertical wall of the hexagonal core has double the thickness of the inclined walls), the core walls of each cell shape have identical thicknesses. The relative core density of the sandwich panel varies from 0.054 - 0.108, and the thicknesses of the core walls of each cell shape are selected to have a specified relative core density. Sandwich panels consisting of honeycomb cores of different shapes and core densities are analysed for the intracellular buckling loads under uniaxial compression in direction-1 and direction-2 using the proposed semi-analytical approach considering the cell boundaries as rotationally restrained. Linear buckling analysis is carried out using ABAQUS on the sandwich panels consisting of the honeycomb cores of different shapes to compare with the predictions from the proposed approach. Comparisons of the buckling loads between the different cell shapes are shown in Fig.6.20 - 6.21.

Figure. 6.20(a) compares intracellular buckling loads of different cell shapes with equal inscribed circles under uniaxial compression in direction-1. It can be seen from Fig.6.20(a) that the predictions for intracellular buckling loads from the Fokker formula are equal regardless of different cell shapes. In contrast, the predictions from the proposed approach and FE significantly differ from those from the Fokker formula, mainly because the proposed semi-analytical approach and FE analysis consider the effect of different cell shapes and the core density on the intracellular buckling loads,

while the Fokker formula cannot differentiate the cell shapes having inscribed circles with equal diameters and does not consider the effect of core density on the restraint along the boundaries of the cells. Considering the different cell shapes of equal inscribed circles and with equal core density, the hexagonal cell shape provides the highest intracellular buckling loads under uniaxial compression in both direction-1 and direction-2. Although the square cell has the lowest buckling loads under compression in direction-1, the rhombus cell shape (rotated square) provides the second-highest buckling loads under loading in direction-1 and direction-2. The triangular cell shape provides better results than the square cell under the loading in direction-1. However, intracellular buckling loads of triangular cells become lowest under the axial compression in direction-2. Comparing the corresponding buckling loads for different core densities under the loading in direction-1 and direction-2 for different cell shapes, they are not equal, which is caused by effect of the geometry of the cell and the fibre orientations of plies on the buckling loads. Considering the square cell and rhombus, both provide slightly better buckling loads for the loading in direction-1 than direction-2 because of the difference in the material stiffness of the face sheet in both directions; however, for other shapes, the differences are due to the combination of the effects of geometry and material. At the same time, the Fokker formula predicts the same buckling loads for direction-1 and direction-2 as it is analogous to the buckling formula of a simply-supported square plate.

Comparing the results from the proposed approach with the FE results, it can be seen that there is a considerable difference between the results for the square, rhombus and triangular cores in comparison to the hexagonal core; this is mainly due to the influence of increased in-plane stiffness of those cores than the hexagonal core. Therefore, compression loads applied along the edges of face sheets in FE models (Fig. 6.6) may differ considerably from the intracellular buckling stress at the factsheet, as the face sheet will not carry the full compression load. Nevertheless, consistency in the prediction trend of the intracellular buckling loads from the proposed approach and FE predictions can be seen. As core density becomes lower, buckling of the core walls starts to interact with the intracellular buckling of the face sheets, causing some change in the trend, which needs to be further studied to understand the behaviour.

Considering the different cell shapes with equal area, the predictions from the proposed approach and FE in Fig.6.21 show that still the hexagonal cell has the

highest buckling loads for the loading in both direction-1 and direction-2 and square and triangular cells have the lowest buckling load for loading in direction-1 and direction-2 respectively. However, the Fokker formula contradicts the results of the proposed approach and FE and predicts the lowest and highest buckling loads for the hexagonal and triangular cell, respectively, as the diameter of the inscribed circle of hexagonal is larger than the diameter of the inscribed circle of a triangular cell having an equal area of the hexagonal cell. The analysis highlights the contradictions of using the Fokker formula to predict the intracellular buckling loads of the sandwich panels in the inverse design and, the importance of considering different geometries and the effect of core density on the boundary restraint in predicting the intracellular buckling loads.

It's widely recognized that any flaws associated with materials or geometry within the core or face sheet can influence buckling loads, potentially leading to lower values. The management of these imperfections is primarily attributed to manufacturing techniques and quality control processes, which can vary significantly. A thorough understanding of the specific formulation considering various imperfections such as initial curvature, voids, material inhomogeneity, etc., requires investigation in detailed design process, often necessitating advanced numerical models or experimental studies which is beyond the scope of the present study.

However, if we aim to account for imperfections' effects on buckling during the preliminary material and geometry selections in the sandwich panel design, few approaches can be adopted. One option involves incorporating knockdown factors based on anticipated imperfections, while another involves employing conservative estimates, such as assuming simply supported boundaries for the edges. These strategies provide practical means to address imperfection-related concerns at the early stages of design without necessitating exhaustive detailed analyses.

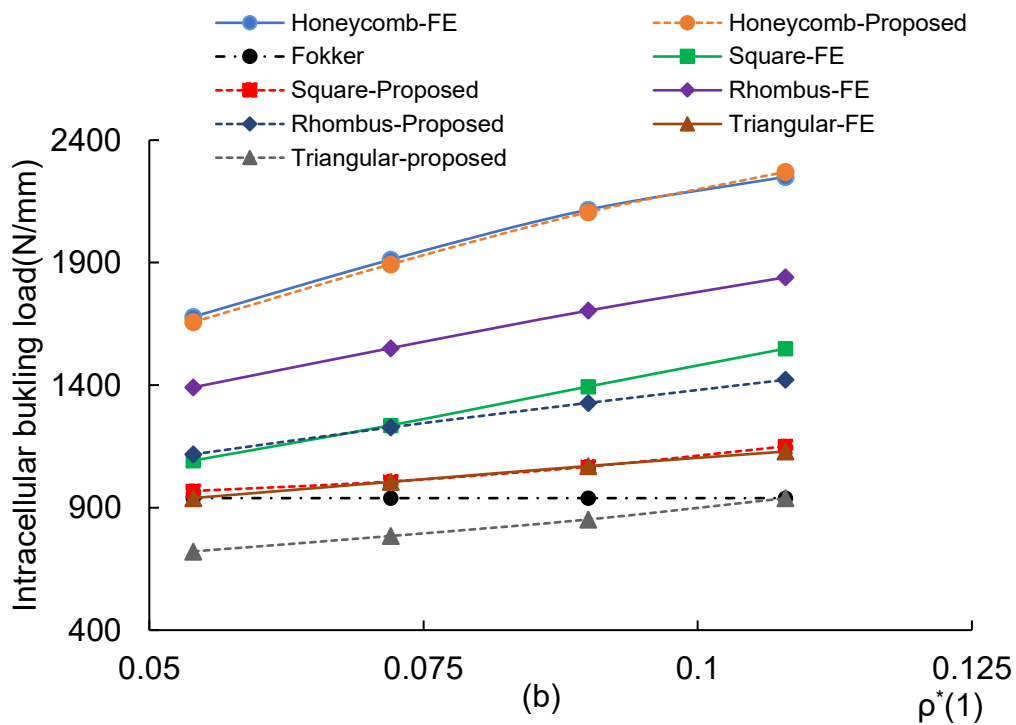
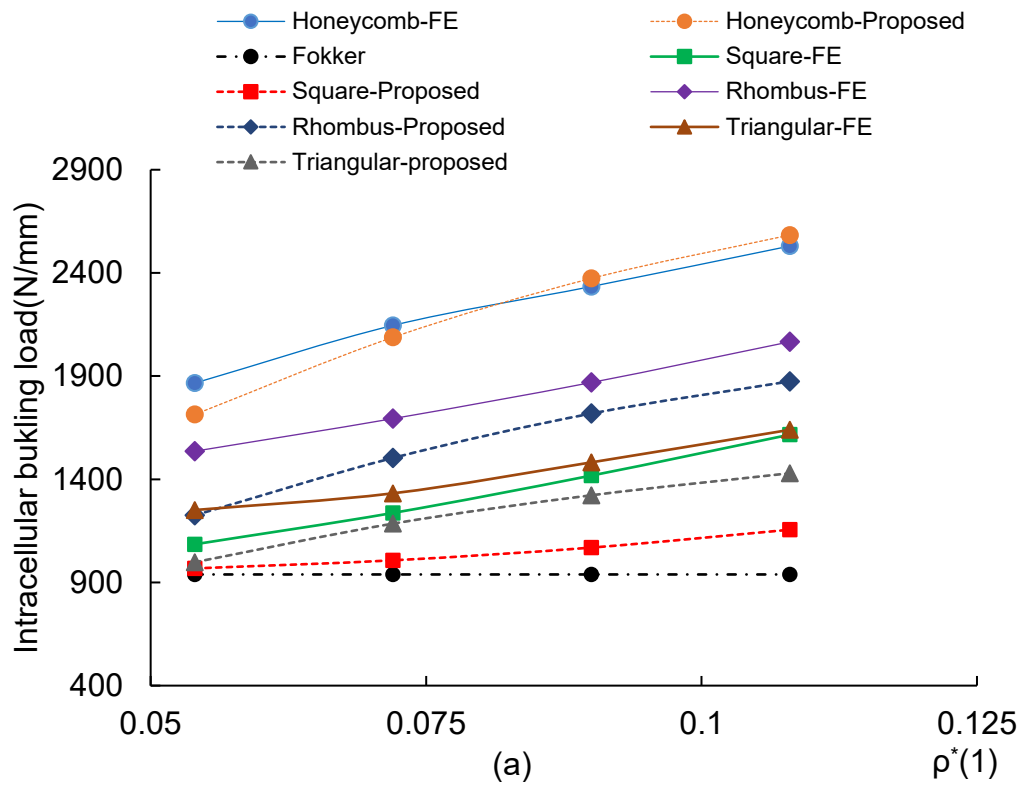


Fig. 6.20: Comparison of intracellular buckling loads of different cell shapes consisting of equal inscribed circle under uniaxial compression (a) direction-1 and (b) direction-2.

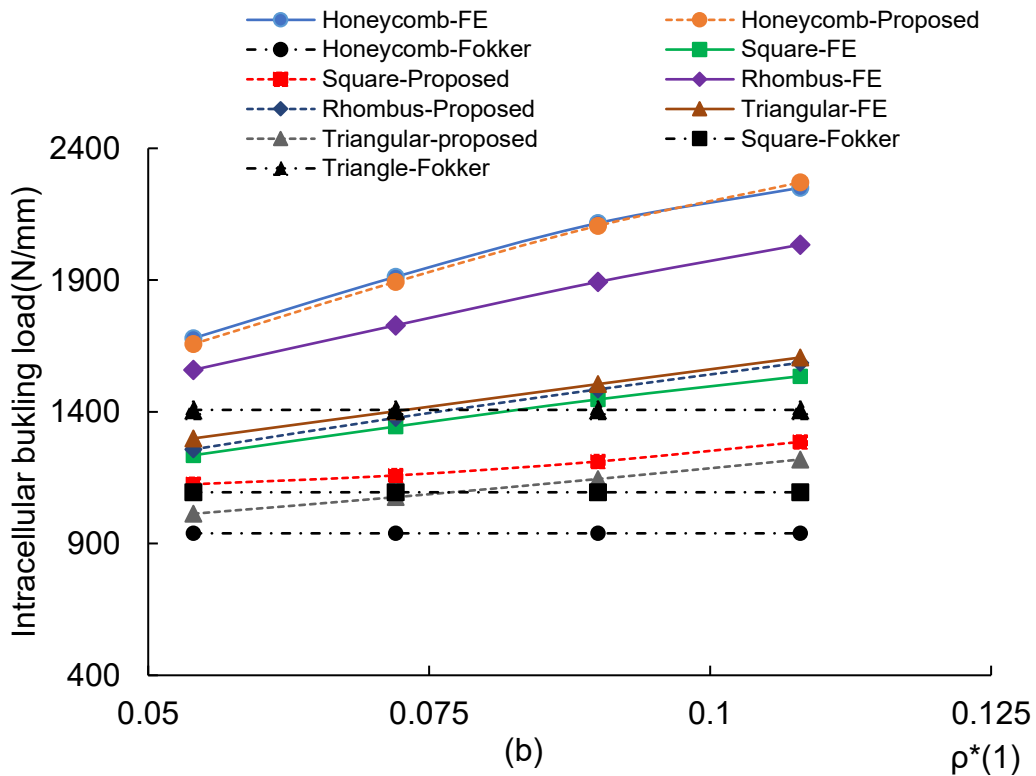
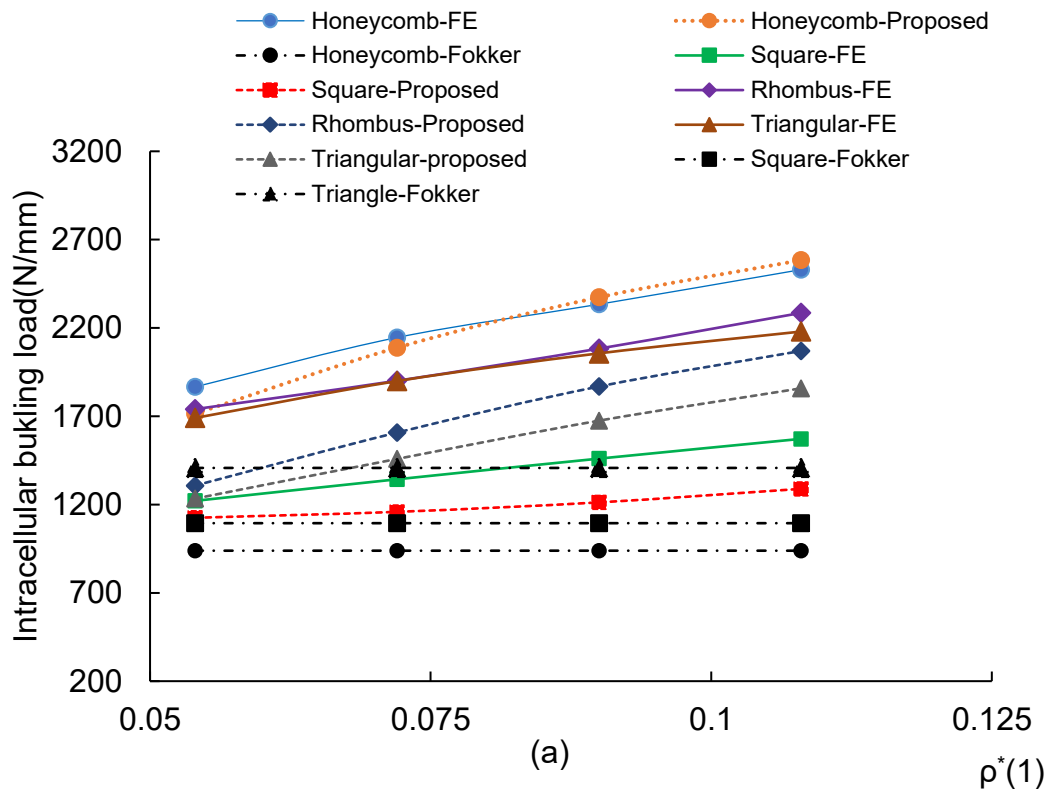


Fig. 6.21: Comparison of intracellular buckling loads of different cell shapes of equal area under uniaxial compression in (a) direction-1 and (b) direction-2.

6.5 Conclusions

A novel approach to predict the intracellular buckling load of sandwich panels with honeycomb cores was presented. The proposed semi-analytical approach was validated for the hexagonal cell with different geometric and material configurations. The proposed approach was formulated to take into account the geometric shape of the cell, rotational restraints at the boundaries, and different loading conditions. Existing closed-form solutions for intracellular buckling loads give significantly conservative results and are found to be not consistent with the FE results. While the proposed approach with simply-supported boundaries for the cell gives conservative results, predictions with rotationally restrained boundaries for the cell are very close to the FE results under various conditions, such as different cell sizes, core densities, face sheet fibre lay-ups, and different loading conditions. The proposed approach is more general and can be used to predict shear buckling loads of different cell shapes and material configurations.

The proposed semi-analytical approach can be easily manipulated to vary parameters such as cell size, core density, loading ratios, face sheet's fibre lay-up, thickness, etc., and the buckling loads can be predicted to reasonable accuracy with less computational effort compared to FE. Therefore, the proposed approach can be used effectively for the inverse design of the sandwich panels.

6.6 References

- Allen, H. G. (1969). *Analysis and Design of Structural Sandwich Panels*: Pergamon.
- ABAQUS version 2021. Dassault Systemes Simulia Corporation. Providence, RI, USA.
- Ashton, J. E. 1969. Approximate Solutions for Unsymmetrically Laminated Plates. *Journal of Composite Materials*. 3(1). 189–191.
- Birman, V., & Bert, C. W. (2004). Wrinkling of composite-facing sandwich panels under biaxial loading. *Journal of Sandwich Structures & Materials*, 6(3), 217-237.
- Blaas, C. (1984). *Local instability for sandwich panels*. Fokker report TR-N-84-CSE-061.
- Bleich, F. (1952). Buckling strength of metal structures. New York, NY: McGraw-Hill.
- Chai, G. B. (1994). Buckling of generally laminated composite plates with various edge support conditions. *Composite Structures*. 29(3). 299-310.
- Higginson, K., Fernando, D., Veidt, M., Burnton, P., You, Z., & Heitzmann, M. (2021). Local buckling of FRP thin-walled plates, shells and hollow sections with curved edges and arbitrary lamination. *Thin-Walled Structures*, 168, 108242.

- Hemp, W. (1948). On a theory of sandwich construction.
- Hoff, N. J., & Mautner, S. (1945). The buckling of sandwich-type panels. *Journal of the Aeronautical Sciences*, 12(3), 285-297.
- Kollár, L. P. (2003). Local buckling of fiber reinforced plastic composite structural members with open and closed cross sections. *Journal of Structural Engineering*, 129(11), 1503-1513.
- Leissa, A. W. (1985). Buckling of laminated composite plates and shell panels (No. OSURF-762513/713464). Ohio State Univ Research Foundation Columbus.
- Ley, R. P., Lin, W., & Mbanefo, U. (1999). *Facesheet wrinkling in sandwich structures* (No. NAS 1.26: 208994).
- MathWorks Inc. (2022). MATLAB version: 9.13.0 (R2022b), Natick, Massachusetts: The MathWorks Inc.
- Niu, K., & Talreja, R. (1999). Modeling of Wrinkling in Sandwich Panels under Compression. *Journal of Engineering Mechanics*, 125(8), 875-883.
- Norris, C. B. (1964). *Short-column compressive strength of sandwich constructions as affected by size of cells of honeycomb core materials* (Vol. 26): US Department of Agriculture, Forest Service, Forest Products Laboratory.
- Plantema, F. J. (1966). *Sandwich construction: the bending and buckling of sandwich beams, plates, and shells*: Wiley.
- Pozorski, Z., Pozorska, J., Kreja, I., & Smakosz, Ł. (2021). On Wrinkling in Sandwich Panels with an Orthotropic Core. *Materials*, 14(17), 5043.
- Qiao, P., & Shan, L. (2007). Explicit local buckling analysis of rotationally restrained composite plates under biaxial loading. *International Journal of Structural Stability and Dynamics*, 7(03), 487-517.
- Thomsen, O. T., & Banks, W. M. (2004). An improved model for the prediction of intra-cell buckling in CFRP sandwich panels under in-plane compressive loading. *Composite Structures*, 65(3-4), 259-268.
- Timoshenko, S.P. and Gere, J.M. (1961) *Theory of Elastic Stability*. Second Edition, McGraw-Hill Book Co. Inc., New York.
- Vonach, W. K., & Rammerstorfer, F. G. (2000). The effects of in-plane core stiffness on the wrinkling behavior of thick sandwiches. *Acta Mechanica*, 141(1-2), 1-10.
- Wei, X., Wu, Q., Gao, Y., Yang, Q., & Xiong, J. (2022). Composite honeycomb sandwich columns under in-plane compression: Optimal geometrical design and three-dimensional failure mechanism maps. *European Journal of Mechanics-A/Solids*, 91, 104415.
- Yang, B., & Wang, D. (2017). Buckling strength of rectangular plates with elastically restrained edges subjected to in-plane impact loading. *Proceedings of the Institution of Mechanical Engineers, Part C: Journal of Mechanical Engineering Science*.231(20):3743-3752.
- Zenkert, D. (1997). *The handbook of sandwich construction*: Engineering Materials Advisory Services.

Chapter 7:

Conclusions

7.1 Summary of key findings and impacts

In recent years, all-composite honeycomb core sandwich panels have gained wide popularity in lightweight sandwich structure applications due to their excellent specific stiffness, strength, and multifunctional advantages. A detailed literature review in Chapter 2 on the past research studies related to the sandwich panels revealed that the application of the inverse design for all-composite honeycomb core sandwich panels is limited due to the lack of versatile and robust design tools to consider various materials and geometry configurations as well as different loadings. This PhD thesis aimed to address this gap by developing innovative methodologies to facilitate the inverse design of all-composite honeycomb core sandwich panels while considering key variables related to geometry, materials and loadings.

Chapter 3 focused on developing an analytical model for homogenising the laminated composite honeycomb cores with various geometry and material configurations. The proposed model, based on the strain energy approach, demonstrated excellent agreement with FE analysis results, outperforming existing analytical models in terms of accuracy and broader applicability to different material and geometry configurations of the core. Chapter 4 investigated the effectiveness and accuracy of the equivalent models in predicting sandwich panel responses against 3D models with actual discrete core structures. The study showed that equivalent models based on FSDT provided reasonably accurate predictions for various honeycomb core configurations, with proper estimation of the shear correction factor and effective stiffness matrix of the core.

Chapter 5 introduced a novel semi-analytical approach to predict the critical shear buckling load of laminated composite honeycomb cores. The proposed model accounted for the bend-twist coupling effects of the laminate on the shear buckling, which significantly influenced the shear buckling strength of the laminated composite honeycomb core. The study highlighted the effect of different core shapes, ply

arrangements and shear loading conditions on the shear buckling strength. The study also highlighted the effect of different boundary conditions on the accuracy of predicting the shear buckling strength of the core. Chapter 6 addressed the intracellular buckling of laminated composite face sheets, developing a semi-analytical approach capable of predicting buckling loads with high accuracy. Unlike the existing models for intracellular buckling, the proposed model was developed considering different cell shapes of composite face sheets under various compressive loadings.

The impacts of this research are significant in several key areas:

- **Advancement of Lightweight Sandwich Panel Design:** By developing accurate methodologies for the inverse design of all-composite honeycomb core sandwich panels, this research facilitates the creation of lightweight structures with enhanced stiffness and strength using different materials and core shapes. This is particularly valuable in industries where weight reduction is critical, such as aerospace, automotive, and marine engineering.
- **Closing Knowledge Gaps:** The research addresses existing knowledge gaps in the inverse design of composite honeycomb core sandwich panels. Through comprehensive analysis and validation against FE analysis results, the study provides robust analytical and semi-analytical models that improve our understanding of the stiffness and strength of the panel behaviour under various conditions.
- **Versatile Design Tools:** The developed models offer versatility by accommodating different core shapes, material configurations, and loading conditions. This enables designers to tailor panel designs to specific performance requirements more efficiently and accurately, ultimately leading to more optimised structures.
- **Cost and Time Savings:** The use of equivalent models based on effective stiffness and semi-analytical models to predict the local buckling failures offers significant time savings in modelling and analysis compared to complex 3D models and experiments. This makes the inverse design process more accessible and cost-effective for engineers and researchers.
- **Potential for Multidisciplinary Applications:** The methodologies and findings of this research have implications beyond sandwich panel design. They can be applied to various fields involving composite materials and structural

optimisation, expanding the reach of lightweight design principles across different engineering disciplines and industries.

7.2 Recommendations for future research

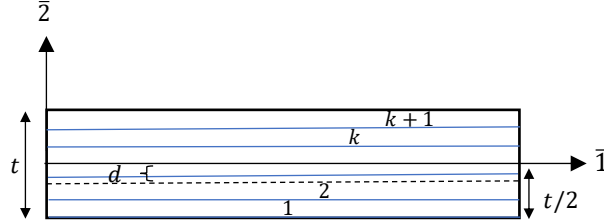
The present research study generates numerous future research avenues that either directly extend or relate to the current thesis. Below, a summary of some potential directions is provided for the readers of this thesis:

- The current investigation concentrated on developing analytical tools for the inverse design of all-composite honeycomb core sandwich panels. As a prospective endeavour, these design tools could be integrated with suitable search algorithms to achieve optimal designs of such panels tailored to specific performance targets.
- The current study assumed small deformations for the core walls, neglecting geometric non-linearity. Exploring non-linear homogenisation models for core walls undergoing large deformations could serve as another extension of this study.
- While the model proposed for the local buckling of the honeycomb core in Chapter 5 only considered transverse shear force, incorporating the effect of normal force could enhance prediction accuracy, particularly when the core in-plane stiffness contribution to the sandwich panels is significant. Extending the model to account for combined loadings in core buckling could further improve predictive capabilities.
- Although the current study addressed the impact of bend-twist coupling on the local buckling of composite honeycomb cores and face sheets, further investigation into extensional-shear and membrane-bending coupling effects is recommended.
- The study delineated separate buckling failure models for wrinkling and intracellular buckling modes; however, the interaction between these modes may not be accurately captured by either model. Developing a unified formulation for buckling that accounts for interactions among different variables associated with face sheets and core could be a promising avenue for future research.

- The developed design tools were predicated on the assumption of structural perfection and were validated using FE models. However, further exploration via experiments is warranted to scrutinize the local buckling phenomena of honeycomb cores and face sheets, as well as the effective stiffness of laminated composite honeycomb cores under real-world manufacturing conditions, where imperfections are inevitable.
- While the current study relied on simplified linear buckling predictions for inverse design, employing non-linear buckling analyses based on detailed 3D models of sandwich panels could offer deeper insights into the effects of imperfections and post-buckling behaviour across various face sheet and core configurations.

Appendix

A1. Shear correction factor



Ply-1 bottom and top axis $\bar{2}$ values are \bar{x}_2^1 and \bar{x}_2^2 respectively.

Ply-k bottom and top axis $\bar{2}$ values are \bar{x}_2^k and \bar{x}_2^{k+1} respectively.

The stress equilibrium within the section in the direction- $\bar{1}$ assuming cylindrical bending can be written as:

$$\frac{\partial \bar{\sigma}_{11}}{\partial \bar{x}_1} + \frac{\partial \bar{\tau}_{12}}{\partial \bar{x}_2} = 0. \quad (\text{A.1})$$

From the moment equilibrium about the axis- $\bar{3}$, we can write:

$$\bar{F}_{12} + \frac{\partial \bar{M}_{11}}{\partial x_1} = 0. \quad (\text{A.2})$$

From Eq. (A.1) and (A.2), we can write:

$$\bar{\tau}_{12} = - \int_{-(\frac{t}{2}+d)}^{\bar{x}_2} \left(\frac{\partial \bar{\sigma}_{11}}{\partial \bar{x}_1} \right) d\bar{x}_2, \quad (\text{A.3})$$

$$\bar{\tau}_{12} = - \int_{-(\frac{t}{2}+d)}^{\bar{x}_2} \left(\frac{\partial \bar{M}_{11}}{\partial x_1} \right) \left(\frac{\bar{Q}_{11}(\bar{x}_2)}{\bar{D}_{11}} \right) \bar{x}_2 d\bar{x}_2, \quad (\text{A.4})$$

$$\bar{\tau}_{12} = - \int_{-(\frac{t}{2}+d)}^{\bar{x}_2} \bar{F}_{12} \left(\frac{\bar{Q}_{11}(\bar{x}_2)}{\bar{D}_{11}} \right) \bar{x}_2 d\bar{x}_2, \quad (\text{A.5})$$

$$\bar{\tau}_{12} = - \left(\frac{\bar{F}_{12}}{\bar{D}_{11}} \right) g(\bar{x}_2). \quad (\text{A.6})$$

where $g(\bar{x}_2) = \int_{-(\frac{t}{2}+d)}^{\bar{x}_2} \bar{Q}_{11}(\bar{x}_2) \bar{x}_2 d\bar{x}_2$.

The strain energy due to the transverse shear per unit middle surface area of the laminate is:

$$U_s = \frac{1}{2} \int_{-(\frac{t}{2}+d)}^{(t/2-d)} \frac{(\bar{\tau}_{12})^2}{\bar{Q}_{44}(\bar{x}_2)} d\bar{x}_2, \quad (\text{A.7})$$

$$U_s = \frac{1}{2} \left(\frac{\bar{F}_{12}}{\bar{D}_{11}} \right)^2 \int_{-(\frac{t}{2}+d)}^{(t/2-d)} \frac{g(\bar{x}_2)^2}{\bar{Q}_{44}(\bar{x}_2)} d\bar{x}_2. \quad (\text{A.8})$$

For the equivalent section with constant transverse shear strain, the strain energy due to the transverse shear per unit middle surface area is:

$$\bar{U}_s = \frac{1}{2} \int_{-(\frac{t}{2}+d)}^{(\frac{t}{2}-d)} \bar{\gamma}_{12} \bar{Q}_{44}(\bar{x}_2) \bar{\gamma}_{12} d\bar{x}_2 = \frac{(\bar{F}_{12})^2}{\bar{A}_{44}}. \quad (\text{A.9})$$

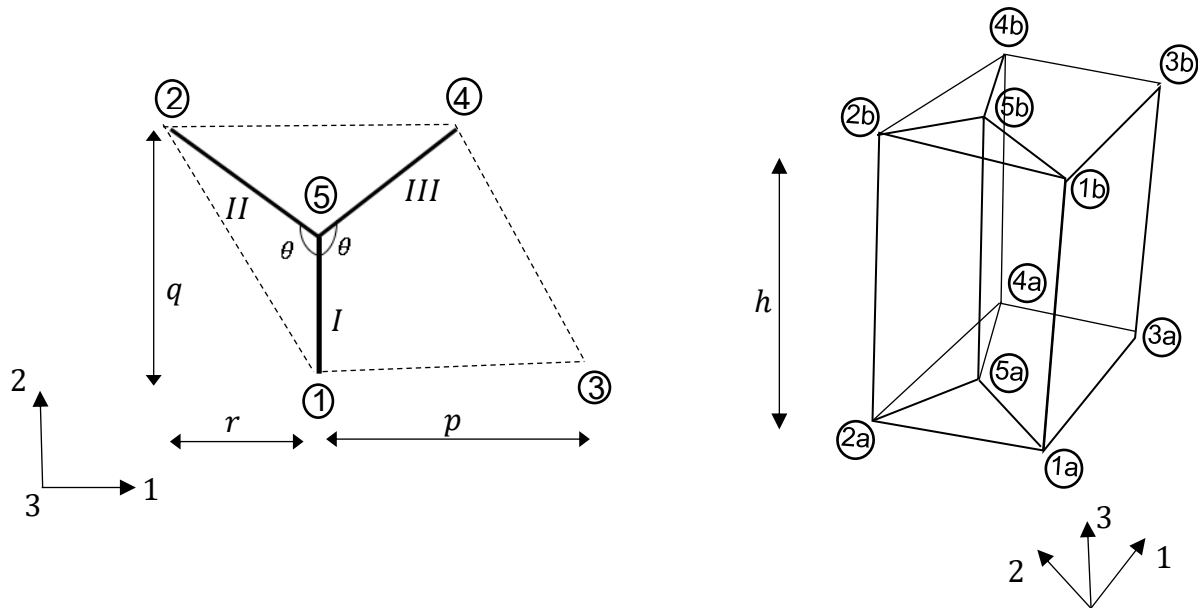
From Eqs. (3A.8) and (3A.9), we can write shear correction factor as:

$$k_1 = \frac{\bar{U}_s}{U_s} = \frac{\bar{D}_{11}^2}{\bar{A}_{44} \int_{-(\frac{t}{2}+d)}^{(\frac{t}{2}-d)} \frac{g(\bar{x}_2)^2}{\bar{Q}_{44}(\bar{x}_2)} d\bar{x}_2}. \quad (\text{A.10})$$

Equivalent shear stiffness is given as:

$$S_{eq} = k_1 \bar{A}_{44}. \quad (\text{A.11})$$

A2. Average strain components of RVE of periodic honeycomb core



Let say the coordinates of points (1a) and (1b) are (x_1^o, x_2^o, x_3^o) and $(x_1^o, x_2^o, x_3^o + h)$

Outward unit normal vector for the surface (1a-1b-3b-3a):

$$\hat{\mathbf{n}}_{1-3} = \langle 0, -1, 0 \rangle \quad (\text{A.12})$$

Outward unit normal vector for the surface (2a-2b-4b-4a):

$$\hat{\mathbf{n}}_{2-4} = \langle 0, 1, 0 \rangle \quad (\text{A.13})$$

Outward unit normal vector for the surface (1a-2a-2b-1b):

$$\hat{\mathbf{n}}_{2-4} = \frac{-1}{\sqrt{q^2+r^2}} \langle q, r, 0 \rangle \quad (\text{A.14})$$

Outward unit normal vector for the surface (3a-4a-4b-3b):

$$\hat{\mathbf{n}}_{2-4} = \frac{1}{\sqrt{q^2+r^2}} \langle q, r, 0 \rangle \quad (\text{A.15})$$

The global strain of the RVE can be written as:

$$\varepsilon_{ij} = \frac{1}{2V_{RVE}} \int_{\Gamma} (u_i n_j + u_j n_i) d\Gamma. \quad (\text{A.16})$$

$$\begin{aligned} \varepsilon_{11} &= \frac{1}{2 * h * p * q} \int_{\Gamma} \left[2(u_{1(2-4)} - u_{1(1-3)}) * 0 + 2 * (u_{1(3-4)} - u_{1(1-2)}) * \frac{q}{\sqrt{q^2 + r^2}} \right] d\Gamma, \\ &= \frac{1}{2 * h * p * q} * \left(2 * (u_{1(3-4)} - u_{1(1-2)}) * \frac{q}{\sqrt{q^2 + r^2}} \right) * (\sqrt{q^2 + r^2} * h), \\ &= \frac{(u_{1(3-4)} - u_{1(1-2)})}{p}, \\ &= \frac{(u_{1(3)} - u_{1(1)})}{p}. \end{aligned} \quad (\text{A.17})$$

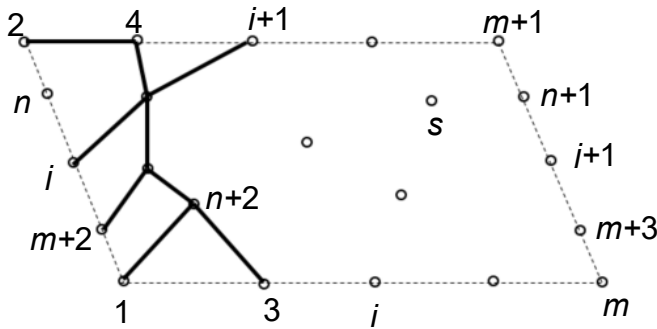
$$\begin{aligned} \varepsilon_{22} &= \frac{1}{2 * h * p * q} \int_{\Gamma} \left[2(u_{2(2-4)} - u_{2(1-3)}) * 1 + 2 * (u_{2(3-4)} - u_{2(1-2)}) * \frac{r}{\sqrt{q^2 + r^2}} \right] d\Gamma, \\ &= \frac{1}{2 * h * p * q} \\ &\quad * \left[2(u_{2(2-4)} - u_{2(1-3)}) * p * h + \left(2 * (u_{2(3-4)} - u_{2(1-2)}) * \frac{r}{\sqrt{q^2 + r^2}} \right) \right. \\ &\quad \left. * (\sqrt{q^2 + r^2} * h) \right], \\ &= \frac{(u_{1(2-4)} - u_{1(1-3)})}{p} + \frac{r (u_{2(3-4)} - u_{2(1-2)})}{q p}, \\ &= \frac{(u_{1(2)} - u_{1(1)})}{p} + \frac{r (u_{2(3)} - u_{2(1)})}{q p}. \end{aligned} \quad (\text{A.18})$$

$$\begin{aligned}
\varepsilon_{12} &= \frac{1}{2 * h * p * q} \int_{\Gamma} \left[(u_{1(2-4)} - u_{1(1-3)}) * 1 + (u_{1(2-4)} - u_{1(1-3)}) * 0 \right. \\
&\quad \left. + (u_{1(3-4)} - u_{1(1-2)}) * \frac{r}{\sqrt{q^2 + r^2}} + (u_{2(3-4)} - u_{2(1-2)}) * \frac{q}{\sqrt{q^2 + r^2}} \right] d\Gamma, \\
&= \frac{1}{2 * h * p * q} \\
&\quad * \left[2(u_{1(2-4)} - u_{1(1-3)}) * p * h \right. \\
&\quad \left. + \frac{1}{\sqrt{q^2 + r^2}} \left((u_{1(3-4)} - u_{1(1-2)}) * r + (u_{2(3-4)} - u_{2(1-2)}) * q \right) \right. \\
&\quad \left. * (\sqrt{q^2 + r^2} * h) + \right], \\
&= \frac{1}{2} \left(\frac{(u_{2(3-4)} - u_{2(1-2)})}{p} + \frac{(u_{1(2-4)} - u_{1(1-3)})}{q} + \frac{r(u_{1(3-4)} - u_{1(1-2)})}{q p} \right). \\
&= \frac{1}{2} \left(\frac{(u_{2(3)} - u_{2(1)})}{p} + \frac{(u_{1(2)} - u_{1(1)})}{q} + \frac{r(u_{1(3)} - u_{1(1)})}{q p} \right).
\end{aligned} \tag{A.19}$$

$$\begin{aligned}
\varepsilon_{13} &= \frac{1}{2 * h * p * q} \int_{\Gamma} \left[(u_{1(2-4)} - u_{1(1-3)}) * 0 + (u_{3(2-4)} - u_{3(1-3)}) * 0 \right. \\
&\quad \left. + (u_{1(3-4)} - u_{1(1-2)}) * 0 + (u_{3(3-4)} - u_{3(1-2)}) * \frac{q}{\sqrt{q^2 + r^2}} \right] d\Gamma, \\
&= \frac{1}{2 * h * p * q} * \left[\left((u_{3(3-4)} - u_{3(1-2)}) * \frac{q}{\sqrt{q^2 + r^2}} \right) * (\sqrt{q^2 + r^2} * h) + \right] \\
&= \frac{1}{2} \left(\frac{(u_{3(3-4)} - u_{3(1-2)})}{p} \right). \\
&= \frac{1}{2} \left(\frac{(u_{3(3)} - u_{3(1)})}{p} \right).
\end{aligned} \tag{A.20}$$

$$\begin{aligned}
\varepsilon_{23} &= \frac{1}{2 * h * p * q} \int_{\Gamma} \left[(u_{2(2-4)} - u_{2(1-3)}) * 0 + (u_{3(2-4)} - u_{3(1-3)}) * 1 \right. \\
&\quad \left. + (u_{2(3-4)} - u_{2(1-2)}) * 0 + (u_{3(3-4)} - u_{3(1-2)}) * \frac{r}{\sqrt{q^2 + r^2}} \right] d\Gamma, \\
&= \frac{1}{2 * h * p * q} \\
&\quad * \left[(u_{3(2-4)} - u_{3(1-3)}) * p * h + \left((u_{3(3-4)} - u_{3(1-2)}) * \frac{r}{\sqrt{q^2 + r^2}} \right) \right. \\
&\quad \left. * (\sqrt{q^2 + r^2} * h) + \right] \\
&= \frac{1}{2} \left(\frac{(u_{3(2-4)} - u_{3(1-3)})}{p} + \frac{r}{q} \frac{(u_{3(3-4)} - u_{3(1-2)})}{p} \right). \\
&= \frac{1}{2} \left(\frac{(u_{3(2)} - u_{3(1)})}{p} + \frac{r}{q} \frac{(u_{3(3)} - u_{3(1)})}{p} \right).
\end{aligned}
\tag{A.21}$$

A3. Equations to find the nodal displacements of RVE



Equations for solving nodal displacements.

- I. Applying the periodic boundary conditions to the RVE, we will have the followings:

$$\begin{aligned}
\varphi(i) &= \varphi(i + 1), & i &= 1, 3, \dots, m \\
u_{(m)l} - u_{(i)l} &= u_{(m+1)l} - u_{(i+1)l}, & i &= 1, 3, \dots, m, \quad l = 1, 2, 3 \\
\varphi(j) &= \varphi(j + 1), & j &= (m + 2), (m + 4), \dots, n \\
u_{(2)l} - u_{(j)l} &= u_{(m+1)l} - u_{(j+1)l}, & j &= (m + 2), (m + 4), \dots, n, \quad l = 1, 2, 3 \\
\varphi(1) &= \varphi(m). & &
\end{aligned}
\tag{A.22}$$

II. RVE does not undergo any rigid body motions, then we will have the followings:

$$u_{(1)1} = 0, \quad u_{(1)2} = 0, \quad u_{(1)3} = 0, \quad \text{and} \quad u_{(m)2} = 0. \quad (\text{A.23})$$

III. Resultant forces at all internal nodes and at all pairs of corresponding nodes i and

$i + 1$ should be zero, which gives the followings:

$$\begin{aligned} F_{(1)l} + F_{(2)l} + F_{(m)l} + F_{(m+1)l} &= 0, & l = 1,2,3 \\ M_{(1)} + M_{(2)} + M_{(m)} + M_{(m+1)} &= 0, \\ F_{(i)l} + F_{(i+1)l} &= 0, & i = 3,5, \dots, (m-2) \text{ and} \\ M_{(i)} + M_{(i+1)} &= 0, & i = (m+2), (m+4), \dots, n, \quad l = 1,2,3 \\ F_{(k)l} &= 0, & k = (n+2), (n+3), \dots, s, \quad l = 1,2,3 \\ M_{(k)l} &= 0. \end{aligned} \quad (\text{A.24})$$

Equations in (A.22), (A.23) and (A.24) together with the Eqs. (A.17) - (A.21) will provide $(4s + 3)$ equations to solve for the nodal displacements of RVE. Equations in (A.24) will provide three redundant equations which should be eliminated to solve for the nodal displacements.

A4. MATLAB program for the homogenisation of the hexagonal core

Hexagonal.m

```

clc
clear
syms L teta t E h u real
syms V11 V12 V13 V21 V22 V23 V31 V32 V33 k real
syms C1 C2 C3 C4 x1 y1 x2 y2 x3 y3 z X Y real
syms v11 v12 v13 dw1 v31 v32 v33 dw3 v41 v42 v43 dw4 v51 v52 v53 dw5 v21 v22 v23
dw2 real
syms E11 E22 E33 E23 E13 E12 real

L1=50;           %Vertical walls
L2=50;           %inclined walls
h=150;           %height of the honeycomb
t1=3.12;         %thickness of vertical leg
t2=3.12;         %thickness of inclined leg
t3=3.12;
teta=120*pi/180; % Angle between inclined and vertical

%%Material properties of FRP materials of (A,B &C) with respect to its principle
axes
E1A=204000;

```

```

E1B=38600;
E1C=131000;
E2A=18500;
E2B=8270;
E2c=10300;
GA=5590;
GB=4140;
Gc=6900;
VA=0.23;
VB=0.26;
VC=0.22;

%%% Define thickness of each ply of each wall

layer_thickness1=t2/5*[1,1,1,1,1];%0,0,0,0,0]+t3/5*[0,0,0,0,0,1,1,1,1,1];

layer_thickness2=t2/5*[1,1,1,1,1];
layer_thickness3=t3/5*[1,1,1,1,1];

%%% Material properties of each ply of each wall

E1layer1=[E1A,E1A,E1A,E1A,E1A];
E2layer1=[E2A,E2A,E2A,E2A,E2A];
Glayer1=[GA,GA,GA,GA,GA];
vlayer1=[VA,VA,VA,VA,VA];

E1layer2=[E1B,E1B,E1A,E1B,E1B];
E2layer2=[E2B,E2B,E2A,E2B,E2B];
Glayer2=[GB,GB,GA,GB,GB];
vlayer2=[VB,VB,VA,VB,VB];

E1layer3=[E1B,E1A,E1B,E1A,E1B];
E2layer3=[E2B,E2A,E2B,E2A,E2B];
Glayer3=[GB,GA,GB,GA,GB];
vlayer3=[VB,VA,VB,VA,VB];

%%% Ply orientation of each ply of each wall

nOrient1=[0*pi/12,3*pi/12,6*pi/12,3*pi/12,0*pi/12];
nOrient2=[6*pi/12,0*pi/12,0*pi/12,0*pi/12,6*pi/12];
nOrient3=[6*pi/12,0*pi/12,0*pi/12,0*pi/12,6*pi/12];

% Calculate the section stiffness of each wall

[A1,B1,D1,Se1]=MaterialPropThick(t1,layer_thickness1,E1layer1,E2layer1,Glayer1,vla
yer1,nOrient1);
[A2,B2,D2,Se2]=MaterialPropThick(t1,layer_thickness1,E1layer1,E2layer1,Glayer1,vla
yer1,nOrient1);
[A3,B3,D3,Se3]=MaterialPropThick(t1,layer_thickness1,E1layer1,E2layer1,Glayer1,vla
yer1,nOrient1);

%%%Define the characteristic dimensions of the RVE

a=2*L2*sin(teta);
b=(L1+L2*cos(pi-teta));
c=L2*sin(teta);
V=a*b*h;          %volume of RVE

```

```

disp('relative coredensity');
Dr=(t3*L2*h+t2*L2*h+t1*L1*h)/V; %% Relative core density
disp(Dr)

%%Define 9 independent strain states to calculate the effective stiffness
%%tensor

for i=1:1:9
    switch i
        case 1
            e11=1;e22=0;E33=0;e23=0;e13=0;e12=0;
        case 2
            e11=0;e22=1;E33=0;e23=0;e13=0;e12=0;
        case 3
            e11=0;e22=0;E33=1;e23=0;e13=0;e12=0;
        case 4
            e11=0;e22=0;E33=0;e23=0;e13=1;e12=0;
        case 5
            e11=0;e22=0;E33=0;e23=1;e13=0;e12=0;
        case 6
            e11=0;e22=0;E33=0;e23=0;e13=0;e12=1;
        case 7
            e11=1;e22=1;E33=0;e23=0;e13=0;e12=0;
        case 8
            e11=1;e22=0;E33=1;e23=0;e13=0;e12=0;
        case 9
            e11=0;e22=1;E33=1;e23=0;e13=0;e12=0;
    end

    %%Define stiffness matrix of wall 1_Vertical wall

    L=L1;
    A=A1;B=B1;D=D1;                %%In-plane stiffness
    Seq=Se1;                        %%Transverse shear stiffness.
    n=12*D(1,1)/(L^2*Seq);          %%%Seq=kGA

    K1=[(A(1,1)*h)/L,0, (A(1,3)*h)/L, 0, -(A(1,1)*h)/L, 0, -(A(1,3)*h)/L, 0;
        0,(h*(Seq*L^2*n^2 + 12*D(1,1)))/(L^3*(n + 1)^2),0, (h*(Seq*L^2*n^2 +
        12*D(1,1)))/(2*L^2*(n + 1)^2),0,-(h*(Seq*L^2*n^2 + 12*D(1,1)))/(L^3*(n +
        1)^2),0,(h*(Seq*L^2*n^2 + 12*D(1,1)))/(2*L^2*(n + 1)^2);
        (A(1,3)*h)/L,0,(A(3,3)*h)/L,0, -(A(1,3)*h)/L,0, -(A(3,3)*h)/L,0;
        0, (h*(Seq*L^2*n^2 + 12*D(1,1)))/(2*L^2*(n + 1)^2), 0, (h*(Seq*L^2*n^2 +
        4*D(1,1)*n^2 + 8*D(1,1)*n + 16*D(1,1)))/(4*L*(n + 1)^2), 0, -(h*(Seq*L^2*n^2
        + 12*D(1,1)))/(2*L^2*(n + 1)^2), 0, (h*(Seq*L^2*n^2 - 4*D(1,1)*n^2 -
        8*D(1,1)*n + 8*D(1,1)))/(4*L*(n + 1)^2);
        -(A(1,1)*h)/L, 0, -(A(1,3)*h)/L,0, (A(1,1)*h)/L,0, (A(1,3)*h)/L,0;
        0, -(h*(Seq*L^2*n^2 + 12*D(1,1)))/(L^3*(n + 1)^2), 0,-(h*(Seq*L^2*n^2 +
        12*D(1,1)))/(2*L^2*(n + 1)^2),0, (h*(Seq*L^2*n^2 + 12*D(1,1)))/(L^3*(n +
        1)^2),0,-(h*(Seq*L^2*n^2 + 12*D(1,1)))/(2*L^2*(n + 1)^2);
        -(A(1,3)*h)/L,0, -(A(3,3)*h)/L,0, (A(1,3)*h)/L,0, (A(3,3)*h)/L,0;
        0, (h*(Seq*L^2*n^2 + 12*D(1,1)))/(2*L^2*(n + 1)^2), 0, (h*(Seq*L^2*n^2 -
        4*D(1,1)*n^2 - 8*D(1,1)*n + 8*D(1,1)))/(4*L*(n + 1)^2), 0, -(h*(Seq*L^2*n^2
        + 12*D(1,1)))/(2*L^2*(n + 1)^2), 0, (h*(Seq*L^2*n^2 + 4*D(1,1)*n^2 +
        8*D(1,1)*n + 16*D(1,1)))/(4*L*(n + 1)^2)];

```

```
K2=h*[-A(1,2) 0 -A(2,3) 0 A(1,2) 0 A(2,3) 0]';%%Stiffness matrix with respect
to the local axes
```

```
%%Transformation matrix for wall 1_vertical wall
```

```
T1=[cos(pi/2) -sin(pi/2) 0 0 0 0 0 0;...
     sin(pi/2) cos(pi/2) 0 0 0 0 0 0;...
     0 0 1 0 0 0 0 0;...
     0 0 0 1 0 0 0 0;...
     0 0 0 0 cos(pi/2) -sin(pi/2) 0 0;...
     0 0 0 0 sin(pi/2) cos(pi/2) 0 0;...
     0 0 0 0 0 0 1 0;...
     0 0 0 0 0 0 0 1];
K11t=T1*K1*T1';
K21t=T1*K2;
```

```
%%Define global force-displacement relationship
```

```
F1=K11t*[v11 v12 v13 dw1 v51 v52 v53 dw5]'+K21t*E33;
```

```
%%Define stiffness matrix of wall 2_Inclined wall 1
```

```
L=L2;
A=A2;B=B2;D=D2;
Seq=Se2;
n=12*D(1,1)/(L^2*Seq); %%Seq=kGA
```

```
K1=[(A(1,1)*h)/L,0, (A(1,3)*h)/L, 0, -(A(1,1)*h)/L, 0, -(A(1,3)*h)/L, 0;
     0,(h*(Seq*L^2*n^2 + 12*D(1,1)))/(L^3*(n + 1)^2),0, (h*(Seq*L^2*n^2 +
     12*D(1,1)))/(2*L^2*(n + 1)^2),0,-(h*(Seq*L^2*n^2 +
     12*D(1,1)))/(L^3*(n + 1)^2),0,(h*(Seq*L^2*n^2 + 12*D(1,1)))/(2*L^2*(n
     + 1)^2);
     (A(1,3)*h)/L,0,(A(3,3)*h)/L,0, -(A(1,3)*h)/L,0, -(A(3,3)*h)/L,0;
     0, (h*(Seq*L^2*n^2 + 12*D(1,1)))/(2*L^2*(n + 1)^2), 0,
     (h*(Seq*L^2*n^2 + 4*D(1,1)*n^2 + 8*D(1,1)*n + 16*D(1,1)))/(4*L*(n +
     1)^2), 0, -(h*(Seq*L^2*n^2 + 12*D(1,1)))/(2*L^2*(n + 1)^2), 0,
     (h*(Seq*L^2*n^2 - 4*D(1,1)*n^2 - 8*D(1,1)*n + 8*D(1,1)))/(4*L*(n +
     1)^2);
     -(A(1,1)*h)/L, 0, -(A(1,3)*h)/L,0, (A(1,1)*h)/L,0, (A(1,3)*h)/L,0;
     0, -(h*(Seq*L^2*n^2 + 12*D(1,1)))/(L^3*(n + 1)^2), 0, -(h*(Seq*L^2*n^2
     + 12*D(1,1)))/(2*L^2*(n + 1)^2),0, (h*(Seq*L^2*n^2 +
     12*D(1,1)))/(L^3*(n + 1)^2),0,-(h*(Seq*L^2*n^2 +
     12*D(1,1)))/(2*L^2*(n + 1)^2);
     -(A(1,3)*h)/L,0, -(A(3,3)*h)/L,0, (A(1,3)*h)/L,0, (A(3,3)*h)/L,0;
     0, (h*(Seq*L^2*n^2 + 12*D(1,1)))/(2*L^2*(n + 1)^2), 0, (h*(Seq*L^2*n^2
     - 4*D(1,1)*n^2 - 8*D(1,1)*n + 8*D(1,1)))/(4*L*(n + 1)^2), 0, -
     (h*(Seq*L^2*n^2 + 12*D(1,1)))/(2*L^2*(n + 1)^2), 0, (h*(Seq*L^2*n^2 +
     4*D(1,1)*n^2 + 8*D(1,1)*n + 16*D(1,1)))/(4*L*(n + 1)^2)];
```

```
K2=h*[-A(1,2) 0 -A(2,3) 0 A(1,2) 0 A(2,3) 0]';%%Stiffness matrix with respect
to the local axes
```

```
%%Transformation matrix for inclined wall 1
```

```
T2=[cos((5*pi/2-teta)) -sin((5*pi/2-teta)) 0 0 0 0 0 0;...
```

```

sin((5*pi/2-teta)) cos((5*pi/2-teta)) 0 0 0 0 0;...
0 0 1 0 0 0 0;...
0 0 0 1 0 0 0;...
0 0 0 0 cos((5*pi/2-teta)) -sin((5*pi/2-teta)) 0 0;...
0 0 0 0 sin((5*pi/2-teta)) cos((5*pi/2-teta)) 0 0;...
0 0 0 0 0 0 1 0;...
0 0 0 0 0 0 0 1];

```

```

K12t=T2*K1*T2';
K22t=T2*K2;
%%Define global force-displacement relationship
F2=K12t*[v21 v22 v23 dw2 v51 v52 v53 dw5]'+K22t*E33;

```

```

%%Define stiffness matrix of wall 2_Inclined wall 2
L=L2;
A=A3;B=B3;D=D3;
Seq=Se3;
n=12*D(1,1)/(L^2*Seq); %%Seq=kGA

```

```

K1=[(A(1,1)*h)/L,0, (A(1,3)*h)/L, 0, -(A(1,1)*h)/L, 0, -(A(1,3)*h)/L, 0;
0,(h*(Seq*L^2*n^2 + 12*D(1,1)))/(L^3*(n + 1)^2),0, (h*(Seq*L^2*n^2 +
12*D(1,1)))/(2*L^2*(n + 1)^2),0, -(h*(Seq*L^2*n^2 +
12*D(1,1)))/(L^3*(n + 1)^2),0,(h*(Seq*L^2*n^2 + 12*D(1,1)))/(2*L^2*(n
+ 1)^2);
(A(1,3)*h)/L,0,(A(3,3)*h)/L,0, -(A(1,3)*h)/L,0, -(A(3,3)*h)/L,0;
0, (h*(Seq*L^2*n^2 + 12*D(1,1)))/(2*L^2*(n + 1)^2), 0, (h*(Seq*L^2*n^2
+ 4*D(1,1)*n^2 + 8*D(1,1)*n + 16*D(1,1)))/(4*L*(n + 1)^2), 0, -
(h*(Seq*L^2*n^2 + 12*D(1,1)))/(2*L^2*(n + 1)^2), 0, (h*(Seq*L^2*n^2
- 4*D(1,1)*n^2 - 8*D(1,1)*n + 8*D(1,1)))/(4*L*(n + 1)^2);
-(A(1,1)*h)/L, 0, -(A(1,3)*h)/L,0, (A(1,1)*h)/L,0, (A(1,3)*h)/L,0;
0, -(h*(Seq*L^2*n^2 + 12*D(1,1)))/(L^3*(n + 1)^2), 0, -(h*(Seq*L^2*n^2
+ 12*D(1,1)))/(2*L^2*(n + 1)^2),0, (h*(Seq*L^2*n^2 +
12*D(1,1)))/(L^3*(n + 1)^2),0, -(h*(Seq*L^2*n^2 +
12*D(1,1)))/(2*L^2*(n + 1)^2);
-(A(1,3)*h)/L,0, -(A(3,3)*h)/L,0, (A(1,3)*h)/L,0, (A(3,3)*h)/L,0;
0, (h*(Seq*L^2*n^2 + 12*D(1,1)))/(2*L^2*(n + 1)^2), 0,
(h*(Seq*L^2*n^2 - 4*D(1,1)*n^2 - 8*D(1,1)*n + 8*D(1,1)))/(4*L*(n +
1)^2), 0, -(h*(Seq*L^2*n^2 + 12*D(1,1)))/(2*L^2*(n + 1)^2), 0,
(h*(Seq*L^2*n^2 + 4*D(1,1)*n^2 + 8*D(1,1)*n + 16*D(1,1)))/(4*L*(n +
1)^2)];

```

```

K2=h*[-A(1,2) 0 -A(2,3) 0 A(1,2) 0 A(2,3) 0]';%%Stiffness matrix with
respect to the local axes

```

```

%%Transformation matrix for inclined wall 2
T3=[cos(pi/2+teta) -sin(pi/2+teta) 0 0 0 0 0;...
sin(pi/2+teta) cos(pi/2+teta) 0 0 0 0 0;...
0 0 1 0 0 0 0;...
0 0 0 1 0 0 0;...
0 0 0 0 cos(pi/2+teta) -sin(pi/2+teta) 0 0;...
0 0 0 0 sin(pi/2+teta) cos(pi/2+teta) 0 0;...
0 0 0 0 0 0 1 0;...
0 0 0 0 0 0 0 1];

```

```

K13t=T3*K1*T3';
K23t=T3*K2;

```



```

F3=K13t*[v41 v42 v43 dw4 v51 v52 v53 dw5]'+K23t*E33;

%%Equations for force equilibrium
S1=F1(1)+F2(1)+F3(1);
S2=F1(2)+F2(2)+F3(2);
S3=F1(3)+F2(3)+F3(3);
S4=F1(4)+F2(4)+F3(4);
S5=F1(5)+F2(5)+F3(5);
S6=F1(6)+F2(6)+F3(6);
S7=F1(7)+F2(7)+F3(7);
S8=F1(8)+F2(8)+F3(8);

%%Periodic boundary conditions
S9=dw1-dw2;
S10=dw3-dw4;
S11=dw1-dw3;
S12=(v41-v21)+(v11-v31);
S13=(v42-v22)+(v12-v32);
S14=(v43-v23)+(v13-v33);

%%Strain definition of RVE
E11=(v31-v11)/a;
E22=(v22-v12)/b+c/a*(v32-v12)/b;
E23=1/2*((v23-v13)/b+c/a*(v33-v13)/b);
E13=1/2*(v33-v13)/a;
E12=1/2*((v32-v12)/a+(v21-v11)/b+c/a*(v31-v11)/b);

%%Solving equations to get the displacement
[A,B]=equationsToMatrix([S1==0,S2==0,S3==0,S4==0,S5==0,S6==0,S7==0,S8==0,S9==0,S10
==0,S11==0,S12==0,...
S13==0,S14==0,v11==0,v12==0,v13==0,v32==0,E11-e11==0,E22-
e22==0,E23-e23==0,E13-e13==0,E12-e12==0],[v11 v12 v13 dw1 v21 v22 v23 dw2 v31 v32
v33 dw3 v41 v42 v43 dw4 ,...
v51 v52 v53 dw5]);

C=linsolve(A,B);
V11=C(1); V12=C(2);V13=C(3);DW1=C(4);
V21=C(5); V22=C(6);V23=C(7);DW2=C(8);
V31=C(9);V32=C(10);V33=C(11);DW3=C(12);
V41=C(13);V42=C(14);V43=C(15);DW4=C(16);
V51=C(17);V52=C(18);V53=C(19);DW5=C(20);

%%Displacement vector of each wall in global coordinate system
V1=[V11 V12 V13 DW1 V51 V52 V53 DW5]';
V2=[V21 V22 V23 DW2 V51 V52 V53 DW5]';
V3=[V41 V42 V43 DW4 V51 V52 V53 DW5]';

%%Strain energy of walls
A=A1;B=B1;D=D1;
L=L1;
W1=1/2*V1'*K11t*V1+V1'*K21t*E33+1/2*A(2,2)*E33^2*L*h;

A=A2;B=B2;D=D2;
L=L2;
W2=1/2*V2'*K12t*V2+V2'*K22t*E33+1/2*A(2,2)*E33^2*L*h;

A=A3;B=B3;D=D3;

```

```

L=L2;
W3=1/2*V3'*K13t*V3+V3'*K23t*E33+1/2*A(2,2)*E33^2*L*h;

W(i)=W1+W2+W3; %%%total strain energy of the RVE

%%Calculating the stiffness of component of effective elastic
%%tensor for 3D analysis
switch i
    case 1
        C1111=2*W(1)/(V);
    case 2
        C2222=2*W(2)/(V);
    case 3
        C3333=2*W(3)/(V);
    case 4
        C1313=0.5*W(4)/(V);
    case 5
        C2323=0.5*W(5)/(V);
    case 6
        C1212=0.5*W(6)/(V);
    case 7
        C1122=(W(7)-W(1)-W(2))/(V);
    case 8
        C1133=(W(8)-W(1)-W(3))/(V);
    case 9
        C2233=(W(9)-W(2)-W(3))/(V);

end
end

C=[C1111 C1122 C1133 0 0 0;C1122 C2222 C2233 0 0 0; C1133 C2233 C3333 0 0 0;....
    0 0 0 C2323 0 0; 0 0 0 0 C1313 0;0 0 0 0 0 C1212];
disp(vpa(C,5))
S=inv(C);
u21=-S(1,2)/S(2,2);
u31=-S(1,3)/S(3,3);
u32=-S(2,3)/S(3,3);
u13=-S(3,1)/S(1,1);
u23=-S(3,2)/S(1,1);

%disp(vpa(u21,5));
u12=-S(2,1)/S(1,1);
%disp(vpa(u12,5));
E1111=1/S(1,1);

E2222=1/S(2,2);
E3333=1/S(3,3);

%%Effective stiffness properties for the plane stress condition
Q11=E1111/(1-u21*u12);
Q22=E2222/(1-u21*u12);
Q12=u12*E2222/(1-u21*u12);
Q66=1/S(6,6);
G23=1/S(4,4);
G13=1/S(5,5);

disp('*****')
disp(vpa(Q11,5))

```

```

disp(vpa(Q22,5))
disp(vpa(Q12,5))
disp(vpa(Q66,5))
disp(vpa(G13,5))
disp(vpa(G23,5))

```

```

function [An,Bn,Dn,Seq]=MaterialPropThick(tot_thickness,layer_thickness,E1layer,
E2layer, Glayer, vlayer,nOrient)

```

```

syms z

```

```

% plate thickness

```

```

nc=length(layer_thickness);

```

```

for n=1:1:nc

```

```

    ct=cos(nOrient(n));

```

```

    st=sin(nOrient(n));

```

```

    E1=E1layer(n);

```

```

    E2=E2layer(n);

```

```

    G1=Glayer(n);

```

```

    v1=vlayer(n);

```

```

    v2=E2/E1*v1;

```

```

    Q=[E1/(1-v1*v2) v1*E2/(1-v1*v2) 0;v1*E2/(1-v1*v2) E2/(1-v1*v2) 0;0 0 G1];

```

```

    Q11t=ct^4*Q(1,1)+st^4*Q(2,2)+2*ct^2*st^2*(Q(1,2)+2*Q(3,3));

```

```

    Q22t=st^4*Q(1,1)+ct^4*Q(2,2)+2*ct^2*st^2*(Q(1,2)+2*Q(3,3));

```

```

    Q12t=ct^2*st^2*(Q(1,1)+Q(2,2)-4*Q(3,3))+(ct^4+st^4)*Q(1,2);

```

```

    Q66t=ct^2*st^2*(Q(1,1)+Q(2,2)-2*Q(1,2))+(ct^2-st^2)^2*Q(3,3);

```

```

    Q16t=ct*st*(ct^2*Q(1,1)-st^2*Q(2,2)-(ct^2-st^2)*(Q(1,2)+2*Q(3,3)));

```

```

    Q26t=ct*st*(st^2*Q(1,1)-ct^2*Q(2,2)+(ct^2-st^2)*(Q(1,2)+2*Q(3,3)));

```

```

    TrQt(:, :, n)=[Q11t, Q12t, Q16t; Q12t, Q22t, Q26t; Q16t, Q26t, Q66t];

```

```

    %%disp(TrQt(:, :, n))

```

```

end

```

```

z1k=0;

```

```

z2k=0;

```

```

for n=1:1:nc

```

```

    if(n==1)

```

```

        z1k(n)=-tot_thickness/2+layer_thickness(n);

```

```

        z2k(n)=z1k(n)-layer_thickness(n);

```

```

    else

```

```

        z1k(n)=layer_thickness(n)+z1k(n-1);

```

```

        z2k(n)=z1k(n)-layer_thickness(n);

```

```

    end

```

```

end

```

```

thick=layer_thickness;

```

```

A11=0;A22=0;A12=0;A16=0;A26=0;A66=0;

```

```

B11=0;B22=0;B12=0;B16=0;B26=0;B66=0;

```

```

D11=0;D22=0;D12=0;D16=0;D26=0;D66=0;

```

```

A44=0;

```

```

%B1n=0;

```

```

%A1n=0;

```

```

for n=1:1:nc

```

```

%Membrane
A11=A11+TrQt(1,1,n)*(z1k(n)-z2k(n));
A1n(n)=A11;
A22=A22+TrQt(2,2,n)*(z1k(n)-z2k(n));
A12=A12+TrQt(1,2,n)*(z1k(n)-z2k(n));
A16=A16+TrQt(1,3,n)*(z1k(n)-z2k(n));
A26=A26+TrQt(2,3,n)*(z1k(n)-z2k(n));
A66=A66+TrQt(3,3,n)*(z1k(n)-z2k(n));

B11=B11+TrQt(1,1,n)*(z1k(n)^2-z2k(n)^2)/2;
B1n(n)=B11;
B22=B22+TrQt(2,2,n)*(z1k(n)^2-z2k(n)^2)/2;
B12=B12+TrQt(1,2,n)*(z1k(n)^2-z2k(n)^2)/2;
B16=B16+TrQt(1,3,n)*(z1k(n)^2-z2k(n)^2)/2;
B26=B26+TrQt(2,3,n)*(z1k(n)^2-z2k(n)^2)/2;
B66=B66+TrQt(3,3,n)*(z1k(n)^2-z2k(n)^2)/2;

%Bending
D11=D11+TrQt(1,1,n)*(z1k(n)^3-z2k(n)^3)/3;
D22=D22+TrQt(2,2,n)*(z1k(n)^3-z2k(n)^3)/3;
D12=D12+TrQt(1,2,n)*(z1k(n)^3-z2k(n)^3)/3;
D16=D16+TrQt(1,3,n)*(z1k(n)^3-z2k(n)^3)/3;
D26=D26+TrQt(2,3,n)*(z1k(n)^3-z2k(n)^3)/3;
D66=D66+TrQt(3,3,n)*(z1k(n)^3-z2k(n)^3)/3;

A44=A44+Glayer(n)*(z1k(n)-z2k(n));
end

A=[A11 A12 A16; A12 A22 A26; A16 A26 A66];
B=[B11 B12 B16; B12 B22 B26; B16 B26 B66];
D=[D11 D12 D16; D12 D22 D26; D16 D26 D66];

K=[A,B;B,D];

C=inv(K);
nd=-C(1,4)/C(4,4);

An=A;
Bn= zeros(3);
Dn=D-2*nd*B+nd^2*A;

Gssum=0;

for n=1:1:nc
    if(n==1)
        G=@(z)(TrQt(1,1,n)*(z.^2-(-tot_thickness/2)^2)/2-nd*TrQt(1,1,n)*(z-
tot_thickness/2)).^2;
        Gssum=integral(G,-tot_thickness/2,z1k(n))./Glayer(n);
    end
    if(n>1)
        G=@(z)(B1n(n-1)-nd*A1n(n-1)+TrQt(1,1,n)*(z.^2-z2k(n).^2)./2-
nd*TrQt(1,1,n)*(z-z2k(n))).^2;
        Gssum=Gssum+integral(G,z2k(n),z1k(n))./Glayer(n);
    end
end

```

end

```
Seq=A44*(Dn(1,1)^2/(Gssum*A44));
```

End

A4. MATLAB program for the shear buckling of the hexagonal core

```
clc
clear
syms L teta teta1 t E h u L1 L2 t1 t2 q k real
syms V11 V12 V13 V21 V22 V23 V31 V32 V33 k real
syms C1 C2 C3 C4 x1 y1 x2 y2 x3 y3 z X Y K R NCR1 NCR2 NCR3 real
syms v11 v12 v13 dw1 v31 v32 v33 dw3 v41 v42 v43 dw4 v51 v52 v53 dw5 v21 v22 v23
dw2 real
syms E11 E22 E33 E23 E13 E12 real
syms A11 A12 A16 A22 A26 A66 D11 D22 D12 D16 D26 D66 B11 B12 B22 B16 B26 B66 real
syms a11 a12 a16 a22 a26 a66 d11 d22 d12 d16 d26 d66 B11 B12 B22 B16 B26 B66 real

L1=50;          %Vertical leg
L2=50;          %inclined leg
h=150;          %height of the honeycomb
t1=4.6875;      %thickness of vertical leg
t2=4.6875/2;    %% %thickness of inclined leg

teta=pi/180*120 ;

%%Angle between the

E1A=204000;
E1B=38600;
E1C=131000;
E2A=18500;
E2B=8270;
E2c=10300;
GA=5590;
GB=4140;
Gc=6900;
VA=0.23;
VB=0.26;
VC=0.22;

layer_thickness1=t1/10*[1,1,1,1,1,1,1,1,1,1];
layer_thickness2=t2/5*[1,1,1,1,1];

%%vertical leg
%E1layer1=[E1B,E1B,E1B,E1B,E1B];
%E2layer1=[E2B,E2B,E2B,E2B,E2B];
%Glayer1=[GB,GB,GB,GB,GB];
%vlayer1=[VB,VB,VB,VB,VB];
E1layer1=[E1B,E1B,E1B,E1B,E1B,E1B,E1B,E1B,E1B,E1B];
E2layer1=[E2B,E2B,E2B,E2B,E2B,E2B,E2B,E2B,E2B,E2B];
Glayer1=[GB,GB,GB,GB,GB,GB,GB,GB,GB,GB];
vlayer1=[VB,VB,VB,VB,VB,VB,VB,VB,VB,VB];

%%inclined
```

```

E1layer2=[E1B,E1B,E1B,E1B,E1B];
E2layer2=[E2B,E2B,E2B,E2B,E2B];
Glayer2=[GB,GB,GB,GB,GB];
vlayer2=[VB,VB,VB,VB,VB];

%%vertical leg
nOrient1=[3*pi/12,-3*pi/12,90*pi/12, -3*pi/12, 3*pi/12,3*pi/12,-3*pi/12,90*pi/12,
-3*pi/12, 3*pi/12];
%nOrient1=[3*pi/12,-3*pi/12,0*pi/12, -3*pi/12, 3*pi/12];

nOrient2=[3*pi/12,-3*pi/12,90*pi/12, -3*pi/12, 3*pi/12];

[A1,B1,D1]=MaterialProp(t1,layer_thickness1,E1layer1,E2layer1,Glayer1,vlayer1,nOri
ent1);
[A2,B2,D2]=MaterialProp(t2,layer_thickness2,E1layer2,E2layer2,Glayer2,vlayer2,nOri
ent2);
D1=double(D1);

A1(1,3)=0;
A2(1,3)=0;
A1(2,3)=0;
A2(2,3)=0;

a1=inv(A1);
a2=inv(A2);

a=2*L2*sin(teta); %%
b=(L1+L2*cos(pi-teta));
c=L2*sin(teta);
V=a*b*h; %%volume of RVE

disp('coredensity');
Dr=(2*t2*L2*h+t1*L1*h)/V;
disp(Dr)

A66=A1(3,3);
a66=A2(3,3);
m66=A2(3,3);

n=1;
k=0;

e13=1*q/2;e23=0*q/2;

V1s=(n*q*(L2*m66*sin(teta) + L1*a66*k + L1*k*m66 - L2*a66*sin(teta) -
L2*a66*k*cos(teta) - L2*k*m66*cos(teta)))/(L1*a66 + L1*m66 + A66*L2);
V2s=-(n*q*(2*L1*m66*sin(teta) - A66*L1*k + A66*L2*sin(teta) +
A66*L2*k*cos(teta)))/(L1*a66 + L1*m66 + A66*L2);
V3s=(n*q*(A66*L1*k + A66*L2*sin(teta) + 2*L1*a66*sin(teta) -
A66*L2*k*cos(teta)))/(L1*a66 + L1*m66 + A66*L2);

if(e13==0)
V1s=(n*q*(a66 + m66)*(L1 - L2*cos(teta)))/(L1*a66 + L1*m66 + A66*L2);

V2s=(A66*n*q*(L1 - L2*cos(teta)))/(L1*a66 + L1*m66 + A66*L2);

```

```
V3s=(A66*n*q*(L1 - L2*cos(teta)))/(L1*a66 + L1*m66 + A66*L2);
end
```

```
%%Calculate critical strain under simply supported
```

```
%wall_1_vertical wall_1
```

```
if(double(V1s/q)<0)
NL1=Critical_Load(D1,L1,h,1e-25, -1);
else
NL1=Critical_Load(D1,L1,h,1e-25,1);
end
```

```
ecr1=NL1/A1(3,3);
```

```
if(abs(double(V1s/q))<0.000000000000001)
    ecrRVE1=1e12;
else
ecrRVE1=solve(ecr1-V1s==0,q);
end
```

```
disp(vpa(ecrRVE1,5));
```

```
%%inclined wall_1
```

```
    if(double(V2s/q)<0)
        NL2=Critical_Load(D2,L2,h,1e-25,-1);

    else
        NL2=Critical_Load(D2,L2,h,1e-25,1);

    end
```

```
ecr2=(double(NL2)/A2(3,3));
ecrRVE2=solve(ecr2-V2s==0,q);
disp(vpa(ecrRVE2,5));
```

```
if(ecrRVE2>1e12)
    ecrRVE2=1e12;
end
```

```
disp(vpa(ecrRVE2,5));
```

```
%wall 3 %Inclined wall_2
```

```
    if(double(V3s/q)<0)
        NL3=Critical_Load(D2,L2,h,1e-25,-1);

    else
        NL3=Critical_Load(D2,L2,h,1e-25,1);

    end
```

```

ecr3=NL3/A2(3,3);
ecrRVE3=solve(ecr3-V3s==0,q);

disp(vpa(ecrRVE3,5));

if(ecrRVE3>1e12)
    ecrRVE3=1e12;
end

disp(vpa(ecrRVE3,5));

ecrRVE=[abs(ecrRVE1), abs(ecrRVE2),abs(ecrRVE3)];
disp(vpa(ecrRVE,5))
ecrRVEmin=min(ecrRVE);
linearIndices = find(ecrRVE==ecrRVEmin);

if(abs(ecrRVE1)-abs(ecrRVE2)>0.00000001&& abs(ecrRVE1)-abs(ecrRVE3)>0.00000001&&
abs(abs(ecrRVE2)-abs(ecrRVE3))<0.000000000001)
    V11s=V1s;
    e1=subs(V11s,q,ecrRVEmin);

    %disp('inclined_one_and_two');
    legCritical='inclined_one_and_two';
    ksp=min(1/2*2*D1(1,1)/(L1)*(1-abs(e1/ecr1)));

    %wall 2 %Inclined wall

    if(double(V2s/q)<0)
        [NL2,Dir,X]=Critical_Load(D2,L2,h,ksp,-1);
        disp(vpa(NL2))
        disp(Dir)
        disp(X)
    else
        [NL2,Dir,X]=Critical_Load(D2,L2,h,ksp,1);
        disp(vpa(NL2))
        disp(Dir)
        disp(X)
    end
    ecr2=NL2/A2(3,3);
    ecrRVE2=solve(ecr2-V2s==0,q);
    disp('inclined one and two');
    disp(vpa(ecrRVE2,5));

end

if(abs(ecrRVE2)-abs(ecrRVE1)>0.00000001&& abs(ecrRVE3)-abs(ecrRVE1)>0.000000001)
    V22s=V2s;
    V33s=V3s;
    e2=subs(V22s,q,ecrRVEmin);
    e3=subs(V33s,q,ecrRVEmin);
    legCritical='vertical';
    ksp=2*D2(1,1)/(L2)*(1-abs(e2/ecr2))+2*D2(1,1)/(L2)*(1-abs(e3/ecr3));
    disp('vertical');

    if(double(V1s/q)<0)

```



```

NL1=Critical_Load(D1,L1,h,ksp,-1);
ecr1=-NL1/A1(3,3);
ecrRVE1=solve(ecr1-V1s==0,q);
disp(vpa(ecrRVE1,5));
else
NL1=Critical_Load(D1,L1,h,ksp,1);
ecr1=NL1/A1(3,3);
ecrRVE1=solve(ecr1-V1s==0,q);
disp(vpa(ecrRVE1,5));
end

```

end

```

if((abs(ecrRVE1)-
abs(ecrRVE2)>0.000000001)&&(abs(ecrRVE3)abs(ecrRVE2))>0.0000000001&&abs(ecrRVE3)~
=abs(ecrRVE2))
V11s=V1s;
V33s=V3s;
e1=subs(V11s,q,ecrRVEmin);
e3=subs(V33s,q,ecrRVEmin);
legCritical='inclined_one_only';
ksp=2*D1(1,1)/(L1)*(1-abs(e1/ecr1))+2*D2(1,1)/(L2)*(1-abs(e3/ecr3));

disp('inclined_one_only');

if(double(V2s/q)<0)
[NL2,Dir,X]=Critical_Load(D2,L2,h,ksp,-1);
disp(vpa(NL2))
disp(Dir)
disp(X)
else
[NL2,Dir,X]=Critical_Load(D2,L2,h,ksp,1);
disp(vpa(NL2))
disp(Dir)
disp(X)
end
ecr2=NL2/A2(3,3);
ecrRVE2=solve(ecr2-V2s==0,q);
disp('inclined one ');
disp(vpa(ecrRVE2,5));

```

end

```

if((abs(ecrRVE1)-
abs(ecrRVE3)>0.000000001)&&(abs(ecrRVE2)abs(ecrRVE3))>0.0000000001&&abs(ecrRVE3)~
=abs(ecrRVE2))
V11s=V1s;
V22s=V2s;
e1=subs(V11s,q,ecrRVEmin);
e2=subs(V22s,q,ecrRVEmin);
%disp(vpa(e2,5));
legCritical='inclined_two_only';
disp('inclined_two_only');
ksp=double(2*D1(1,1)/(L1)*(1-abs(e1/ecr1))+2*D2(1,1)/(L2)*(1-
abs(e2/ecr2)));

```

```

if(double(V3s/q)<0)

```

```

[NL3,Dir,X]=Critical_Load(D2,L2,h,ksp,-1);
disp(vpa(NL3))
disp(Dir)
disp(X)
else
[NL3,Dir,X]=Critical_Load(D2,L2,h,ksp,1);
disp(vpa(NL3))
disp(Dir)
disp(X)
end

ecr3=NL3/A2(3,3);
ecrRVE3=solve(ecr3-V3s==0,q);
disp('inclined two ');

disp(vpa(ecrRVE3,5));

```

end

```
function [Ncr,Dir,X]=Critical_Load(D1,z,L1,h,K,A1,dir)
```

```

syms R x y real positive
syms B A real positive

```

```
D = [D1(2,2),D1(1,2),D1(1,1),D1(2,3),D1(1,3),D1(3,3)];
```

```

%disp('buckling')
%disp(D);
D11=D(1);
D12=D(2);
D22=D(3);
D16=D(4);
D26=D(5);
D66=D(6);

```

```
b=L1;
```

```

K=double(K);
if(K<1e-10)
R=0;

```

else

```
R=double(1/(1+4*pi*D(3)/(K*b)));
```

end

```

N=@(x)dir*(6*x(1)*((x(1)*K*pi^2*(R - 1)^2)/b + (x(1)*D22*pi^3*(32*R + 3*pi - 6*pi*R
+ 51*pi*R^2 - 32*R^2))/(12*b^2) + (D11*pi^3*(32*R + 3*pi - 6*pi*R + 12*pi*R^2 -
32*R^2))/(12*x(1)^3*b^2) + (D12*pi^3*(32*R + 3*pi - 6*pi*R + 15*pi*R^2 -
32*R^2))/(6*x(1)*b^2) + (D66*pi^3*(32*R + 3*pi - 6*pi*R + 15*pi*R^2 -
32*R^2))/(3*x(1)*b^2) - (x(2)*D16*pi^3*(32*R + 3*pi - 6*pi*R + 12*pi*R^2 -
32*R^2))/(3*x(1)^3*b^2) - (x(2)*D26*pi^3*(96*R + 9*pi - 18*pi*R + 45*pi*R^2 -
96*R^2))/(3*x(1)*b^2) + (x(2)^2*D12*pi^3*(32*R + 3*pi - 6*pi*R + 12*pi*R^2 -
32*R^2))/(6*x(1)^3*b^2) + (x(2)^2*D22*pi^3*(32*R + 3*pi - 6*pi*R + 15*pi*R^2 -

```

```

32*R^2))/(2*x(1)*b^2) + (x(2)^4*D22*pi^3*(32*R + 3*pi - 6*pi*R + 12*pi*R^2 -
32*R^2))/(12*x(1)^3*b^2) - (x(2)^3*D26*pi^3*(32*R + 3*pi - 6*pi*R + 12*pi*R^2 -
32*R^2))/(3*x(1)^3*b^2) + (x(2)^2*D66*pi^3*(32*R + 3*pi - 6*pi*R + 12*pi*R^2 -
32*R^2))/(3*x(1)^3*b^2)))/(x(2)*pi*(32*R + 3*pi - 6*pi*R + 12*pi*R^2 - 32*R^2));

```

```

options = optimoptions('fmincon','Display','off');

```

```

if(dir==1)

```

```

lb=[0,0];

```

```

lu=[h/b,pi/2];

```

```

Xo=(lb+lu)/2;

```

```

[X,Ncr]=fmincon(N,Xo,[],[],[],[],lb,lu,[],options);

```

```

Dir=dir;

```

```

disp(vpa(Ncr));

```

```

end

```

```

if(dir==-1)

```

```

lb=[0,-pi/2];

```

```

lu=[h/b,0];

```

```

Xo=(lb+lu)/2;

```

```

[X,Ncr]=fmincon(N,Xo,[],[],[],[],lb,lu,[],options);

```

```

disp(vpa(Ncr));

```

```

Dir=dir;

```

```

end

```

```

disp(vpa(Ncr));

```

```

end

```

A4. MATLAB program for the intracellular buckling of the hexagonal cell

```

clc

```

```

clear

```

```

syms Amn m n p q x y a b D11 D12 D22 D16 D26 D66 B1 B2 B3 C1 C2 C3 teta L real

```

```

teta=120*pi/180;

```

```

L1=50; %%vertical leg length

```

```

L2=50; %%inclined leg length

```

```

t1=4.6875;

```

```

t2=4.6875/2;

```

```

h=150;

```

```

tf=5;

```

```

a=2*L2*sin(teta); %%%(2*pi-2*teta)/2

```

```

b=(L1+L2*cos(pi-teta));

```

```

c=L2*sin(teta);
V=a*b*h;           %volume of RVE

disp('coredensity');
Dr=(2*t2*L2*h+t1*L1*h)/V;
disp(Dr)

%%Angle between the

E1A=204000;
E1B=386000;
E1C=131000;
E2A=185000;
E2B=82700;
E2C=103000;
GA=55900;
GB=41400;
GC=69000;
VA=0.23;
VB=0.26;
VC=0.22;

%%vertical leg
layer_thickness1=t1/10*[1,1,1,1,1,1,1,1,1,1];

%%inclinded leg
layer_thickness2=t2/5*[1,1,1,1,1];

%%face sheet
layer_thicknessf=tf/5*[1,1,1,1,1];

%%vertical leg
E1layer1=[E1B,E1B,E1B,E1B,E1B,E1B,E1B,E1B,E1B,E1B];
E2layer1=[E2B,E2B,E2B,E2B,E2B,E2B,E2B,E2B,E2B,E2B];
Glayer1=[GB,GB,GB,GB,GB,GB,GB,GB,GB,GB];
vlayer1=[VB,VB,VB,VB,VB,VB,VB,VB,VB,VB];

%%inclined
E1layer2=[E1B,E1B,E1B,E1B,E1B];
E2layer2=[E2B,E2B,E2B,E2B,E2B];
Glayer2=[GB,GB,GB,GB,GB];
vlayer2=[VB,VB,VB,VB,VB];

%%Facesheet
E1layerf=[E1B,E1B,E1B,E1B,E1B]; %[E1C,E1C,E1C,E1C,E1C];
E2layerf=[E2B,E2B,E2B,E2B,E2B]; %[E2C,E2C,E2C,E2C,E2C];
Glayerf=[GB,GB,GB,GB,GB]; %[GC,GC,GC,GC,GC];
vlayerf=[VB,VB,VB,VB,VB]; %[VC,VC,VC,VC,VC];

nOrient1=[0*pi/12,6*pi/12,6*pi/12,6*pi/12,0*pi/12,0*pi/12,6*pi/12,6*pi/12,6*pi/12,
0*pi/12];%[0*pi/12,0*pi/12,0*pi/12,0*pi/12,6*pi/12];
    %inclined
    nOrient2=[0*pi/12,6*pi/12,6*pi/12,6*pi/12,0*pi/12];
    nOrientf=[0*pi/12,6*pi/12,0*pi/12,6*pi/12,0*pi/12];

```

```

[A1,B1,D1]=MaterialProp(t1,layer_thickness1,E1layer1,E2layer1,Glayer1,vlayer1,nOrient1);%stiffness of the vertical wall section
[A2,B2,D2]=MaterialProp(t2,layer_thickness2,E1layer2,E2layer2,Glayer2,vlayer2,nOrient2); %%stiffness of inclined wall section
[Af,Bf,Df]=MaterialProp(tf,layer_thicknessf,E1layerf,E2layerf,Glayerf,vlayerf,nOrientf);%stiffness of the vertical wall section

disp(vpa(Af))

%Axial compression

ao = 2*L2*sin(teta);
bo =L1;

Df(1,3)=0;
Df(2,3)=0;

D = Df;

T = 4;

%H = 0.1;
a1 = -cos(teta)/(L2*sin(teta)^2);
c1 = ao/2;
c = a1;
e = -2*a1*c1;

y1 = @(x)a1*x.^2-2*a1*c1*x;
y1x = @(x)2*a1*x-2*a1*c1;
y1xx = @(x)2*a1;
y2 = @(x)bo-y1(x);
y2x = @(x)-y1x(x);

a=ao;
%ay=@(y)0;
%ayy=@(y)0;

b = @(x)bo-2*y1(x);
bx = @(x)-2*y1x(x);
bxx = @(x)-2*y1xx(x);

%Ky=@(x)2*D/b(x);
%Kx=2*D/a;
%Axial compression
kx=(0.5*6*(2*D1(2,2)+4*D2(2,2))/(6*h));
ky=0.5*6*D2(2,2)/h;

bn=bx(ao/2);
R1=1/(1+4*pi*Df(1,1)/(kx*ao^3/4));
R2=1/(1+4*pi*Df(2,2)/(ky*bo^3/2));
disp('R1,R2')
disp(vpa(R1));
disp(vpa(R2));
%%functions and derivatives
xm=@(x,m)(1-R1)*sin(m*pi*x/a) + R1*(1 - cos(2*m*pi*x/a));

xmx=@(x,m)(1-R1)*(m*pi/a).*cos(m*pi*x/a)+(2*m*pi*R1./a).*sin(2*m*pi*x/a);

```

$xmxx = @ (x, m) 4 * m^2 * \pi^2 / a^2 * R1 * \cos(2 * m * \pi * x / a) - (1 - R1) * m^2 * \pi^2 / a^2 * \sin(m * \pi * x / a);$
 $yn = @ (x, y, n) (1 - R2) * \sin(n * \pi * (y - y1(x)) / b(x)) + R2 * (1 - \cos(2 * n * \pi * (y - y1(x)) / b(x)));$ %%%1%%R-Degree of rotational restraint

$ynx = @ (x, y, n) R2 * \sin(2 * n * \pi * (y - y1(x)) / b(x)) * (-2 * n * \pi * (y - y1(x)) * bx(x) / b(x) ^2 - 2 * n * \pi * y1x(x) / b(x)) + (1 - R2) * ((-n * \pi * b(x) * y1x(x) - bx(x) * n * \pi * (y - y1(x))) / (b(x) ^2)) * \cos(n * \pi * (y - y1(x)) / b(x));$

$ynxx = @ (x, y, n) (1 - R2) * (-\sin(n * \pi * (y - y1(x)) / b(x)) * (-n * \pi * bx(x) / b(x) ^2) * (y - y1(x)) - n * \pi * y1x(x) / b(x)) ^2 + \cos(n * \pi * (y - y1(x)) / b(x)) * ((2 * n * \pi * bx(x) ^2 / b(x) ^3) * (y - y1(x)) + 2 * n * \pi * bx(x) * y1x(x) / b(x) ^2 - (n * \pi * bxx(x) / b(x) ^2) * (y - y1(x)) - n * \pi * y1xx(x) / b(x))) + \dots$
 $R2 * (\cos(2 * n * \pi * (y - y1(x)) / b(x)) * (-2 * n * \pi * bx(x) / b(x) ^2) * (y - y1(x)) - 2 * n * \pi * y1x(x) / b(x)) ^2 + \sin(2 * n * \pi * (y - y1(x)) / b(x)) * ((4 * n * \pi * bx(x) ^2 / b(x) ^3) * (y - y1(x)) + 4 * n * \pi * bx(x) * y1x(x) / b(x) ^2 - (2 * n * \pi * bxx(x) / b(x) ^2) * (y - y1(x)) - 2 * n * \pi * y1xx(x) / b(x)));$

$ynxy = @ (x, y, n) - (1 - R2) * n * \pi * \cos(n * \pi * (y - y1(x)) / b(x)) * bx(x) / b(x) ^2 - 2 * n * \pi * R2 * \sin(2 * n * \pi * (y - y1(x)) / b(x)) * bx(x) / b(x) ^2 + 2 * n * \pi * R2 * \cos(2 * n * \pi * (y - y1(x)) / b(x)) * (-2 * n * \pi * (y - y1(x)) * bx(x) / b(x) ^2 - 2 * n * \pi * y1x(x) / b(x)) / b(x) - (1 - R2) * n * \pi * \sin(n * \pi * (y - y1(x)) / b(x)) * (-n * \pi * (y - y1(x)) * bx(x) / b(x) ^2 - n * \pi * y1x(x) / b(x)) / b(x);$

$yny = @ (x, y, n) (1 - R2) * (n * \pi / b(x)) * \cos(n * \pi * (y - y1(x)) / b(x)) + (2 * n * \pi * R2 / b(x)) * \sin(2 * n * \pi * (y - y1(x)) / b(x));$

$ynyy = @ (x, y, n) 4 * n^2 * \pi^2 * R2 * \cos(2 * n * \pi * (y - y1(x)) / b(x)) / b(x) ^2 - (1 - R2) * n^2 * \pi^2 * \sin(n * \pi * (y - y1(x)) / b(x)) / b(x) ^2;$

%functions and derivatives - p/q

$xp = @ (x, p) (1 - R1) * \sin(p * \pi * x / a) + R1 * (1 - \cos(2 * p * \pi * x / a));$

$xpx = @ (x, p) (1 - R1) * (p * \pi / a) * \cos(p * \pi * x / a) + (2 * p * \pi * R1 / a) * \sin(2 * p * \pi * x / a);$

$xpxx = @ (x, p) 4 * p^2 * \pi^2 / a^2 * R1 * \cos(2 * p * \pi * x / a) - (1 - R1) * p^2 * \pi^2 / a^2 * \sin(p * \pi * x / a);$

$yq = @ (x, y, q) (1 - R2) * \sin(q * \pi * (y - y1(x)) / b(x)) + R2 * (1 - \cos(2 * q * \pi * (y - y1(x)) / b(x)));$

$yqx = @ (x, y, q) R2 * \sin(2 * q * \pi * (y - y1(x)) / b(x)) * (-2 * q * \pi * (y - y1(x)) * bx(x) / b(x) ^2 - 2 * q * \pi * y1x(x) / b(x)) + (1 - R2) * ((-q * \pi * b(x) * y1x(x) - bx(x) * q * \pi * (y - y1(x))) / (b(x) ^2)) * \cos(q * \pi * (y - y1(x)) / b(x));$

$yqxx = @ (x, y, q) (1 - R2) * (-\sin(q * \pi * (y - y1(x)) / b(x)) * (-q * \pi * (y - y1(x)) * bx(x) / b(x) ^2 - q * \pi * y1x(x) / b(x)) ^2 + \cos(q * \pi * (y - y1(x)) / b(x)) * ((2 * q * \pi * (y - y1(x)) * bx(x) ^2 / b(x) ^3 + 2 * q * \pi * bx(x) * y1x(x) / b(x) ^2 - q * \pi * (y - y1(x)) * bxx(x) / b(x) ^2 - q * \pi * y1xx(x) / b(x))) + \dots$
 $R2 * (\cos(2 * q * \pi * (y - y1(x)) / b(x)) * (-2 * q * \pi * (y - y1(x)) * bx(x) / b(x) ^2 - 2 * q * \pi * y1x(x) / b(x)) ^2 + \sin(2 * q * \pi * (y - y1(x)) / b(x)) * ((4 * q * \pi * (y - y1(x)) * bx(x) ^2 / b(x) ^3 + 4 * q * \pi * bx(x) * y1x(x) / b(x) ^2 - 2 * q * \pi * (y - y1(x)) * bxx(x) / b(x) ^2 - 2 * q * \pi * y1xx(x) / b(x)));$

```

yqx = @(x,y,q) - (1-R2)*(q*pi.*bx(x)./b(x).^2).*cos(q*pi*(y-y1(x))./b(x)) -
(2*q*pi*R2.*bx(x)./b(x).^2).*sin(2*q*pi*(y-y1(x))./b(x)) + 2*q*pi*R2*cos(2*q*pi*(y-
y1(x))./b(x)).*(-2*q*pi*(y-y1(x)).*bx(x)./b(x).^2 - 2*q*pi*y1x(x)./b(x))./b(x) - (1-
R2)*q*pi*sin(q*pi*(y-y1(x))./b(x)).*(-q*pi*(y-y1(x)).*bx(x)./b(x).^2 -
q*pi*y1x(x)./b(x))./b(x));

```

```

yqy = @(x,y,q)(1-R2)*q*pi*cos(q*pi*(y-y1(x))./b(x))./b(x) + 2*q*pi*R2*sin(2*q*pi*(y-
y1(x))./b(x))./b(x);

```

```

yqyy = @(x,y,q)4*q^2*pi^2*R2*cos(2*q*pi*(y-y1(x))./b(x))./b(x).^2 - (1-
R2)*q^2*pi^2*sin(q*pi*(y-y1(x))./b(x))./b(x).^2;

```

%functions

```

Nx = @(x)1;
Ny = @(x,y)0;

```

```

I1_ = @(x,y,m,p,n,q)(xm(x,m).*ynxx(x,y,n)+2*xmx(x,m).*ynx(x,y,n)+xmx(x,m).*yn(x,y,n)).
*(xp(x,p).*yqxx(x,y,q)+2*xpx(x,p).*yqx(x,y,q)+xpx(x,p).*yq(x,y,q)); %D11

```

```

I2_ = @(x,y,m,p,n,q)(xm(x,m).*ynxx(x,y,n)+2*xmx(x,m).*ynx(x,y,n)+xmx(x,m).*yn(x,y,n)).
*(xp(x,p).*yqyy(x,y,q)+(xp(x,p).*yqxx(x,y,q)+2*xpx(x,p).*yqx(x,y,q)+xpx(x,p).*yq
(x,y,q)).*(xm(x,m).*ynyy(x,y,n))); %D12

```

```

I3_ = @(x,y,m,p,n,q)xm(x,m).*xp(x,p).*ynyy(x,y,n).*yqyy(x,y,q); %D22

```

```

I4_ = @(x,y,m,p,n,q)((xm(x,m).*ynxx(x,y,n)+2*xmx(x,m).*yny(x,y,n)+xmx(x,m).*yn(x,y,n))
.*(xp(x,p).*yqxy(x,y,q)+xpx(x,p).*yqy(x,y,q)+(xp(x,p).*yqxx(x,y,q)+2*xpx(x,p).*yq
x(x,y,q)+xpx(x,p).*yq(x,y,q)).*(xm(x,m).*ynxy(x,y,n)+xm(x,m).*yny(x,y,n))); %D16

```

```

I5_ = @(x,y,m,p,n,q)(xm(x,m).*ynyy(x,y,n)).*(xp(x,p).*yqxy(x,y,q)+xpx(x,p).*yqy(x,y,q))+
xpx(x,p).*yqyy(x,y,q)).*(xm(x,m).*ynxy(x,y,n)+xmx(x,m).*yny(x,y,n))); %D26

```

```

I6_ = @(x,y,m,p,n,q)((xm(x,m).*ynxy(x,y,n)+xmx(x,m).*yny(x,y,n)).*(xp(x,p).*yqxy(x,y,q)
+xpx(x,p).*yqy(x,y,q))); %D66

```

```

I7_ = @(x,y,m,p,n,q)(xm(x,m).*ynx(x,y,n)+yn(x,y,n).*xmx(x,m)).*(xp(x,p).*yqx(x,y,q)+yq(
x,y,q).*xpx(x,p)).*Nx(x);

```

```

I8_ = @(x,y,m,p,n,q)((xm(x,m).*ynx(x,y,n)+yn(x,y,n).*xmx(x,m)).*(xp(x,p).*yqy(x,y,q)) +
(xp(x,p).*yqx(x,y,q)+yq(x,y,q).*xpx(x,p)).*(xm(x,m).*yny(x,y,n))).*Nxy(x,y);

```

```

I9_ = @(x,y,m,p,n,q)xm(x,m).*yqy(x,y,q).*xp(x,p).*yny(x,y,n).*Ny(x,y);

```

```

I10_ = @(x,y,m,p,n,q)xm(x,m).*yqy(x,y,q).*xp(x,p).*yny(x,y,n).*ky;

```

```

I11_ = @(x,y,m,p,n,q)(xmx(x,m).*yq(x,y,q)+xm(x,m).*yqx(x,y,q)).*(xpx(x,p).*yn(x,y,n)
+xpx(x,p).*ynx(x,y,n)).*kx;

```

%gaussian

```

x_tr = @(X)X.*ao/2 +ao/2;

```

```

y_tr = @(X,Y)Y.*(bo/2-0.25*ao^2*c*X.^2-0.5*ao^2*c*X-0.25*ao^2*c-0.5*ao*e*X-
0.5*ao*e)+bo/2;

```

```

F_int

```

```

= @(X,Y,m,p,n,q)(Df(1,1).*I1_(x_tr(X),y_tr(X,Y),m,p,n,q)+Df(1,2).*I2_(x_tr(X),y_tr(
X,Y),m,p,n,q)+Df(2,2).*I3_(x_tr(X),y_tr(X,Y),m,p,n,q)+2*Df(1,3).*I4_(x_tr(X),y_tr(
X,Y),m,p,n,q)+2*Df(2,3).*I5_(x_tr(X),y_tr(X,Y),m,p,n,q)+4*Df(3,3).*I6_(x_tr(X),y_t
r(X,Y),m,p,n,q)).*(0.5*ao*(bo/2-0.25*ao^2*c*X.^2-0.5*ao^2*c*X-0.25*ao^2*c-
0.5*ao*e*X-0.5*ao*e));

```

```

F_ext

```

```

= @(X,Y,m,p,n,q)(I7_(x_tr(X),y_tr(X,Y),m,p,n,q)+I8_(x_tr(X),y_tr(X,Y),m,p,n,q)+I9_(

```

```

x_tr(X),y_tr(X,Y),m,p,n,q)).*(0.5*ao*(bo/2-0.25*ao^2*c*X.^2-0.5*ao^2*c*X-
0.25*ao^2*c-0.5*ao*e*X-0.5*ao*e));
F_spring1=@(X,Y,m,p,n,q)I10_(x_tr(X),y_tr(X,Y),m,p,n,q).*(0.5*ao*(bo/2-
0.25*ao^2*c*X.^2-0.5*ao^2*c*X-0.25*ao^2*c-0.5*ao*e*X-0.5*ao*e));
F_spring2=@(X,Y,m,p,n,q)I11_(x_tr(X),y_tr(X,Y),m,p,n,q).*(0.5*ao*(bo/2-
0.25*ao^2*c*X.^2-0.5*ao^2*c*X-0.25*ao^2*c-0.5*ao*e*X-0.5*ao*e));

```

```

node = [-0.996893484074649, -0.983668123279747, -0.960021864968307, -
0.926200047429274, -0.882560535792052, -0.829565762382768, -0.76777432104826, -
0.697850494793315, -0.620526182989242, -0.536624148142019, -0.447033769538089, -
0.352704725530878, -0.254636926167889, -0.153869913608583, -
0.0514718425553177, 0.0514718425553177, 0.153869913608583, 0.254636926167889, 0.352704
725530878, 0.447033769538089, 0.536624148142019, 0.620526182989242, 0.697850494793315,
0.76777432104826, 0.829565762382768, 0.882560535792052, 0.926200047429274, 0.96002186
4968307, 0.983668123279747, 0.996893484074649];

```

```

weight
=[0.0079681924961666, 0.018466468311091, 0.0287847078833234, 0.0387991925696271, 0.048
4026728305941, 0.0574931562176191, 0.0659742298821805, 0.0737559747377052, 0.080755895
2294202, 0.086899787201083, 0.0921225222377861, 0.0963687371746443, 0.0995934205867953
, 0.101762389748405, 0.102852652893558, 0.102852652893558, 0.101762389748405, 0.0995934
205867953, 0.0963687371746443, 0.0921225222377861, 0.086899787201083, 0.08075589522942
02, 0.0737559747377052, 0.0659742298821805, 0.0574931562176191, 0.0484026728305941, 0.0
387991925696271, 0.0287847078833234, 0.018466468311091, 0.0079681924961666];

```

```

PE_U1=@(m,p,n,q)(sum(F_int(node',node(1),m,p,n,q).*(weight(1)*weight)')+sum(F_int(
node',node(2),m,p,n,q).*(weight(2)*weight)')+sum(F_int(node',node(3),m,p,n,q).*(we
ight(3)*weight)')+sum(F_int(node',node(4),m,p,n,q).*(weight(4)*weight)')+sum(F_int
(node',node(5),m,p,n,q).*(weight(5)*weight)')+sum(F_int(node',node(6),m,p,n,q).*(w
eight(6)*weight)')+...

```

```

sum(F_int(node',node(7),m,p,n,q).*(weight(7)*weight)')+sum(F_int(node',node(8),m,p
,n,q).*(weight(8)*weight)')+sum(F_int(node',node(9),m,p,n,q).*(weight(9)*weight)')
+sum(F_int(node',node(10),m,p,n,q).*(weight(10)*weight)')+sum(F_int(node',node(11)
,m,p,n,q).*(weight(11)*weight)')+sum(F_int(node',node(12),m,p,n,q).*(weight(12)*we
ight)')+...

```

```

sum(F_int(node',node(13),m,p,n,q).*(weight(13)*weight)')+sum(F_int(node',node(14),
m,p,n,q).*(weight(14)*weight)')+sum(F_int(node',node(15),m,p,n,q).*(weight(15)*wei
ght)')+sum(F_int(node',node(16),m,p,n,q).*(weight(16)*weight)')+sum(F_int(node',no
de(17),m,p,n,q).*(weight(17)*weight)')+sum(F_int(node',node(18),m,p,n,q).*(weight(
18)*weight)')+...

```

```

sum(F_int(node',node(19),m,p,n,q).*(weight(19)*weight)')+sum(F_int(node',node(20),
m,p,n,q).*(weight(20)*weight)')+sum(F_int(node',node(21),m,p,n,q).*(weight(21)*wei
ght)')+sum(F_int(node',node(22),m,p,n,q).*(weight(22)*weight)')+sum(F_int(node',no
de(23),m,p,n,q).*(weight(23)*weight)')+sum(F_int(node',node(24),m,p,n,q).*(weight(
24)*weight)')+...

```

```

sum(F_int(node',node(25),m,p,n,q).*(weight(25)*weight)')+sum(F_int(node',node(26),
m,p,n,q).*(weight(26)*weight)')+sum(F_int(node',node(27),m,p,n,q).*(weight(27)*wei
ght)')+sum(F_int(node',node(28),m,p,n,q).*(weight(28)*weight)')+sum(F_int(node',no
de(29),m,p,n,q).*(weight(29)*weight)')+sum(F_int(node',node(30),m,p,n,q).*(weight(
30)*weight)'));

```

```

PE_S=@(m,p,n,q)(sum(F_spring1(node',node(1),m,p,n,q).*(weight)')+
sum(F_spring1(node',node(30),m,p,n,q).*(weight)')+sum(F_spring2(node(1),node,m,p,n
,q).*(weight))+ sum(F_spring2(node(30),node,m,p,n,q).*(weight)));

```



```
PE_V1=@(m,p,n,q)(sum(F_ext(node(1),node',m,p,n,q).*(weight(1)*weight)')+sum(F_ext(
node(2),node',m,p,n,q).*(weight(2)*weight)')+sum(F_ext(node(3),node',m,p,n,q).*(we
ight(3)*weight)')+sum(F_ext(node(4),node',m,p,n,q).*(weight(4)*weight)')+sum(F_ext
(node(5),node',m,p,n,q).*(weight(5)*weight)')+sum(F_ext(node(6),node',m,p,n,q).*(w
eight(6)*weight)')+...
```

```
sum(F_ext(node(7),node',m,p,n,q).*(weight(7)*weight)')+sum(F_ext(node(8),node',m,p
,n,q).*(weight(8)*weight)')+sum(F_ext(node(9),node',m,p,n,q).*(weight(9)*weight)')
+sum(F_ext(node(10),node',m,p,n,q).*(weight(10)*weight)')+sum(F_ext(node(11),node'
,m,p,n,q).*(weight(11)*weight)')+sum(F_ext(node(12),node',m,p,n,q).*(weight(12)*w
eight)')+...
```

```
sum(F_ext(node(13),node',m,p,n,q).*(weight(13)*weight)')+sum(F_ext(node(14),node',
m,p,n,q).*(weight(14)*weight)')+sum(F_ext(node(15),node',m,p,n,q).*(weight(15)*wei
ght)')+sum(F_ext(node(16),node',m,p,n,q).*(weight(16)*weight)')+sum(F_ext(node(17)
,node',m,p,n,q).*(weight(17)*weight)')+sum(F_ext(node(18),node',m,p,n,q).*(weight(
18)*weight)')+...
```

```
sum(F_ext(node(19),node',m,p,n,q).*(weight(19)*weight)')+sum(F_ext(node(20),node',
m,p,n,q).*(weight(20)*weight)')+sum(F_ext(node(21),node',m,p,n,q).*(weight(21)*wei
ght)')+sum(F_ext(node(22),node',m,p,n,q).*(weight(22)*weight)')+sum(F_ext(node(23)
,node',m,p,n,q).*(weight(23)*weight)')+sum(F_ext(node(24),node',m,p,n,q).*(weight(
24)*weight)')+...
```

```
sum(F_ext(node(25),node',m,p,n,q).*(weight(25)*weight)')+sum(F_ext(node(26),node',
m,p,n,q).*(weight(26)*weight)')+sum(F_ext(node(27),node',m,p,n,q).*(weight(27)*wei
ght)')+sum(F_ext(node(28),node',m,p,n,q).*(weight(28)*weight)')+sum(F_ext(node(29)
,node',m,p,n,q).*(weight(29)*weight)')+sum(F_ext(node(30),node',m,p,n,q).*(weight(
30)*weight)')));
```

```
K_U=[];
```

```
for p=1:1:T
    for q=1:1:T
        G=[];
        for m=1:1:T
            for n=1:1:T
                % FFint=@(X,Y)F_int(X,Y,m,p,n,q);
                %G1(n)=integral2(FFint,-1,1,-1,1);
                G1(n)=PE_U1(m,p,n,q);
            end
            G=horzcat(G1,G);
        end
        K_U=vertcat(G,K_U);
    end
end
```

```
end
```

```
K_U2=[];
```

```
for p=1:1:T
    for q=1:1:T
        G=[];
        for m=1:1:T
            for n=1:1:T
```

```

        FSp1=@(X)F_spring1(X,-1,m,p,n,q);
        FSp2=@(X)F_spring1(X,1,m,p,n,q);
        FSp3=@(Y)F_spring2(-1,Y,m,p,n,q);
        FSp4=@(Y)F_spring2(1,Y,m,p,n,q);
        FSp5=@(X)F_spring2(X,-1,m,p,n,q);
        FSp6=@(X)F_spring2(X,1,m,p,n,q);
        G1(n)=integral(FSp1,-1,1)+integral(FSp2,-1,1)+integral(FSp3,-
1,1)+integral(FSp4,-1,1)+integral(FSp5,-1,1)+integral(FSp6,-1,1);

        % G1(n)=PE_S(m,p,n,q);
        end
        G=horzcat(G1,G);
    end

    K_U2=vertcat(G,K_U2);
end

end

K_V=[];
for p=1:1:T
    for q=1:1:T
        G=[];
        for m=1:1:T
            for n=1:1:T
                %FFext=@(X,Y)F_ext(X,Y,m,p,n,q);
                %G1(n)=integral2(FFext,-1,1,-1,1);
                G1(n)=PE_V1(m,p,n,q);
            end
            G=horzcat(G1,G);
        end

        K_V=vertcat(G,K_V);
    end
end

end

K_UU=K_U+K_U2;
%A=inv(K_V)*K_U;
Eig=eig(K_UU,K_V);
%disp(Eig)
minEig=min(abs(Eig));
disp(vpa(minEig,5));
%end

```

A4. Intracellular buckling mode shapes of different cell shapes of equal area under uniaxial compression in direction-1 and direction-2

